



TECHNISCHE UNIVERSITÄT MÜNCHEN

Fakultät für Chemie

**Photodissociation Dynamics
in the Presence of Conical Intersections**

DISSERTATION

zur Erlangung des akademischen Grades

Doktor der Naturwissenschaften

vorgelegt von

David Picconi

Garching bei München, 2017



TECHNISCHE UNIVERSITÄT MÜNCHEN

Theoretische Chemie

PHOTODISSOCIATION DYNAMICS
IN THE PRESENCE OF CONICAL INTERSECTIONS

David Picconi

Vollständiger Abdruck der von der Fakultät für Chemie der Technischen Universität München zur Erlangung des akademischen Grades eines

Doktors der Naturwissenschaften

genehmigten Dissertation.

Vorsitzender: Prof. Dr. Corinna Hess

Prüfer der Dissertation:

1. Prof. Dr. Wolfgang Domcke
2. Prof. Dr. Ville Kaila
3. Prof. Dr. Regina de Vivie-Riedle (LMU München)

Die Dissertation wurde am 09.05.2017 bei der Technische Universität München eingereicht und durch die Fakultät für Chemie am 21.06.2017 angenommen.

Abstract

This thesis presents computational studies of molecular photodissociation reactions in the presence of conical intersections. Novel signatures of conical intersections are identified: Fano line shapes in the absorption spectrum and strong mode-specific vibrational excitations in the photofragment state distributions. Approximate methodologies are developed for the calculation of the photoabsorption profile and the product state distributions. These methods are computationally efficient and allow the assignment of the vibrational structures of the absorption and the total kinetic energy release spectra. The photodissociation of ozone and pyrrole are taken as prototypical reactions. For pyrrole, a new *ab initio* potential energy surface has been developed. Quantum dynamical calculations are used to simulate the photodissociation dynamics and to calculate the total absorption cross section, the final product distributions and the resonance Raman spectrum. The techniques of scattering theory for polyatomic fragments are combined with efficient methods for quantum dynamics, such as the multi-configurational time-dependent Hartree (MCTDH) approach. The calculated observables are compared with the experimental measurements and interpreted on the basis of the topography of the potential energy surfaces. The methods developed in this work are suitable for the study of photodissociation in large classes of polyatomic aromatic molecules.

Zusammenfassung

In dieser Arbeit wurden molekulare Photodissoziations-Reaktionen in der Gegenwart von konischen Durchschneidungen numerisch untersucht. Zwei neuartige Signaturen von konischen Durchschneidungen werden identifiziert: (i) Das Absorptionsspektrum zeigt Fano-Linienprofile; (ii) Starke Anregungen von spezifischen Schwingungsmoden werden in der Zustandsverteilung der Photofragmente beobachtet. Um das Absorptionsspektrum und die Zustandsverteilung der Produkte zu berechnen, wurden approximative Methoden entwickelt. Diese Methoden sind numerisch effizient und erlauben die Assignierung von Schwingungsstrukturen im Absorptionsspektrum und im *total kinetic energy release* (TKER) Spektrum. Die Photodissoziations-Reaktionen von Ozon und Pyrrol werden als repräsentative Beispiele betrachtet. Für Pyrrol wurde eine neue *ab initio* Potentialfläche entwickelt. Der Wirkungsquerschnitt der Photodissoziation, die Zustandsverteilung der Produkte und das Resonanz-Raman-Spektrum wurden mit Hilfe von quantendynamischen Simulationen berechnet. Die Technik der Streutheorie für mehratomige Fragmente wird mit effizienten Methoden der Quanten-Dynamik, wie dem *multi-configurational time dependent Hartree* (MCTDH) Ansatz, kombiniert. Die berechneten Observablen werden mit experimentellen Messungen verglichen und mit Bezug auf die Topographie der Potentialflächen interpretiert. Die hier entwickelten Methoden können auf eine große Klasse von mehratomigen aromatischen Molekülen angewandt werden.

This doctoral thesis is based on contributions to international peer-reviewed scientific journals. The work presented in this thesis has been published, has been submitted for publication, or is in a preprint form for forthcoming submission to an international scientific journal, by the time of submission of this thesis. This work describes novel effects of conical intersections on spectroscopic observables for photodissociation reactions and presents approximate methods for the calculation of absorption spectra and photofragment distributions. An overview on the theoretical concepts and the quantum chemical and quantum dynamical methodologies is given. A conspectus is given for three published papers, a submitted paper, and one manuscript in preparation. These contributions are included in the Appendix.

D. P., Garching bei München, May 2017

CONTENTS

1	INTRODUCTION	1
2	THEORY I. NONADIABATIC EFFECTS AND EXCITED STATE DYNAMICS	9
2.1	Molecular Hamiltonian and nonadiabatic effects	9
2.2	Group Born-Oppenheimer approximation and diabatic states	12
2.3	Conical intersections	14
2.4	One-photon transitions	15
2.5	Excited state dynamics	17
3	THEORY II. PHOTODISSOCIATION AS A HALF-COLLISION PROCESS	19
3.1	Jacobi coordinates	20
3.2	Schrödinger equation in Jacobi coordinates	21
3.3	Vibronic states of dissociative molecules	25
3.4	Partial cross sections and photofragment distributions	29
3.4.1	Excited state dynamics and product state distributions	29
4	COMPUTATIONAL METHODS	31
4.1	Electronic structure calculations. The CASSCF method	31
4.1.1	Dynamical correlation. The CASPT2 and MRCI methods	32
4.2	Methods of nuclear quantum dynamics	33
4.2.1	Grid representation and Chebyshev Propagation	33
4.2.2	The multi-configurational time-dependent Hartree method (MCTDH)	35
5	PUBLICATIONS AND MANUSCRIPTS	39
5.1	Signatures of a conical intersection in photofragment distributions and absorption spectra: Photodissociation in the Hartley band of ozone	40
5.2	Intermediate photofragment distributions as probes of non-adiabatic dynamics at conical intersections: application to the Hartley band of ozone	42

5.3	Partial dissociative emission cross sections and product state distributions of the resulting photofragments	44
5.4	Photodissociation dynamics and photofragment distributions in the first absorption band of pyrrole: I. Vibronic Franck-Condon Herzberg-Teller excitation of the ${}^1A_2(\pi\sigma^*) \leftarrow \tilde{X}{}^1A_1(\pi\pi)$ transition	45
5.4.1	Total kinetic energy release spectra of pyrrole: Theory vs Experiment	47
5.4.2	Calculation of the photofragment distributions using the MCTDH package	53
5.5	Fano resonances in the photoinduced H-atom elimination dynamics in the $\pi\sigma^*$ states of pyrrole	54
6	CONCLUSIONS AND PERSPECTIVES	57
	ACKNOWLEDGEMENTS	71
	APPENDIX	73

INTRODUCTION

Photo-initiated chemical reactivity is a field of active theoretical and experimental investigation.¹⁻³ The detailed mechanistic description of the excited state molecular dynamics is of fundamental chemical interest, and instrumental to the ability of controlling reaction outcomes. Photochemistry embraces a large class of reactions triggered by the absorption of a photon of suitable energy. Excited state proton transfer,^{4,5} ring-opening and ring-closure reactions,^{6,7} cis-trans isomerizations in alkenes^{8,9} are just few examples.

This thesis deals with quantum mechanical simulations of photodissociation reactions in small and medium sized molecules from first principles. Bond breaking reactions can occur when the molecule absorbs a photon of energy $E_{\text{ph}} = \hbar\omega$ which is higher than the dissociation energy of one or more bonds, $E_{\text{ph}} > D_0$, where D_0 is the energy difference between the ground states of the dissociated fragments and the parent molecule.

The absorption of a photon promotes an electronic excitation after which the molecule is placed in a transition state located on the potential energy surface (PES) of an excited electronic state. The most favourable reaction path from the parent molecule to the photofragments depends on the topography of the PES, and on the excitation energy. A general rule governing photodissociation dynamics is the following energy balance:

$$E_{\text{ph}} = D_0 + E_{\text{kin}} + E_{\text{int}} , \quad (1.1)$$

where E_{kin} is the kinetic energy associated with the relative inter-fragment motion and E_{int} is the internal energy of the fragments, comprising the electronic, vibrational and rotational energy. The complete description of the fragmentation process involves not only the identification of the resulting molecular products, but also the determination of their quantum mechanical state.

The subject of this work are photodissociation reactions involving the solely breakage of a specific bond, forming a well defined pair of photofragments. In this case, an ensemble of parent molecules, photoexcited with a specific photon energy, produces an ensemble of chemically identical fragment pairs. However, the individual photoproducts are formed in a distribution of internal fragment states. Since the excess energy $E_{\text{ph}} - D_0$ is fixed, Equation (1.1) implies that

photofragments with high internal energy content (as for example, a high degree of vibrational excitation) separate with a slower velocity, whereas internally cold fragments are associated with a higher translational energy. The final state populations, analyzed as a function of the photon energy, are the ‘hallmarks’ of the reaction mechanism. Generally speaking, vibrational modes active in the reaction dynamics are expected to be excited in the fragments.

Particularly interesting is the analysis of product state distributions in the presence of reactive conical intersections, i. e. electronic degeneracies encountered along the dissociation path. Conical intersections are prominent features of several classes of photochemical reactions. They are ubiquitous in molecular systems with a large number of degrees of freedom, and their impact on photochemical reactivity is under extensive scrutiny.^{10–14} Examples include photodissociation of atmospheric trace gases (O_3 , CO_2 , H_2O),^{15,16} alkyl halides¹⁷ and acidic aromatic systems (pyrrole, phenol, etc.).^{18–20}

Figure 1.1 illustrates two prototypical one-dimensional dissociation profiles exhibiting conical intersections of different topographies. Panel (a) shows the potential energy cuts of the excited

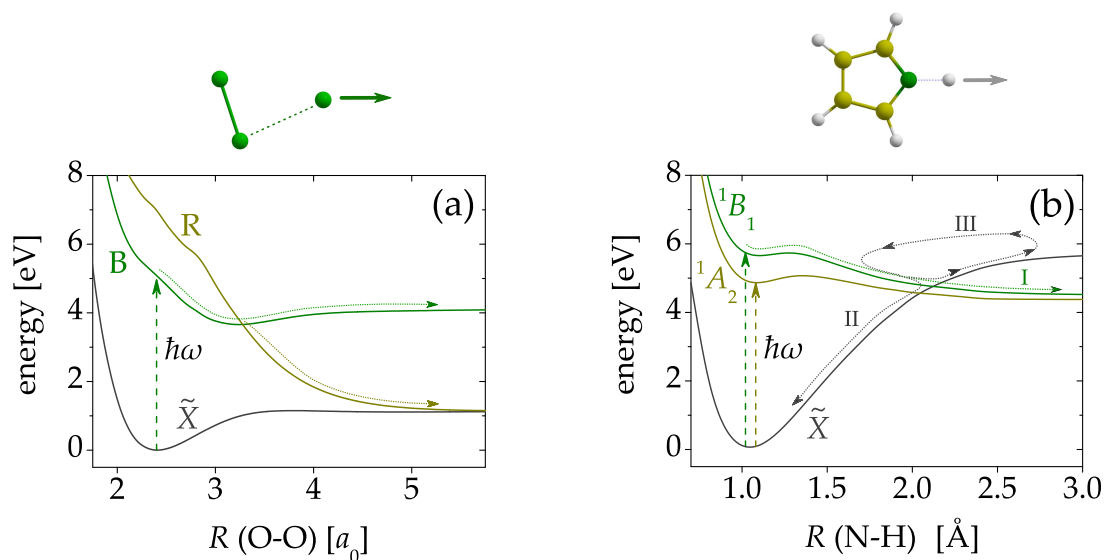


Figure 1.1: (a) Potential energy cuts for the ozone molecule along the O–O bond distance coordinate. Ozone molecules, photoexcited to the B state, can either dissociate directly on the B surface, or undergo an internal conversion via the R state. The ground state \tilde{X} is not involved in the dissociation reaction. (b) Potential energy cuts for the pyrrole molecule along the N–H bond distance coordinate. The electronic excitation to the lowest $\pi\sigma^*$ states (1A_2 and 1B_1) is considered. Two dissociation pathways are sketched: A direct one (I) and a second one (III) involving a temporary sojourn in the bound \tilde{X} state. The pathway II represents the relaxation to the ground state.

singlet states B and R of ozone, involved in the dynamics following the excitation to the Hartley²¹ and Huggins²² bands.²³ Photoexcited molecules are initially located on the B state and two electronic channels are open for $E_{\text{ph}} > 4.0$ eV. During the O \cdots O₂ bond breaking, molecules reach the B/R crossing and branch between the two states: $\approx 90\%$ of the molecules continue the dissociation on the B surface, while the remaining $\approx 10\%$ internally converts to the R state and dissociates on the steep potential descent. The ground electronic state \tilde{X} is not involved in the dissociation process. The vibrational and rotational state distributions of the oxygen molecules emerging in the two channels have been measured in detail.²⁴

A different arrangement of the PESs is depicted in Figure 1.1(b). The dissociation profiles are shown for the two lowest singlet $\pi\sigma^*$ states of pyrrole (labelled 1A_2 and 1B_1). In the long wavelength excitation range, these repulsive states can be directly populated. Along the dissociation pathway, intersections are encountered with the bound electronic ground state (\tilde{X}), which make several reaction mechanisms possible. Molecules can dissociate directly on the 1A_2 or the 1B_1 states (pathway I), or relax to the \tilde{X} state (pathway II). An alternative dissociation path starts from a $\pi\sigma^*$ state and involves a temporary sojourn on the \tilde{X} state and back (pathway III).

Detailed studies of photodissociation dynamics for a number of molecular systems have been performed in the last decades, benefiting from a tremendous improvement of spectroscopic techniques. Chemical reactions have been studied both in the time and in the energy domain.

A wide class of time-dependent methods belong to the pump-probe category. They are based on the interaction of a molecule with a pair of light pulses. The first pulse ('pump') excites the molecule and initiates the photodissociation. The second pulse ('probe') is delayed in time and is used to monitor a spectroscopic observable as a function of the time delay. The most common probes are resonance-enhanced multi-photon ionization (REMPI)²⁵ and ion yield spectroscopy²⁶ of the detached atom, as well as photoelectron spectroscopy^{27,28}. These experiments provide information on the time scales of the reaction. The presence of multiple time scales in time-dependent spectroscopic signals can reveal a multi-step dissociation process or a simultaneous presence of several dissociation mechanisms.

Energy-dependent quantities can be measured using photofragment translational spectroscopies. These techniques include velocity map ion imaging^{29,30} and H (Rydberg) atom tagging,^{31,32} which have been exhaustively reviewed in the recent literature.

The ozone and pyrrole molecules, whose excited state dynamics is studied in this work, provide excellent examples of the use of translational spectroscopies. Figure 1.2 shows total kinetic energy release (TKER) spectra for the photodissociation of ozone and pyrrole, corresponding to the

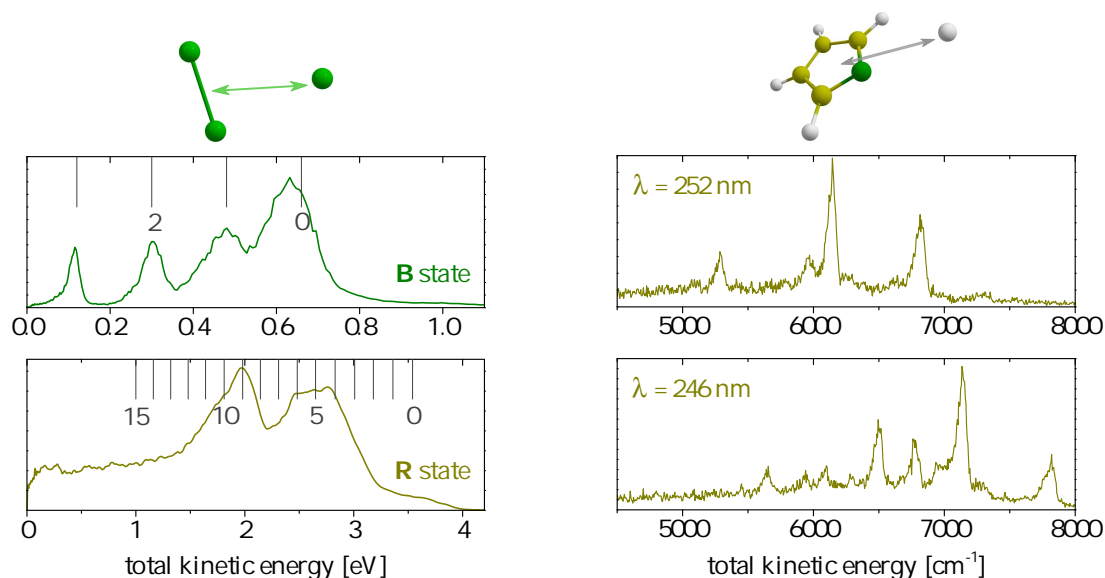


Figure 1.2: Total kinetic energy release (TKER) spectra for the photodissociation of ozone (left panels) and pyrrole (right panels), taken from References 24 and 33. For ozone, the distributions were measured for the fragments formed in the states B and R for the excitation wavelength $\lambda = 266$ nm; the vibrational quantum numbers are indicated as combs.

diagrams of Figure 1.1. The TKER spectra are distributions of the translational energy of the relative atom–fragment motion, measured for a fixed excitation energy. By energy conservation, the TKER profiles are reporters of the internal energy distributions of the co-fragments. The reason why they are called ‘spectra’ is that they exhibit peaks corresponding to the vibrational energy levels of the oxygen and pyrrolyl fragment molecules; the intensities give the corresponding state populations.

In ozone, the only fragment vibrational mode is the O – O stretch. The molecules following the *diabatic* dissociation pathway on the B state end up in the upper electronic channel and exhibit a cold product state distribution. The vibrational progression is visible in the TKER spectrum as broad peaks, and includes few energy levels. Molecules dissociating along the *adiabatic* path undergo a B \rightarrow R transition, and form fragments in the ground electronic state. For a given photon energy, the product state distributions are dramatically different between the upper and lower channel. In the R state, the kinetic energy for the relative O – O₂ motion is higher and the resulting oxygen molecules are, at the same time, vibrationally hotter. The higher translational energy, associated with the photoproducts in the lower channel, is due to a higher excess energy $E_{\text{ph}} - D_0$. On the other hand, the reason for the considerably higher vibrational excitation is not clear. The main purpose of the computational studies of this reaction is to reveal the mechanism for the energy distribution between the different electronic, vibrational and rotational degrees of

freedom: How do the TKER spectra depend on the excitation energy? In the R channel, does the additional energy flow preferentially into the O – O₂ translation or the O₂ vibration? Is the O₂ vibrational excitation formed in the region of the conical intersection or in the subsequent descent along the repulsive potential?

The molecule of pyrrole has a higher complexity and is a prototype for a number of photodissociation reactions involving a H–heteroatom bond rupture in $\pi\sigma^*$ states. The $\pi\sigma^*$ states are formed by promoting an electron from a valence π orbital of the aromatic ring to a σ^* orbital localised on the N atom.³⁴ The presently accumulated evidence indicates that the excitation in the wavelength range 254 – 240 nm directly populates the lowest $\pi\sigma^*$ (1A_2) state and the pyrrolyl co-fragment is formed in the ground electronic state on a femtosecond time scale.^{26,28} The TKER spectra have been measured by Ashfold and coworkers, using the Rydberg tagging technique, for a wide range of excitation energies.³³ The peak assigned to the ground vibrational state, corresponding to the maximum translational energy available, is easily identified in the TKER spectra. The peaks at lower translational energies are associated with vibrational states involving one or two quanta excitations on the pyrrolyl modes. The final populations of the individual vibrational states are given by the peak intensities. Some peaks can be attributed simply from the knowledge of the pyrrolyl frequencies, but the complete assignment of the TKER spectra is a challenging task for this and other polyatomic systems. Moreover, a comprehensive analysis of the peak intensities is still missing and spectroscopic signatures of the $\tilde{X}/\pi\sigma^*$ conical intersections are still not well understood.

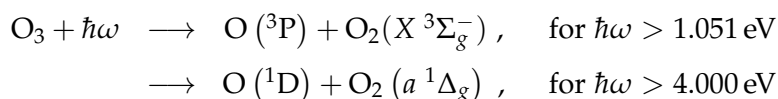
The detailed understanding of the dissociation mechanism, the interpretation of the wavelength-dependent intensity patterns in the TKER spectra and the elucidation of the role of conical intersections require a combination of experimental results and computer simulations.

In order to model excited state reactions from first principles, the methods of quantum chemistry must be combined with techniques of molecular (quantum) dynamics and with scattering theory. A schematic modelling strategy involves the following steps:

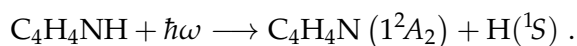
1. *The characterization of the electronic states involved in the reaction.* This task consists in a set of electronic structure calculations for many molecular geometries. First, the states which can potentially participate to the reaction must be identified; second, one needs to establish the level of theory which is adequate to describe the features of the PESs along the possible reaction pathways. If the molecular motion is described quantum mechanically, the PESs must be pre-calculated and set up in an appropriate functional form.

2. *The time evolution of the photoexcited molecule, using classical or quantum mechanics.* In classical simulations, a number of initial nuclear coordinates and momenta are sampled from an appropriate distribution function. The molecular motion is evaluated according to Hamilton equations, using the PESs obtained from quantum chemical calculations. As a result, a set of phase space trajectories is obtained. In the application to photodissociation, classical dynamics calculations are fast, and can be easily implemented evaluating the potentials ‘on-the-fly’. The drawback is the inadequate or approximate description of quantum mechanical features: Tunnelling, internal conversion, interference between reaction paths, zero-point energies, initial vibrationally excited states, etc. Moreover, electronic spectroscopies are usually formulated in terms of transitions between quantum energy levels, and the definition of spectroscopic signals in terms of classical trajectories is not always straightforward.^{35,36} In quantum dynamics calculations, the nuclear motion is described using a wavefunction which is propagated in time according to the time-dependent Schrödinger equation. The resulting wave packet motion accounts for all quantum mechanical effects and allows the exact definition of spectroscopic observables. However, the integration of Schrödinger equation is numerically demanding, and can be performed exactly only for systems with few degrees of freedom ($< 10 - 20$) or using simple model Hamiltonians.³⁷ For molecules with many degrees of freedom, one needs to perform a large number of quantum chemical calculations which are necessary to pre-calculate the PESs.
3. *The analysis of the results.* Observables are calculated from trajectories (in classical simulations) or from time-dependent wave packets (in quantum mechanical calculations). The results of the calculations are compared with experimental measurements to assess the quality of the model used in the simulation. In the final stage, connections are established between the observables and the reaction mechanism, and the signatures of the PES topography are possibly found in spectroscopic signals. The connection between excited state dynamics and the final state populations is provided by scattering theory.

This work reports simulations of two photo-initiated bond-breaking reactions: The photodissociation of ozone in the Hartley band,



and the photodissociation of pyrrole, following the excitation to the lowest $\pi\sigma^*$ state



Both reactions were studied using quantum mechanical calculations on *ab initio*-derived potential energy surfaces.

The near ultraviolet excitation of ozone is of fundamental importance in atmospheric chemistry and has been extensively studied both theoretically and experimentally.^{38-43,23} The dissociation following the excitation to the B state (see Figure 1.1) involves the electronic states B and R. Excited state dynamics simulations were performed for the energy range in which both electronic channels are open. The PESs calculated by Schinke and McBane⁴⁴ at the multi-reference configuration interaction (MRCI) level were used, and their quality was assessed by comparison of the calculated absorption spectrum and product state distributions with the experimental measurements (Section 5.1).^{24,45,46} The study of this reaction had two main goals: i) To establish a connection between the final vibrational populations, derived from the TKER spectra (see Figure 1.2), and the energy exchange occurring at the B/R conical intersection; ii) To identify spectroscopic signals which exhibit 'hallmarks' of the intersection. The bond rupture mechanism was visualized using vibrational state populations of the emerging, but still interacting, photofragments. Such intermediate distributions were related to the peak amplitudes in the resonance Raman profile of the dissociating molecule (Sections 5.2 and 5.3).⁴⁷⁻⁴⁹

Being a triatomic molecule, the electronic structure of ozone can be studied with high level of theory and the full-dimensional construction of the PESs is computationally possible. Furthermore, several methods are available to perform numerically exact quantum dynamical simulations (Section 4.2.1).^{50,51}

The study of the photodissociation of pyrrole requires that the standard analysis performed for triatomic molecules is extended to polyatomic systems. Pyrrole is a prototypical heteroaromatic molecule, whose structure is present in a number of biomolecules, as for example the amino acid tryptophan and porphyrin and chlorin compounds. The electronic structure and the UV-induced photodissociation of pyrrole have been extensively debated in a number of experimental and theoretical studies.^{52,53,25,54-63} This work focuses on the excited state dynamics in the long wavelength region of the absorption spectrum. The purpose of the investigation was to interpret the TKER spectra of Ref. 33, as well as time-resolved experiments,^{26,28} and to look for evidences of the $\tilde{X}/\pi\sigma^*$ conical intersections in spectroscopic observables.

Full-dimensional potential energy surfaces for the \tilde{X} , 1A_2 and 1B_1 states of pyrrole were constructed with *ab initio* CASPT2 calculations. Next, different sets of quantum dynamical simulations were performed. One set employed reduced-dimensionality PESs of the three states, including from three to six degrees of freedom. The focus was on the linear absorption profiles of the

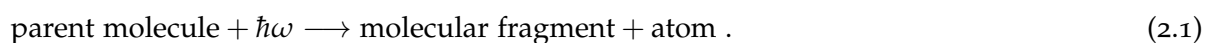
${}^1A_2 \leftarrow \tilde{X}$ and ${}^1B_1 \leftarrow \tilde{X}$ excitations. The presence of the $\tilde{X}/\pi\sigma^*$ conical intersections is revealed in the spectrum through the appearance of narrow peaks which originate from a Fano interference between direct dissociation and a second reaction pathway involving a temporary sojourn in the \tilde{X} state (Section 5.5).

Another set of quantum mechanical calculations involved the electronic states \tilde{X} and 1A_2 (Section 5.4). The nuclear motion was studied for several models, including up to 15 degrees of freedom, namely the three coordinates of the detaching hydrogen atom, and the most active normal modes of the pyrrolyl ring. The time-dependent nuclear wavefunction was used to calculate the absorption spectrum and the product state distributions. The spectroscopic observables were carefully analyzed in order to make connections with the initial state after the excitation and with the topographic features of the PESs. To the best of our knowledge, these set of calculations are the first attempt to simulate in detail the vibrational structure of the TKER spectra arising from the photodissociation of a polyatomic system (>4-5 atoms) using quantum dynamics. The computed TKER profiles were critically compared with the experimental measurements and an assignment of the most intense peaks was suggested.

This thesis is organized as follows. The publications on which this work is based are listed in Chapter 5. Chapters 2 and 3 provide the basic concepts of the theories of nonadiabatic molecular dynamics and photodissociation. The computational methods are briefly described in Chapter 4. Concluding statements and future perspectives are presented in Chapter 6.

THEORY I. NONADIABATIC EFFECTS AND EXCITED STATE DYNAMICS

The dissociation reactions described in this work are triggered by the absorption of a single photon whose energy is sufficient to break a single bond. I refer to photodissociation into two-particle arrangement channel with one fragment being an atom. The overall reaction is outlined as



The quantum mechanical description of a dissociation process requires the theory of *scattering*. Indeed, a photodissociation reaction can be viewed as the second half of a collision process. In a full collision, the reactants approach each other from infinite distance, form an intermediate complex, and evolve toward the products. In photodissociation, the excited state intermediate complex is generated by photon absorption. Since we are interested in reactions involving several electronic states, we need to combine the theory of scattering with the formalism of *nonadiabatic molecular quantum mechanics*.

This and the next Chapter provide a summary of the theoretical machinery which was used in this work. Only the topics necessary for the understanding of the papers of Chapter 5 are presented. More exhaustive reviews or textbooks are cited for the interested reader.

2.1 Molecular Hamiltonian and nonadiabatic effects

In order to define the molecular Hamiltonian, the molecular configurations are described with a set of nuclear (\mathbf{R}) and electronic (\mathbf{r}) coordinates. In the actual calculations, the origin of the system of reference is typically chosen to be the center of nuclear masses, and the positions of the electrons are represented by Cartesian coordinates [$\mathbf{r} = (x_1, y_1, z_1, \dots, x_N, y_N, z_N)$]. The precise definition of the nuclear degrees of freedom is usually adapted to the molecular process of interest and is not

important at the moment. In Section 3.1 a set of coordinates particularly suitable for dissociation reactions will be discussed.

Using the coordinates (\mathbf{r}, \mathbf{R}) , the Schrödinger form of the molecular Hamiltonian is

$$\mathcal{H} = \mathcal{T}_{\text{nuc}} + \mathcal{T}_{\text{el}} + \mathcal{U}(\mathbf{r}, \mathbf{R}) , \quad (2.2)$$

where \mathcal{T}_{nuc} and \mathcal{T}_{el} are the nuclear and electronic kinetic energy operators, respectively, and $\mathcal{U}(\mathbf{r}, \mathbf{R})$ is the total Coulomb potential of electrons and nuclei.

The standard procedure^{64,65} to characterize the electron-nuclear state of the molecule consists, as a first step, in identifying the nuclear geometry-dependent eigenstates of the electronic Hamiltonian:

$$\mathcal{H}_{\text{el}} = \mathcal{T}_{\text{el}} + \mathcal{U}(\mathbf{r}, \mathbf{R}) , \quad (2.3a)$$

$$\mathcal{H}_{\text{el}}(\mathbf{R})\psi_i(\mathbf{r}; \mathbf{R}) = V_i(\mathbf{R})\psi_i(\mathbf{r}; \mathbf{R}) . \quad (2.3b)$$

One needs to fix the nuclear geometry \mathbf{R} and solve the Schrödinger equation for the electrons, Eq. (2.3b), using an appropriate quantum chemical method (see Section 4.1). The resulting electronic wavefunctions $\psi_i(\mathbf{r}; \mathbf{R})$ depend parametrically on the nuclear geometry and are denoted *adiabatic* electronic states. The corresponding eigenvalues $V_i(\mathbf{R})$ are also geometry-dependent and are called *adiabatic potential energy surfaces* (PES).

The set of electronic states $\{\psi_i(\mathbf{r}; \mathbf{R})\}$ is orthogonal and complete,

$$\int \psi_i^*(\mathbf{r}; \mathbf{R})\psi_j(\mathbf{r}; \mathbf{R})d\mathbf{r} = \delta_{ij} , \quad (2.4a)$$

$$\sum_i \psi_i(\mathbf{r}; \mathbf{R})\psi_i(\mathbf{r}'; \mathbf{R}) = \delta(\mathbf{r} - \mathbf{r}') , \quad (2.4b)$$

and defines an electronic basis set, which is used to define a representation of the total molecular wavefunction $\Psi(\mathbf{r}, \mathbf{R})$ for the combined electron-nuclear state. As a result, we obtain a set $\{\chi_i(\mathbf{R})\}$ of nuclear wavefunctions, one for each electronic state,

$$\chi_i(\mathbf{R}) = \langle \psi_i(\mathbf{r}; \mathbf{R}) | \Psi(\mathbf{r}, \mathbf{R}) \rangle_{\mathbf{r}} , \quad (2.5)$$

where the integral $\langle \rangle_{\mathbf{r}}$ is performed only over the electronic coordinates. The norm of the nuclear wavefunctions defines the *adiabatic state population*: $P_i = \langle \chi_i(\mathbf{R}) | \chi_i(\mathbf{R}) \rangle$.

Analogously, the Hamiltonian (2.2) is represented in the adiabatic electronic basis. This amounts to constructing a Hamiltonian matrix $\{H_{ij}(\mathbf{R})\}$, whose elements are operators in the \mathbf{R} -space,

$$H_{ij}(\mathbf{R}) = \langle \psi_i(\mathbf{r}; \mathbf{R}) | \mathcal{H} | \psi_j(\mathbf{r}; \mathbf{R}) \rangle_{\mathbf{r}} . \quad (2.6)$$

$$\begin{aligned}
 \Psi(\mathbf{r}, \mathbf{R}) &\Rightarrow \begin{pmatrix} \chi_1(\mathbf{R}) \\ \chi_2(\mathbf{R}) \\ \vdots \end{pmatrix} & \mathcal{H} &\Rightarrow \begin{pmatrix} H_{11}(\mathbf{R}) & H_{12}(\mathbf{R}) & \cdots \\ H_{21}(\mathbf{R}) & H_{22}(\mathbf{R}) & \cdots \\ \vdots & \vdots & \ddots \end{pmatrix} \\
 \Psi'(\mathbf{r}, \mathbf{R}) = \mathcal{H}\Psi(\mathbf{r}, \mathbf{R}) &\Rightarrow \begin{pmatrix} \chi'_1(\mathbf{R}) \\ \chi'_2(\mathbf{R}) \\ \vdots \end{pmatrix} = \begin{pmatrix} H_{11}(\mathbf{R}) & H_{12}(\mathbf{R}) & \cdots \\ H_{21}(\mathbf{R}) & H_{22}(\mathbf{R}) & \cdots \\ \vdots & \vdots & \ddots \end{pmatrix} \begin{pmatrix} \chi_1(\mathbf{R}) \\ \chi_2(\mathbf{R}) \\ \vdots \end{pmatrix}
 \end{aligned}$$

Figure 2.1: Representation of the molecular Hamiltonian and wavefunction using an electronic basis. Each electronic state has an associated nuclear wavefunction $\chi_i(\mathbf{R})$. The action of the Hamiltonian mixes the different components through the off-diagonal operators $H_{ij}(\mathbf{R})$ ($i \neq j$).

The correspondence between molecular Hamiltonian and wavefunction and their representation in terms of matrices and vectors is illustrated in Figure 2.1.

Combining Equations (2.2), (2.3) and (2.4), the following expression for the Hamiltonian matrix can be derived:

$$H_{ij}(\mathbf{R}) = (\mathcal{T}_{\text{nuc}} + V_i(\mathbf{R})) \delta_{ij} + \Lambda_{ij}(\mathbf{R}), \quad (2.7)$$

with⁶⁴

$$\Lambda_{ij}(\mathbf{R}) = \int \psi_i^*(\mathbf{r}; \mathbf{R}) [\mathcal{T}_{\text{nuc}}, \psi_j(\mathbf{r}; \mathbf{R})] \, d\mathbf{r}. \quad (2.8)$$

The terms $\mathcal{T}_{\text{nuc}} + V_i(\mathbf{R})$, appearing on the diagonal of the adiabatic Hamiltonian matrix, represent Hamiltonian operators associated with i -th electronic state. The electronic Schrödinger equation defines, for each electronic state, a potential energy surface which governs the dynamics within that state. The kinematic terms $\Lambda_{ij}(\mathbf{R})$ of Equation (2.8) originate from the dependence of the electronic wavefunctions on the nuclear coordinates. For $i \neq j$, the off-diagonal terms Λ_{ij} account for the interaction between the nuclear wavefunctions $\chi_i(\mathbf{R})$ which belong to different electronic states. When the adiabatic basis is used, the terms $\Lambda_{ij}(\mathbf{R})$ are called *nonadiabatic couplings*, and describe the process of internal conversion, i. e. the nonradiative population transfer between electronic states, mediated by the nuclear motion.

The interested reader can find detailed descriptions of the nonadiabatic couplings in References 64 and 65. The exact expression of the operators $\Lambda_{ij}(\mathbf{R})$ depends on the choice of the nuclear coordinates, and will not be discussed here. I limit myself by remarking only two important properties:

1. Because of the commutator $[\mathcal{T}_{\text{nuc}}, \psi_i(\mathbf{r}; \mathbf{R})]$, the operators $\Lambda_{ij}(\mathbf{R})$ are given as the sum of a local and a differential operator⁶⁴. They are general kinematic operators which depend on both the nuclear coordinates and momenta. They become negligible when the electronic wavefunctions are weakly dependent on the nuclear geometry.
2. It can be shown that the off-diagonal terms $\Lambda_{ij}(\mathbf{R})$ are inversely proportional to the adiabatic potential energy difference,⁶⁵ $\Lambda_{ij}(\mathbf{R}) \sim (V_i(\mathbf{R}) - V_j(\mathbf{R}))^{-1}$. Therefore, the nonadiabatic couplings can be safely neglected at geometries where the energy gap between the electronic states is large. In contrast, they become singular at the molecular geometries for which the adiabatic PESs are close in energy.

In photo-initiated reactions, it is important to determine whether the molecule evolves toward near-degeneracy geometries. In this case, the passage from an electronic state to a neighbouring state is expected to be fast and effective.

2.2 Group Born-Oppenheimer approximation and diabatic states

The reactions studied in this work occur in an energy range which includes a limited number of electronic states. It is then useful for calculation purposes to truncate the Hamiltonian matrix (2.7) in order to include only the rows and columns corresponding to the electronic states of interest (group Born-Oppenheimer approximation).

The resulting truncated Hamiltonian matrix has a finite size and contains the couplings (Λ_{ij}) between the selected electronic states. The *ab initio* evaluation of such terms is not always computationally cheap. Moreover, the nonadiabatic couplings diverge in proximity of electronic degeneracies. In the presence of cusps of singularities, nuclear quantum dynamical simulations converge slowly with respect to the number of basis functions or grid points.⁶⁶

The usual approach to quantum mechanical calculations is to perform an orthogonal transformation between the electronic adiabatic states and represent the Hamiltonian in a basis of *diabatic states*. The adiabatic-to-diabatic transformation is easily illustrated in a two-state model. In this case, the Hamiltonian has the following adiabatic representation:

$$\mathcal{H} = \begin{pmatrix} \mathcal{T}_{\text{nuc}} + \Lambda_{11}(\mathbf{R}) & \Lambda_{12}(\mathbf{R}) \\ \Lambda_{21}(\mathbf{R}) & \mathcal{T}_{\text{nuc}} + \Lambda_{22}(\mathbf{R}) \end{pmatrix} + \begin{pmatrix} V_1(\mathbf{R}) & 0 \\ 0 & V_2(\mathbf{R}) \end{pmatrix}. \quad (2.9)$$

The diabatic electronic states $\{\tilde{\psi}_1, \tilde{\psi}_2\}$ are obtained by an orthogonal transformation of the adiabatic wavefunctions $\{\psi_1, \psi_2\}$. The transformation matrix is parametrized by a mixing angle $\alpha(\mathbf{R})$,

$$\begin{pmatrix} \tilde{\psi}_1(\mathbf{r}; \mathbf{R}) \\ \tilde{\psi}_2(\mathbf{r}; \mathbf{R}) \end{pmatrix} = \begin{pmatrix} \cos \alpha(\mathbf{R}) & \sin \alpha(\mathbf{R}) \\ -\sin \alpha(\mathbf{R}) & \cos \alpha(\mathbf{R}) \end{pmatrix} \begin{pmatrix} \psi_1(\mathbf{r}; \mathbf{R}) \\ \psi_2(\mathbf{r}; \mathbf{R}) \end{pmatrix}, \quad (2.10)$$

and the aim of the transformation is to remove the inter-state nonadiabatic couplings. Ideally, the operators $\Lambda_{12}(\mathbf{R})$ should be calculated, and the angle $\alpha(\mathbf{R})$ should be chosen in order to nullify the transformed nonadiabatic couplings $\tilde{\Lambda}_{12} = \int \tilde{\psi}_1^* [\mathcal{T}_{\text{nuc}}, \tilde{\psi}_2] d\mathbf{r}$. However, it is generally impossible in polyatomic systems to define a small set of strictly diabatic states.⁶⁶ Several methods have been proposed to approximately impose the condition $\tilde{\Lambda}_{ij} \approx 0$, so that the kinematic inter-state couplings can be neglected in molecular quantum mechanical calculations. The working Hamiltonian is then usually represented in the diabatic basis

$$\tilde{\mathcal{H}} = \begin{pmatrix} \mathcal{T}_{\text{nuc}} & 0 \\ 0 & \mathcal{T}_{\text{nuc}} \end{pmatrix} + \begin{pmatrix} W_1(\mathbf{R}) & W_{12}(\mathbf{R}) \\ W_{12}(\mathbf{R}) & W_2(\mathbf{R}) \end{pmatrix} \quad (2.11)$$

where the potential matrix becomes non-diagonal

$$\begin{pmatrix} W_1(\mathbf{R}) & W_{12}(\mathbf{R}) \\ W_{12}(\mathbf{R}) & W_2(\mathbf{R}) \end{pmatrix} = \begin{pmatrix} \cos \alpha(\mathbf{R}) & -\sin \alpha(\mathbf{R}) \\ \sin \alpha(\mathbf{R}) & \cos \alpha(\mathbf{R}) \end{pmatrix} \begin{pmatrix} V_1(\mathbf{R}) & 0 \\ 0 & V_2(\mathbf{R}) \end{pmatrix} \begin{pmatrix} \cos \alpha(\mathbf{R}) & \sin \alpha(\mathbf{R}) \\ -\sin \alpha(\mathbf{R}) & \cos \alpha(\mathbf{R}) \end{pmatrix}. \quad (2.12)$$

The fact that the kinematic couplings are negligible implies that the diabatic electronic wavefunctions do not undergo fast configurational changes under nuclear geometrical distortions. The diabatic potentials $W_i(\mathbf{R})$ and $W_{ij}(\mathbf{R})$ are smooth functions of the nuclear coordinates, and are therefore suitable for numerical simulations.

The electronic Schrödinger equation (2.3b) can be solved using the methods of quantum chemistry which yield adiabatic, rather than diabatic, potential energy surfaces. When the electronic states are well separated in energy, the adiabatic and diabatic PESs coincide (apart from a reordering). Near degeneracies, either the behaviour of the adiabatic PESs or the dependence of electronic properties on the nuclear geometry can be investigated to find the mixing angle $\alpha(\mathbf{R})$ and to construct the diabatic potentials.⁶⁶

2.3 Conical intersections

The adiabatic potential energy surfaces $V_i(\mathbf{R})$ are formally defined as eigenvalues of the diabatic potential matrix,[†]

$$V_{1,2}(\mathbf{R}) = \frac{W_1(\mathbf{R}) + W_2(\mathbf{R})}{2} \pm \sqrt{\left(\frac{W_1(\mathbf{R}) - W_2(\mathbf{R})}{2}\right)^2 + W_{12}^2(\mathbf{R})}, \text{ with } V_1(\mathbf{R}) \leq V_2(\mathbf{R}). \quad (2.13)$$

Electronic degeneracies occur at geometries for which $V_1(\mathbf{R}) = V_2(\mathbf{R})$, i. e. when the conditions

$$\begin{aligned} W_1(\mathbf{R}) &= W_2(\mathbf{R}) \\ W_{12}(\mathbf{R}) &= 0 \end{aligned} \quad (2.14)$$

are fulfilled.

In diatomic molecules, the only nuclear degree of freedom is the atom-atom distance (R) and it is generally impossible to find a geometry for which Equations (2.14) are simultaneously satisfied.[‡] In polyatomic molecules, true adiabatic crossings can occur, especially when the number of degrees of freedom is large. Given an intersection geometry \mathbf{R}_0 , a particular role in the dynamics is played by the degrees of freedom which are able to remove the electronic degeneracy. In order to identify such nuclear coordinates, we consider the variation of the energy difference $V_2 - V_1$ as a function of the displacement δR_i from \mathbf{R}_0 along a coordinate R_i . Straightforward algebra gives

$$\delta(V_2 - V_1) = \left[\left(\frac{\partial(W_1 - W_2)}{\partial R_i} \right)_{\mathbf{R}_0}^2 + 4 \left(\frac{\partial W_{12}}{\partial R_i} \right)_{\mathbf{R}_0}^2 \right]^{\frac{1}{2}} |\delta R_i|. \quad (2.15)$$

Equation (2.15) has the following physical interpretation: At a two-state crossing ($V_1 = V_2$), it is possible to find at most two ‘directions’ in the nuclear space along which the degeneracy is lifted. These are collective coordinates defined as the gradients $\partial(W_1 - W_2)/\partial \mathbf{R}$ (*tuning mode*, along which the degeneracy is removed the fastest) and $\partial W_{12}/\partial \mathbf{R}$ (*coupling mode*, along which the inter-state coupling grows the fastest). Provided that the tuning mode and the coupling mode are non-zero and do not coincide, the crossing is denoted as *conical intersection*.

Figure 2.2 shows illustrative topographies of conical intersections, in which the tuning mode is a dissociation coordinate. In a molecule with N degrees of freedom, the intersection is characterized by a two-dimensional *branching space* and a $(N - 2)$ -dimensional *seam space*, spanned by coordinates along which the degeneracy is maintained.

[†] Equation (2.13) is valid only for real coupling functions $W_{12}(\mathbf{R})$, therefore it cannot be applied in the case of a coupling induced by the spin-orbit interaction.

[‡] If the symmetry of the electronic wavefunctions is such that $W_{12}(R) = 0$, then a *symmetry-allowed* intersection is possible.

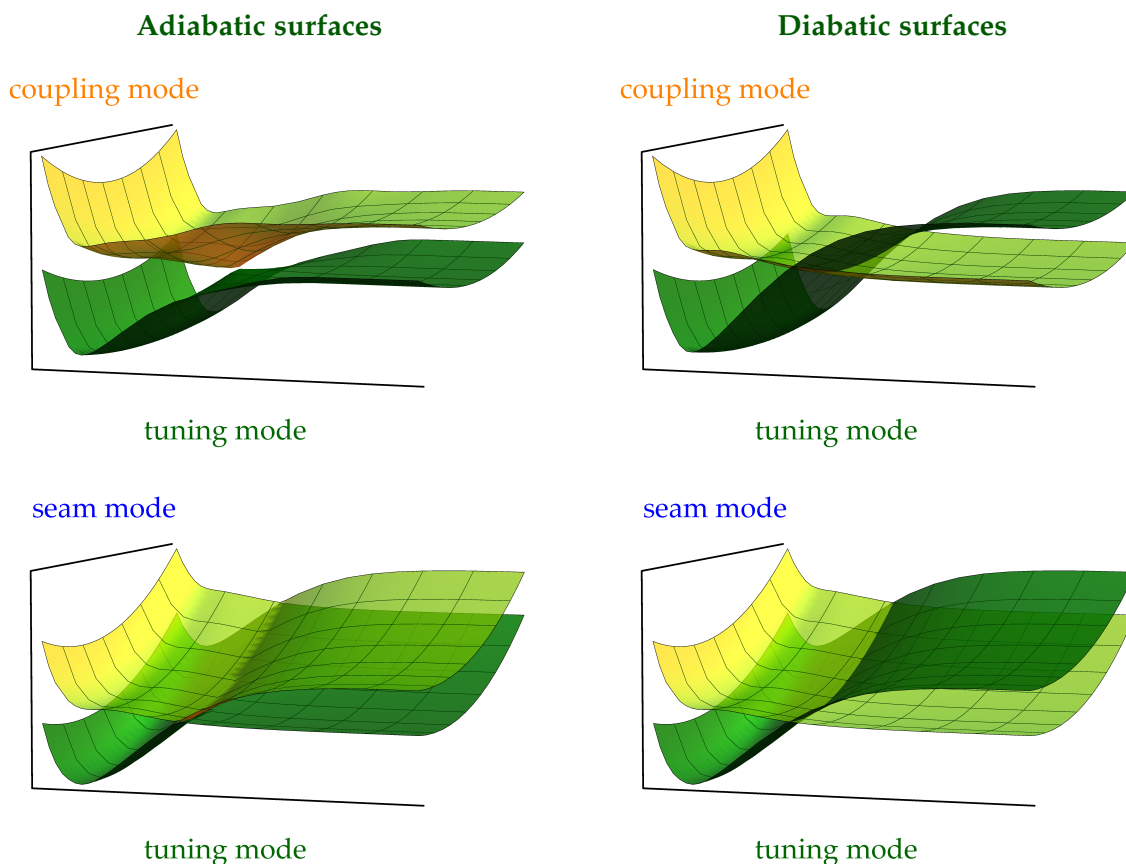


Figure 2.2: Illustrative sketch of a reactive conical intersection for which the tuning mode is a dissociation coordinate. The surfaces are based on the PESs of pyrrole and are plotted in the adiabatic (left panels) and the diabatic (right panels) representations. The conical intersection topography is represented in the branching space (top panels) and in the space defined by the tuning mode and a seam mode (bottom panels).

2.4 One-photon transitions

A molecule in a stationary electronic state can be promoted to another electronic state by interaction with an electromagnetic field. In the limit of weak fields, the transition can be ascribed to the absorption or emission of a photon and described using first-order perturbation theory.

We describe the molecule using a group Born-Oppenheimer representation with N_{el} electronic states $\{|0\rangle, |1\rangle, \dots, |N_{\text{el}} - 1\rangle\}$. In the diabatic representation, the molecular Hamiltonian has the form[†]

$$\mathcal{H} = \mathcal{T}_{\text{nuc}} \mathbf{1} + \sum_{\alpha, \beta=0}^{N_{\text{el}}-1} |\alpha\rangle W_{\alpha\beta}(\mathbf{R}) \langle\beta|, \quad (2.16)$$

[†] The diabatic Hamiltonian was indicated as $\tilde{\mathcal{H}}$ in Section 2.2. Here, we drop the tilde (\sim) for clarity of notation.

where the identity operator is defined as $\mathbf{1} = \sum_{\alpha} |\alpha\rangle\langle\alpha|$.

The eigenstates of the Hamiltonian (2.16) can be written as linear combinations of diabatic states:

$$\begin{aligned}\mathcal{H}|\Psi_n\rangle &= E_n|\Psi_n\rangle \\ |\Psi_n\rangle &= \sum_{\alpha=0}^{N_{el}-1} \Psi_n^{(\alpha)}(\mathbf{R})|\alpha\rangle\end{aligned}\quad (2.17)$$

Without loss of generality, we take as initial stationary state the ground state of the electron-nuclear Hamiltonian \mathcal{H} .[‡] In our studies, this state is always localized on the lowest diabatic state $|0\rangle$. We therefore drop the superscript (α) in Equation (2.17) and express the initial wavefunction as

$$|\Psi_0\rangle = \Psi_0^{(1)}(\mathbf{R})|1\rangle \equiv \Psi_0(\mathbf{R})|0\rangle. \quad (2.18)$$

When the molecule interacts with light, the absorption of one photon can stimulate a transition from the state $|\Psi_0\rangle$ to any of the states $|\Psi_n\rangle$. Macroscopically, the molecular light-induced transitions can be observed through the attenuation of a light beam passing through a sample of molecules. According to Beer's law, the intensity of the beam decreases exponentially as a function of the optical path l and the density of absorbing molecules ρ ,

$$I = I_0 e^{-\sigma \rho l}. \quad (2.19)$$

The *total absorption cross section* $\sigma(\omega)$ depends on the frequency of the incident light and it is an intrinsic molecular property. The explicit expression for $\sigma(\omega)$ can be derived from the first-order perturbation theory of the light-matter interaction^{67,68} and involves the matrix elements of the electric dipole operator,

$$\sigma(\omega) = \sum_n \frac{\pi}{\hbar \epsilon_0 c} \omega_{n0} \delta(\omega - \omega_{n0}) |\langle \Psi_n | \boldsymbol{\mu} \cdot \boldsymbol{\varepsilon} | \Psi_0 \rangle|^2, \quad (2.20)$$

where $\omega_{n0} = (E_n - E_0) / \hbar$, $\boldsymbol{\varepsilon}$ is the polarization vector of the electric field, and $\boldsymbol{\mu} = (\mu_x, \mu_y, \mu_z)$ is the vector dipole operator. The main physical content of Equation (2.20) is that a radiation of frequency ω can promote a transition only between states whose energy difference is in resonance with ω . Moreover, transitions for which the matrix element $\langle \Psi_n | \boldsymbol{\mu} \cdot \boldsymbol{\varepsilon} | \Psi_0 \rangle$ is zero are forbidden in the first order.

In numerical simulations, the dipole operator must be expressed in the same representation used for the Hamiltonian and the wavefunctions,

$$\boldsymbol{\mu} = \sum_{\alpha, \beta=1}^{N_{el}} |\alpha\rangle \boldsymbol{\mu}_{\alpha\beta}(\mathbf{R}) \langle \beta|. \quad (2.21)$$

[‡] This is the only populated state in the zero-temperature limit.

The diagonal functions $\mu_{\alpha\alpha}(\mathbf{R})$ are the diabatic state dipole moments. In the case of an isolated electronic state, they are responsible for the transitions between the rotational and vibrational sub-levels, which are not discussed in this work. The off-diagonal terms $\mu_{\alpha\beta}(\mathbf{R})$ are responsible for electronic excitations and are called electronic transition dipole moment functions or, more simply, *transition dipole moments*.[§]

Two remarks about the formula for the absorption cross section, Equation (2.20), are worthwhile:

- The Hamiltonian (2.16) can have a discrete as well as a continuous spectrum. In the second case the quantum number n becomes a continuous variable, and the summation must be replaced by an integral.
- In case the Hamiltonian has degenerate states $|\Psi_{n_1}\rangle, |\Psi_{n_2}\rangle, \dots$, with $E_{n_1} = E_{n_2} = \dots$, the total cross section at the resonance frequency $\omega = \omega_{n_0}$ is the sum of a number of *partial cross sections*, $\sigma(\omega) = \sigma_1(\omega) + \sigma_2(\omega) + \dots$, where $\sigma_i(\omega) \sim |\langle \Psi_{n_i} | \boldsymbol{\mu} \cdot \boldsymbol{\varepsilon} | \Psi_0 \rangle|^2$. This is the case of dissociative Hamiltonians, which are the core of this work, and it will be discussed in detail in Chapter 3

2.5 Excited state dynamics

The action of the transition dipole moment times the field polarization vector on the initial wavefunction [Equation (2.18)] generates vibrational wavefunctions with components on all the ‘bright’ electronic states,

$$\boldsymbol{\mu} \cdot \boldsymbol{\varepsilon} |\Psi_0\rangle = \sum_{\alpha}^{N_{el}} \boldsymbol{\mu}_{\alpha 1}(\mathbf{R}) \cdot \boldsymbol{\varepsilon} \Psi_0(\mathbf{R}) |\alpha\rangle. \quad (2.22)$$

The wave packet

$$|\Phi_0\rangle = \boldsymbol{\mu} \cdot \boldsymbol{\varepsilon} |\Psi_0\rangle \quad (2.23)$$

is not an eigenstate of the Hamiltonian (2.16). Therefore, it evolves in time following the time-dependent Schrödinger equation (TDSE),

$$i\hbar \frac{\partial |\Phi, t\rangle}{\partial t} = \mathcal{H} |\Phi, t\rangle, \quad \text{with } |\Phi, 0\rangle = |\Phi_0\rangle. \quad (2.24)$$

[§] The functions $\mu_{\alpha\beta}(\mathbf{R})$ can be calculated from the knowledge of the molecular geometry and the (diabatic) electronic wavefunctions,

$$\mu_{\alpha\beta}(\mathbf{R}) = \sum_I^{\text{nuclei}} e Z_I X_I \delta_{\alpha\beta} - \sum_i^{\text{electrons}} \langle \tilde{\psi}_{\alpha} | e \mathbf{x}_i | \tilde{\psi}_{\beta} \rangle.$$

e is the electron charge (in absolute value), Z_I is the atomic number of the nucleus I , X_I and x_i are the vectors of Cartesian coordinates for the nuclei and the electrons, respectively.

The total absorption cross section, Equation (2.20), can be related to the dynamics following the initial excitation via the autocorrelation function⁶⁸

$$S(t) = \langle \Phi, 0 | \Phi, t \rangle . \quad (2.25)$$

The Fourier transform of $S(t)$ gives

$$\begin{aligned} \int_{-\infty}^{+\infty} S(t) dt &= \int_{-\infty}^{+\infty} \langle \Phi, 0 | e^{-\frac{i}{\hbar} \mathcal{H}t} | \Phi, 0 \rangle e^{i\omega t} dt \\ &= \sum_n \int_{-\infty}^{+\infty} \langle \Phi, 0 | e^{-\frac{i}{\hbar} \mathcal{H}t} | \Psi_n \rangle \langle \Psi_n | \Phi, 0 \rangle e^{i\omega t} dt \\ &= \sum_n \int_{-\infty}^{+\infty} |\langle \Psi_n | \boldsymbol{\mu} \cdot \boldsymbol{\varepsilon} | \Psi_0 \rangle|^2 e^{-\frac{i}{\hbar} E_n t} e^{i\omega t} dt \\ &= \sum_n |\langle \Psi_n | \boldsymbol{\mu} \cdot \boldsymbol{\varepsilon} | \Psi_0 \rangle|^2 2\pi \delta \left(\omega - \frac{E_n}{\hbar} \right) , \end{aligned} \quad (2.26)$$

where the completeness relation $\sum_n |\Psi_n\rangle \langle \Psi_n| = \mathbf{1}$ and the property $\int_{-\infty}^{+\infty} e^{i\omega t} dt = 2\pi\delta(\omega)$ have been used.

Since the initial wavefunction $|\Phi_0\rangle$ is real, the autocorrelation function fulfils the symmetry relation $S(-t) = S(t)^*$, which allows us to write

$$\int_{-\infty}^{+\infty} S(t) dt = 2\text{Re} \int_0^{+\infty} S(t) dt . \quad (2.27)$$

Finally, comparing Equations (2.20) and (2.26) we obtain an alternative expression for the total absorption cross section,

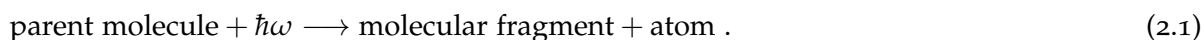
$$\sigma(\omega) = \frac{\omega}{\hbar\epsilon_0 c} \text{Re} \int_0^{+\infty} \langle \Phi, 0 | \Phi, t \rangle e^{i\frac{E_0}{\hbar}t} e^{i\omega t} dt , \quad (2.28)$$

where E_0 is the energy of the ground state $|\Psi_0\rangle$. Equation (2.28) allows the calculation of the absorption spectrum without the necessity of explicitly finding the molecular eigenstates.

Quantum dynamical calculations for chemical reactions consist in solving the time-dependent Schrödinger equation for the (nonadiabatic) nuclear motion, following the photo-excitation. The analysis of the time-dependent molecular wavefunction gives insight into the chemical mechanism, and it is used to calculate spectroscopic observables (among them the photoabsorption profile). The combination of theoretical and experimental data can be used in most cases to elucidate the details of the photo-initiated molecular motion.

THEORY II. PHOTODISSOCIATION AS A HALF-COLLISION PROCESS

In this Chapter, photodissociation of molecules into reaction channels with one atomic and one polyatomic fragment, as outlined in Equation (2.1), is described quantum mechanically:



The key points of the theory of scattering are summarized with particular emphasis on the methods to calculate *product state distributions*, the most important observables to characterize dissociation reactions.

I take as starting point the diabatic representation introduced in Chapter 2, Equation (2.16), and assume that the diabatic potentials $W_{\alpha\beta}(\mathbf{R})$ are known. Up to this stage, the set of nuclear coordinates \mathbf{R} was unspecified. In order to describe a molecular dissociation we need to introduce a coordinate system which is tailored to the description of this class of reactions. This coordinate system, described in Section 3.1, necessarily includes the atom–fragment distance R .

Once the coordinates are defined, the molecular Hamiltonian \mathcal{H} is obtained by expressing the kinetic energy operator \mathcal{T}_{nuc} and the potentials in the chosen set of coordinates. The Hamiltonian $\mathcal{H}_{\text{frag}}$ for the molecular fragment is obtained in the limit $R \rightarrow \infty$. The photodissociation reaction is governed by the Hamiltonian \mathcal{H} , according to the time-dependent Schrödinger equation (2.24). The reaction mechanism is responsible for the observable photo-fragment state populations.

Most reviews and monographs dealing with the quantum mechanical theory of atom–fragment photodissociation concentrate on triatomic molecules.^{68–70} The extension of the theory to high-dimensional systems involves the description of the coupling between the angular momenta of the detached atom and the polyatomic fragment. An overview of the algebraic treatment of this problem, useful for future applications, is given in Sections 3.1 and 3.2. Most of the concepts used in scattering theory can be derived for the case of rotationless parent molecules, in which case the theory simplifies considerably. This illustration is given in Sections 3.3 and 3.4.

3.1 Jacobi coordinates

In order to completely specify the position of the nuclei of a molecule in space, we need to define the origin and the orientation of a set of space-fixed Cartesian axes (XYZ). The position of each nucleus will be uniquely defined by three Cartesian coordinates. For a molecule with N atoms, this requires $3N$ numbers.

The translational motion of the molecule as a whole (along X , Y or Z) is dynamically separable from the motion along any other degree of freedom,⁷¹ and is of no concern for chemical reactions. We eliminate any reference to global translations by fixing the origin of the XYZ system to the nuclear center of mass. This reduces the dimension of the nuclear configuration space to $3N - 3$.[†]

The orientation of the XYZ axes is fixed in space and it is chosen according to the particular process one is interested in. In the case of photo-initiated reactions, the Z axis is typically oriented in the direction of polarization of the electric field promoting the initial excitation. The XYZ system of coordinates is also denoted as *laboratory frame* or *space-fixed frame*.

A system of coordinates, appropriate for the description of a atom-fragment dissociation reaction, can now be defined. First, we identify the vector connecting the center of mass of the fragment to the detaching atom. We denote the length of this vector by R , and the polar and azimuthal angles defining its orientation in the space-fixed frame by Θ and Φ . The value of R measures the distance between the fragments. For very large R , the atom is detached and the potential is independent of the angles Θ and Φ .

We are left now with $3N - 6$ coordinates which must describe the nuclear configuration of the molecular fragment and its spatial orientation. This set of coordinates is defined as follows:

- A *reference geometry* is taken as the fragment ground state equilibrium geometry.
- A *body-fixed frame* (xyz) is anchored to the fragment and oriented toward its principal axes of inertia, evaluated at the equilibrium geometry.[‡] The origin of the xyz system is fixed at the

[†] Denoting as M_r and (X_r, Y_r, Z_r) respectively the mass and the Cartesian coordinates of the nucleus r , the definition of the origin of XYZ into the center of mass of the nuclei sets the constraints

$$\sum_{r=1}^N M_r X_r = \sum_{r=1}^N M_r Y_r = \sum_{r=1}^N M_r Z_r = 0.$$

[‡] A similar convention (\mathbf{r} -embedding) for a diatomic fragment ($N = 3$) considers the xyz system oriented in such a way that the whole triatomic molecule lies in the xz plane, with the fragment bond distance along the z axis. Another possible choice (\mathbf{R} -embedding) considers the triatomic molecule on the xz plane with the z axis parallel to the vector connecting the detaching atom and the center of mass of the diatomic fragment.

center of mass of the fragment, and its orientation with respect to the XYZ system is defined using the three Euler angles $\Omega = (\gamma_1, \gamma_2, \gamma_3)$.⁷⁰

- $3(N - 1) - 6$ *internal coordinates* $\mathbf{Q} = (Q_1, \dots, Q_{3N-9})$ are defined to describe the molecular fragment geometry.[§]

To summarize, the nuclear configurations are completely described by the coordinate system $\{R, \Theta, \Phi, \Omega, \mathbf{Q}\}$. The potential operators $W_{\alpha\beta}$ are functions of the internal degrees of freedom only, and do not depend on how the molecule is oriented in space. Therefore, the potential is most conveniently constructed in a set of coordinates which includes the body-fixed polar angles (θ, ϕ) , defined with respect to the xyz axes, instead of the space-fixed angles (Θ, Φ) .

3.2 Schrödinger equation in Jacobi coordinates

Using the Jacobi system of coordinates, the nuclear kinetic energy operator can be defined as⁷²

$$\mathcal{T}_{\text{nuc}} = -\frac{\hbar^2}{2\mu_R} \frac{\partial^2}{\partial R^2} + \frac{\mathcal{L}^2}{2\mu_R R^2} + \mathcal{T}_{\text{rot}} + \mathcal{T}_{\mathbf{Q}} \quad (3.1)$$

where μ_R is the reduced mass of the atom-fragment pair, \mathcal{L} is the angular momentum operator describing the orbital motion of the detached atom, and $\mathcal{T}_{\mathbf{Q}}$ is the kinetic energy operator associated with the internal fragment motion. \mathcal{T}_{rot} is the kinetic energy operator for the rotational motion of the molecular fragment, which is conveniently expressed in terms of the body-fixed components of the fragment angular momentum operator $\mathcal{P} = (\mathcal{P}_x, \mathcal{P}_y, \mathcal{P}_z)$ and the inertia tensor,[†]

$$\mathcal{T}_{\text{rot}} = \frac{1}{2} (\mathcal{P}_x, \mathcal{P}_y, \mathcal{P}_z) \begin{pmatrix} I_{xx}(\mathbf{Q}) & I_{xy}(\mathbf{Q}) & I_{xz}(\mathbf{Q}) \\ I_{yx}(\mathbf{Q}) & I_{yy}(\mathbf{Q}) & I_{yz}(\mathbf{Q}) \\ I_{zx}(\mathbf{Q}) & I_{zy}(\mathbf{Q}) & I_{zz}(\mathbf{Q}) \end{pmatrix} \begin{pmatrix} \mathcal{P}_x \\ \mathcal{P}_y \\ \mathcal{P}_z \end{pmatrix}. \quad (3.2)$$

[§] For a diatomic fragment only the inter-atomic distance is necessary.

[†] The operators \mathcal{P}_i are defined in terms of the Jacobi angles as

$$\begin{aligned} \mathcal{P}_x &= i\hbar \left(\frac{\cos \gamma_3}{\sin \gamma_2} \frac{\partial}{\partial \gamma_1} - \sin \gamma_3 \frac{\partial}{\partial \gamma_2} - \cot \gamma_2 \cos \gamma_3 \frac{\partial}{\partial \gamma_3} \right) \\ \mathcal{P}_y &= i\hbar \left(-\frac{\sin \gamma_3}{\sin \gamma_2} \frac{\partial}{\partial \gamma_1} - \cos \gamma_3 \frac{\partial}{\partial \gamma_2} + \cot \gamma_2 \sin \gamma_3 \frac{\partial}{\partial \gamma_3} \right) \\ \mathcal{P}_z &= -i\hbar \frac{\partial}{\partial \gamma_3} \end{aligned}$$

and satisfy anomalous anti-commutation relations:

$$[\mathcal{P}_1, \mathcal{P}_2] = -i\hbar \mathcal{P}_3, \quad [\mathcal{P}_2, \mathcal{P}_3] = -i\hbar \mathcal{P}_1, \quad [\mathcal{P}_3, \mathcal{P}_1] = -i\hbar \mathcal{P}_2.$$

The elements of the inertia tensor $I_{jk}(\mathbf{Q})$ depend on the internal coordinates \mathbf{Q} . A simplification of Equation (3.2), useful in numerical applications, is obtained by assuming that the molecular fragment undergoes small distortions from its asymptotic equilibrium geometry, $\mathbf{Q} \approx \mathbf{Q}_0$, so that the inertia tensor is approximated by a constant diagonal matrix,

$$\begin{aligned} I_{jk}(\mathbf{Q}) &\approx I_{jk}(\mathbf{Q}_0) = I_{jj}(\mathbf{Q}_0)\delta_{jk} \\ \mathcal{T}_{\text{rot}} &\approx \frac{1}{2} \left(\frac{\mathcal{P}_x^2}{I_x} + \frac{\mathcal{P}_y^2}{I_y} + \frac{\mathcal{P}_z^2}{I_z} \right). \end{aligned} \quad (3.3)$$

Neglecting fragment vibrations in the kinetic energy operator leads to the neglect of the Coriolis coupling between vibrations and rotations. This is the approximation adopted in the subsequent derivations. The diabatic potentials and couplings $W_{\alpha\beta}$ can be expressed as functions of the body-fixed Jacobi coordinates $\{R, \theta, \phi, \mathbf{Q}\}$. The Hamiltonian operator depends, in addition, on the three Euler angles $\Omega = (\gamma_1, \gamma_2, \gamma_3)$.

In order to define the form of the nuclear wavefunction, one needs to consider the total angular momentum operator $\mathcal{J} = \mathcal{L} + \mathcal{P}$ which is associated to the rotation of the whole molecule as a rigid body. The triad $\{\mathcal{H}, \mathcal{J}^2, \mathcal{J}_Z\}$, where \mathcal{J}_Z is the projection of \mathcal{J} on the space-fixed Z axis, is a set of commuting operators. As a consequence, the nuclear wavefunction Ψ^{JM} can be labelled with the quantum numbers J and M which identify the eigenvalues of \mathcal{J}^2 and \mathcal{J}_Z and are conserved during the dynamics driven by the Hamiltonian \mathcal{H} .

The wavefunction Ψ^{JM} is typically represented via an expansion in a basis of angular functions \mathcal{Y}^{JM} which are simultaneous eigenstates of \mathcal{J} and \mathcal{J}_Z ,⁷³

$$\Psi^{JM}(\mathbf{Q}, R, \Omega, \Theta, \Phi) = \sum_{jlk} \psi_{jlk}^J(\mathbf{Q}, R) \mathcal{Y}_{jlk}^{JM}(\Omega, \Theta, \Phi). \quad (3.4)$$

The angular functions are linear combinations of products of Wigner rotation matrices (for the angles $\Omega = (\gamma_1, \gamma_2, \gamma_3)$) and spherical harmonics (for the angles Θ and Φ),

$$\mathcal{Y}_{jlk}^{JM}(\Omega, \Theta, \Phi) = \sum_{m_j=-j}^j \sum_{m_l=-l}^l \langle jm_jlm_l|JM \rangle \sqrt{\frac{2j+1}{8\pi^2}} D_{m_jk}^j(\Omega)^* Y_{lm_l}(\Theta, \Phi), \quad (3.5)$$

where the quantum numbers j , l and k are associated with the operators \mathcal{P}^2 , \mathcal{L}^2 and \mathcal{P}_z , respectively, and m_j and m_l are associated with \mathcal{P}_Z and \mathcal{L}_Z (i. e. the components of \mathcal{P} and \mathcal{L} along the space-fixed Z axis). The basis set $\left\{ \sqrt{\frac{2j+1}{8\pi^2}} D_{m_jk}^j(\Omega)^* Y_{lm_l}(\Theta, \Phi) \right\}$ consists in simultaneous eigenstates of the operators $\{\mathcal{P}^2, \mathcal{P}_Z, \mathcal{L}^2, \mathcal{L}_Z, \mathcal{P}_z\}$, whereas the functions $\left\{ \mathcal{Y}_{jlk}^{JM}(\Omega, \Theta, \Phi) \right\}$ are simultaneous eigenstates of $\{\mathcal{J}^2, \mathcal{J}_Z, \mathcal{P}^2, \mathcal{L}^2, \mathcal{P}_z\}$. The orthogonal transformation between the two basis sets is defined by the Clebsch-Gordan coefficients $\langle jm_jlm_l|JM \rangle$.

The functions (3.5) form an orthonormal basis,

$$\int_0^{2\pi} d\gamma_1 \int_0^\pi \sin \gamma_2 d\gamma_2 \int_0^{2\pi} d\gamma_3 \int_0^\pi \sin \Theta d\Theta \int_0^{2\pi} d\Phi \mathcal{Y}_{j'l'k'}^{JM}(\Omega, \Theta, \Phi)^* \mathcal{Y}_{jlk}^{JM}(\Omega, \Theta, \Phi) = \delta_{jj'} \delta_{ll'} \delta_{kk'} . \quad (3.6)$$

The matrix elements of the rotational kinetic energy operator, $\frac{\mathcal{L}^2}{2\mu_R R^2} + \mathcal{T}_{\text{rot}}$, can be calculated analytically in the basis $\{\mathcal{Y}_{jlk}^{JM}(\Omega, \Theta, \Phi)\}$.[‡]

The nuclear wavefunctions associated with a diabatic electronic state can be written using space-fixed or body-fixed coordinates. The space-fixed form, in which the position of the detaching atom is expressed via the angles Θ and Φ , is useful for the calculation of observables related to the direction of polarization of the electric field, conventionally fixed along the Z axis (an example is the anisotropy parameter^{68,69}). The use of the body-fixed frame, in which the angles (θ, ϕ) are used, is generally more appropriate in the solution of the Schrödinger equation itself, because this is the coordinate system in which the potential is set up. The matrix elements of the potential functions are more conveniently evaluated in the body-fixed frame.

The spherical harmonics functions are transformed from the XYZ - to the xyz -system using Wigner rotation matrices,

$$Y_{lm_l}(\Theta, \Phi) = \sum_{m_l'=-l}^l D_{m_l m_l'}^l(\Omega)^* Y_{lm_l'}(\theta, \phi) . \quad (3.7)$$

[‡] This is achieved by considering that the spherical harmonics Y_{lm_l} are eigenfunctions of \mathcal{L}^2 ,

$$\mathcal{L}^2 Y_{lm_l} = \hbar l(l+1) Y_{lm_l} .$$

The matrix elements of \mathcal{T}_{rot} can be evaluated using the following formulas for the action of \mathcal{P}_x , \mathcal{P}_y and \mathcal{P}_z on the rotation matrices:

$$\begin{aligned} \mathcal{P}_x D_{mk}^j(\Omega)^* &= \frac{\hbar}{2} \sqrt{j(j+1) - k(k+1)} D_{m,k+1}^j(\Omega)^* + \frac{\hbar}{2} \sqrt{j(j+1) - k(k-1)} D_{m,k-1}^j(\Omega)^* \\ \mathcal{P}_y D_{mk}^j(\Omega)^* &= \frac{i\hbar}{2} \sqrt{j(j+1) - k(k+1)} D_{m,k+1}^j(\Omega)^* - \frac{i\hbar}{2} \sqrt{j(j+1) - k(k-1)} D_{m,k-1}^j(\Omega)^* \\ \mathcal{P}_z D_{mk}^j(\Omega)^* &= \hbar k D_{mk}^j(\Omega)^* . \end{aligned}$$

Inserting Equation (3.7) into Equation (3.5), the angular functions \mathcal{Y}^{JM} can be expressed in the body-fixed frame,^{70§}

$$\begin{aligned}
\mathcal{Y}_{jlk}^{JM}(\Omega, \theta, \phi) &= \sum_{m_j=-j}^j \sum_{m_l=-l}^l \sum_{m'_l=-l}^l \langle jm_j l m_l | JM \rangle \sqrt{\frac{2j+1}{8\pi^2}} D_{m_j k}^j(\Omega)^* D_{m_l m'_l}^l(\Omega)^* Y_{lm'_l}(\theta, \phi) \\
&= \sqrt{\frac{(2j+1)(2J+1)}{8\pi^2}} \sum_{m'_l=-l}^l \left(\sum_{m_j=-j}^j \sum_{m_l=-l}^l (-1)^{j-l+M} \begin{pmatrix} j & l & J \\ m_j & m_l & -M \end{pmatrix} D_{m_j k}^j(\Omega)^* D_{m_l m'_l}^l(\Omega)^* \right) Y_{lm'_l}(\theta, \phi) \\
&= \sqrt{\frac{(2j+1)(2J+1)}{8\pi^2}} \sum_{m'_l=-l}^l (-1)^{j-l+k+m'_l} \begin{pmatrix} j & l & J \\ k & m'_l & -k-m'_l \end{pmatrix} D_{M, k+m'_l}^J(\Omega) Y_{lm'_l}(\theta, \phi). \tag{3.8}
\end{aligned}$$

According to Equation (3.8), the angular functions \mathcal{Y}_{jlk}^{JM} are expanded in terms of products of (i) a spherical harmonic $Y_{lm'_l}(\theta, \phi)$, depending on the position of the detaching atom *in the body-fixed frame*, and (ii) a rotation matrix $D_{M, k+m'_l}^J(\Omega)$, describing the orientation of the body-fixed frame with respect to the space-fixed frame. The quantum number m'_l is associated with the operator \mathcal{L}_z which is the component of \mathcal{L} along the body-fixed z axis.

While the rotational kinetic energy operator \mathcal{T}_{rot} is easily expressed in the $\{\mathcal{Y}_{jlk}^{JM}\}$ basis, it is more convenient to evaluate the (θ, ϕ) -dependent potential functions in the body-fixed $\{D_{M, k+m'_l}^J Y_{lm'_l}\}$ basis. Obviously, in simulations the same basis has to be used for all the operators. The use of the latter basis is generally more advisable, because the potentials might not have an analytical expression and need to be evaluated by numerical quadrature over the (θ, ϕ) spherical angles. The

[§] The derivation of Equation (3.8) makes use of some identities which arise from the theory of the coupling of angular momenta. First, the Clebsch-Gordan coefficients are expressed using the Wigner 3j-symbols,

$$\langle a\alpha b\beta | c-\gamma \rangle = (-1)^{a-b-\gamma} \sqrt{2c+1} \begin{pmatrix} a & b & c \\ \alpha & \beta & \gamma \end{pmatrix}.$$

Then the following sum rule is used,

$$\sum_{\alpha\beta} \begin{pmatrix} a & b & c \\ \alpha & \beta & \gamma \end{pmatrix} D_{\alpha\alpha'}^a(\Omega) D_{\beta\beta'}^b(\Omega) = \begin{pmatrix} a & b & c \\ \alpha' & \beta' & \gamma' \end{pmatrix} D_{\gamma\gamma'}^c(\Omega)^*,$$

together with the symmetry property of the rotation matrices, $D_{\alpha\alpha'}^a(\Omega) = (-1)^{\alpha-\alpha'} D_{-\alpha, -\alpha'}^a(\Omega)$.

These and other formulas, useful for the formal manipulation of equations involving angular momentum coupling, can be found on textbooks specialized on the quantum mechanical theory of angular momentum, as for example Ref. 74.

$\{D_{M,k+m'_l}^J Y_{lm'_l}\}$ basis renders the evaluation of the potential simpler and can be used to represent also the operator \mathcal{T}_{rot} exploiting the inverse of the transformation (3.8),[¶]

$$D_{M,k+m'_l}^J(\Omega)Y_{lm'_l}(\theta, \phi) = \sqrt{8\pi^2} \sum_j \sqrt{\frac{2j+1}{2J+1}} (-1)^{j-l+k+m'_l} \begin{pmatrix} j & l & J \\ k & m'_l & -k-m'_l \end{pmatrix} \mathcal{Y}_{jlk}^{JM}(\Omega, \theta, \phi). \quad (3.9)$$

In this case the total wavefunction, Equation (3.4), takes the form

$$\Psi^{JM}(\mathbf{Q}, R, \Omega, \Theta, \Phi) = \sum_{lm'_l k} \psi_{lm'_l k}^J(\mathbf{Q}, R) D_{M,k+m'_l}^J(\Omega) Y_{lm'_l}(\theta, \phi). \quad (3.10)$$

To summarize, Equations (3.4), (3.5), (3.8) and (3.9) are the fundamental equations for the quantum mechanical description of the angular motion of a atom–fragment system. First, the quantum numbers (J, M) must be defined. They determine the state of the total angular momentum, and are conserved during the molecular motion. The angular dependence of the nuclear wavefunction is represented by a basis of angular functions depending on three indices (two for a triatomic system, see References 68 and 69). For a given $|J, M\rangle$ state, not all the triads (jlk) or $(lm'_l k)$ appear in the expansions (3.4) and (3.10), which are greatly simplified in cases of low J .

3.3 Vibronic states of dissociative molecules

The form of the wavefunction of a molecule dissociating according to Equation (2.1) was discussed in Section 3.2. This Section deals with the general properties of photodissociation Hamiltonians and scattering eigenstates.

In the discussion below the case of rotationless molecules, $J = 0$, is specifically considered. This is the simplest case for the evaluation of the expansion (3.4) and it exhibits most of the features of the dissociative systems.

For $J = 0$, the $3j$ -symbol appearing in Equation (3.8) simplifies to

$$\begin{pmatrix} j & l & 0 \\ k & m'_l & -k-m'_l \end{pmatrix} = \delta_{m'_l, -k} \delta_{jl} \frac{(-1)^{j-k}}{\sqrt{2j+1}}, \quad (3.11)$$

[¶]The equivalence of Equations (3.8) and (3.9) is less obscure if one considers another identity, coming – again – from the theory of angular momentum coupling,⁷⁴

$$\sum_c (2c+1) \begin{pmatrix} a & b & c \\ \alpha & -\alpha-\gamma & \gamma \end{pmatrix} \begin{pmatrix} a & b & c \\ \alpha' & -\alpha'-\gamma & \gamma \end{pmatrix} = \delta_{\alpha\alpha'}.$$

so that the quantum numbers j and l , associated with the operators \mathcal{P}^2 and \mathcal{L}^2 , become equal. Moreover, the dependence on Ω disappears (therefore all molecular orientations are equally probable), and the body-fixed angular functions coincide with the spherical harmonics,

$$\mathcal{Y}_{lm'_l}^{00}(\Omega, \theta, \phi) = Y_{lm'_l}(\theta, \phi) . \quad (3.12)$$

The body-fixed form of a generic nuclear wavefunction for $J = 0$ is therefore

$$\Psi(\mathbf{Q}, R, \theta, \phi) = \sum_{lm'_l} \psi_{lm'_l}(R, \mathbf{Q}) Y_{lm'_l}(\theta, \phi) . \quad (3.13)$$

The fact that $j = l$ implies that the condition $J = 0$ can be formally imposed setting $\mathcal{L} + \mathcal{P} = \mathbf{0}$. Therefore, the expression for the diabatic Hamiltonian, Equation (2.16), becomes for $J = 0$:

$$\mathcal{H} = \left(-\frac{\hbar^2}{2\mu_R} \frac{\partial^2}{\partial R^2} + \frac{\mathcal{P}^2}{2\mu_R R^2} + \frac{1}{2} \left(\frac{\mathcal{P}_x^2}{I_x} + \frac{\mathcal{P}_y^2}{I_y} + \frac{\mathcal{P}_z^2}{I_z} \right) + \mathcal{T}_{\mathbf{Q}} \right) \mathbf{1} + \sum_{\alpha, \beta=1}^{N_{\text{el}}} |\alpha\rangle W_{\alpha\beta}(\mathbf{Q}, R, \theta, \phi) \langle \beta| . \quad (3.14)$$

In order to study the eigenfunctions of the system, we analyze their behaviour in the limit of long atom–fragment distance ($R \rightarrow \infty$). For large R , the interaction between the atom and the polyatomic fragment vanishes, therefore the diabatic potentials $W_{\alpha\beta}$ become independent on R , θ and ϕ . The asymptotic form of the Hamiltonian is

$$\lim_{R \rightarrow \infty} \mathcal{H} = \left(-\frac{\hbar^2}{2\mu_R} \frac{\partial^2}{\partial R^2} \right) \mathbf{1} + \mathcal{H}_{\text{frag}} , \quad (3.15)$$

where $\mathcal{H}_{\text{frag}}$ is the Hamiltonian for the fragment,

$$\mathcal{H}_{\text{frag}} = \left(\frac{\mathcal{P}_x^2}{I_x} + \frac{\mathcal{P}_y^2}{I_y} + \frac{\mathcal{P}_z^2}{I_z} + \mathcal{T}_{\mathbf{Q}} \right) \mathbf{1} + \sum_{\alpha, \beta=1}^{N_{\text{el}}} |\alpha\rangle W_{\alpha\beta}^{\text{frag}}(\mathbf{Q}) \langle \beta| . \quad (3.16)$$

The kinetic energy operator $-\hbar^2/(2\mu_R)\partial^2/\partial R^2$, associated with the inter-fragment translational energy, is the only term depending on the distance R . Its eigenfunctions are plane waves $e^{\pm ikR}$, corresponding to the eigenvalues $\hbar^2 k^2/(2\mu_R)$.

At this stage, I assume, for clarity, that the diabatic couplings vanish as $R \rightarrow \infty$, $W_{\alpha\beta}^{\text{frag}}(\mathbf{Q}) = W_{\alpha\alpha}^{\text{frag}} \delta_{\alpha\beta}$, so that the electronic states of the fragment can be considered as isolated. This is typical for ‘reactive’ conical intersections, found at intermediate values of the dissociation distance R (in this case the tuning mode). In many cases, the separation of the fragments after the intersection correlates with an increasing energy difference between the electronic states, so that nonadiabatic effects are negligible for the fragments. As a consequence, the label of the electronic state (α)

becomes a good quantum number for the fragment eigenstates and a fragment Hamiltonian can be defined for each state,

$$\mathcal{H}_{\text{frag}}^{\alpha} = \left(\frac{\mathcal{P}_x^2}{I_x} + \frac{\mathcal{P}_y^2}{I_y} + \frac{\mathcal{P}_z^2}{I_z} - \frac{\hbar}{2} \sum_i \omega_i \frac{\partial^2}{\partial Q_i^2} \right) \mathbf{1} + W_{\alpha\alpha}^{\text{frag}}(\mathbf{Q}) . \quad (3.17)$$

If the diabatic couplings are non-zero also for the fragments, the fragment eigenstates have components on all the coupled diabatic states, and they are expressed as combinations akin to Equation (2.17).

Considering uncoupled electronic states, additional quantum numbers can be defined for the fragment energy levels. The rotational operator \mathcal{T}_{rot} , for which the approximation (3.3) has been used, is the only term of $\mathcal{H}_{\text{frag}}^{\alpha}$ depending on the angles θ and ϕ . In the spherical harmonic basis $\{Y_{lm}(\theta, \phi)\}$, \mathcal{T}_{rot} has a block-structure, each block corresponding to a different value of l . Therefore, l is a good quantum number for the eigenstates of \mathcal{T}_{rot} ,

$$\mathcal{T}_{\text{rot}} \tilde{Y}_{l\tau}(\theta, \phi) = E_{l\tau}^{\text{rot}} \tilde{Y}_{l\tau}(\theta, \phi) \quad (3.18)$$

which are labelled by a quantum number τ which identifies the rotational state within each l -block. The eigenfunctions $\tilde{Y}_{l\tau}(\theta, \phi)$ are expressed in terms of the spherical harmonics,⁷³

$$\tilde{Y}_{l\tau}(\theta, \phi) = \sum_{m'_l} U_{\tau m'_l}^l Y_{lm'_l}(\theta, \phi) , \quad (3.19)$$

where $\{U_{\tau m'_l}^l\}$ is an orthogonal matrix.[†]

Summarizing, assuming uncoupled electronic states in the fragment, we have the following Schrödinger equation for the asymptotic Hamiltonian:

$$\left(\lim_{R \rightarrow \infty} \mathcal{H} \right) \sqrt{\frac{\mu_R}{2\pi\hbar k}} e^{\pm ikR} \tilde{Y}_{l\tau}(\theta, \phi) \chi_{\alpha n}(\mathbf{Q}) |\alpha\rangle = E \sqrt{\frac{\mu_R}{2\pi\hbar k}} e^{\pm ikR} \tilde{Y}_{l\tau}(\theta, \phi) \chi_{\alpha n}(\mathbf{Q}) |\alpha\rangle , \quad (3.20)$$

where the total energy is the sum of the relative atom–fragment translational energy, the fragment rotational energy and the fragment electronic and vibrational energy,

$$E = \frac{\hbar^2 k^2}{2\mu_R} + E_{l\tau}^{\text{rot}} + E_{\alpha n}^{\text{vib}} . \quad (3.21)$$

Equations (3.20) and (3.21) are crucial for the development of the theory of scattering, and two properties deserve a remark:

[†] For symmetric fragments, $I_x = I_y$, the spherical harmonics *are* the eigenfunctions of \mathcal{T}_{rot} ,

$$\frac{1}{2} \left(\frac{\mathcal{P}_x^2}{I_x} + \frac{\mathcal{P}_y^2}{I_x} + \frac{\mathcal{P}_z^2}{I_z} \right) \psi_{lm}(\theta, \phi) = \epsilon_{lm} \psi_{lm}(\theta, \phi) , \quad \text{with } \epsilon_{lm} = \frac{\hbar^2}{2} \left(l(l+1) + \left(\frac{1}{I_z} - \frac{1}{I_x} \right) m^2 \right) \psi_{lm}(\theta, \phi) .$$

- The spectrum of the asymptotic Hamiltonian is *continuous*. Even if the fragment has a discrete spectrum, the translational kinetic energy $\hbar^2 k^2 / (2\mu_R)$ can take any positive value. Eigenstates exist for all energies above the fragment ground state.
- A given total energy E can be associated with N_{open} of energy levels for the fragment, namely all electronic, vibrational, rotational states for which $E_{l\tau}^{\text{rot}} + E_{\alpha n}^{\text{vib}} < E$.[‡] Such fragment eigenstates are called *open channels* at the energy E . The solutions of the asymptotic Schrödinger equation (3.20) associated with the functions e^{+ikR} (outgoing wave) and e^{-ikR} (incoming wave) are degenerate. Therefore, the total number of degenerate eigenstates of the asymptotic Hamiltonian is equal to twice the number of open channels.

The analysis of the asymptotic Hamiltonian is important to classify the continuum eigenstates of the full Hamiltonian (3.14), named *scattering eigenstates*. Given an energy E for which N_{open} fragment channels are open, it is possible to define a set of N_{open} orthogonal scattering eigenstates having the property:⁶⁸

$$\begin{aligned} \mathcal{H}\Psi_E^{\alpha l \tau n}(R, \theta, \phi, \mathbf{Q}) &= E\Psi_E^{\alpha l \tau n}(R, \theta, \phi, \mathbf{Q}) \\ \Psi_E^{\alpha l \tau n}(R, \theta, \phi, \mathbf{Q}) &\stackrel{R \rightarrow \infty}{\equiv} \sqrt{\frac{\mu_R}{2\pi\hbar k_{\alpha l \tau n}}} e^{+ik_{\alpha l \tau n} R} \tilde{Y}_{l\tau}(\theta, \phi) \chi_{\alpha n}(\mathbf{Q}) |\alpha\rangle \\ &+ \sum'_{\alpha' l' \tau' n'} S_{\alpha l \tau n, \alpha' l' \tau' n'}(E) \sqrt{\frac{\mu_R}{2\pi\hbar k_{\alpha' l' \tau' n'}}} e^{-ik_{\alpha' l' \tau' n'} R} \tilde{Y}_{l'\tau'}(\theta, \phi) \chi_{\alpha' n'}(\mathbf{Q}) |\alpha'\rangle, \end{aligned} \quad (3.22)$$

where the energy-dependent wavevector is $k_{\alpha l \tau n} = \sqrt{2\mu_R/\hbar^2 (E - E_{l\tau}^{\text{rot}} - E_{\alpha n}^{\text{vib}})}$ and the sum Σ' extends only over the states with $k_{\alpha l \tau n} > 0$.[§]

For fixed energy E , the wavefunctions of Eq. (3.22) define one possible set of N_{open} degenerate solutions of the full Schrödinger equation. Since the asymptotic form of the scattering eigenstates consists of an outgoing wave associated with a specific fragment eigenstate, and a superposition of incoming waves for all open eigenstates, these wavefunctions are appropriate to describe dissociation into specific electronic (α), vibrational (n) and rotational (l, τ) channels.

[‡] It is sufficient to choose the appropriate value of k according to Equation (3.21). Indeed, the energy E is usually taken as a ‘continuum quantum number’, instead of k . This explains the choice of the normalization factors $\sqrt{\mu_R/(2\pi\hbar k)}$, which leads to plane waves normalized on the energy scale,

$$\int_{-\infty}^{+\infty} \sqrt{\frac{\mu_R}{2\pi\hbar k'}} e^{\mp ik'R} \sqrt{\frac{\mu_R}{2\pi\hbar k}} e^{\pm ikR} dR = \delta(E' - E).$$

[§] The energy-dependent matrix-elements $S_{\alpha l \tau n, \alpha' l' \tau' n'}(E)$ define the so-called *scattering matrix* which is more often used in the context of full collisions.

3.4 Partial cross sections and photofragment distributions

A molecule absorbing a photon with energy $E_{\text{ph}} = \hbar\omega$ larger than the dissociation energy of a specific bond is excited into the dissociative continuum. The interaction with light can induce transitions from the initial molecular state $|\Psi_0\rangle$, having the energy E_0 , to one of the degenerate scattering eigenstates of energy $E_0 + \hbar\omega$. According to Eq. (2.20), the absorption cross section at the frequency ω is the sum of the cross sections of all scattering states,

$$\sigma(\omega) = \sum_{\alpha l \tau n} \sigma_{\alpha l \tau n}(\omega) = \frac{\pi}{\hbar \epsilon_0 c} \sum_{\alpha l \tau n}^{\text{open channels}} \left| \langle \Psi_E^{\alpha l \tau n} | \boldsymbol{\mu} \cdot \boldsymbol{\varepsilon} | \Psi_0 \rangle \right|^2, \quad \text{with } E = E_0 + \hbar\omega \quad (3.23)$$

The cross-sections $\sigma_{\alpha l \tau n}(\omega)$ refer to specific electronic-vibrational-rotational channels and are called *partial cross sections*.

The photon energy-dependent normalized partial cross sections

$$p_{\alpha l \tau n}(E_{\text{ph}}) = \frac{\sigma_{\alpha l \tau n}(\omega)}{\sigma(\omega)} \quad (3.24)$$

have an important physical meaning: They represent the probability of forming the fragment in a given electronic-vibrational-rotational state, after the dissociation induced by the absorption of a photon of energy E_{ph} .

In typical photodissociation experiments, an ensemble of molecules is irradiated with pulse of long duration (narrow on the energy scale). A number of molecular fragments are formed and the distribution over the fragment quantum states, given by Eq. (3.24), is measured.

The product state populations carry detailed information on the dissociation mechanism. Generally speaking, a vibrational mode active during the reaction is expected to be excited in the product. The detailed characterisation and interpretation of partial cross sections is a challenging task and requires a careful comparison of experimental data and computer simulations.

3.4.1 Excited state dynamics and product state distributions

In Section 2.5 a link has been made between the total absorption cross section and the wave packet dynamics following the photoabsorption. The connection is based on the autocorrelation function $S(t)$, whose Fourier transform gives the spectrum $\sigma(\omega)$ [see Eq. (2.28)].

In the same way, the partial cross sections can be expressed as half-Fourier transforms of appropriate cross-correlation functions, which can be obtained with quantum wave packet propagation.

This method to calculate product state distributions was derived by Balint-Kurti *et al.*, and consists of the following steps (see the original work, Ref. 75, and Section 5.2 for detailed derivations):

- The initial wave packet $|\Phi_0\rangle = \boldsymbol{\mu} \cdot \boldsymbol{\varepsilon} |\Psi_0\rangle$ is propagated in time according to the time-dependent Schrödinger equation (2.24).

- The product energy levels are calculated as eigenstates of the fragment Hamiltonian $\mathcal{H}_{\text{frag}}|\Phi_i^{\text{frag}}\rangle = E_i|\Phi_i^{\text{frag}}\rangle$ (here i is a collective quantum number). If the electronic, rotational and vibrational degrees of freedom are separable the eigenstates have the form

$$|\Phi_{\alpha l \tau n}^{\text{frag}}\rangle = \tilde{Y}_{l\tau}(\theta, \phi) \chi_{\alpha n}(\mathbf{Q}) |\alpha\rangle.$$

- The cross-correlation functions

$$S_i(t) = \left\langle \Phi_i^{\text{frag}} \left| \delta(R - R_\infty) \right| \Phi, t \right\rangle \quad (3.25)$$

are calculated as overlaps of the fragment eigenstates with the time-dependent wavefunction, evaluated on an ‘analysis line’ $R = R_\infty$ placed in the asymptotic region, in which the potential is R -independent.

- The partial cross sections are calculated from the absolute value of the half-Fourier transform of the cross-correlation functions as

$$\sigma_i(\omega) = \frac{8\pi^2\omega k_i}{3c\varepsilon_0} \left| \int_0^\infty S_i(t) e^{iE_0 t/\hbar} e^{i\omega t} dt \right|^2, \quad (3.26)$$

where $k_i = \sqrt{2\mu_R (E_{\text{ph}} - D_0 - E_i) / \hbar^2}$ and E_0 is the energy of the molecular state prior to electronic excitation, as in Equation (2.28).

COMPUTATIONAL METHODS

The quantum mechanical study of photodissociation reactions from first principles requires both electronic structure calculations, used to calculate the potential energy surfaces, and wave packet propagations to solve the time-dependent Schrödinger equation for the nuclear motion.

The quantum chemical calculations described in this work were performed using the program package MOLPRO.⁷⁶ The wave packet dynamics was simulated using domestic codes (for ozone) or the Heidelberg MCTDH package.⁷⁷

A brief description of these methods is given below.

4.1 Electronic structure calculations. The CASSCF method

From the quantum chemical viewpoint, the accurate determination of dissociative potential energy surfaces requires *multi-reference methods*. In these methods, the electronic wavefunction is approximated as a linear combination of Slater determinants or, better, configuration state functions. The use of many configurations is necessary to obtain a size consistent and qualitatively correct description of the electronic wavefunctions along the dissociation path. Moreover, the electronic configuration of an adiabatic state can vary rapidly for small geometrical changes in the proximity of an intersection of potential energies. If the intersection involves the ground state, the electronic wavefunctions in the proximity of the electronic degeneracy are inherently of multi-reference character.

At the simplest level, the multi-reference character is taken into account by calculating the electronic wavefunctions using multi-configurational self-consistent field (MCSCF) methods. The method of choice is the complete active space self-consistent field (CASSCF) method.

The CASSCF wavefunction is defined as a linear combination of Slater determinants, obtained from two sets of molecular orbitals: n_{inact} *inactive* orbitals which are doubly occupied in all determinants, and n_{act} *active* orbitals, whose occupation numbers can vary between 0, 1 and 2, in order to accommodate $N_{\text{el}} - 2n_{\text{inact}}$ electrons (here N_{el} is the total number of electrons). The total

electronic wavefunctions for the electronic states of interest are obtained as an expansion in all determinants which can be formed by all possible excitations within the active space.

The molecular orbitals are, in turn, expanded in a one-electron basis set, defined by atomic orbitals. The dimension of this basis set is generally much larger than the number of occupied orbitals. Therefore, the set of molecular orbitals is completed by a large number of *virtual* orbitals.

The electronic wavefunctions are formally used to define an energy functional as expectation value of the electronic Hamiltonian. In *state averaged* calculations, the average energy (or a weighted combination of energies) of the included electronic states is optimized with respect to the molecular orbitals and the combination coefficients of the Slater determinants.

In practice, the CASSCF method is not a 'black-box' method. The user needs to have chemical intuition to choose the correct active orbitals to describe the region of interest of the potential energy surfaces. In many cases, a qualitatively correct wavefunction, taking account of so-called static electron correlation, can be obtained with relatively few configurations.

An overview of the MCSCF method is given in numerous textbooks of computational chemistry, such as in Reference 78. A more detailed description can be found in the book of Reference 79.

4.1.1 *Dynamical correlation. The CASPT2 and MRCI methods*

When the active orbitals are properly chosen, the CASSCF wavefunction is qualitatively correct. However, the correct description of many features of potential energy surfaces (such as barrier heights, equilibrium and conical intersection geometries) requires an improvement of the CASSCF wavefunction which accounts for the so-called *electron dynamical correlation*.⁷⁸

Improved wavefunctions are obtained with additional Slater determinants, obtained by electron excitations from the occupied to the virtual orbitals. Different strategies can be used to obtain the coefficients for the new configurations.

In the multi-reference configuration interaction (MRCI) method, a variational procedure is followed.⁸⁰ The electronic wavefunction, given as a linear combination of the CASSCF wavefunction and the additional excited configurations, is used to evaluate the electronic energy, which is optimized with respect to the expansion coefficients. The MRCI method was used by Schinke and McBane⁴⁴ to construct the ground and excited state PESs of the ozone molecule used in the quantum dynamical calculations of this work.

In the complete active space second-order perturbation theory (CASPT2) method, the coefficients of the excited configurations are derived in a perturbative manner.⁸¹ The electronic Hamiltonian is

expressed as sum of an effective Hamiltonian, whose eigenstates are the CASSCF wavefunctions, and a perturbation operator. The wavefunction and the electronic energy are expanded up to the first and second perturbative order, respectively. Only single and double electronic excitations from the CASSCF wavefunction are necessary. Rayleigh-Schrödinger perturbation theory is used to derive the combination coefficients and the second-order corrected energy. In this work, CASPT2 calculations were used to determine the potential energy surfaces of the ground and the $\pi\sigma^*$ states of pyrrole.

4.2 Methods of nuclear quantum dynamics

The quantum mechanical study of the nuclear motion requires the solution of the time-dependent Schrödinger equation (2.24) for the nuclei,

$$i\hbar \frac{\partial |\Phi, t\rangle}{\partial t} = \mathcal{H} |\Phi, t\rangle, \quad \text{with } |\Phi, 0\rangle = |\Phi_0\rangle. \quad (2.24)$$

As discussed in Section (3.2), the wavefunction Φ for the atom-fragment photodissociation is labelled with the total angular momentum quantum numbers (J, M) and depends, in general, on the Jacobi coordinates (R, θ, ϕ) , the Euler angles Ω , and the fragment internal coordinates \mathbf{Q} . In this Section, the coordinates are generically indicated as x_κ , $\kappa = 1, \dots, f$.

With modern computer architectures, the TDSE can be solved exactly for low-dimensional problems (up to five or six vibrational degrees of freedom), using standard polynomial methods, such as Chebyshev propagation.⁵¹ In order to propagate the wavefunction for high-dimensional systems, several accurate techniques have been developed,³⁷ among which the most popular is the multi-configurational time-dependent Hartree method (MCTDH).^{82,83}

4.2.1 Grid representation and Chebyshev Propagation

For low-dimensional systems, such as a triatomic molecule, the wavefunction can be represented on a multi-dimensional grid, typically using a discrete variable representation (DVR).⁸⁴ If a direct tensor product grid is used, the wavefunction has the form

$$\Phi(x_1, \dots, x_f) = \sum_{j_1=1}^{N_1} \dots \sum_{j_f=1}^{N_f} C_{j_1 \dots j_f}(t) \theta_{j_1}^{(1)}(x_1) \cdot \dots \cdot \theta_{j_f}^{(f)}(x_f), \quad (4.1)$$

where $\theta_{j_k}^{(\kappa)}$ is the DVR function for the coordinate x_κ , localized at the j_k -th point on the grid for x_κ . The integers N_κ are the grid dimensions and the complex numbers $C_{j_1 \dots j_f}(t)$ are time-dependent coefficients associated with the multi-dimensional grid points.

Using the representation of Equation (4.1), the TDSE can be written in the form

$$i\hbar \frac{\partial \mathbf{C}_J}{\partial t} = \sum_K H_{JL} \mathbf{C}_L, \quad (4.2)$$

where $J = (j_1 \dots j_f)$ is a multi-index and $H_{JL} = \langle \theta_{j_1}^{(1)} \dots \theta_{j_f}^{(f)} | \mathcal{H} | \theta_{l_1}^{(1)} \dots \theta_{l_f}^{(f)} \rangle$ is the matrix-representation of the Hamiltonian in the (multi-dimensional) DVR basis.

Equation (4.2) can be solved using efficient polynomial methods: With $\mathbb{H} = \{H_{JL}\}$ and $\mathbf{C} = \{\mathbf{C}_J\}$, Equation (4.2) is solved as

$$i\hbar \frac{\partial \mathbf{C}}{\partial t} = \mathbb{H} \mathbf{C} \implies \mathbf{C}(t) = \exp\left(-\frac{i}{\hbar} \mathbb{H} t\right) \mathbf{C}(0). \quad (4.3)$$

The propagator is represented as $\exp\left(-\frac{i}{\hbar} \mathbb{H} t\right) = \sum_n a_n P_n(\mathbb{H})$, where $P_n(\mathbb{H})$ is a polynomial of the Hamiltonian matrix.

In Chebyshev propagation, the Hamiltonian matrix is first rescaled to the domain $[-1, 1]$:

$$\mathbb{H} \longrightarrow \mathbb{H}_{\text{norm}} = \frac{2\mathbb{H} - \mathbb{1}(E_{\text{max}} + E_{\text{min}})}{E_{\text{max}} - E_{\text{min}}}, \quad (4.4)$$

where E_{min} and E_{max} are estimations for the minimum and maximum eigenvalues of \mathbb{H} . Then, the coefficient vector is calculated as^{51,85}

$$\mathbf{C}(t) = e^{-\frac{i}{2\hbar}(E_{\text{max}} + E_{\text{min}})t} \sum_{n=0}^{N_{\text{iter}}} (-i)^n (2 - \delta_{n0}) J_n\left(\frac{E_{\text{max}} - E_{\text{min}}}{2\hbar} t\right) \mathbf{C}_n, \quad (4.5)$$

where the coefficients are expressed in terms of the Bessel functions $J_n(\alpha)$, and the vectors \mathbf{C}_n are generated by the recurrence relation:

$$\begin{aligned} \mathbf{C}_0 &= \mathbf{C}(t=0) \\ \mathbf{C}_1 &= \mathbb{H}_{\text{norm}} \mathbf{C}_0 \\ \mathbf{C}_{n+1} &= 2 \mathbb{H}_{\text{norm}} \mathbf{C}_n - \mathbf{C}_{n-1}. \end{aligned} \quad (4.6)$$

Equation (4.5) shows that the time-dependence of the wavefunction is given by the Bessel function coefficients and the spatial dependence is in the \mathbf{C}_n vectors. Autocorrelation or cross-correlation functions are calculated by storing the overlaps of the \mathbf{C}_n vectors either with \mathbf{C}_0 or with the vectors of interest (associated, for example, with fragment eigenstates); such time-independent overlaps are then weighted with the time-dependent J_n coefficients whose Fourier transform is obtained analytically.

The computational effort of this numerically exact method is mainly given by cost of the $\mathbb{H}C_n$ matrix-vector multiplication. Assuming, for simplicity, $N_1 = \dots = N_f = N$, and that the kinetic energy operator is given as a sum of single-coordinate terms and the potential operator is diagonal on a DVR grid, the computational cost is proportional to fN^{f+1} .⁸⁶ This exponential scaling, common to all polynomial integrators, limits the use of the method to systems with few degrees of freedom.

4.2.2 The multi-configurational time-dependent Hartree method (MCTDH)

The MCTDH method^{83,82} is based on the representation of the wavefunction in terms of configurations. A set of time-dependent single-particle functions (SPFs) is used for each degree of freedom, and the configurations are built as Hartree products of SPFs. SPFs are typically represented on a DVR grid and the exact description of Section 4.2.1 is recovered when the number of SPF approaches the size of the DVR basis.

The time-dependent wavefunction is given by the following *ansatz*:

$$\Phi(x_1, \dots, x_f, t) = \sum_{j_1}^{n_1} \dots \sum_{j_f}^{n_f} C_{j_1 \dots j_f}(t) \phi_{j_1}^{(1)}(x_1, t) \cdot \dots \cdot \phi_{j_f}^{(f)}(x_f, t), \quad (4.7)$$

where the $\phi_{j_\kappa}^{(\kappa)}(x_\kappa, t)$ are n_κ SPFs for the degree of freedom x_κ , and the $C_{j_1 \dots j_f}(t)$ are expansion coefficients. In the MCTDH wavefunction, not only the coefficients, but also the ‘basis functions’ $\phi_{j_\kappa}^{(\kappa)}$ depend on time.

The equations of motion are derived from the time-dependent variational principle,

$$\left\langle \delta\Phi \left| i\hbar \frac{\partial}{\partial t} - \mathcal{H} \right| \Phi \right\rangle = 0. \quad (4.8)$$

The variations $\delta\Phi$ must be performed with respect to the coefficients,

$$\frac{\delta\Phi}{\delta C_J} = \phi_{j_1}^{(1)}(x_1, t) \cdot \dots \cdot \phi_{j_f}^{(f)}(x_f, t) = \Phi_J(t), \quad \text{with } J = (j_1 \dots j_f), \quad (4.9)$$

and to the SPFs,

$$\begin{aligned} \frac{\delta\Phi}{\delta\phi_l^{(\kappa)}} &= \sum_{j_1}^{n_1} \dots \sum_{j_{\kappa-1}}^{n_{\kappa-1}} \sum_{j_{\kappa+1}}^{n_{\kappa+1}} \dots \sum_{j_f}^{n_f} A_{j_1 \dots j_{\kappa-1} l j_{\kappa+1} \dots j_f} \phi_{j_1}^{(1)} \cdot \dots \cdot \phi_{j_{\kappa-1}}^{(\kappa-1)} \phi_{j_{\kappa+1}}^{(\kappa+1)} \cdot \dots \cdot \phi_{j_f}^{(f)} \\ &= \tilde{\Phi}_J^{(\kappa)}(x_1, \dots, x_{\kappa-1}, x_{\kappa+1}, x_f), \end{aligned} \quad (4.10)$$

where the single-hole functions $\tilde{\Phi}_J^{(\kappa)}$ have been defined as combinations of Hartree products between $(f - 1)$ SPFs.

Inserting Equations (4.9) and (4.10) into Equation (4.8), the MCTDH working equations are obtained after some cumbersome rearrangements: [†]

$$i\hbar \frac{\partial C_J}{\partial t} = \sum_L \langle \Phi_J | \mathcal{H} | \Phi_L \rangle C_L \quad (4.11)$$

$$i\hbar \frac{\partial \phi_j^{(\kappa)}}{\partial t} = \left(1 - \mathcal{P}^{(\kappa)}\right) \sum_{l=1}^{n_\kappa} \left[\left(\rho^{(\kappa)}\right)^{-1} \langle \mathbb{H}^{(\kappa)} \rangle \right]_{jl} \phi_l^{(\kappa)}. \quad (4.12)$$

Equation (4.12) requires the evaluation of the projection operator

$$\mathcal{P}^{(\kappa)} = \sum_{j=1}^{n_\kappa} |\phi_j^{(\kappa)}\rangle \langle \phi_j^{(\kappa)}|,$$

and of the product between the inverse of the density matrix

$$\begin{aligned} \rho_{jl}^{(\kappa)} &= \langle \tilde{\Phi}_j^{(\kappa)} | \tilde{\Phi}_l^{(\kappa)} \rangle \\ &= \sum_{j_1=1}^{n_1} \dots \sum_{j_{\kappa-1}=1}^{n_{\kappa-1}} \sum_{j_{\kappa+1}=1}^{n_{\kappa+1}} \dots \sum_{j_f=1}^{n_f} A_{j_1 \dots j_{\kappa-1} j_{\kappa+1} \dots j_f}^* A_{j_1 \dots j_{\kappa-1} l j_{\kappa+1} \dots j_f} \end{aligned}$$

and the mean field operators

$$H_{jk}^{(\kappa)} = \langle \tilde{\Phi}_j^{(\kappa)} | \mathcal{H} | \tilde{\Phi}_l^{(\kappa)} \rangle.$$

The computational cost for the MCTDH algorithm is the sum of two parts.⁸³ One contribution is due to the action of the mean field matrices $\langle \mathbb{H}^{(\kappa)} \rangle_{jl}$ on the SPF functions. It grows linearly with the number of degrees of freedom f and with the average number n of SPFs for each degree of freedom and quadratically with the average dimension N of the one-particle DVR grid. The total effort scales as $\sim nfN^2$. The second contribution is due to the cost of building the mean field matrices and grows as $\sim f^2 n^{f+1}$. The total computational cost is therefore

$$\text{computational cost} \approx c_1 f n N^2 + c_2 f^2 n^{f+1}, \quad (4.13)$$

with coefficients of proportionality, c_1 and c_2 . The effort of the standard method of Section 4.2.1 is proportional to fN^{f+1} . It follows that, for large values of n and f , the gain factor of the MCTDH

[†] In order to remove redundancies between SPFs and coefficients, the constraints

$$\langle \phi_j^{(\kappa)} | \phi_l^{(\kappa)} \rangle = \delta_{jl}$$

and

$$\left\langle \phi_j^{(\kappa)} \left| \frac{\partial \phi_l^{(\kappa)}}{\partial t} \right. \right\rangle = 0$$

are used.

scheme is proportional to $f^{-1}(N/n)^{f+1}$: For a high number f of degrees of freedom and for a large mean contraction efficiency (N/n) , the MCTDH method is much more efficient than the standard wave packet propagation method.

PUBLICATIONS AND MANUSCRIPTS

This Chapter shows the most relevant publications related to the doctoral work. Each paper is introduced by a brief conspectus. The papers are attached in the Appendix.

The contributions are:

- Paper 1. **Signatures of a conical intersection in photofragment distributions and absorption spectra: Photodissociation in the Hartley band of ozone.** D. Picconi and S. Yu. Grebenshchikov, *The Journal of Chemical Physics* **141**, 074311 (2014); <http://dx.doi.org/10.1063/1.4892919>.
- Paper 2. **Intermediate photofragment distributions as probes of non-adiabatic dynamics at conical intersections: application to the Hartley band of ozone.** D. Picconi and S. Yu. Grebenshchikov, *Phys. Chem. Chem. Phys.* **17**, 28931 (2015); <http://dx.doi.org/10.1039/c5cp04564a>.
- Paper 3. **Partial dissociative emission cross sections and product state distributions of the resulting photofragments.** D. Picconi and S. Yu. Grebenshchikov, *Chemical Physics* **481**, 231 (2016); <https://doi.org/10.1016/j.chemphys.2016.08.011>.
- Paper 4. **Photodissociation dynamics and photofragment distributions in the first absorption band of pyrrole: I. Vibronic Franck-Condon Herzberg-Teller excitation of the ${}^1A_2(\pi\sigma^*) \leftarrow \tilde{X}{}^1A_1(\pi\pi)$ transition.** D. Picconi and S. Yu. Grebenshchikov, in preparation.
- Paper 5. **Fano resonances in the photoinduced H-atom elimination dynamics in the $\pi\sigma^*$ states of pyrrole.** S. Yu. Grebenshchikov and D. Picconi, submitted to *Phys. Chem. Chem. Phys.*

5.1 Signatures of a conical intersection in photofragment distributions and absorption spectra: Photodissociation in the Hartley band of ozone[†]

The topic of Paper 1 is the photodissociation of ozone in the Hartley band, simulated using the potential energy surfaces of Schinke and McBane.⁴⁴ Novel signatures of reactive conical intersections are identified in the photofragment distributions. The calculations included the excited singlet states B and R, which form a conical intersection outside the Franck-Condon zone, as shown in Fig. 1.1, and are performed using a modified version of the Chebyshev propagation method (see Section 4.2.1).⁸⁵

A number of spectroscopic observables were calculated: Temperature-dependent absorption spectrum, photon energy-dependent rotational, vibrational and translational energy distributions (see Section 3.4), and the state-specific anisotropy parameter.^{68,69} The calculated observables were compared with experimental measurements in order to assess the quality of the PESs. The relevant features and the vibrational structures of the absorption spectrum were fully reproduced, and nice agreement was found for the product state distributions.

The absorption envelope is thoroughly discussed. Previous *ab initio* calculations of the high resolution Hartley spectrum predicted the spectral envelope strongly congested by intense narrow resonance-like features.^{87,88,23} In the present calculations, based on the recently constructed PESs of Ref. 44, the intensity of the resonance peaks is considerably attenuated and the diffuseness of the experimental spectrum is reproduced.

A major finding of Paper 1 concerns the impact of the conical intersection on the photofragment state distributions. The electronic excitation initiates the dynamics on the B state. Along the dissociation pathway the B/R intersection is encountered and the population branches between the two electronic channels. Between 8% and 10% of the molecules undergo internal conversion to the R state and dissociate on the lower channel which is associated with a high content of O – O₂ translational energy. The degree of vibrational excitation of the O₂ product is also much higher for molecules which follow the adiabatic path, as shown in Fig. 5 of Paper 1. In the upper electronic channel, diabatically connected with the B state, the vibrational distribution has a

[†] *Individual candidate contribution.* I performed quantum mechanical dissociation calculations for $J = 0$ using a FORTRAN code based on Chebyshev propagation. These calculations were used to evaluate photofragment rotational, vibrational and translational distributions reported in Figures 3, 4 and 5. We analyzed together the distributions and established the connections with the energy exchange at the intersection. I implemented the calculation of the energy-components of the evolving wave packets [Eq. (21)] in the Chebyshev code and created Figures 2 and 6 using the package MATHEMATICA. I contributed in writing the manuscript and the supporting information.

maximum for the ground state, $\nu = 0$, and the population decreases quickly for increasing ν . In lower electronic channel, the shape of the vibrational distribution is dramatically different, although the O_2 equilibrium distance is very similar for the two channels: For low values of ν , the population increases for increasing ν , reaching a maximum around $\nu \approx 6 - 11$.

This effect is not merely due to a higher excess energy $E_{\text{ph}} - D_0$ for molecules emerging in the lower channel, but it is a signature of the B/R conical intersection. A proof is partially given by the behaviour of the average vibrational and translational energies ($\langle E_{\text{vib}} \rangle$ and $\langle E_{\text{kin}} \rangle$, respectively) as a function of the excitation energy, reported in Fig. 4 of Paper 1. For molecules following the adiabatic pathway, the inter-fragment kinetic energy is nearly independent on the photon energy (counter-intuitively, $\langle E_{\text{kin}} \rangle$ even decreases for increasing E_{ph}), and the additional excess energy preferentially flows into the vibrational motion.

The vibrational excitation associated with the adiabatic path can be explained as follows. The coupling mode of the B/R conical intersection nearly coincides with vibrational coordinate of the O_2 fragment. Only the molecules with substantial energy on the short O – O bond sample the region of the PES in which the B/R diabatic coupling is large, and undergo a B \rightarrow R transition. Fig. 6 of the paper shows that, just after the internal conversion, the wave packet on the R state represents an overstretched O – O bond and this vibrational excitation is carried over into the fragments.

5.2 Intermediate photofragment distributions as probes of non-adiabatic dynamics at conical intersections: application to the Hartley band of ozone[†]

Paper 2 extends the work of Paper 1 on the ozone molecule and focuses on the high degree of vibrational excitation in the O₂ fragment emerging from the lower electronic channel. In order to visualize the energy distribution along the dissociation path, a new analysis method was developed and related with photoemission spectroscopy. The goal was to study the formation of vibrational excitation and to separate the effect of the conical intersection from the effects of the post-intersection dynamics. To this end, an intermediate population analysis was implemented, based on an extension of the method of Balint-Kurti et al.⁷⁵ (see Section 3.4.1) to short distances. The intermediate distributions were obtained from cross-correlation functions, defined by a modification of Equation (3.25) in which: (i) An intermediate distance R_* was used, instead of R_∞ ; (ii) the fragment eigenfunctions Φ_j^{frag} were replaced by local eigenstates, evaluated at $R = R_*$, which gradually converge to the fragment eigenstates as $R_* \rightarrow R_\infty$.

The analysis of the intermediate vibrational distributions reveals that the vibrational excitation in the R channel is formed upon the passage through the B/R intersection and therefore is a true ‘hallmark’ of the intersection (see Fig. 1 of the paper). The shape of the intermediate distributions can be rationalized using Landau-Zener theory,^{89,90} whereby the probability P_{BR} of the B \rightarrow R diabatic transition depends on the Massey parameter $\bar{\zeta}$, given by the product of the adiabatic energy gap ΔE^{ad} and the sojourn time τ in the crossing region:

$$P_{\text{BR}} = 1 - \exp(-\bar{\zeta}) = 1 - \exp(-\Delta E^{\text{ad}}\tau) . \quad (5.1)$$

Ozone molecules with a highly excited O – O bond lack translational energy in the O – O₂ coordinate, spend long time in the intersection region and are likely to make a B \rightarrow R transition. Massey parameter $\bar{\zeta}$ is related to the topographical features of the conical intersection and can be reverse engineered from the intermediate vibrational distributions evaluated in proximity of the intersection.

[†] *Individual candidate contribution.* I implemented the calculation of intermediate state distributions in the Chebyshev code and evaluated the intermediate vibrational distributions. Different definitions of the intermediate fragment eigenstates were explored. We derived the Landau-Zener model of Section 4 and I performed the calculations of the Massey parameter [Figure 2(a-d)]. We established the relation between the intermediate state distributions and the resonance Raman amplitudes. I contributed in writing the manuscript, wrote the Appendix A and made Figures 3 and 4 using the software MATHEMATICA.

The mechanism of the vibrational energy exchange at the conical intersection is rooted in the arrangement of the ozone PESs, shown in Figure 1.1, and in the fact the coupling mode is conserved in the photofragment. The potential energy diagram of ozone is prototypical for the photodissociation of a number of molecules, such as atmospheric trace gases (N_2O ,¹⁵ CO_2 ¹⁶), halogenoalkanes¹⁷ or heteroaromatic molecules¹⁹.

Given the importance of the intermediate state populations to characterize the local shape of the intersecting states, it is worth asking whether such transient distributions could be detected experimentally. A possible route is suggested in Section 5 of the paper, in which the intermediate populations are reconstructed from the photoemission spectrum of the dissociating ozone. The quantum mechanical calculations reproduce nicely the experimental resonance Raman spectrum and the intermediate T -matrix elements [cf. Equation (3.25)]

$$T_i(\omega) = \int_0^\infty S_i(t) e^{iE_0 t/\hbar} e^{i\omega t} dt, \quad (5.2)$$

are obtained as a combination of resonance Raman amplitudes. Although a so-called ‘complete’ experiment, which provides both the intensity and the phase of the scattering spectrum, is technically challenging,⁹¹ resonance Raman spectroscopy is shown to be highly informative concerning the features of the potential energy surfaces in the intersection region.

5.3 Partial dissociative emission cross sections and product state distributions of the resulting photofragments[†]

Paper 3 describes an extension of the connection established in Paper 2 between the resonance Raman amplitudes and the vibrational state distributions associated with the intermediate stages of photodissociation. The focus is on the emission from an excited electronic state into the dissociative scattering states of a lower electronic state: The continuous emission spectrum can be decomposed into partial cross sections, using a procedure akin to the one described in Section 3.4 for the absorption spectrum.

Since the emission energy-dependent partial cross sections are related to the populations of the fragment eigenstates, they can be inferred ‘non-optically’ from product state distributions. Their calculation can be performed with the procedure outlined in Section 3.4.1, whereby the evaluation of the scattering eigenstates is not needed. This analysis is illustrated by calculating the continuous emission spectra for the molecules NaI, CO₂ and pyrrole. In pyrrole, the calculations are based on the CASPT2 potential energy surfaces used in Papers 4 and 5. The emission spectrum is evaluated for the optically allowed ${}^1A_2 \leftarrow {}^1B_1$ transition, and decomposed in partial cross sections corresponding to the different excitations in the totally symmetric modes.

The description of continuous spectra in terms of partial cross sections can be extended to other optical transitions to unbound electronic states. An application under extensive development is dissociative photoionization spectroscopy,^{92,93} in which a molecule is ionized to a dissociative cationic state. The resulting continuous photoelectron spectrum can be decomposed in partial cross sections, related to the state populations of the fragment ions. Partial photoelectron cross sections can be inferred from the detection of recoiling ionized molecular fragments.

[†] *Individual candidate contribution.* I contributed in developing the theory and in writing the paper. I developed the nine-dimensional potential energy surface for the states 1B_1 and 1A_2 of pyrrole. I performed the calculations of continuous emission spectrum and the partial emission cross sections of pyrrole.

5.4 Photodissociation dynamics and photofragment distributions in the first absorption band of pyrrole: I. Vibronic Franck-Condon Herzberg-Teller excitation of the ${}^1A_2(\pi\sigma^*) \leftarrow \tilde{X}{}^1A_1(\pi\pi)$ transition[†]

The topic of Paper 4 is the photodissociation of pyrrole, following excitation to the low-lying ${}^1A_2(\pi\sigma^*)$ state. Novel *ab initio* diabatic potential energy surfaces of the ground electronic state and the low-lying $\pi\sigma^*$ states of pyrrole have been constructed, and used to perform quantum dynamical simulations of the photodissociation reaction. Approximate approaches have been developed to calculate the absorption spectrum and the photofragment distributions. The approximated spectroscopic observables nicely agree with the numerically exact results of MCTDH calculations.

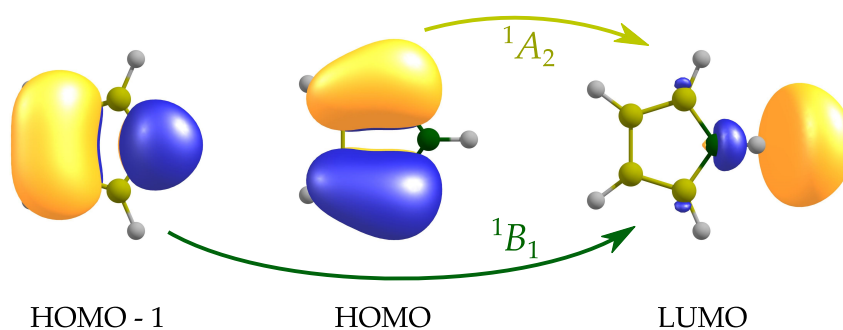


Figure 5.1: Dominant orbital excitations involved in the formation of the two lowest $\pi\sigma^*$ states of pyrrole.

Pyrrole is a typical example of chromophores which exhibit $\pi\sigma^*$ photochemistry¹⁹ and has been extensively studied both theoretically and experimentally.^{52,53,25,54-63} The two lowest lying $\pi\sigma^*$ states, 1A_2 and 1B_1 , are formed by the promotion of an electron from ring-centered π orbitals to σ^* orbitals which are localised on the N atom (see Figure 5.1). The σ^* orbital has a Rydberg ($3s$) character in the vertical excitation region, but acquires progressively more anti-bonding character

[†] *Individual candidate contribution.* We performed extensive quantum chemical calculations, in order to analyze the electronic structure of pyrrole in the vertical absorption region and to establish the methodology for the construction of the diabatic PESs. I designed the construction of the Hamiltonian based on dissociation distance-dependent Hessian calculations. I performed the CASPT2 calculations for the vibrational sub-space (\mathbf{Q} coordinates), using the package MOLPRO. I developed Fortran codes for the automatic generation the input files for MOLPRO and for the construction of the Hessian matrix from the MOLPRO output. We developed the approximation methods for the absorption and the TKER spectral calculations. I performed the MCTDH calculations, tested the approximate methods. I developed Python scripts in order to evaluate the product state distributions using the Heidelberg MCTDH code. I co-designed the manuscript, elaborated the figures, wrote Sections V-VI and most of Sections I-IV.

upon extension of the N–H bond.³⁴ This is the reason why the potential energy surfaces of the $\pi\sigma^*$ states are repulsive.

The ${}^1A_2 \leftarrow \tilde{X}$ excitation is Franck-Condon forbidden, but the 1A_2 state can be populated for excitation energies $E_{\text{ph}} < 5.1 \text{ eV}$ ³³ via intensity borrowing from neighbouring $\pi\pi^*$ states.^{57,63}

In the frequency domain, the absorption spectrum of the two lowest $\pi\sigma^*$ states has been scarcely explored. The absorption band for the ${}^1A_2 \leftarrow \tilde{X}$ transition is overlaid by the intense band of the close-lying $\pi\pi^*$ state (see Fig. 1 of the paper) and the only calculated spectra were obtained by Roos et al. fifteen years ago.⁵⁶ The translational kinetic energy release (TKER) spectra measured by Ashfold and coworkers for long excitation wavelengths were never completely assigned nor reproduced theoretically.

In this work, new CASPT2 calculations were performed on a range of pyrrole geometries which uniformly covers the inner Franck-Condon region and the asymptotic zone of the separated H-atom and pyrrolyl fragments. These computations were used to construct a 24-dimensional (24D) diabatic molecular Hamiltonian. Different Hamiltonian models, including a growing number f of degrees of freedom ($f = 6, 11, 15$) were extracted from the 24D Hamiltonian, and used to perform quantum mechanical simulations of the photodissociation reaction, using the MCTDH method (see Section 4.2.2). The ${}^1A_2 \leftarrow \tilde{X}$ transition was described using a coordinate-dependent transition dipole moment (TDM) operator, defined according to the Herzberg-Teller approximation.

Each model has different symmetry properties and for each case the features of the calculated absorption profiles and the photon energy-dependent TKER spectra are interpreted in detail in terms of the topography of the potential energy surfaces and the form of the TDM function. As suggested by experimental studies,³³ the photodissociation of pyrrole is characterized by a high degree of vibrational adiabaticity in the modes transverse to the dissociation path: The modes which are initially excited by the TDM function carry the excitation over to the fragments.

Another major finding of Paper 4 is methodological. Exact quantum mechanical calculations of photodissociation cross sections are performed using potential energy surfaces which are derived by a large number of *ab initio* calculations. This procedure becomes prohibitive if one intends to study dissociation of a series of chromophores belonging to one class. For such studies, simplified procedures are desirable. For this reason, a computational scheme was developed to quantitatively analyze the diffuse absorption envelopes in the dissociative excited states and the subsequent ultrafast formation of the photofragments. The method, first applied to pyrrole, requires a minimum input of *ab initio*-derived data and was tested for pyrrole. The absorption spectra are approximated as a convolution of two profiles, one due to the pyrrolyl ring and one due to the detaching atom.

In another – related – method, the TKER spectra are obtained via the adiabatic mapping of the excitation in the vertical region onto the vibrational states of the free pyrrolyl. The spectra and TKER distributions, obtained with these approximations, compare well with the exact MCTDH calculations.

The comparison between experimental and calculated TKER profiles is discussed separately in Section 5.4.1. The implementation of the photofragment distribution calculation using the MCTDH code is given in Section 5.4.2

5.4.1 Total kinetic energy release (TKER) spectra of pyrrole: Theory vs Experiment

This Section is a logical extension of the discussion of Paper 4, in which the TKER distributions for different models of pyrrole photodissociation have been analyzed.

The calculated photon energy-dependent TKER spectra for the ${}^1A_2 \leftarrow \tilde{X}$ excitation are compared to the experimental results, obtained by Ashfold and coworkers in the long wavelength absorption region using the Rydberg tagging technique.³³ Experiments are typically performed by varying the angle α , between the electric field polarization vector and the detection axis, along which the velocity of the detached H atom is measured (in this way, the anisotropy parameter can be measured). A proper comparison is made between the average TKER spectra $P(E_{\text{kin}}|E_{\text{ph}}) = [P_x(E_{\text{kin}}|E_{\text{ph}}) + P_y(E_{\text{kin}}|E_{\text{ph}}) + P_z(E_{\text{kin}}|E_{\text{ph}})] / 3$, calculated for rotationless pyrrole, and the TKER profiles measured at the magic angle $\alpha = 54.7^\circ$ (corresponding to the spectra integrated over α).

The experimental profiles are compared with the calculated distributions associated with the same maximum available kinetic energy, $E_{\text{kin}}^{\text{max}} = E_{\text{ph}} - D_0$, which defines the position of the pyrrolyl ground state peak. Wave packet calculations were performed for the coupled \tilde{X} and 1A_2 states using the MCTDH method. The potential energy surfaces described in Paper 4 were used. Pyrrole was described using 15 coordinates including the Jacobi coordinates of the detaching H atom (R, θ, ϕ) and three pyrrolyl normal modes for each symmetry, $Q_{a_1}(1, 2, 5)$, $Q_{a_2}(1, 2, 3)$, $Q_{b_1}(1, 2, 3)$ and $Q_{b_2}(1, 3, 5)$.[†] The pyrrolyl normal modes are sketched in Figure 5.2.

The high degree of vibrational adiabaticity implies that the final state distributions are largely shaped in the Franck-Condon region, i. e. by the transition dipole moment (TDM) function. In order

[†] These are the same coordinates used in the 15D calculations of Sections V C and VI C of Paper 4. For the normal modes, the corresponding irreducible representation of the C_{2v} point group is indicated.

The form of the Hamiltonian is given in Section II A of Paper 4. The modes not included in the calculation are set to the pyrrolyl equilibrium geometry ($\mathbf{Q} = \mathbf{0}$).

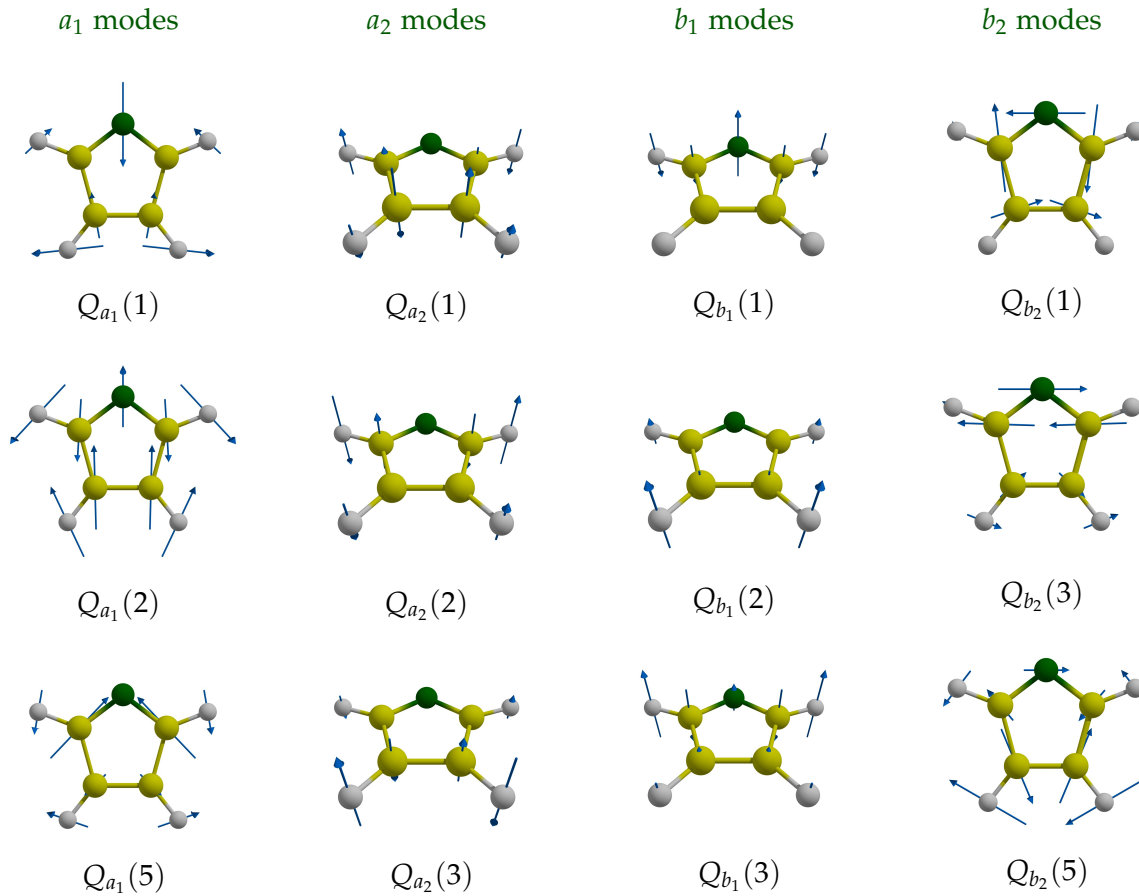


Figure 5.2: Sketches of the pyrrolyl normal modes included wave packet calculations of pyrrole photodissociation.

to provide a flexible representation of the coordinate dependence of the TDM in the Franck-Condon region, the following TDM function was used for the ${}^1A_2 \leftarrow \tilde{X}$ transition:

$$\mu_x^{A_2}(\mathbf{R}, \mathbf{Q}) = \mu_{x,\theta,1}^{A_2}(R) \sin \theta \sin \phi + \mu_{x,\theta,2}^{A_2}(R) \sin(2\theta) \sin \phi + \sum_{\Gamma_i=b_2} \mu_{x,i}^{A_2}(R) Q_{b_2}(i), \quad (5.3a)$$

$$\mu_y^{A_2}(\mathbf{R}, \mathbf{Q}) = \mu_{y,\theta,1}^{A_2}(R) \sin \theta \cos \phi + \mu_{y,\theta,2}^{A_2}(R) \sin(2\theta) \cos \phi + \sum_{\Gamma_i=b_1} \mu_{y,i}^{A_2}(R) Q_{b_1}(i), \quad (5.3b)$$

$$\mu_z^{A_2}(\mathbf{R}, \mathbf{Q}) = \sum_{\Gamma_i=a_2} \mu_{z,i}^{A_2}(R) Q_{a_2}(i). \quad (5.3c)$$

The TDM components of Eqs. (5.3) are similar to the Herzberg-Teller expression used in the calculations of Paper 4 (see Eq. (13) of Paper 4), with two main differences: i) The real spherical harmonics d_{xz} and d_{yz} are included as angular functions, in addition to p_x and p_y ; ii) The Herzberg-Teller

coefficients are replaced with R -dependent functions, given by a second-order Taylor expansion around the \tilde{X} state minimum R_{FC} :[‡]

$$\mu(R) = \mu^{(0)}(R_{\text{FC}}) + \mu^{(1)}(R_{\text{FC}}) (R - R_{\text{FC}}) + \mu^{(2)}(R_{\text{FC}}) (R - R_{\text{FC}})^2 . \quad (5.4)$$

In quantum dynamical calculations, the initial wavefunctions for the three polarizations are calculated by acting with the TDM functions (5.3a), (5.3b) and (5.3c) on the ground vibrational wavefunction of the \tilde{X} state.

Figures 5.3(a) and (b) show the TKER spectra obtained by the 15D MCTDH calculations using the TDM functions of Eq. (5.3) and by the experiment, respectively. As discussed in Paper 4, the peaks in the spectra correspond to the vibrational energy levels of pyrrolyl, their width is given by the rotational distribution and their intensities represent vibrational state populations. Symmetry selection rules determine which states can be populated for different TDM components (see Section VI C of Paper 4).

In Figure 5.3(a) the polarization-averaged spectrum $P(E_{\text{kin}}|E_{\text{ph}})$ is depicted as a green dashed line. Since all polarizations are included, this profile exhibits peaks corresponding to vibrational states belonging to all irreducible representations. The inspection of the profiles for the different polarizations (not reported here) suggests that the peak intensities associated with vibrational states of B_1 symmetry are underestimated in the calculation. Although the green spectrum of Figure 5.3 is already sufficient to assign of the vibrational peaks, we facilitate the comparison with the experiment by increasing the population of the B_1 vibrational states by a factor three. After this adjustment, the profile depicted as black line is obtained, whose intensity pattern becomes similar to the experimental TKER spectra. The underestimation of the population of the B_1 vibrational states in the calculation is discussed below.

In both the calculated and the experimental distributions, the populated vibrational states are comprised in an energy window of $\approx 2500 \text{ cm}^{-1}$. Test calculations for the dissociation on the uncoupled 1A_2 state (not reported here) show that the intensity pattern of the TKER profile is nearly unaffected by the presence of the \tilde{X}/A_2 crossing. Therefore, the experimental profiles for low excitation energies are not expected to exhibit signatures of the conical intersection.

In the experimental TKER profiles for $E_{\text{kin}}^{\text{max}} = 6861 \text{ cm}^{-1}$ and $E_{\text{kin}}^{\text{max}} = 7184 \text{ cm}^{-1}$, three groups of peaks are recognizable. The first group includes only the peak A, associated with the vibrational

[‡] The TDM function was calculated using the state-averaged CASSCF(8,7) method on two-dimensional grids (R_i, Q_j) and (R_i, θ_j) with $\phi = 0^\circ$ and $\phi = 90^\circ$, including the states \tilde{X} , 1A_2 and 1B_1 . The grid points R_i cover the range $[3.6, 4.5] a_0$ with a step of $0.15 a_0$. The points θ_j cover the range $[0^\circ, 15^\circ]$ with a step of 1.5° . The points Q_j cover the range $[0, 1]$ with a step of 0.1. The grid data were fitted to the functions of Equation (5.3) and (5.4).

ground state of pyrrolyl; the second group consists in the peaks C and D; the third group includes the peaks C' and D'. For higher excitation energies, an increased intensity is observed in two additional pairs of states, indicated with the letters E, F and E', F', and in a weakly populated low energy state (peak B, more visible in the spectra recorded at $\alpha = 0^\circ$ and reported in Reference 33).

The three-group-structure is reproduced by our calculations. The peak C is attributed to the fundamental excitation of $Q_{b_1}(2)$ ($\omega = 757 \text{ cm}^{-1}$), as suggested by the experimentalists. The one quantum excitation of the mode $Q_{b_2}(1)$ ($\omega = 710 \text{ cm}^{-1}$) contributes to the intensity of peak C, too. Peak D is given by the fundamental excitations of the modes $Q_{a_2}(3)$, also identified

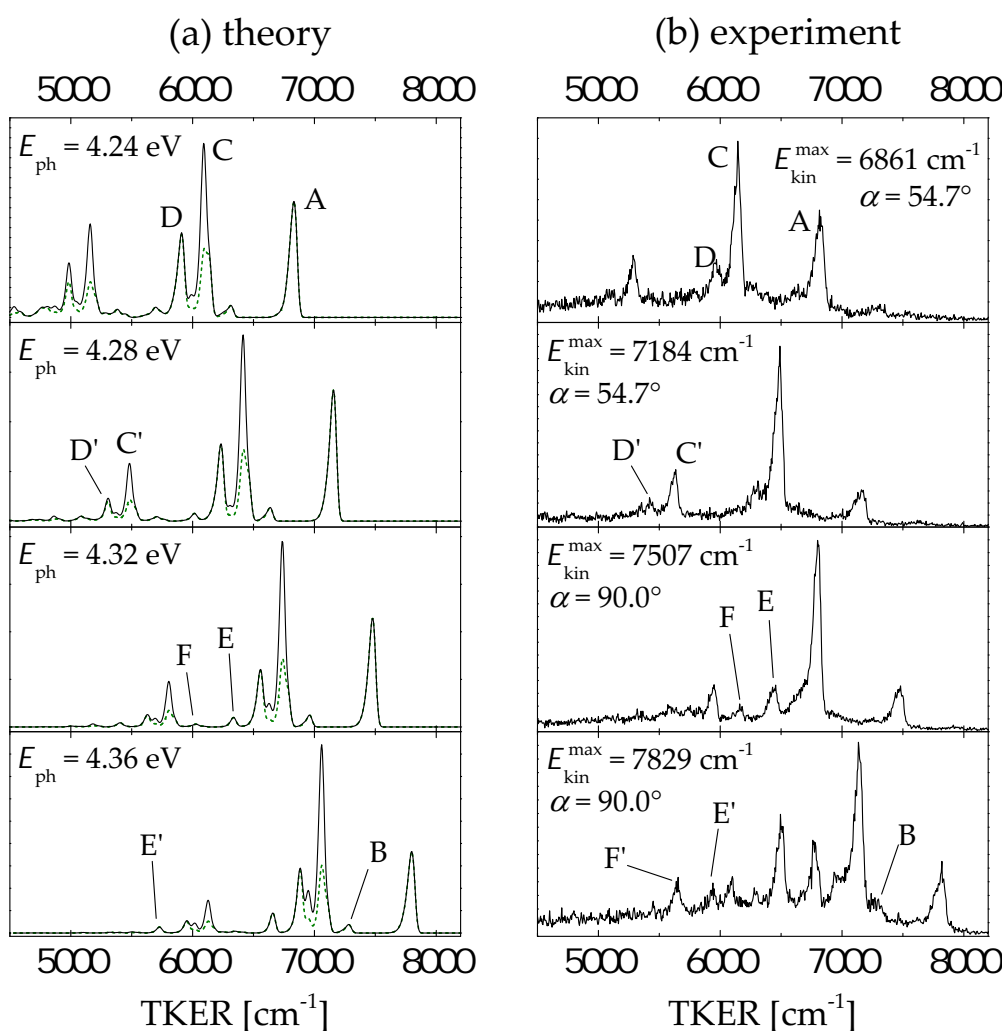


Figure 5.3: (a) The polarization-averaged TKER spectrum $P(E_{\text{kin}}|E_{\text{ph}})$ is depicted as a green dashed line. The TKER profile shown as continuous black line is obtained by increasing the population of the vibrational states of B_1 symmetry by a factor three. (b) Experimental TKER profiles. The detection angle α is reported in each panel. From top to bottom, the experimental excitation wavelengths are 252 nm, 250 nm, 248 nm and 246 nm.

by the experimentalists, and $Q_{a_1}(1)$. The intensity of the peak D seems slightly overestimated in the calculations; on the other hand, the population of the $Q_{a_2}(3)$ mode is experimentally shown to be strongly dependent on the detection angle α (it is high for $\alpha = 0^\circ$ and low for $\alpha = 90^\circ$): The A_2 vibrational states, excited via the z-polarized transition, are associated with a large anisotropy parameter. The peaks E and F correspond to the states with one quantum on the modes $Q_{b_2}(3)$ and $Q_{b_2}(5)$. In comparison with the experiment, the population of these modes is slightly underestimated in the calculations. The tiny peak B, emerging at higher photon energies, is attributed to the mode $Q_{a_2}(1)$. Finally, the third group of peaks, $C' - F'$, is reproduced by the calculation, and is due to combination states, obtained from the states of the second group (peaks C-F) with an additional quantum on the $Q_{a_1}(1)$ mode. Such progression of the lowest frequency a_1 mode was not recognized in Reference 33, and the peaks at low kinetic energy were assigned to other combination states, nearly unpopulated in our simulations.

I am unaware of previous quantum mechanical calculations of vibrationally resolved TKER profiles for high-dimensional fragments. Since the experimental absorption profile for pyrrole is not available, the experimental TKER spectra are the key spectroscopic observables to validate the model used in our calculations. Although the calculated TKER spectra do not match the experiment perfectly, they allow the complete vibrational assignment. For this reason, our quantum dynamical calculations can be considered reliable.

Calculated TKER spectra might be affected by a number of factors:

- The quality of quantum chemical calculations and the functional form of the potential energy surfaces. The final mode populations are strongly dependent on the mode frequency, and on the dissociation profile. In addition, our PESs are quadratic in the normal modes, therefore they forbid the exchange of vibrational excitation between modes of different symmetries, which could modify the vibrational pattern in the TKER spectra, and allow additional fragment states to be populated.

The underestimation of the population of B_1 states can be attributed either to a too low R -dependent Herzberg-Teller coefficient for the b_1 modes or, more probably, to the lack of correlation between the b_1 modes and the out-of-plane H bending: Coupling terms, similar to the bilinear $Q_{b_1}(i)Q_{b_1}(j)$ terms and neglected in our PES, would allow a vibrational excitation exchange between normal modes and angular coordinates, and would affect the b_1 mode populations.

- The quality of the TDM function, which strongly affects the intensity, position on the excitation energy scale, and width of the partial cross sections. Since the photodissociation of pyrrole

occurs in a time scale < 50 fs, the final distributions are largely shaped by the TDM function. For most vibrational states, the excitation in the low-energy range corresponds to the tails of the partial cross section envelopes, which decay rapidly to zero. For this reason, small inaccuracies in the PES topography or in the TDM functions can lead to rather wrong TKER spectra: Even a small shift in the relative positions of the partial cross sections of different fragment states produces a large difference in the respective final populations. This is expected to be a serious issue for high-dimensional fragments, and in particular for the ${}^1A_2 \leftarrow \tilde{X}$ excitation in pyrrole, because the three TDM components have similar magnitude and form different fragments states.

- The coupling strength at the conical intersection. In our potential, the \tilde{X}/A_2 coupling is weak, so that the extent of $A_2 \rightarrow \tilde{X}$ transfer is $< 10\%$. A stronger coupling can be expected to increase the transition probability, and affect the final population of the coupling modes (a_2). Indeed, Blank et al.⁵² estimated that, at the excitation wavelength $\lambda = 248$ nm (corresponding to $E_{\text{kin}}^{\text{max}} = 7507 \text{ cm}^{-1}$), 42% of the photoexcited molecules undergo internal conversion to the ground state. A quantum yield of 22% was derived by Wei et al. for $\lambda = 243$ nm.²⁵ However, experiments performed at longer wavelengths suggest a lower extent of transfer to \tilde{X} , in agreement with our calculations.^{33,26}
- Discrepancies between the calculated and the measured quantum yield can be due to a too low value of the \tilde{X}/A_2 coupling strength, or to additional deactivation pathways, not included in our PES. According to the surface hopping simulations of Barbatti et al.,⁶² the N–H stretching dissociation is the dominant mechanism for the internal conversion at low excitation energies. Other pathways, involving out-of-plane ring puckering motions, are activated at higher energies.⁵² These mechanisms might be favoured by the y - and z -polarizations, which excite out-of-plane degrees of freedom, and modify the final populations of the a_2 and b_1 modes. Additional fragmentation channels might produce H atoms (detected in Rydberg tagging experiments) or might be activated for specific polarizations. In our calculations, only the the N–H bond dissociation is considered. Blank et al. observed a C–H bond cleavage occurring with a 11% quantum yield at $\lambda = 248$ nm,⁵² and additional fragmentation channels have been reported for higher excitation energies.^{52,25,53}

5.4.2 Calculation of the photofragment distributions using the MCTDH package

Quantum wave packet calculations for pyrrole were performed using the Heidelberg MCTDH package.⁷⁷ The time-dependent wavefunction was stored in the MCTDH format on a time grid with a spacing of 1 fs. A Python script was developed to process the wavefunction in order to calculate the product state distributions using the procedure of Section 3.4.1.

The script works as follows:

1. The pyrrolyl mode frequencies $\omega_1, \dots, \omega_n$, inertia constants I_x, I_y, I_z and the dissociation energy D_0 are initialized. The analysis line $R - R_\infty$ is chosen in the asymptotic region ($R_\infty = 9.5 a_0$).
2. Fragment eigenfunctions are approximated as products of a multi-dimensional harmonic oscillator wavefunctions and a spherical harmonic $Y_{lm}(\theta, \phi)$. The energy levels are identified by a set of vibrational quantum numbers $\nu = (\nu_1, \dots, \nu_f)$ and the angular quantum numbers (l, m) . For the low energy side of the absorption spectrum, only the states with less than three vibrational quanta are significantly populated.
3. A for loop is performed over the fragment energy levels. For each eigenstate:

- (a) The eigenenergy is calculated as

$$E_{\nu lm} = \sum_{i=1}^n \hbar \omega_i \left(n_i + \frac{1}{2} \right) + \frac{\hbar^2}{4} \left[\left(\frac{1}{I_x} + \frac{1}{I_y} \right) l(l+1) + \left(\frac{2}{I_z} - \frac{1}{I_x} - \frac{1}{I_y} \right) m^2 \right]. \quad (5.5)$$

This value is then used to evaluate the photon-energy dependent wavevectors $k_{\nu lm} \sim (E_{\text{ph}} - D_0 - E_{\nu lm})^{\frac{1}{2}}$ [cf. Equation (3.26)].

- (b) A MCTDH input is generated to perform the calculation of the fragment eigenfunction multiplied by the $\delta(R - R_\infty)$ [cf. Equation (3.25)]. The mctdh program is executed to generate the projection function in the MCTDH format.
 - (c) The program `crosscorr` from the MCTDH package is executed to evaluate the cross-correlation functions using Equation (3.25).
 - (d) The program `crosspec` from the MCTDH package is executed to calculate the partial cross sections on a given energy grid using Equation (3.26). The energy-dependent state populations $P_{\nu lm}(E_{\text{ph}})$ are read from the output of `crosspec` and stored in an array.
4. For a selected set of photon energies, a stick TKER spectrum is constructed from the pairs $(E_{\text{ph}} - D_0 - E_{\nu lm}, P_{\nu lm}(E_{\text{ph}}))$. The final TKER profile is obtained by a convolution with a Gaussian function with a standard deviation of $\sim 10 \text{ cm}^{-1}$.

5.5 Fano resonances in the photoinduced H-atom elimination dynamics in the $\pi\sigma^*$ states of pyrrole[†]

Paper 5 describes the effect of the Fano interference between two dissociation pathways on the photoabsorption spectrum. This kind of interference is predicted to be generally operative in the photodissociation occurring in $\pi\sigma^*$ states which cross the bound electronic ground state. In this case, the photoabsorption spectrum exhibit narrow asymmetric peaks, which can be regarded as signatures of the conical intersection. The mechanism is described for the photodissociation of pyrrole, using quantum dynamical calculations on reduced-dimensionality potential energy surfaces which are obtained from *ab initio* calculations.

An illustration of the interfering dissociation pathways is given in Figure 1.1(b), for the ${}^1B_1 \leftarrow \tilde{X}$ excitation. The two pathways are shown in the diabatic representation: One of them is the direct dissociation on the diabatic $\pi\sigma^*$ surface (pathway I), the other one involves a temporary sojourn in the bound \tilde{X} state (pathway III).

The interaction of bound states with a continuum gives rise to so-called Fano resonance states, first described in the context of atomic autoionization processes.⁹⁴ The bright Fano resonances emerge in the absorption spectrum as peaks with asymmetric line shapes. In pyrrole, the interference is mediated by the $\tilde{X}/\pi\sigma^*$ conical intersections. The asymmetric peaks in the calculated spectra correspond to bound energy levels whose nature is different for the two $\tilde{X}/\pi\sigma^*$ intersections.

For the $\tilde{X}/{}^1A_2$ intersection, the diabatic coupling is weak, and the interfering pathways are best described in the diabatic picture. Only the continuum scattering states are bright and give rise to a broad absorption envelope. Fano peaks emerge on top of the broad background and their position on the energy scale corresponds to high lying vibrational levels of the bound \tilde{X} state.

For the $\tilde{X}/{}^1B_1$ intersection, the diabatic coupling is large and a description based on the adiabatic representation is more appropriate. In this case, the bright interfering states are vibrational states of the upper cone of the intersection and, to a lesser extent, scattering states in the continuum (associated with the lower adiabatic state).

Fano interference can have a profound effect on the final photofragment distributions and therefore can be detected in translational or photofragment excitation (PHOFEX) spectra.⁹⁵ Especially

[†] *Individual candidate contribution.* This paper is equally contributed by the two authors. Fano peaks were first identified by myself in test calculations based on the two-dimensional model which includes the states \tilde{X} and 1A_2 (Fig. 1(b) of Paper 5). We related the peak positions to the energy levels of the \tilde{X} diabatic surface. S. G. further developed the theory, analysing in detail the cases of weak and strong diabatic coupling. I performed the calculations for the six- and three-dimensional models of Figures 2 and 3, contributed to write the paper, and wrote the Supporting Information.

in the case of strong diabatic coupling, the resulting dissociation products are expected to have a high degree of excitation in the vibrational or rotational degrees of freedom correlating with the coupling mode at the intersection.

CONCLUSIONS AND PERSPECTIVES

This dissertation analyzes molecular photodissociation reactions in the presence of conical intersections in the exit channel. The main findings can be summarized as follows:

- Novel signatures of the conical intersections are identified in different spectroscopic observables. In the photofragment state distributions, specific degrees of freedom become strongly vibrationally excited upon passage through a conical intersection (Sections 5.1 and 5.2). In the absorption spectrum, the intersection between the initially populated repulsive state and the bound ground state gives rise to asymmetric Fano peaks (5.5).
- Photoemission spectra provide information about the intermediate stages of photodissociation (Sections 5.2 and 5.3). Using resonance Raman amplitudes, one can reconstruct the vibrational populations of the dissociating, but still interacting, photofragments at arbitrary intermediate distances along the reaction path.
- Approximate methodologies are developed to calculate the photoabsorption profiles and the product state distributions of dissociating molecules (Section 5.4). The convolution-based calculation of the absorption spectra and the overlap integral-based mapping approach to photofragment distributions require a minimal input obtained by quantum chemical calculations and allow the assignment of the vibrational structure of the spectroscopic observables.
- A new set of potential energy surfaces are constructed for the ground electronic state and the two lowest $\pi\sigma^*$ states of pyrrole (Section 5.4). Quantum dynamical calculations, performed using these potentials, allow the complete assignment of the TKER spectra of pyrrole for long excitation wavelengths.

Two molecules, ozone and pyrrole, served as prototypes in these studies. The reactions are studied computationally, using *ab initio* quantum chemistry to construct the potential energy surfaces, and quantum dynamical calculations to simulate the photodissociation dynamics. Several

spectroscopic observables are calculated: The total absorption cross section, the final product distributions and the resonance Raman spectrum.

The calculated observables are compared with the available experimental measurements, and related to the topography of the potential energy surfaces. In the systems under study, conical intersections are encountered along the dissociation pathway. The electronic degeneracy is manifested in different spectroscopic signatures, specific of the particular arrangement of the crossing surfaces. In this sense, ozone and pyrrole can be viewed as prototypical systems for larger classes of molecules, in which similar effects due to such conical intersections can be expected.

The main feature of the photochemistry of ozone in the Hartley band is the presence of two electronic dissociation channels emerging from a conical intersection shifted away from the Franck-Condon zone into the exit channel, as shown in Figure 1.1. Surface topographies of the same kind are found in a number of photodissociation reactions (see Section 5.2). Such exit channel conical intersections imprint a hallmark on the photoproducts: The fragments formed following the adiabatic pathway exhibit an excitation in the coordinate mapped to the coupling mode of the intersection (for ozone, this is the stretch of the short O–O bond). This effect is due to a ‘selection’ of the molecules following the adiabatic path, occurring in the crossing region. The intersection acts like a sieve, which allows the diabatic transition only to the molecules with substantial vibrational excitation in the coupling mode, and this excitation is carried over to the fragments.

An intermediate population analysis has been developed, in order to characterize the energy redistribution along the dissociation path and to visualize the impact of the intersection. Transient vibrational state distributions reveal that the excitation of the coupling mode is formed just after the internal conversion and not in the post-intersection dynamics. Such intermediate distributions are not only a theoretical construction, but they also provide a connection with emission spectroscopy, inasmuch as they can be reconstructed from resonance Raman amplitudes. Spectroscopies based on emission have been extensively used in the context of photodissociation.^{96–98} The importance of transient distributions encourages the development of experimental techniques to recover the complex amplitude or phase from the intensity of emitted light.⁹¹

For the pyrrole molecule, the topography of the intersecting surfaces is different (see Figure 1.1) and is characteristic of the chromophores exhibiting $\pi\sigma^*$ photochemistry.^{33,20} The conical intersections are between the dissociative states and the bound \tilde{X} state and only the electronic channels correlating with the $\pi\sigma^*$ states are open. A general feature of this arrangement is the interaction between the bound vibrational states of the diabatic \tilde{X} potential and the scattering states associated with the repulsive $\pi\sigma^*$ profiles. This interference gives rise to narrow Fano peaks, which

emerge on top of a broad continuous absorption profile. Interestingly, the absorption spectrum shows signatures of the conical intersection, even if the crossing geometry is far from the vertical excitation region. The study performed on pyrrole predicts that Fano resonances can be observed experimentally from photofragment excitation spectra,⁹⁵ in which the final population of a specific fragment eigenstate is monitored as a function of the excitation energy.

Studies of the product state distributions of pyrrole have been essential in understanding its dissociation mechanism, allowing the excitation to the $^1A_2(\pi\sigma^*)$ state. Most of the reviews and monographs dealing with the quantum mechanical theory of photodissociation consider only triatomic molecules.^{68,69} Although the extension of the theory to high-dimensional systems is rather straightforward (see Chapter 3), the computational effort required for accurate simulations increases considerably.

The simulation of the TKER spectra of pyrrole has required several steps: (i) The construction of 24-dimensional potential energy surfaces of the \tilde{X} and $\pi\sigma^*$ states; (ii) The implementation of the procedure of Balint-Kurti (see Section 3.4.1) in combination with the MCTDH package; (iii) A number of wave packet simulations to identify the relevant degrees of freedom and to understand how the transition dipole moment function and the topography of the potential energy surfaces can be traced back to the final product distributions. To my knowledge, the simulations illustrated in Section 5.4.1 are the first calculations which allow the vibrational assignment of TKER spectra for a polyatomic fragment. The most intense peaks of the TKER spectra are associated with the most displaced (totally symmetric) modes and with the modes which mostly induce the $^1A_2 \leftarrow \tilde{X}$ transition.

Accurate quantum calculations for sizeable molecules are computationally demanding. The tremendous growth of experimental measurements encourages the development of approximated methods which require a minimum amount of *ab initio* calculations and allow the systematic study of broad classes of photodissociation reactions. The convolution and adiabatic mapping approximations, tested in Section 5.4, provide quantitatively correct estimates of the absorption spectrum and the photofragment distributions. For the adiabatic mapping, the requirement is a high degree of vibrational adiabaticity, whereby the vibrational excitation created by the initial photon absorption is carried over to the fragments.

Vibrational adiabaticity is observed in many classes of photodissociations of heteroaromatic molecules,¹⁸ for which the methodologies developed in this work can be applied. Further applications embrace a number of different fields, from photobiological reactions, atmospheric chemistry, chemical laser technology and solar energy utilization.

As an example, a connection can be made between the $\pi\sigma^*$ photochemistry, described herein for pyrrole, and the water splitting reaction which is catalysed by a redox-active chromophore.^{99–101} Considering a hydrogen-bonded water-chromophore complex, $X - H_2O$, the splitting of the water molecule can be achieved by the two photodissociation reactions



Possible photocatalysts are heteroaromatic molecules, for which the species $XH\cdot$ is a hypervalent radical with a H–heteroatom bond. In recent work, the photodissociation of the pyridinyl radical ($X = \text{pyridine}$), involving a repulsive $\pi\sigma^*$ state, was studied quantum mechanically using a reduced-dimensionality potential energy surface.¹⁰² The arrangement of the potential energy surfaces of the ground and the $\pi\sigma^*$ states of pyridinyl is similar to the one of pyrrole. In the second step of the reaction (6.1), the dissociation on the $\pi\sigma^*$ state (cf. pathway I in Figure 1.1) competes with the relaxation to the ground state (cf. pathway II in Figure 1.1). The detailed understanding of the photodissociation mechanism, advocated in this work, is crucial to improve the quantum yield for the dissociation and, in a broader sense, to design optimal catalysts for photochemical reactions.

BIBLIOGRAPHY

- [1] Nicholas J. Turro, V. Ramamurthy, and J. C. Scaiano. *Principles of Molecular Photochemistry: An Introduction*. University Science Books, USA, 2000.
- [2] M. N. R. Ashfold, D. Murdock, , and T. A. A. Oliver. Molecular photofragmentation dynamics in the gas and condensed phases. *Annual Review of Physical Chemistry*, 68:63, 2017.
- [3] T. Kumpulainen, B. Lang, A. Rosspeintner, and E. Vauthey. Ultrafast elementary photochemical processes of organic molecules in liquid solution. *Chemical Reviews*, 2017.
- [4] J. T. Hynes, J. P. Klinman, H.-H. Limbach, and R. L. Schowen. *Hydrogen-Transfer Reactions*. Wiley-VCH, Weinheim, 2007.
- [5] K.-L. Han and G.-J. Zhao. *Hydrogen Bonding and Transfer in the Excited State*. John Wiley & Sons, West Sussex, 2011.
- [6] S. Deb and M. P. Weber. The ultrafast pathway of photon-induced electrocyclic ring-opening reactions: The case of 1,3-cyclohexadiene. *Annual Review of Physical Chemistry*, 62:19, 2011.
- [7] B. C. Arruda and R. J. Sension. Ultrafast polyene dynamics: The ring opening of 1,3-cyclohexadiene derivatives. *Phys. Chem. Chem. Phys.*, 16:4439, 2014.
- [8] P. Kukura, D. W. McCamant, S. Yoon, D. B. Wandschneider, and R. A. Mathies. Structural observation of the primary isomerization in vision with femtosecond-stimulated Raman. *Science*, 310:1006, 2005.
- [9] B. G. Levine and T. J. Martínez. Isomerization through conical intersections. *Annual Review of Physical Chemistry*, 58:613, 2007.
- [10] *Conical Intersections: Theory, Computation and Experiment*, edited by W. Domcke, D. R. Yarkony and H. Köppel. World Scientific, Singapore, 2011.
- [11] G. A. Worth and L. S. Cederbaum. Beyond Born-Oppneheimer: Molecular dynamics through a conical intersection. *Annual Review of Physical Chemistry*, 55:127, 2004.

- [12] J. S. Lim and S. K. Kim. Experimental probing of conical intersection dynamics in the photodissociation of thioanisole. *Nature Chemistry*, 2:627, 2010.
- [13] S. Matsika and P. Krause. Nonadiabatic events and conical intersections. *Annual Review of Physical Chemistry*, 62:621, 2011.
- [14] W. Domcke and D. R. Yarkony. Role of conical intersections in molecular spectroscopy and photoinduced chemical dynamics. *Annual Review of Physical Chemistry*, 63:325, 2012.
- [15] M. N. Daud, G. G. Balint-Kurti, and A. Brown. Ab initio potential energy surfaces, total absorption cross sections, and product quantum state distributions for the low-lying electronic states of N₂O. *The Journal of Chemical Physics*, 122:054305, 2005.
- [16] S. Yu. Grebenshchikov. Photochemistry of carbon dioxide from first principles: Application to photoabsorption of hot CO₂. *Journal of CO₂ Utilization*, 15:32, 2016.
- [17] R. de Nalda, J. Durá, A. García-Vela, J. G. Izquierdo, and L. Bañares. A detailed experimental and theoretical study of the femtosecond A-band photodissociation of CH₃I. *The Journal of Chemical Physics*, 128:244309, 2008.
- [18] M. N. R. Ashfold, B. Cronin, A. L. Devine, R. N. Dixon, and M. G. D. Nix. The role of $\pi\sigma^*$ excited states in the photodissociation of heteroaromatic molecules. *Science*, 312:1637, 2006.
- [19] M. N. R. Ashfold, G. A. King, D. Murdock, M. G. D. Nix, T. A. A. Oliver, and A. G. Sage. $\pi\sigma^*$ excited states in molecular photochemistry. *Phys. Chem. Chem. Phys.*, 12:1218, 2010.
- [20] H. S. You, S. Han, J.-H. Yoon, J. S. Lim, J. Lee, S.-Y. Kim, D.-S. Ahn, J. S. Lim, and S. K. Kim. Structure and dynamic role of conical intersections in the $\pi\sigma^*$ -mediated photodissociation reactions. *International Reviews in Physical Chemistry*, 34:429, 2015.
- [21] W. N. Hartley. On the absorption spectrum of ozone. *Journal of the Chemical Society, Transactions*, 39:111, 1881.
- [22] W. Huggins and M. Huggins. On a new group of lines in the photographic spectrum of Sirius. *Proceedings of the Royal Society of London*, 48:216, 1890.
- [23] S. Yu. Grebenshchikov, Z.-W. Qu, H. Zhu, and R. Schinke. New theoretical investigations of the photodissociation of ozone in the Hartley, Huggins, Chappuis, and Wulf bands. *Phys. Chem. Chem. Phys.*, 9:2044, 2007.

- [24] Paul L. Houston. *Modern trends in chemical reaction dynamics: experiment and theory, Part I*, edited by X. Yang and K. Liu. World Scientific, Singapore, 2004. Chapter 6, p. 281.
- [25] J. Wei, J. Riedel, A. Kuczmann, F. Renth, and F. Temps. Photodissociation of pyrrole: Evidence for mode specific dynamics from conical intersections. *Faraday Discussion*, 127:267, 2004.
- [26] G. M. Roberts, C. A. Williams, H. Yu, A. S. Chatterley, J. D. Young, S. Ullrich, and V. G. Stavros. Probing ultrafast dynamics in photoexcited pyrrole: Timescales for $^1\pi\sigma^*$ mediated H-atom elimination. *Faraday Discussion*, 163:95, 2013.
- [27] A. Stolow and J. G. Underwood. Time-resolved photoelectron spectroscopy of nonadiabatic dynamics in polyatomic molecules. *Advances in Chemical Physics*, 139:497, 2008.
- [28] S. P. Neville G. Wu, O. Schalk, T. Sekikawa, M. N. R. Ashfold, G. A. Worth, and A. Stolow. Excited state non-adiabatic dynamics of pyrrole: A time-resolved photoelectron spectroscopy and quantum dynamics study. *The Journal of Chemical Physics*, 142:074302, 2015.
- [29] D. Townsend, W. Li, S. K. Lee, R. L. Gross, and A. G. Suits. Universal and state-resolved imaging of chemical dynamics. *Journal of Physical Chemistry A*, 109:8661, 2005.
- [30] M. N. R. Ashfold, N. H. Nahler, A. J. Orr-Ewing, O. P. J. Vieuxmaire, R. L. Toomes, T. N. Kitsopoulos, I. Anton-Garcia, D. Chestakov, S.-M. Wu, and D. H. Parker. Imaging the dynamics of gas phase reactions. *Phys. Chem. Chem. Phys.*, 8:26, 2006.
- [31] M. N. R. Ashfold, G. A. King, M. G. D. Nix, and T. A. A. Oliver. *Handbook of High Resolution Spectroscopy*, edited by M. Quack and F. Merkt. Wiley, Chichester, UK, 2009.
- [32] X. M. Yang. State-to-state dynamics of elementary chemical reactions using Rydberg H-atom translational spectroscopy. *International Reviews in Chemical Physics*, 24:37, 2005.
- [33] B. Cronin, M. G. D. Nix, R. H. Qadiri, and M. N. R. Ashfold. High resolution photofragment translational spectroscopy studies of the near ultraviolet photolysis of pyrrole. *Phys. Chem. Chem. Phys.*, 6:5031, 2004.
- [34] B. Marchetti, T. N. V. Karsili, M. N. R. Ashfold, and W. Domcke. A 'bottom up, *ab initio* computational approach to understanding fundamental photophysical processes in nitrogen containing heterocycles, DNA bases and base pairs. *Phys. Chem. Chem. Phys.*, 12:1218, 2010.

- [35] R. Crespo-Otero and M. Barbatti. Spectrum simulation and decomposition with nuclear ensemble: Formal derivation and application to benzene, furan and 2-phenylfuran. *Theoretical Chemistry Accounts*, 131:1237, 2012.
- [36] G. Brancato and N. Rega. *Computational Strategies for Spectroscopy*, edited by V. Barone. John Wiley & Sons, Inc., Hoboken, NJ, 2012. Chapter 11, p. 517.
- [37] *Multidimensional Quantum Dynamics*, edited By H.-D. Meyer, F. Gatti and G. A. Worth. WILEY-VCH Verlag GmbH & Co. KGaA, Weinheim, 2009.
- [38] D.E. Freeman, K. Yoshino, J.R. Esmond, and W.H. Parkinson. High resolution absorption cross-section measurements of ozone at 195 k in the wavelength region 240–350 nm. *Planetary and Space Science*, 32:239, 1984.
- [39] B. R. Johnson and J. L. Kinsey. Dynamical interpretation of the Hartley-absorption oscillations in O₃. *Physical Review Letters*, 62:1607, 1989.
- [40] R. Bacis, A.J. Bouvier, and J.M. Flaud. The ozone molecule: electronic spectroscopy. *Spectrochimica Acta Part A*, 54:17, 1998.
- [41] P. J. Hay, R. T. Pack, R. B. Walker, and E. J. Heller. Photodissociation of ozone in the Hartley band. Exploratory potential energy surfaces and molecular dynamics. *The Journal of Physical Chemistry*, 86:862, 1982.
- [42] C. Leforestier and F. LeQuéré. Theoretical study of the ultraviolet photodissociation of ozone. Comparison with experiments. *The Journal of Chemical Physics*, 101:3806, 1994.
- [43] E. Baloitcha and G. G. Balint-Kurti. Theory of the photodissociation of ozone in the Hartley continuum: Potential energy surfaces, conical intersections, and photodissociation dynamics. *The Journal of Chemical Physics*, 123:014306, 2005.
- [44] R. Schinke and G. C. McBane. Photodissociation of ozone in the Hartley band: Potential energy surfaces, nonadiabatic couplings, and singlet/triplet branching ratio. *The Journal of Chemical Physics*, 132:044305, 2010.
- [45] J. Malicet, D. Daumont, J. Charbonnier, C. Parisse, A. Chakir, and J. Brion. Ozone UV spectroscopy. II. Absorption cross-sections and temperature dependence. *Journal of Atmospheric Chemistry*, 21:263, 1995.

- [46] J. J. Valentini, G. P. Derrity, D. L. Phillips, J.-C. Nieh, and K. D. Tabor. CARS spectroscopy of $O_2(^1\delta_g)$ from the Hartley band photodissociation of O_2 : Dynamics of the dissociation. *The Journal of Chemical Physics*, 86:6745, 1987.
- [47] D. Picconi and S. Yu. Grebenshchikov. Intermediate photofragment distributions as probes of non-adiabatic dynamics at conical intersections: Application to the Hartley band of ozone. *Phys. Chem. Chem. Phys.*, 17:28931, 2015.
- [48] D. G. Imre, J. L. Kinsey, and R. W. Field. Spectroscopic characterization of repulsive potential energy surfaces: Fluorescence spectrum of ozone. *The Journal of Physical Chemistry*, 86:2564, 1982.
- [49] D. Picconi and S. Yu. Grebenshchikov. Partial dissociative emission cross sections and product state distributions of the resulting photofragments. *Chemical Physics*, 481:231, 2016.
- [50] David J. Tannor. *Introduction to Quantum Mechanics. A Time-Dependent Perspective*. University Science Books, Sausalito, California, 2006.
- [51] H. Tal-Ezer and R. Kosloff. An accurate and efficient scheme for propagating the time dependent Schrödinger equation. *The Journal of Chemical Physics*, 81:3967, 1984.
- [52] D. A. Blank, S. W. North, and Y. T. Lee. The ultraviolet photodissociation dynamics of pyrrole. *Chemical Physics*, 187:35, 1994.
- [53] H. Lippert, H.-H. Ritze, I. V. Hertel, and W. Radloff. Femtosecond time-resolved hydrogen-atom elimination from photoexcited pyrrole molecules. *ChemPhysChem*, 5:1423, 2004.
- [54] L. Rubio-Lago, D. Zaouris, Y. Sakellariou, D. Sofikitis, T. N. Kitsopoulos, F. Wang, X. Yang, B. Cronin, A. L. Devine, G. A. King, M. G. D. Nix, M. N. R. Ashfold, and S. S. Xantheas. Photofragment slice imaging studies of pyrrole and the Xe – pyrrole cluster. *The Journal of Chemical Physics*, 127:064306, 2007.
- [55] A. B. Trofimov and J. Schirmer. Polarization propagator study of electronic excitation in key heterocyclic molecules. I. Pyrrole. *Chemical Physics*, 214:153, 1997.
- [56] B. O. Roos, P.-Å. Malmqvist, V. Molina, L. Serrano-Andrés, and M. Merchán. Theoretical characterization of the lowest-energy absorption band of pyrrole. *The Journal of Chemical Physics*, 116:7526, 2002.

- [57] M. H. Palmer and P. J. Wilson. The singlet electronic states of pyrrole: A theoretical study by both ab initio multi-reference configuration interaction methods and time-dependent density functional theory and a reconsideration of the experimental VUV spectral data. *Molecular Physics*, 101:2391, 2003.
- [58] H. Köppel, E.V. Gromov, and A. B. Trofimov. Multi-mode–multi-state quantum dynamics of key five-membered heterocycles: spectroscopy and ultrafast internal conversion. *Chemical Physics*, 304:35, 2004.
- [59] V. Vallet, Z. Lan, S. Mahapatra, A. L. Sobolewski, and W. Domcke. Time-dependent quantum wave-packet description of the $^1\pi\sigma^*$ photochemistry of pyrrole. *Faraday Discussions*, 127:283, 2004.
- [60] V. Vallet, Z. Lan, S. Mahapatra, A. L. Sobolewski, and W. Domcke. Photochemistry of pyrrole: Time-dependent quantum wave-packet description of the dynamics at the $^1\pi\sigma^* - s_0$ conical intersections. *The Journal of Chemical Physics*, 123:144307, 2005.
- [61] M. Pastore, C. Angeli, and R. Cimiraglia. The vertical electronic spectrum of pyrrole: A second and third order n -electron valence state perturbation theory study. *Chemical Physics Letters*, 422:522, 2006.
- [62] M. Barbatti, J. Pittner, M. Pederzoli, U. Werner, R. Mitrić, V. Bonacic-Koutecký, and H. Lischka. Non-adiabatic dynamics of pyrrole: Dependence of deactivation mechanisms on the excitation energy. *Chemical Physics*, 375:26, 2010.
- [63] S. Neville and G. A. Worth. A reinterpretation of the electronic spectrum of pyrrole: A quantum dynamics study. *The Journal of Chemical Physics*, 140:034317, 2014.
- [64] H. Köppel, W. Domcke, and L. S. Cederbaum. Multi-mode molecular dynamics beyond the Born-Oppenheimer approximation. *Advances in Chemical Physics*, 57:59, 1984.
- [65] Lorenz S. Cederbaum. *Conical Intersections: Electronic Structure, Dynamics and Spectroscopy*, edited by W. Domcke, D. R. Yarkony and H. Köppel. World Scientific, Singapore, 2004. Chapter 1, p. 3.
- [66] Horst Köppel. *Conical Intersections: Electronic Structure, Dynamics and Spectroscopy*, edited by W. Domcke, D. R. Yarkony and H. Köppel. World Scientific, Singapore, 2004. Chapter 4, p. 175.
- [67] David P. Craig and Thiru Thirunamachandran. *Molecular Quantum Electrodynamics*. Academic Press Inc., 1984.

- [68] Reinhard Schinke. *Photodissociation Dynamics*. Cambridge University Press, 1993.
- [69] G. G. Balint-Kurti. Wavepacket theory of photodissociation and reactive scattering. *Advances in Chemical Physics*, 128:249, 2004.
- [70] Mark S. Child. *Molecular Collision Theory*. Academic Press Inc., 1984. Chapter 6.
- [71] E. Bright Wilson Jr., J. C. Decius, and Paul C. Cross. *Molecular Vibrations: The Theory of Infrared and Raman Vibrational Spectra*. McGraw-Hill Book Company, Inc., 1955.
- [72] J. Tennyson and B. T. Sutcliffe. The *ab initio* calculation of the vibrational-rotational spectrum of triatomic systems in the close-coupling approach, with KCN and H₂Ne as examples. *The Journal of Chemical Physics*, 77:4061, 1982.
- [73] B. J Garrison, Jr. W. A. Lester, and W. H. Miller. Coupled-channel study of rotational excitation of a rigid asymmetric top by atom impact: (H₂CO, He) at interstellar temperatures. *The Journal of Chemical Physics*, 65:6, 1976.
- [74] David M. Brink and George R. Satchler. *Angular Momentum*. Oxford University Press, 1993.
- [75] G. G. Balint-Kurti, R. N. Dixon, and C. C. Marston. Time-dependent quantum dynamics of molecular photofragmentation processes. *J. Chem. Soc. Faraday Trans.*, 86:1741, 1990.
- [76] H.-J. Werner, P. J. Knowles, G. Knizia, F. R. Manby, M. Schütz, et al. MOLPRO, version 2008.1, a package of ab initio programs, 2008. see <http://www.molpro.net>.
- [77] G. A. Worth, M. H. Beck, A. Jäckle, and H.-D. Meyer. The MCTDH Package. H.-D. Meyer, Version 8.3 (2002), Version 8.4 (2007). O. Vendrell and H.-D. Meyer, Version 8.5 (2011). see <http://mctdh.uni-hd.de/>.
- [78] Frank Jensen. *Introduction to Computational Chemistry*. John Wiley & Sons Ltd, Chichester, UK, 2007.
- [79] Trygve Helgaker, Poul Jorgensen, and Jeppe Olsen. *Molecular Electronic-Structure Theory*. John Wiley & Sons Ltd,, 2008.
- [80] P. J. Knowles and H.-J. Werner. Internally contracted multiconfiguration-reference configuration interaction calculations for excited states. *Theoretica Chimica Acta*, 84:95, 1992.
- [81] H.-J. Werner. Third-order multireference perturbation theory. The CASPT3 method. *Molecular Physics*, 89:64, 1996.

- [82] H.-D. Meyer, U. Manthe, , and L. S. Cederbaum. The multi-configurational timedependent Hartree approach. *Chemical Physics Letters*, 165:73, 1990.
- [83] M. H. Beck, A. Jäckle, G. A. Worth, and H.-D. Meyer. The multiconfiguration time-dependent Hartree (MCTDH) method: A highly efficient algorithm for propagating wavepackets. *Physics Report*, 324:1, 2000.
- [84] J. C. Light, I. P. Hamilton, , and J. V. Lill. Generalized discrete variable approximation in quantum mechanics. *The Journal of Chemical Physics*, 82:1400, 1985.
- [85] V. A. Mandelshtam and H. S. Taylor. A simple recursion polynomial expansion of the Green's function with absorbing boundary conditions. Application to the reactive scattering. *The Journal of Chemical Physics*, 103:2903, 1995.
- [86] D. T. Colbert and W. H. Miller. A novel discrete variable representation for quantum mechanical reactive scattering via the S-matrix Kohn method. *The Journal of Chemical Physics*, 96:1982, 1992.
- [87] N. Balakrishnan and G. D. Billing. Three-dimensional wave packet studies of ozone photodissociation in the Hartley band: Converged autocorrelation functions and absorption spectra. *The Journal of Chemical Physics*, 101:2968, 1994.
- [88] M. Alacid and C. Leforestier. The role of rotation in the calculated ultraviolet photodissociation spectrum of ozone. *The Journal of Chemical Physics*, 114:1685, 2001.
- [89] Lev Davidovich Landau and Evgenii Mikhailovich Lifshits. *Quantum Mechanics: Non-relativistic Theory*. Pergamon, New York, 1976.
- [90] E. Teller. The crossing of potential surfaces. *The Journal of Physical Chemistry*, 41:109, 1937.
- [91] Z. Q. Feng and Soo-Y. Lee. Complex Raman amplitude recovery and dynamics from the Raman excitation profile: application to iodobenzene and azulene. *Journal of Raman spectroscopy*, 32:447, 2001.
- [92] M. Kotur, T. C. Weinacht, C. Zhou, K. A. Kistler, and S. Matsika. Distinguishing between relaxation pathways by combining dissociative ionization pump probe spectroscopy and *ab initio* calculations: A case study of cytosine. *The Journal of Chemical Physics*, 134:184309, 2011.

- [93] M. Ryszka, R. Pandey, C. Rizk, J. Tabet, B. Barc, M. Dampc, N. J. Mason, and S. Eden. Dissociative multi-photon ionization of isolated uracil and uracil-adenine complexes. *International Journal of Mass Spectrometry*, 396:48, 2016.
- [94] U. Fano. Effects of configuration interaction on intensities and phase shifts. *Physical Review*, 124:1866, 1961.
- [95] D.-S. Ahn, S.-Y. Kim, G.-I. Lim, S. Lee, Y. S. Choi, and S. K. Kim. Mode-dependent Fano resonances observed in the predissociation of diazirine in the s_1 state. *Angewandte Chemie International Edition*, 49:1244, 2010.
- [96] D. Imre, J. L. Kinsey, A. Sinha, and J. Krenos. Chemical dynamics studied by emission spectroscopy of dissociating molecules. *The Journal of Physical Chemistry*, 88:3956, 1984.
- [97] K. Q. Lao, M. D. Person, P. Xayariboun, and L. J. Butler. Evolution of molecular dissociation through an electronic curve crossing: polarized emission spectroscopy of iodomethane at 266 nm. *The Journal of Chemical Physics*, 92:823, 1990.
- [98] B. R. Johnson, C. Kittrell, P. B. Kelly, and J. L. Kinsey. Resonance Raman spectroscopy of dissociative polyatomic molecules. *The Journal of Physical Chemistry*, 100:7743, 1996.
- [99] A. L. Sobolewski and W. Domcke. Computational model of photocatalytic water splitting. *The Journal of Physical Chemistry A*, 112:7311, 2008.
- [100] X. Liu, A. L. Sobolewski, R. Borrelli, and W. Domcke. Computational investigation of the photoinduced homolytic dissociation of water in the pyridine–water complex. *Phys. Chem. Chem. Phys.*, 15:5957, 2013.
- [101] X. Liu, T. N. V. Karsili, A. L. Sobolewski, and W. Domcke. Photocatalytic water splitting with acridine dyes: Guidelines from computational chemistry. *Chemical Physics*, 464:78, 2016.
- [102] J. Ehrmaier, D. Picconi, T. N. V. Karsili, and W. Domcke. Photodissociation dynamics of the pyridinyl radical: Time-dependent quantum wave-packet calculations. *The Journal of Chemical Physics*, 146:124304, 2017.

ACKNOWLEDGEMENTS

I would like to thank my supervisor, Prof. Wolfgang Domcke, who gave me the opportunity to do my doctoral studies in his department and acquire a PhD natural science.

I would also like to thank my colleagues for a friendly working atmosphere and fruitful discussions.

I would like to express special gratitude to Dr. Sergy Grebenshchikov who supervised all my work discussing my results almost day-to-day and sharing with me a lot of scientific ideas.

Finally, I am grateful for the support of my family and my friends, who made my stay in Munich great and enjoyable.

APPENDIX

Complete list of publications

- 10 **Photodissociation dynamics and photofragment distributions in the first absorption band of pyrrole: I. Vibronic Franck-Condon Herzberg-Teller excitation of the ${}^1A_2(\pi\sigma^*) \leftarrow \tilde{X}{}^1A_1(\pi\pi)$ transition.** D. Picconi and S. Yu. Grebenshchikov, *in preparation*.
- 9 **Fano resonances in the photoinduced H-atom elimination dynamics in the $\pi\sigma^*$ states of pyrrole.** S. Yu. Grebenshchikov and D. Picconi, *Phys. Chem. Chem. Phys.* **19**, 14902 (2017); <http://dx.doi.org/10.1039/c7cp01401e>.
- 8 **Photodissociation dynamics of the pyridinyl radical: Time-dependent quantum wavepacket calculations.** J. Ehrmaier, D. Picconi, T. N. V. Karsili and W. Domcke, *The Journal of Chemical Physics* **146**, 124304 (2017); <http://dx.doi.org/10.1063/1.4978283>.
- 7 **Partial dissociative emission cross sections and product state distributions of the resulting photofragments.** D. Picconi and S. Yu. Grebenshchikov, *Chemical Physics* **481**, 231 (2016); <https://doi.org/10.1016/j.chemphys.2016.08.011>.
- 6 **Intermediate photofragment distributions as probes of non-adiabatic dynamics at conical intersections: application to the Hartley band of ozone.** D. Picconi and S. Yu. Grebenshchikov, *Phys. Chem. Chem. Phys.* **17**, 28931 (2015); <http://dx.doi.org/10.1039/c5cp04564a>.
- 5 **Signatures of a conical intersection in photofragment distributions and absorption spectra: Photodissociation in the Hartley band of ozone.** D. Picconi and S. Yu. Grebenshchikov, *The Journal of Chemical Physics* **141**, 074311 (2014); <http://dx.doi.org/10.1063/1.4892919>.
- 4 **Electronic Circular Dichroism in Exciton-Coupled Dimers: Vibronic Spectra from a General All-Coordinates Quantum-Dynamical Approach.** D. Padula, D. Picconi, A. Lami, G. Pescitelli and F. Santoro, *The Journal of Physical Chemistry A* **117**, 3355 (2013); <http://dx.doi.org/10.1021/jp400894v>.

- 3 **Quantum-classical effective-modes dynamics of the $\pi\pi^*/n\pi^*$ decay in 9H-adenine. A quadratic vibronic coupling model.** D. Picconi, F. J. A. Ferrer, R. Improta, A. Lami and F. Santoro, *Faraday Discussions* **163**, 223 (2013); <http://dx.doi.org/10.1039/c3fd20147c>.
- 2 **Hierarchical transformation of Hamiltonians with linear and quadratic couplings for nonadiabatic quantum dynamics: Application to the $\pi\pi^*/n\pi^*$ internal conversion in thymine.** D. Picconi, A. Lami and F. Santoro, *The Journal of Chemical Physics* **136**, 244104 (2012); <http://dx.doi.org/10.1063/1.4729049>.
- 1 **The Interplay between $\pi\pi^*/n\pi^*$ Excited States in Gas-Phase Thymine: A Quantum Dynamical Study.** D. Picconi, V. Barone, A. Lami, F. Santoro and R. Improta, *ChemPhysChem* **12**, 1957 (2011); <http://dx.doi.org/10.1002/cphc.201001080>.

Paper 1

**Signatures of a conical intersection in photofragment distributions and absorption spectra:
Photodissociation in the Hartley band of ozone.** D. Picconi and S. Yu. Grebenshchikov, *The
Journal of Chemical Physics* **141**, 074311 (2014); <http://dx.doi.org/10.1063/1.4892919>.

Signatures of a conical intersection in photofragment distributions and absorption spectra: Photodissociation in the Hartley band of ozone

David Picconi and Sergy Yu. Grebenshchikov^{a)}

Department of Chemistry, Technische Universität München, Lichtenbergstr. 4, 85747 Garching, Germany

(Received 1 July 2014; accepted 1 August 2014; published online 18 August 2014)

Photodissociation of ozone in the near UV is studied quantum mechanically in two excited electronic states coupled at a conical intersection located outside the Franck-Condon zone. The calculations, performed using recent *ab initio* PESs, provide an accurate description of the photodissociation dynamics across the Hartley/Huggins absorption bands. The observed photofragment distributions are reproduced in the two electronic dissociation channels. The room temperature absorption spectrum, constructed as a Boltzmann average of many absorption spectra of rotationally excited parent ozone, agrees with experiment in terms of widths and intensities of diffuse structures. The exit channel conical intersection contributes to the coherent broadening of the absorption spectrum and directly affects the product vibrational and translational distributions. The photon energy dependences of these distributions are strikingly different for fragments created along the adiabatic and the diabatic paths through the intersection. They can be used to reverse engineer the most probable geometry of the non-adiabatic transition. The angular distributions, quantified in terms of the anisotropy parameter β , are substantially different in the two channels due to a strong anticorrelation between β and the rotational angular momentum of the fragment O_2 . © 2014 AIP Publishing LLC. [<http://dx.doi.org/10.1063/1.4892919>]

I. INTRODUCTION

The near ultraviolet (UV) absorption of ozone between 360 nm and 190 nm, comprising the Hartley¹ and the Huggins² bands, has been a subject of numerous experimental and theoretical studies (see, for example, Refs. 3–20, a review Ref. 21, and references therein). The absorption in this wavelength range [Figs. 1(a) and 1(b)] starts with a progression of regular but weak diffuse Huggins bands becoming more prominent with growing energy and—around the photon energy of $E_{\text{ph}} = 32\,300\text{ cm}^{-1}$ —smoothly merging into the Hartley spectrum. The Hartley band, extending up to $53\,000\text{ cm}^{-1}$, consists of a broad background (FWHM 0.75 eV) and a sequence of weak diffuse bands, barely discernible below $\sim 35\,000\text{ cm}^{-1}$, gradually gaining intensity toward the absorption maximum at $38\,500\text{ cm}^{-1}$, and disappearing toward the high energy end of the spectrum. Despite the apparent simplicity of the Hartley band, its diffuse character has never been reproduced in quantum mechanical calculations based on *ab initio* potential energy surfaces (PESs).

The three singlet electronic states involved in photodissociation in the UV range are the ground electronic state \tilde{X}^1A' (the initial state of parent ozone, labeled \tilde{X}), the optically bright state $3^1A'$ (“B”), and another highly excited and purely repulsive $^1A'$ state (“R”).^{9,22} PESs of the B and R states have been recently improved by Schinke and McBane.¹⁴ These PESs are used in the present study and termed SMB PESs. UV light excites ozone into the B state which gives rise to both Hartley and Huggins bands.^{11,21,23} In the B state PES [Figs. 2(a) and 2(c)], the Franck-Condon (FC) point at C_{2v}

geometry corresponds to a saddle which separates two equivalent C_s symmetric shallow minima. The longer of the two O–O bonds in each C_s minimum is stretched to $R_e = 3.20 a_0$ in the direction of dissociation, and the shorter bond with $R_e = 2.28 a_0$ is close to the bond length in the fragment O_2 . The R state PES is purely repulsive [Figs. 2(b) and 2(d)]. The states B and R form a conical intersection (CI) which lies outside the FC zone and near the minima of the B state; the CI occurs at C_s geometries and is “accidental,” i.e., not tied to a high-symmetry configuration of the molecule. Cuts through the diabatic potentials along one O–O bond are shown in Fig. 2(e). Two spin-allowed channels correlate with the singlet states,²⁴

$$E_{\text{ph.}} > 1.051\text{ eV};$$

$$\lambda < 1180\text{ nm} : O_3 + \hbar\omega \rightarrow O(^3P) + O_2(X^3\Sigma_g^-), \quad (1)$$

$$E_{\text{ph.}} > 4.000\text{ eV};$$

$$\lambda < 310\text{ nm} : O_3 + \hbar\omega \rightarrow O(^1D) + O_2(a^1\Delta_g). \quad (2)$$

In the “triplet” channel (1), to which the states \tilde{X} and R converge, the atomic and molecular oxygens are formed in their ground electronic states. In the “singlet” channel (2), both fragments are electronically excited; this channel correlates with the diabatic state B. In the Hartley band, 90% of photoexcited molecules end up in the singlet channel (2). This high quantum yield makes the UV photodissociation of ozone the most important source of the reactive $O(^1D)$ radicals in the stratosphere. Between 7% and 9% of the fragments slide downhill into the triplet channel (1). The remaining 1%–3% of the photoexcited ozone molecules dissociate into

^{a)}Electronic mail: Sergy.Grebenshchikov@ch.tum.de

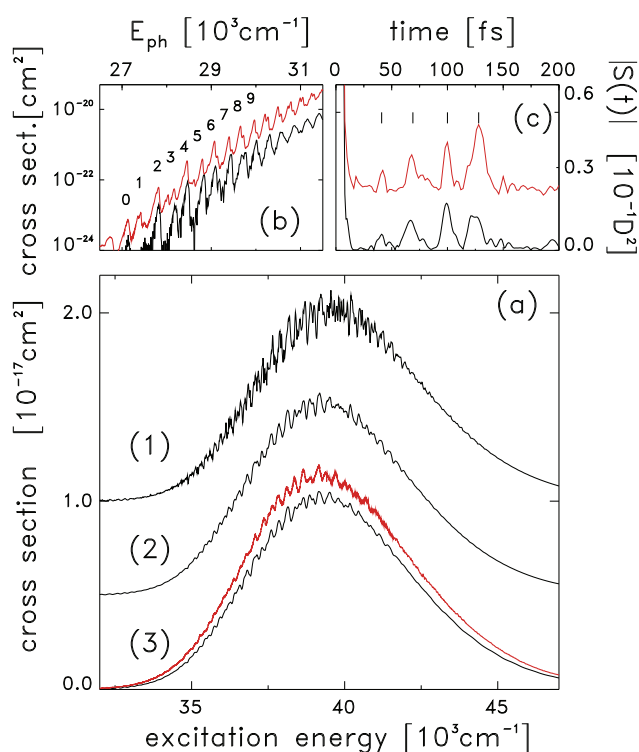


FIG. 1. (a) The UV absorption spectrum of ozone calculated for $T=300$ K (curve (3), black line) and the experimental spectrum of Ref. 3 (red line). The calculated spectrum is shifted by 0.06 eV to higher energies. The sequence of spectra (1-3) illustrates the incoherent and coherent contributions to spectral broadening at 300 K: (1) Spectrum for the B state and one initial rotational state $J_i = \Omega_i = 0$; (2) spectrum for the B state averaged over the Boltzmann distribution of rotational states; and (3) spectrum for coupled B and R states averaged over the Boltzmann distribution. Spectra (1) and (2) are shifted vertically. (b) Absorption spectrum of the Huggins band. Black line is the low energy portion of the theoretical curve (3) in panel (a); red line is the experimental spectrum recorded at 228 K (see Ref. 72). Numbers above absorption peaks indicate the polyad quantum number P . The calculated band origin ($P = 0$) is set to the experimental value of $27\,112\text{ cm}^{-1}$. The intensity of the calculated spectrum is divided by 10 in order to simplify comparison with experiment. (c) Absolute value of the experimental (red) and theoretical (black) autocorrelation function in the first 200 fs following the UV photoexcitation of a thermal ensemble of ozone molecules. Vertical dashes mark the experimental recurrence times. Experimental ACF is obtained by a Fourier transform of the experimental spectrum $\sigma(\omega)/\omega$ of Ref. 72.

the three spin-forbidden channels whose thresholds, located between (1) and (2), correlate with a host of triplet electronic states.^{13,20,24,25} Spin-forbidden photodissociation efficiently competes with the spin-allowed pathways only at wavelengths $\lambda > 320$ nm and is not considered in this paper.

Molecules, photoexcited into the B state, branch between the singlet and the triplet channels at the conical intersection between the B and R PESs. Those taking the diabatic path through the CI, start at the FC point and reach channel (2) along the B state; those taking the adiabatic path hop to the R state at the CI and reach channel (1). The branching space of the C_s -symmetric CI is spanned by the two O–O bonds, with the longer (i.e., breaking) O–O bond being the tuning mode [see Figs. 2(a) and 2(b)] and the shorter (i.e., “fragment”) O–O bond essentially coinciding with the coupling mode. This suggests that the corresponding product state distributions—the translational and vibrational in this case—might bear traces of non-adiabatic dynamics at the CI.

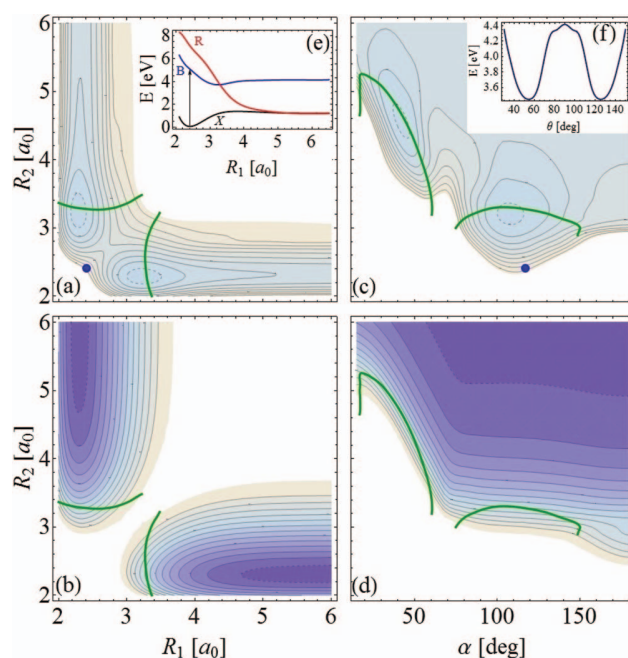


FIG. 2. (a)–(d) Two-dimensional cuts through the PESs of the electronic states B [(a) and (c)] and R [(b) and (d)] in the plane (R_1, R_2) of the two O–O bonds [(a) and (b)] and (R_1, α) [(c) and (d)]. The bond angle is fixed at the FC value of $\alpha = 117^\circ$ in (a) and (b); the bond distance is fixed at $R_1 = 2.42 a_0$ in (c) and (d). The energy of the dashed contour/the contour spacing are 3.6 eV/0.2 eV in panels [(a) and (c)] and 1.2 eV/0.3 eV in panels [(b) and (d)]. Green lines indicate the crossing seam between the diabatic B and R states. Blue dot in (a) and (c) marks the FC point. (e) A cut through the PESs of three electronic states X, B, and R along one O–O bond; $R_2 = 2.42 a_0$ and $\alpha = 117^\circ$. (f) A cut through the B state PES along the Jacobi angle θ ; the other two Jacobi distances are fixed close to the minimum energy along the B/R CI, at $R = 3.8 a_0$ and $r = 2.3 a_0$.

According to a general Landau-Zener type argument,^{15,26,27} the probability P_{BR} of a transition between the two diabatic surfaces depends on the average²⁸ Massey parameter $\bar{\xi}$, i.e., the product of the energy gap between the two adiabatic states $\overline{\Delta E}^{\text{ad}}$ and the sojourn time $\bar{\tau}_x$ in the crossing region:

$$P_{BR} = 1 - \exp(-\bar{\xi}) = 1 - \exp(-\overline{\Delta E}^{\text{ad}} \bar{\tau}_x). \quad (3)$$

The motion through the intersection is mainly diabatic if $\bar{\xi} \ll 1$, and mainly adiabatic if $\bar{\xi} \gg 1$. Molecules moving fast along the tuning mode (small $\bar{\tau}_x$) tend to dissociate into the diabatic singlet channel (1), while the slow molecules (large $\bar{\tau}_x$) are diverted into the adiabatic triplet channel (2). Because the adiabatic gap grows as the O–O bond stretches, the Massey parameter depends on the vibrational state of the “fragment” O_2 vibration. One expects molecules with little excitation in the short O–O bond to move diabatically through the CI (small $\overline{\Delta E}^{\text{ad}}$, small $\bar{\tau}_x$); with growing excitation (larger $\overline{\Delta E}^{\text{ad}}$, larger $\bar{\tau}_x$), the adiabatic probability $1 - P_{BR}$ also grows. The intersection acts as a “beam splitter” sending vibrationally excited molecules into the adiabatic channel and vibrationally cold molecules into the diabatic channel. The influence of the CI on the angular distributions of the photofragments, quantified—for example—in terms of the recoil anisotropy parameter β , is difficult to predict without dynamics calculations. On the one hand, the valence

angle \widehat{OOO} belongs to the “seam space” of the CI and as such is expected to have only a limited impact on the transition. On the other hand, the angular distributions in the two channels might show sensitivity to the difference in sojourn times $\bar{\tau}_x$ at the CI.

In the Hartley energy range, i.e., at energies above the dissociation threshold of the B state, the transitions from B to the steep repulsive R state are accomplished within a nearly single passage through the CI²⁷—the regime favorable for the application of trajectory surface hopping algorithms.²⁹ Two such studies have been reported,^{15,21,27} which concentrated on the kinetic energy release in the “triplet” channel and gave a qualitative explanation of the measured distributions. A quantum mechanical analysis of the photofragment distributions in the SMB PESs and their relation to the B/R conical intersection is still missing.

The present paper reports the integral absorption cross section and the photofragment angular and product state distributions in the Hartley/Huggins bands. A generally good agreement with experiment is found: The calculations reproduce (a) the low intensity of spectral fluctuations in the thermally averaged spectrum of the Hartley band and (b) the highly inverted vibrational distribution in the triplet channel and the cold vibrational distributions in the singlet channel. This agreement indicates a high quality of the SMB PESs. The calculated β parameters in the two channels also agree with the experimental results in terms of their dependence on photon energy and the rotational state of fragment O₂, although the agreement is less accurate than for scalar distributions.

The paper is organized as follows. The quantum mechanical calculations of differential and integral absorption cross sections in rotating ozone are outlined in Sec. II. The absorption spectrum at room temperature is constructed as an average over thermally populated rotational states of the parent ozone and compared with experiment in Sec. III. The calculated and measured product state distributions are compared in Sec. IV. The angular distributions of the photofragments are discussed in Sec. V. Summary and conclusions are given in Sec. VI.

II. QUANTUM MECHANICAL CALCULATIONS

A. Potentials and transition dipole moments

Accurate potential energy and interstate coupling surfaces of the dynamically relevant electronic states are the main prerequisites of a quantum mechanical study of photodissociation. While several potentials of the B and R states have been constructed in the past 25 years,^{10,12,21,30–33} the SMB PESs of Schinke and McBane promise—according to the classical trajectory results of Ref. 15 and the present quantum calculations—to become a “golden standard” in the description of the near UV photodissociation of ozone. Electronic adiabatic energies for these states are obtained using high level *ab initio* calculations on a dense grid of three internal coordinates. Smooth quasi-diabatic potentials $V_B(R_1, R_2, \alpha)$ and $V_R(R_1, R_2, \alpha)$ are determined using “diabatization by eye,” i.e., by reassigning the adiabatic energies around the CI to the apparent diabatic states.^{14,21} The

off-diagonal coordinate dependent diabatic coupling element V_{BR} is constructed separately as a “patch.” The function $V_{BR}(R_1, R_2, \alpha)$ is localized at the CI and adjusted to give the best fit to the energy gap between the adiabatic states along the crossing seam and to the *ab initio* non-adiabatic coupling matrix element, evaluated at selected geometries near the CI.¹⁴

Two-dimensional cuts through the SMB PESs, in the plane (R_1, R_2) of the two O–O bond distances and in the plane (R_1, α) of one bond distance and the bond angle, are shown in Figs. 2(a)–2(d). Two equivalent dissociation channels in Figs. 2(a) and 2(b) correspond to the abstraction of the oxygen atom from either end of the OOO molecule (central O atom cannot be directly removed). The C_s minima of the B state PES are ~ 0.6 eV deep; the barrier between them passes along the C_{2v} symmetry line and lies slightly above dissociation threshold of channel (2). The equilibrium angle, $\alpha_e = 108^\circ$, is only slightly smaller than that in the \tilde{X} state (117°). The R state PES at energies relevant for the dynamics in the Hartley band, is purely repulsive [Fig. 2(b)]. Both R and B states are visibly anisotropic [Figs. 2(c) and 2(d)], and the departing O and O₂ fragments experience a deflecting force even at $O \cdots O_2$ distances of $5 a_0$.

The crossing seam between the diabatic B and R states is marked green in Fig. 2. In the (R_1, R_2) plane, the seam passes close to the C_s minimum of the B state, well outside the C_{2v} FC zone. In each arrangement channel, the branching space of the CI between the B and R states comprises the long bond distance R_1 as a tuning mode (along which the energy gap between the adiabatic states changes the fastest) and the short bond distance R_2 as a coupling mode (along which the interstate coupling changes the fastest). The valence angle parametrizes the displacements along the seam of degeneracy of adiabatic states. A detailed discussion of the properties and topography of the B/R crossing seam is given in Ref. 14.

Knowledge of the coordinate dependent transition dipole moment (TDM) vector with the ground electronic state is necessary for the calculation of absolute integral and differential cross sections. The direct excitation from \tilde{X} into the R state is neglected: The vertical excitation energy of the R state ($E_{\text{ph}} \approx 9$ eV) is much higher than the photon energy range studied in this work and the corresponding TDM is set to zero. The TDM between \tilde{X} and B states is large in the FC zone, $|\mu| \sim 2 D$. The TDM vector lies in the molecular plane denoted (y, z) (x axis is perpendicular to the molecular plane): The transition $3^1A' \leftarrow \tilde{X}^1A'$ is parallel. The *ab initio* coordinate dependent components $\mu_y(R_1, R_2, \alpha)$ and $\mu_z(R_1, R_2, \alpha)$ are taken from Ref. 12.

B. Molecular Hamiltonian, initial state, and cross sections

Photodissociation cross sections for rotating ozone are calculated by solving Schrödinger equation with the molecular Hamiltonian set in the quasi-diabatic representation,³⁴

$$\hat{\mathbf{H}}^0 = \begin{pmatrix} \hat{T} & 0 \\ 0 & \hat{T} \end{pmatrix} + \begin{pmatrix} V_B & V_{BR} \\ V_{BR} & V_R \end{pmatrix}. \quad (4)$$

\hat{T} is the standard³⁵ kinetic energy operator for a rotating triatomic, common for both electronic states and specified in the body fixed frame in Jacobi coordinates (R, r, θ) . Jacobi coordinates comprise the distance R between one oxygen atom and the center of mass of O_2 , the O_2 distance r , and the angle θ between the vectors \mathbf{R} and \mathbf{r} .

Ozone in the ground electronic state \tilde{X} in the rotational state (J_i, Ω_i) is described by the wave function

$$\Psi_X(\mathbf{q}|J_i, \Omega_i) = \psi_X^{J_i, \Omega_i}(\mathbf{q}) |\Theta_{M_i}^{J_i, \Omega_i}\rangle. \quad (5)$$

Here J_i is the total (nuclear) angular momentum, Ω_i is the body-fixed and M_i is the space-fixed projection of J_i , $\psi_X^{J_i, \Omega_i}(\mathbf{q})$ is a given vibrational state, \mathbf{q} denotes three Jacobi coordinates, and the rotational basis functions $|\Theta_{M_i}^{J_i, \Omega_i}\rangle$ are expressed via Wigner D-matrices;^{35,36} the space-fixed axis Z_{SF} points along the electric vector of the incident light, the body-fixed axis Z_{BF} coincides with vector \mathbf{R} . In Eq. (5), the parent O_3 is treated as a symmetric top with conserved helicity Ω_i (centrifugal sudden (CS) approximation). Unless stated otherwise, excitations originating from the vibrational ground state in \tilde{X} are considered. Possible rotational transitions in the parallel optical excitation to the B state are $J_i \rightarrow J_f = J_i, J_i \pm 1$ and $\Omega_i \rightarrow \Omega_f = \Omega_i, \Omega_i \pm 1$. The molecule photoexcited into a specific component (J_f, Ω_f) of the full rovibrational state $\Phi_0(\mathbf{q}|J_f)$ has the wave function

$$\Phi_0(\mathbf{q}|J_f, \Omega_f) = \langle 1\delta, J_i \Omega_i | J_f \Omega_f \rangle (\mu)_\delta \psi_0^{J_i, \Omega_i}(\mathbf{q}) |\Theta_{M_i}^{J_i, \Omega_i}\rangle. \quad (6)$$

Here $\langle \cdot, \cdot | \cdot \rangle$ is the Clebsch-Gordon coefficient, $\delta \equiv \Omega_f - \Omega_i = 0$ or 1 , and $(\mu)_\delta$ are the spherical projections of the TDM vector $\boldsymbol{\mu}$: $(\mu)_{\delta=0} = \mu_z$ and $(\mu)_{\delta=\pm 1} = -(\mu_y)/\sqrt{2}$. The total wave function $\Phi_0(\mathbf{q})$ in the B state immediately after photoexcitation is a linear combination of all $\Phi_0(\mathbf{q}|J_f, \Omega_f)$ with the allowed values of (J_f, Ω_f) .³⁶ The electronic component in the R state is initially empty. The initial state $\Phi_0(\mathbf{q}|J_f)$ for each J_f is propagated separately in order to evaluate photodissociation cross sections, both differential, $d\sigma_{\alpha, v, j}(E_{ph}|J_f \leftarrow J_i)/d\omega_k$, and integral, $\sigma_{\alpha, v, j}(E_{ph}|J_f \leftarrow J_i)$ or $\sigma(E_{ph}|J_f \leftarrow J_i)$.

A. *The total absorption cross section* $\sigma(E_{ph}|J_f \leftarrow J_i)$ for a given J_f is calculated, in the time-dependent formulation,³⁷ as a Fourier transform of the autocorrelation function,

$$\begin{aligned} \sigma(E_{ph}|J_f \leftarrow J_i) &= \frac{2\pi E_{ph}}{3c\epsilon_0} \int_0^\infty \langle \Phi_0 | \Phi(t) \rangle e^{iE_{ph}t} dt \\ &= \frac{2\pi E_{ph}}{3c\epsilon_0} \int_0^\infty \langle \Phi_0 | e^{-i\mathbf{H}t} | \Phi_0 \rangle e^{iE_{ph}t} dt, \quad (7) \end{aligned}$$

and the photon energy E_{ph} is measured from the rovibrational energy level $E_X(J_i, \Omega_i)$ in \tilde{X} . The cross section is averaged over the projections M_i , and $\hbar \equiv 1$ is set. Equivalently, $\sigma(E_{ph}|J_f \leftarrow J_i)$ can be expressed as an expectation value of the time-dependent Green's function,³⁸

$$\sigma(E_{ph}|J_f \leftarrow J_i) = \frac{\pi E_{ph}}{3c\epsilon_0} \langle \Phi_0(\mathbf{q}|J_f) | \text{Im}G^+(E_{ph}) | \Phi_0(\mathbf{q}|J_f) \rangle. \quad (8)$$

The full spectrum for a given initial state $\Psi_X(\mathbf{q}|J_i, \Omega_i)$, is a sum,

$$\sigma(E_{ph}|J_i, \Omega_i) = \sum_{J_f} \sigma(E_{ph}|J_f \leftarrow J_i), \quad (9)$$

restricted to the allowed values of J_f . The temperature dependent absorption spectrum has been constructed by further averaging $\sigma(E_{ph}|J_i, \Omega_i)$ over the normalized Boltzmann population $P_{J_i, \Omega_i}(T)$ of the initial states (J_i, Ω_i) ,

$$\sigma(E_{ph}, T) = \sum_{J_i, \Omega_i} P_{J_i, \Omega_i}(T) \sigma(E_{ph}|J_i, \Omega_i). \quad (10)$$

Values of J_i up to 50 are necessary to simulate absorption at $T = 300$ K, and these calculations are based on the CS approximation: The Coriolis coupling is neglected and each component $\Phi_0(\mathbf{q}|J_f, \Omega_f)$ is processed separately. For $J_i \leq 5$, test calculations including all Ω_f blocks for each J_f and fully accounting for Coriolis coupling have also been carried out. The spectra $\sigma(E_{ph}|J_i, \Omega_i)$ obtained with and without CS approximation are in excellent agreement.

B. *Partial cross sections* $\sigma_{\alpha, v, j}(E_{ph}|J_f \leftarrow J_i)$ for photodissociation into a given scattering channel (α, v, j) , labeled by the electronic (α), vibrational (v), and rotational (j) quantum numbers of the fragment O_2 molecule in a state with the eigenfunction $\chi_{\alpha v j}(r, \theta|J_f, \Omega_f)$ and the eigenvalue $\epsilon_{\alpha v j}$, are given by^{36,39}

$$\sigma_{\alpha, v, j}(E_{ph}|J_f \leftarrow J_i) = \frac{2\pi^2 E_{ph}}{c\epsilon_0} |\langle \psi_{\alpha v j}^-(E_{ph}) | \Phi_0(\mathbf{q}|J_f) \rangle|^2. \quad (11)$$

They are proportional to the square of the amplitude with which the energy-normalized scattering state $\psi_{\alpha v j}^-$ with the incoming wave in channel (α, v, j) enters Φ_0 . Once the partial cross sections are averaged over the Z_{SF} -projections M_i of J_i and summed over the Z_{SF} -projections m_j of j , they can be further reduced into the rotational $(P(v, j))$ and vibrational $(P(v))$ product state distributions, and the electronic branching ratios $B(\alpha)$. In the time dependent method due to Balint-Kurti and co-workers,^{36,40} the averaged partial cross sections are expressed in terms of photodissociation matrix elements $T_{\alpha v j}(J_f, \Omega_f)$, related to the scattering amplitude in Eq. (11) and calculated via Fourier transform of the cross correlation function,

$$\begin{aligned} \sigma_{\alpha, v, j}(E_{ph}|J_f \leftarrow J_i) &= \frac{2\pi E_{ph}}{3c\epsilon_0} \frac{2J_f + 1}{2J_i + 1} \sum_{\Omega_f} |T_{\alpha v j}(J_f, \Omega_f, E_{ph}|R_\infty)|^2, \quad (12) \end{aligned}$$

$$\begin{aligned} T_{\alpha v j}(J_f, \Omega_f, E_{ph}|R_\infty) &= \left(\frac{k_{\alpha v j}}{\mu_R} \right)^{\frac{1}{2}} e^{-ik_{\alpha v j} R_\infty} \int_0^\infty \langle \chi_{\alpha v j} | e^{-i\mathbf{H}t} | \Phi_0 \rangle_{R_\infty} e^{iE_{ph}t} dt. \quad (13) \end{aligned}$$

Here μ_R is the O/O_2 reduced mass and $k_{\alpha v j} = [2\mu_R(E_{ph} - \epsilon_{\alpha v j})]^{1/2}$ is the channel momentum. The cross correlation function is constructed by projecting the evolving wavepacket $\Phi(t)$ onto the internal states $\chi_{\alpha v j}(r, \theta|J_f, \Omega_f)$ at the ‘‘analysis line’’ $R = R_\infty$ in the asymptotic region,⁴⁰ and integration

in round brackets $(\cdot | \cdot | \cdot)_{R_\infty}$ is carried out only over the coordinates θ and r . An equivalent expression in terms of the Green's function is similar to Eq. (8),

$$T_{\alpha v j}(J_f, \Omega_f, E_{\text{ph}} | R_\infty) = \left(\frac{k_{\alpha v j}}{\mu_R} \right)^{\frac{1}{2}} e^{-ik_{\alpha v j} R_\infty} (\chi_{\alpha v j} | \text{Im} G^+(E_{\text{ph}}) | \Phi_0)_{R_\infty}. \quad (14)$$

The partial cross sections reported in this work are calculated for $J_i = 0$ (implying $J_f = 1$ and $\Omega_f = 0, 1$).

C. *The angular distribution* of the photofragments in channel (α, v, j) , averaged over the initial projections M_i and summed over the final projections m_j , can be expressed through the same T -matrix elements,³⁶

$$\begin{aligned} \frac{d\sigma_{\alpha, v, j}(E_{\text{ph}})}{d\omega_k} &\equiv I_{\alpha, v, j}(\theta_k, \phi_k) \\ &= \frac{1}{4\pi} \frac{2\pi^2 E_{\text{ph}}}{c\epsilon_0} \frac{1}{2J_i + 1} \sum_{M_i} \sum_{m_j} \left| \sum_{J_f, \Omega_f} (2J_f + 1)^{\frac{1}{2}} \right. \\ &\quad \times D_{M_i, \Omega_f}^{J_f}(\phi_k, \theta_k, 0) \begin{pmatrix} 1 & J_f & J_i \\ 0 & -M_i & M_i \end{pmatrix} \\ &\quad \left. \times D_{m_j, \Omega_f}^{j*}(\phi_k, \theta_k, 0) T_{\alpha v j}(J_f, \Omega_f, E_{\text{ph}}) \right|^2, \end{aligned} \quad (15)$$

where angles $(\theta_k, \phi_k) = \omega_k$ describe the orientation of the relative momentum of the recoiling O and O₂ with respect to the space-fixed axis Z_{SF}. The angular distribution $I_{\alpha, v, j}$ is cylindrically symmetric about Z_{SF}, and has a universal dependence on polar angle θ_k ,⁴¹

$$I_{\alpha, v, j}(\theta_k, \phi_k) = \frac{\sigma_{\alpha, v, j}(E_{\text{ph}})}{4\pi} (1 + \beta_{\alpha, v, j} P_2(\cos \theta_k)). \quad (16)$$

For $J_i = 0$, the fully fragment state resolved anisotropy parameter $\beta_{\alpha, v, j}$ is expressed through the matrix elements $T_{\alpha v j}(J_f, \Omega_f)$ simply as

$$\beta_{\alpha, v, j}(E_{\text{ph}}) = \frac{2|T_{\alpha v j}(1, 0)|^2 - 2|T_{\alpha v j}(1, 1)|^2}{|T_{\alpha v j}(1, 0)|^2 + 2|T_{\alpha v j}(1, 1)|^2}. \quad (17)$$

Anisotropy parameters $\beta_{\alpha, v}$ (for a given vibrational state v) and β_α (in a given electronic channel α) are calculated with the same equation, in which the matrix elements $|T_{\alpha v j}|^2$ are replaced with $\sum_j |T_{\alpha v j}|^2$ and $\sum_{v j} |T_{\alpha v j}|^2$, respectively.

In practice, calculations of the T -matrix elements and cross sections via Eqs. (8), (14) and (15) are performed in several steps. First, the outgoing boundary conditions are approximately imposed in the asymptotic region by augmenting $\hat{\mathbf{H}}^0$ with a complex absorbing potential $-iW$ ($\text{Re } W > 0$),⁴²

$$\hat{\mathbf{H}} = \hat{\mathbf{H}}^0 - iW \mathbf{1}. \quad (18)$$

Here $\mathbf{1}$ denotes the 2×2 unit matrix, and the same coordinate function W is used in both electronic channels. Next, the

vector $\text{Im } G^+(E) \Phi_0(\mathbf{q} | J_f)$ is approximated by the expansion

$$\text{Im } G^+(E) \Phi_0(\mathbf{q} | J_f) \simeq \sum_{n=0}^{N_{\text{iter}}} [\text{Re } b_n(E)] \Phi_n, \quad (19)$$

in which $b_n(E)$ are the usual energy-dependent factors,⁴³ while the vectors Φ_n are found from a modified Chebyshev recursion relation.⁴⁴ Finally, the Chebyshev autocorrelation coefficients $c_n = \langle \Phi_0(\mathbf{q} | J_f) | \Phi_n \rangle$ with the initial state and the cross correlation coefficients $x_n = (\chi_{\alpha v j} | \Phi_n)_{R_\infty}$ are evaluated. All cross sections are reconstructed from $\{c_n\}$ and $\{x_n\}$. The expansion length, N_{iter} , is a convergence parameter of the calculation.

We also performed calculations with the initial state

$$\tilde{\Phi}_0(\mathbf{q}) = |\mu(\mathbf{q})| \Psi_X(\mathbf{q} | 0, 0), \quad (20)$$

which is the product of the absolute value of the TDM and the ground vibrational state of the non-rotating ozone in \tilde{X} . Such initial state, violating the optical selection rules encoded in Eq. (6) and corresponding to a $J_i = 0 \rightarrow J_f = 0$ transition, is often used in calculations of absorption spectra and partial cross sections.⁴⁵ Direct comparison, presented below, demonstrates that the resulting product state distributions are very close to those calculated for $J_f = 1$.

C. Numerical details

The Hamiltonian, Eq. (4), is set in DVR⁴⁶ with the grid comprising 200 potential-optimized⁴⁷ points in $R \in [1.8, 10.0] a_0$, 140 potential-optimized points in $r \in [1.8, 7.0] a_0$, and $N_\theta = 160$ Gauss-associated Legendre quadrature points in angle. The grid is contracted by retaining only points with potential energy below $V_{\text{cut}} = 12.5$ eV above equilibrium in \tilde{X} . $N_{\text{iter}} = 30\,000$ Chebyshev iterations are sufficient to converge the absorption spectrum and the partial cross sections. The complex absorbing potential $-iW$ is set via a coordinate dependent damping function $\gamma(Q)$ ($Q = R$ or r) as described in Refs. 38, 44, and 48. It becomes non-zero in a $1.0 a_0$ -wide strip at the grid edge, grows quadratically as a function of O/O₂ distance inside the strip, and reaches the strength of 0.10 at the grid edge. The asymptotic ‘analysis line’ is chosen at $R_\infty = 8.5 a_0$.

The temperature dependent absorption spectrum is reconstructed from spectra calculated on the grid of initial angular momenta J_i between 0 and 50 with the step of $\Delta J_i = 5$; the body-fixed projections Ω_i range from 0 to 6 ($\Delta \Omega_i = 2$). With these settings, cross sections at temperatures up to $T \sim 300$ K can be evaluated.

III. THERMALLY AVERAGED ABSORPTION SPECTRUM

The quantum mechanical absorption spectrum at $T = 300$ K is plotted against photon energy E_{ph} in Fig. 1(a) [curve (3)]; the calculated spectrum is shifted by 0.06 eV to higher energies. The width of the spectral envelope is in good agreement with the experimental spectrum of Freeman *et al.*³ (red line). The maximum absorption cross section deviates from experiment by less than 10% reflecting the quality

of the TDM function. Most remarkably, the relative intensities of diffuse structures are small compared to the intensity of the spectral envelope, also in agreement with the experimental results. Thus, the SMB PESs are the first set of fully *ab initio* potentials which allows a quantitative reproduction of the low-amplitude spectral fluctuations in the Hartley band.

Previous *ab initio* studies of the high resolution Hartley spectrum^{10,17,21,31,49} reported the absorption envelope strongly congested by intense narrow resonance-like features. The authors discussed two mechanisms which could attenuate the intensity of spectral fluctuations to the level observed in spectra at 200–300 K: First, the incoherent Boltzmann averaging over absorption spectra with different initial angular momenta of the parent ozone; second, the non-adiabatic transitions at the B/R CI which lead into the triplet channel (1) and additionally broaden individual spectral lines. The present calculations, based on the SMB PESs, offer an insight into the relative importance of these two mechanisms. Their contributions to the calculated spectrum are illustrated in Fig. 1(a) for $T = 300$ K. Curve (1) shows the spectrum corresponding to the initially non-rotating ozone excited in the isolated B state (coupling to R is set to zero). Both the incoherent and the non-adiabatic mechanisms are switched off. The spectral envelope is visibly distorted by fluctuations corresponding to many densely spaced resonance states located near the potential saddle in the FC zone. The intensity of resonance peaks is substantially attenuated compared to previous PESs of the B state (see, for example, Fig. 3 of Ref. 21). This is a new feature of the SMB PES without which diffuseness of the spectrum in the full calculation would be hard to achieve. Curve (2) illustrates the impact of thermal averaging on diffuse structures. This spectrum is calculated by taking a Boltzmann weighted sum over many spectra with different initial rotational states (J_i, Ω_i), all calculated with the isolated B state. Spectral fluctuations are dramatically reduced indicating that it is the thermal mechanism which is dominant in the Hartley band. The effect is achieved by summing over a large number of overlapping resonances whose positions slightly shift as J_i and Ω_i vary. Curve (3) demonstrates how the intensity of spectral fluctuations is brought to the observed level by combining the thermal averaging with the non-adiabatic two-state dynamics.

The thermally averaged quantum mechanical spectrum remains essentially accurate also in the low energy range between $27\,000\text{ cm}^{-1}$ and $\sim 31\,700\text{ cm}^{-1}$. This energy range, containing the weak Huggins bands, is shown in Fig. 1(b). Apart from a few hot bands,⁵⁰ the chain of experimental absorption peaks corresponds to excitations of multiplets of vibrational states (polyads with the quantum number P) supported by the shallow C_s wells of the B state.⁵¹ The calculation reproduces the positions of the absorption peaks and the nearly exponential rise of their intensity with growing E_{ph} . The widths of the absorption bands ($\sim 120\text{ cm}^{-1}$) are also similar to those in the observed spectrum. These widths reflect the energetic spread of the polyads in the B state; individual states in each polyad are merged under the common envelope because of the inhomogeneous broadening many initial rotational states of the parent molecule. The homogeneous width

is due to diabatic transitions from the B state into the dissociative continuum of the repulsive R state and is merely 2.2 cm^{-1} for the $P = 0$ band (this is found in a calculation performed for a single rotational state). Small homogeneous width implies weak diabatic coupling between B and R. For the vibrationally excited states with $P > 0$, the homogeneous widths vary between 0.2 cm^{-1} and 5 cm^{-1} and remain much smaller than the inhomogeneous limit. An experimental estimate⁵² of the homogeneous linewidth, $\sim 2\text{ cm}^{-1}$, lies within the range covered by the calculated values.

One of the remaining puzzles in Hartley spectrum is the origin and the assignment of residual diffuse bands between $32\,000\text{ cm}^{-1}$ and $42\,000\text{ cm}^{-1}$. The spacings between the broadened peaks vary between 150 cm^{-1} and 320 cm^{-1} and do not form any easily recognizable regular pattern. Peak intensities change in an irregular fashion, indicating that the bands are probably the result of overlap of several lines. In a previous study,²¹ we constructed low-resolution “band states”, i.e., linear combinations of many highly vibrationally excited resonance states corresponding to the broadened absorption peaks,⁵³ and used them to illustrate that dominant excitations in the Hartley band involve the symmetric and the antisymmetric stretching modes. Nevertheless, the complexity of nodal patterns rendered a consistent vibrational assignment of progressions impossible. This probably explains why several previous attempts of traditional assignment in the frequency domain^{6–8} encountered considerable difficulties.

Under these circumstances, the assignment in time domain might be better suited for interpretation of the diffuse structures. This approach was advocated by Johnson and Kinsey,^{16–18} who capitalized on the observation that the Fourier transform of the measured spectrum gives an appealingly simple autocorrelation function [Fig. 1(c)], which decays fast and shows only four recurrences at 41 fs, 69 fs, 100 fs, and 128 fs. This implies a simple behavior of the initial excitation in time domain.^{16–18} Figure 1(c) also shows the theoretical autocorrelation function $S_T(t)$ calculated as a Boltzmann average over individual correlation functions $S(t|J_f \leftarrow J_i)$ for different initial states (J_i, Ω_i). The calculated and the experimental autocorrelation functions are in good agreement, both in terms of the recurrence times and the recurrence amplitudes. In particular, the gradual increase of the recurrence amplitudes with increasing recurrence time is well reproduced in the calculation, although the amplitude of the longest recurrence near 128 fs is underestimated. The calculated temperature dependence of the recurrence amplitudes is also in good agreement with experiment¹⁸ (not shown in Fig. 1).

Johnson and Kinsey established a relation between the recurrence times and the periods of certain unstable periodic orbits trapped in the vicinity of the potential ridge separating two dissociation channels in the B state.¹⁶ Each recurrence time corresponds to a specific short-period classical orbit,¹⁶ and at least four such orbits guide the early time dynamics of the initial wavepacket.²¹ The assignment in time domain provides an explicit visualization of molecular motions behind the absorption bands. The exact shapes of these orbits (see, for example, Refs. 16, 19, and 21) are similar for different PESs, implying the universal character of the proposed

assignment; they reflect complicated motions of three oxygen atoms excited ~ 1.0 eV above the C_s minima of the B state.

IV. WAVELENGTH RESOLVED PHOTOFRAGMENT DISTRIBUTIONS

In this section, the quantum mechanical rotational, vibrational, and kinetic energy distributions of O and O₂ calculated for $J_f = 1$ are compared with the available experimental data. While the absorption spectrum reflects mainly the dynamics in the FC zone, the distributions over final states are sensitive to the details of the PESs probed by departing fragments between the FC zone and the dissociation channels.

All photoexcited molecules pass through the CI between B and R states, and the coupling of the electronic and nuclear motions is inevitably imprinted in the O/O₂ distributions. The most direct consequence of the two state dynamics is simultaneous population of two electronic channels across the Hartley band.^{13,24,54,55} Between 90% and 92% of the fragments end up in the singlet channel (2) diabatically connected to the bright B state, while 8% to 10% follow the adiabatic route into the triplet channel (1). The small branching ratio is another indication that the diabatic coupling at the CI is weak.

According to Fig. 2, the breaking O–O bond acts as the coupling mode at the CI, while the shorter “fragment” O–O bond is the tuning mode. Asymptotically, the tuning and the coupling modes correspond to the O...O₂ separation and the vibrational coordinate of O₂, respectively. Thus, the dynamics in the branching space are expected to show up in the kinetic energy distribution (the total kinetic energy release, TKER) and in the product vibrational distribution. The rotational state distribution of O₂ correlates with the motion along the seam mode (the valence angle), i.e., with the domain which is commonly considered to be least influenced by the non-adiabatic dynamics.

A. Rotational state distributions

The calculated rotational distributions of the O₂ fragments are shown in Fig. 3 for the singlet [(a)–(c)] and the triplet [(d)–(i)] electronic channels for several vibrational quantum numbers v of O₂ at two wavelengths near the maximum of the Hartley band. The rotational distributions for $v = 0$ are bell shaped and peaked at $j \gg 1$ (the observation commonly rationalized in terms of the rotational reflection principle⁴⁵), with the average excitation in the more exothermic triplet channel, $\langle j \rangle \sim 75$, being substantially larger than in the singlet channel, $\langle j \rangle \sim 25$. The reason is that the fragments sliding down the steep repulsive potential of the R state are exposed—on average—to a stronger torque than those climbing up the attractive portion of the B state potential. The rotational O₂ distributions in non-rotating ozone (black dashed lines) are virtually indistinguishable from those for $J_f = 1$. This is expected, because the energy of the overall rotation in the $J_f = 1$ state is merely a few cm⁻¹, i.e., small on the scale of either the photon or the internal O₂ energies.

In the singlet channel, the calculations reproduce the main features of the distributions measured by Valentini *et al.* for even values of j ,⁵⁶ including widths of the probability

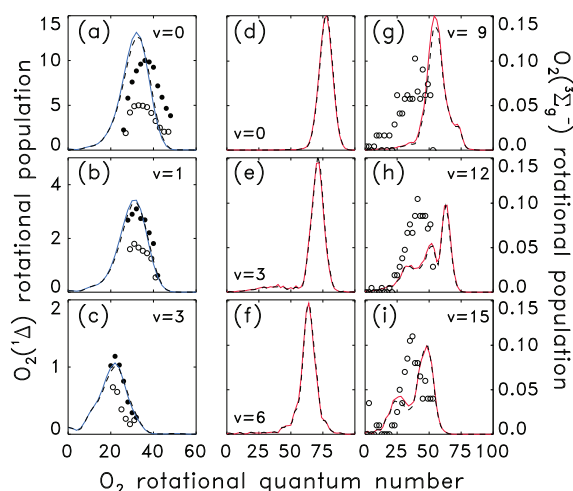


FIG. 3. Rotational state distributions of the O₂(α) diatom in the electronic channel $\alpha = {}^1\Delta_g$ at 240 nm [(a)–(c)] and $\alpha = {}^3\Sigma_g^-$ at 248 nm [(d)–(i)] for several specified values of the vibrational quantum number v of O₂(α). Solid lines represent distributions calculated for $J_f = 1$; black dashed lines are calculated for non-rotating ozone. Circles are the experimental distributions of Ref. 56 [(a)–(c)] and Ref. 57 [(g)–(i)] for the even (solid) and odd (open) values of j . Experimental and calculated distributions are normalized to the same area in each frame; calculated distributions in (d)–(f) are normalized to unit area.

envelopes and the shifts of their maxima to smaller j with growing v . For $v = 0$ [Fig. 3(a)], the calculations predict a distribution peaking at $j = 32$, while the experimental distribution peaks at $j = 36$. Similar discrepancies are observed for $v = 0$ at other wavelengths, too. For $v > 0$, the agreement with the experimental distributions is nearly perfect. On the other hand, the substantial difference in populations of the even and odd j states in the singlet channel, observed in Ref. 56, is not reproduced in our symmetry adapted calculations. A brief discussion, summarizing our results, is given in Appendix A.

Rotational distributions in the triplet channel (1) are shown in panels [(d)–(i)] and compared with the measurements of Daniels and Wiesenfeld⁵⁷ in panels [(g)–(i)]. Only states with $j \leq 55$ are reported in Ref. 57 rendering comparisons with theory somewhat arbitrary. Calculations predict population of similar j states; the widths of the calculated and measured distributions seem to be consistent with each other. Some differences are also apparent. The experimental distributions show hardly any dependence on v , while our calculations predict a substantial shift toward smaller j values as v grows. Nevertheless, the calculated distributions are hotter than the measured ones. A similar trend has been recently observed at longer wavelengths, in the tail of the Huggins band: Measured rotational distributions for $\lambda \geq 320$ nm are noticeably colder than those calculated using the SMB PESs.²⁰

Rotational excitations in two electronic channels are compared in Fig. 4(a) which shows the average rotational energy,

$$\langle E_{\text{rot}}(\alpha) \rangle = \sum_{vj} \epsilon_{\alpha v=0j} P_{\alpha}(v, j),$$

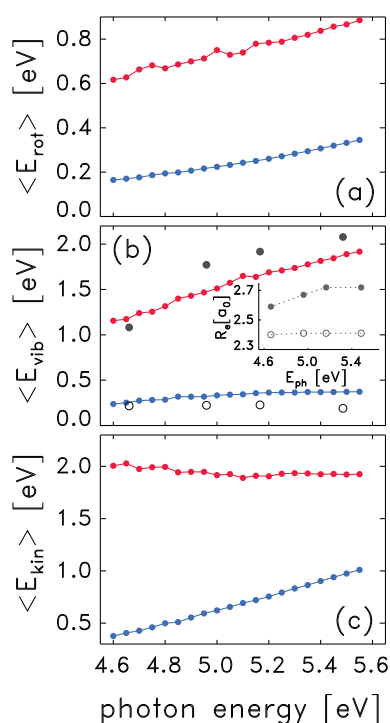


FIG. 4. Average rotational (a), vibrational (b), and translational (c) energies of the photofragments in the singlet (blue) and triplet (red) channels as functions of photon energy. Solid and open circles in panel (b) are average vibrational energies for the distributions fitted with the FC mapping model described in Sec. IV B. Inset in (b) shows the “parent” O–O length R_e reconstructed using FC mapping at several photon energies. Open (solid) circles refer to the singlet (triplet) channel.

as function of the photon energy. Here $\epsilon_{\alpha v j}$ is the asymptotic state of $\text{O}_2(\alpha)$ and $P_\alpha(v, j)$ is the normalized rovibrational distribution in channel α . Rotational excitation in the triplet channel is always stronger than in the singlet channel, but in either case it never exceeds 20% of the kinetic energy release. For E_{ph} growing from 4.6 eV to 5.6 eV, $\langle E_{\text{rot}}(\alpha) \rangle$ grows by about 0.2 eV, independently of the electronic channel—both lines are nearly parallel.

B. Vibrational state distributions

Vibrational distributions reflect the energy content of the coordinate which at the CI plays the part of the coupling mode, and distributions in the complementary electronic channels in Fig. 5 are remarkably different. The distinction between channels is clearly seen both in the ion imaging experiment of Houston⁵⁸ and in the calculations.

In the singlet channel [Figs. 5(a) and 5(b)], the measured and the calculated distributions peak at $v = 0$ and decrease monotonically as v grows and reaches the maximum energetically allowed value. This shape is preserved with growing E_{ph} , and only the tail of the distribution gradually extends to larger v . As a result, the average vibrational excitation,

$$\langle E_{\text{vib}}(\alpha) \rangle = \sum_{vj} \epsilon_{\alpha v j=0} P_\alpha(v, j),$$

depends weakly on photon energy in this channel [Fig. 4(b)].

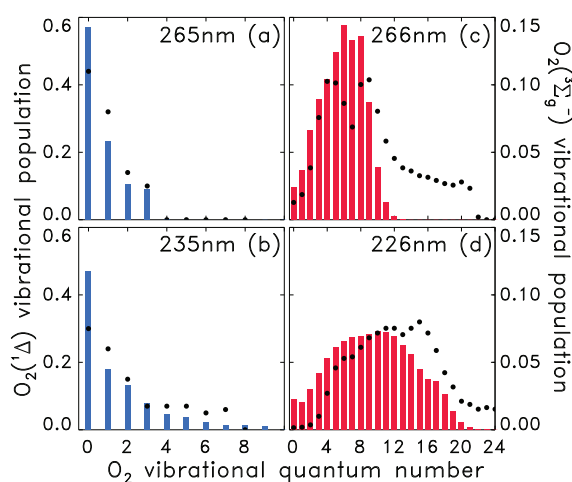


FIG. 5. Vibrational state distributions of the $\text{O}_2(\alpha)$ diatom in the electronic channel $\alpha = {}^1\Delta_g$ [(a) and (b)] and $\alpha = {}^3\Sigma_g^-$ [(c) and (d)] for several indicated wavelengths. Calculations for $J_f = 1$ are shown with histogram boxes, experimental data are shown with solid circles. Distributions in (a) and (b) are normalized to unit area. Distributions in (c) and (d) are normalized to the unit area for $v \leq 15$ and $v \leq 20$, respectively.

In the triplet channel [Figs. 5(c) and 5(d)], the distributions are strongly inverted: The probability rises from a small value at $v = 0$ toward a maximum lying, depending on E_{ph} , between $v = 5$ and 12 and then steeply decreases to zero. Calculated and measured distributions are in good agreement for $v \leq 15$ or so. For $v > 15 - 20$, theory and experiment disagree: In the calculated distributions, these states are empty, while in the measurements all states up to the maximum allowed by energy conservation are populated. It is argued⁵⁹ that the high v end of the experimental distribution is formed via a mechanism involving highly electronically excited states of O_2 (the so-called Herzberg states⁶⁰) as intermediates. This mechanism is not included in the present calculations. The quantum mechanical distributions are qualitatively similar to the semiclassical distributions calculated by McBane *et al.* using trajectory surface hopping.¹⁵ The main difference is in the population of states with $v \approx 0$, which is substantial semiclassically, but small quantum mechanically; the experimental population near $v = 0$ is negligible. The average vibrational excitation in the triplet channel depends strongly on photon energy [Fig. 4(b)]: $\langle E_{\text{vib}} \rangle$ increases by 0.8 eV as E_{ph} grows over 1.0 eV, i.e., almost all extra photon energy goes into heating of the $\text{O}_2({}^3\Sigma_g^-)$ vibrations. This is three times the increase registered for the singlet channel.

The shape of vibrational distributions can be understood using projections of the initial wavepacket onto the final vibrational states of the O_2 fragments. This simple “FC mapping” model⁶¹ is used to fit the calculated distributions and to illuminate an important dynamical difference between the two channels. Quantum mechanical distributions are fitted to a product of vibrational and translational FC factors:

$$P_\alpha(v) \approx \text{FC}_{\text{vib}}(v; R_e - R_e^0) \cdot \text{FC}_{\text{trans}}(E_{\text{ph}} - (v + 1/2)\hbar\omega).$$

The “parent” and the fragment vibrations are treated as harmonic oscillators, rotations are ignored, and the two channels are considered separately. The vibrational FC factor depends

on the shift of the equilibrium O–O bond length in the parent ozone, R_e , relative to the O–O bond length R_e^0 in the fragment $\text{O}_2(^3\Sigma_g^-, ^1\Delta)$; $R_e^0 \approx 2.30 a_0$ is assumed to be known, while R_e is a fitting parameter in the model. Another fitting parameter is the width of the bell-shaped “spectrum” FC_{trans} along the translational energy axis $E_{\text{trans}} = E_{\text{ph}} - (v + 1/2)\hbar\omega$. With the fitted distributions, the average energies $\langle E_{\text{vib}} \rangle$ are calculated for several photon energies. Figure 4(b) demonstrates that this ultra-simple model is capable of reproducing the quantum mechanical dependences $\langle E_{\text{vib}} \rangle$ vs E_{ph} in both electronic channels. The fitted O–O bond distances in $\text{O}_3(\tilde{X})$ are shown in the inset in Fig. 4(b). In the singlet channel, in which $\langle E_{\text{vib}} \rangle$ is virtually independent of E_{ph} , the fit predicts $R_e = 2.42 a_0$ for all energies, which coincides with the equilibrium value in the *ab initio* PES of the \tilde{X} state;²¹ the difference between O–O bond lengths in $\text{O}_3(\tilde{X})$ and O_2 , $(R_e - R_e^0) \sim 0.10 a_0$, is small for this channel, as expected. In the triplet channel, the FC mapping reproduces the steep dependence of $\langle E_{\text{vib}} \rangle$ versus E_{ph} , too. However, the fitted O–O bond, $R_e \sim 2.6 a_0 - 3.0 a_0$, is strongly energy dependent and incompatible with the *ab initio* O–O bond length in $\text{O}_3(\tilde{X})$.

The difference in the fitted R_e values in the two channels is a direct reflection of the difference in slopes of the $\langle E_{\text{vib}} \rangle$ vs. E_{ph} curves. On a somewhat different level, the difference in the fitted R_e values results from an essential distinction between the diabatic (singlet channel) and the adiabatic (triplet channel) passage through the B/R CI. In order to illustrate the physical origin of this difference and of the anomalously extended O–O bonds, which the FC mapping model predicts in the triplet channel, we consider the components of the evolving wavepacket calculated for a fixed photon energy,

$$\Psi(\mathbf{q}|E_{\text{ph}}) = \int_0^\infty e^{-i\mathbf{H}t} \Phi_0(\mathbf{q}) e^{iE_{\text{ph}}t} dt. \quad (21)$$

The resulting stationary states $|\Psi_\alpha|^2$ in both electronic channels α are shown in Fig. 6 in Jacobi coordinates for two values of E_{ph} . The clearly visible oscillations in the fragment O–O bond r , which the probability maxima trace out in either channel, resemble the familiar classical trajectories describing the recoiling vibrationally excited products. In the B state, in which the initial excitation resides, the amplitude of oscillations is small and neither the CI nor the photon energy have any visible impact on the wave function: The oscillations are caused by the slight mismatch in the equilibrium O–O bonds in $\text{O}_3(\tilde{X})$ and in $\text{O}_2(^1\Delta)$, and the FC mapping model accurately catches this effect.

In the R state, the molecules emerge with a visibly overstretched O_2 bond. This overstretching of the coupling mode, found in all calculated wave functions along the adiabatic path through the CI region, is the “mechanistic” origin of the inverted vibrational distributions in the triplet channel. For $E_{\text{ph}} = 4.66 \text{ eV}$ ($\lambda = 266 \text{ nm}$), the probability density in the R state emerges at the short bond stretched to $r \approx 2.6 a_0$; for $E_{\text{ph}} = 5.17 \text{ eV}$ ($\lambda = 240 \text{ nm}$), the short bond is stretched to $r \approx 2.8 a_0$. Arrows in Fig. 6 mark O_2 bond lengths predicted by the FC mapping model for these energies and indicate a remarkable agreement: Apparently, it is this extended short bond at the CI in the R state which the model reverse

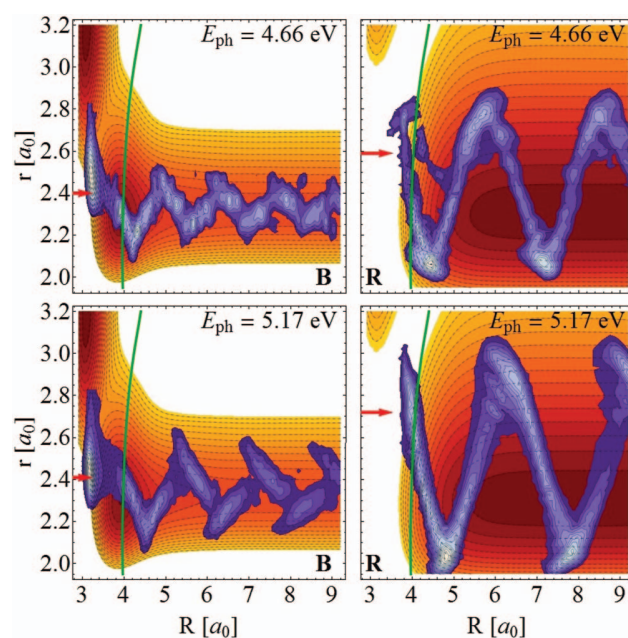


FIG. 6. Contour maps of the fixed energy components $|\Psi_\alpha|^2$ of the evolving wavepacket in the electronic states B (left panels) and R (right panels) shown in the plane (R, r) of the two Jacobi stretching coordinates for two indicated photon energies; only one arrangement channel is shown. The wave functions $|\Psi_\alpha|^2$ are integrated over the Jacobi angle θ . The wave functions are superimposed on the contour maps of the B and R potentials taken at $\theta = 134^\circ$. Thick green lines show the position of the B/R crossing seam. Red arrows mark the O–O bond distances R_e , predicted by the FC mapping model for the singlet and the triplet channels for the same photon energies.

engineers as an “initial condition” from the vibrational distributions in the triplet channel. It has been pointed out in Refs. 15, 21, and 27 that the semiclassical Landau-Zener transition probability into the triplet channel, Eq. (3), grows with growing short O–O bond length at the CI. Indeed, an overstretched coupling mode implies large $\overline{\Delta E}^{\text{ad}}$ and long $\overline{\tau}_x$. These average values are encoded in the vibrational distributions. The length of the initial O–O bond in the R state grows with E_{ph} , and this is the reason for the strong increase of the vibrational excitation of $\text{O}_2(^3\Sigma_g^-)$ fragments with E_{ph} . A detailed study of the quantum mechanical transition probability and the energy redistribution near the B/R CI is reported in a separate paper.⁶²

C. Kinetic energy distributions

The kinetic energy release tracks photodissociation dynamics along the O/O_2 coordinate corresponding to the tuning mode of the CI. Due to conservation of the sum of the internal, E_{int} , and the translational, E_{trans} , energies

$$E_{\text{ph}} = E_{\text{trans}} + E_{\text{int}},$$

TKER is complementary to the above rovibrational distributions. The quantum mechanical TKERs are compared with the experimental data of Houston⁵⁸ in Fig. 7.

In the singlet channel [Figs. 7(a) and 7(b)], TKER is modest because the energy in excess of dissociation threshold of the B state ($D_0 = 3.95 \text{ eV}$) is relatively small. Fragments in

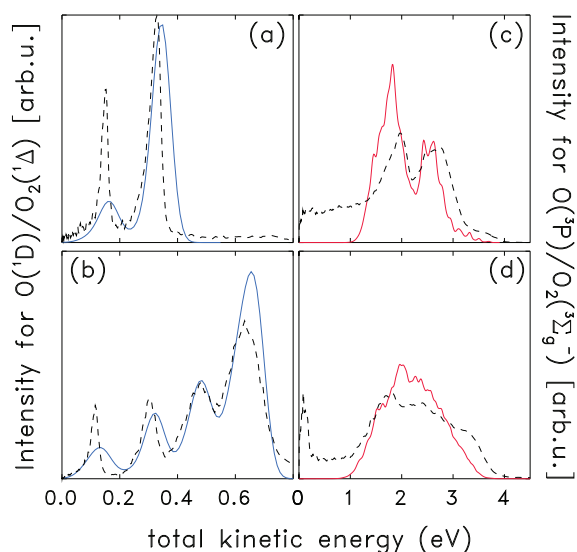


FIG. 7. TKER of O/O_2 fragments in the singlet channel at 289 nm (a) and 268 nm (b) and in the triplet channel at 266 nm (c), and 226 nm (d). Solid lines are calculations for ozone in the rotational state $J_f = 1$. Experimental distributions from Ref. 58, at 285 nm (a), 265 nm (b), 266 nm (c), and 226 nm (d) are shown with dashed lines. Distributions in (a) and (b) are normalized to unit area. Distributions in (c) and (d) are normalized to the unit area in the interval $1.6 \text{ eV} < E_{\text{ph}} < 4.5 \text{ eV}$.

this channel populate low rotational states, and the vibrational structure is clearly resolved in the TKER “spectrum.” Peak intensities are vibrational populations, and the agreement or mismatch between theory and experiment mirror the accuracy with which vibrational distributions are reproduced. Translational distributions are inverted, with the maximum intensity achieved at the largest kinetic energy corresponding to the vibrational state $v = 0$.

The translational distributions in the triplet channel [Figs. 7(c) and 7(d)] differ strongly from those in the singlet channel. The kinetic energies lie between 1 eV and 4 eV and the peaks of individual vibrational states are unresolved under the broad envelope. The calculated and the experimental TKERs compare well above $E_{\text{trans}} \sim 1.2 \text{ eV}$, although the calculated distributions fall off somewhat faster around the highest E_{trans} . Strong disagreement between theory and experiment at low translational energies, corresponding to the extremely vibrationally excited fragments, has been observed also in the classical trajectory calculations¹⁵ and attributed to the Herzberg-state mechanism mentioned in Sec. IV B.⁵⁹

A comparison of the kinetic energy distributions in the two channels is affected by the difference in excess energies. The triplet channel is located nearly 3 eV below the singlet one, and much of this energy surplus ends up in the translational motion as O and O_2 accelerate down the steep R state potential. Less influenced by the threshold energy differences are the dependences of the average translational energies $\langle E_{\text{trans}} \rangle$ on E_{ph} shown in shown in Fig. 4(c). The average TKER in the singlet—diabatic—channel grows by +0.5 eV as E_{ph} increases over 1.0 eV. The change of the average TKER in the triplet—adiabatic—channel over the same range is -0.1 eV . These distinctly opposite trends, which result from the distinctly different average vibrational ener-

gies shown in Fig. 4(b), is a signature which the B/R CI imprints on TKERs in the two complementary channels: The vibrational excitation in the coupling mode along the adiabatic path through the CI clearly affects the $\langle E_{\text{trans}} \rangle$ versus E_{ph} dependence. The impact on $\langle E_{\text{trans}} \rangle$ is strong because the coupling mode in this reaction is a “conserving” vibrational high-frequency mode present in the parent molecule and in the fragment.

V. ANGULAR DISTRIBUTIONS OF THE PHOTOFRAGMENTS

The calculated angular distributions are averaged over the projections m_j of the O_2 angular momentum \mathbf{j} on the direction of laser electric field and characterized in terms of the anisotropy parameter β . The averaged angular distributions are indirectly related to photodissociation lifetimes.^{41,63} In the limiting case of fast dissociation along one O—O bond (impulsive model, Refs. 41 and 64), the anisotropy parameter is estimated from the equilibrium valence angle in the parent ozone (117°), giving $\beta_{\text{val}} = 1.18$. An alternative (and probably kinematically more sound) assumption is that fast dissociation takes place along the initial direction of the Jacobi vector \mathbf{R} connecting the departing O atom with the center of mass of O_2 ; this gives $\beta_{\text{jac}} = 1.8$. These two estimates are not very restrictive: They bracket a considerable part of the interval $[-1, 2]$, to which β is limited, and cover most of the actual range of variation of β observed in the experiment and in the calculations. Nevertheless, they both predict essentially positive β , as expected⁴¹ for a parallel transition. Deviations from these predictions might point to the effects associated with (a) the switching of the direction of dissociation; (b) the finite lifetime; and (c) the influence of the conical intersection. Below we compare the experimental and the calculated wavelength and final state resolved anisotropy parameters in the two electronic dissociation channels.

A. Singlet channel

The β parameters in channel (2) are shown in Fig. 8. Solid lines show β_{O1D} calculated with contributions of all vibrational states v of the fragment O_2 ; symbols represent measured v -resolved anisotropy parameters. Both measured and calculated β are large and positive, in agreement with the parallel character of the $B \leftarrow \tilde{X}$ transition. The calculation with $J_f = 1$ slightly overestimates the experiment, but the deviation lies within the experimental uncertainty reported in Ref. 65 and is almost independent of the excitation energy. In particular, the rise of β_{O1D} with decreasing E_{ph} (growing λ) is well reproduced. The calculated v -resolved anisotropy parameters $\beta_{\text{O1D},v}$ are shown with dashed lines. The parameter $\beta_{\text{O1D},v=0}$ for $v = 0$ is the largest across the Hartley band; $\beta_{\text{O1D},v=1}$ consistently gives the lower bound; β parameters for $v > 1$ lie between these two limits.

The increase of β with decreasing photon energy might appear counterintuitive: Molecular decay is slow at dissociation threshold, and one expects that the axial recoil approximation breaks down and the anisotropy parameter reduces to the long lifetime limit^{63,64} of $\beta \approx 0.30$. Houston and

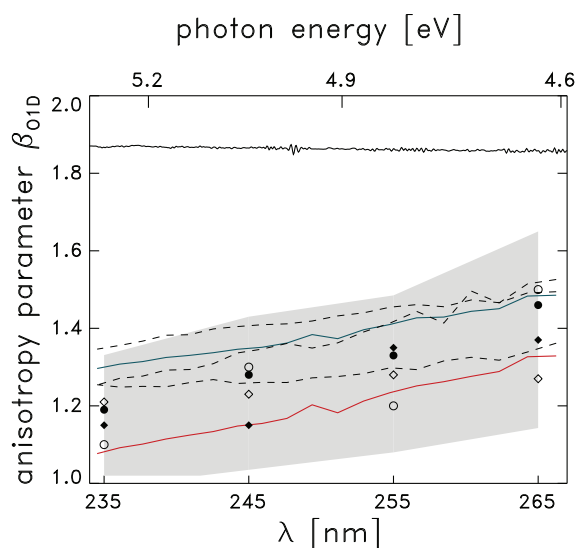


FIG. 8. Measured (symbols, Ref. 65) and calculated (solid and dashed lines) anisotropy parameters in the singlet channel. Experimental β values for the vibrational quantum numbers $v = 0 - 3$ of $O_2(^1\Delta)$ are shown with different symbols. Solid lines refer to the average β_{O1D} values: Black line near 1.83 is a quantum mechanical calculation with $J_f = 1$ but the Coriolis coupling switched off; the blue line is a calculation with the Coriolis coupling “on”; and the red line is a calculation with the Coriolis coupling strength amplified by a factor of $\xi = \sqrt{2}$. Dashed lines show $\beta_{O1D,v}$ for $v = 0 - 2$ calculated with the Coriolis coupling “on.” Shaded area indicates the uncertainty of the experimental data.

co-workers⁶⁵ suggested that increasing β implies that ozone at small photon energies tends to “open up” and bend toward linearity.

The quantum mechanical results point to the strength of the Coriolis coupling as one reason for the observed $\beta_{O1D}(E_{ph})$ dependence, at least in the calculation. This is illustrated in Fig. 8. The Coriolis coupling terms in the Hamiltonian are proportional to the matrix elements

$$C_{J_f\Omega}^{\pm} = \xi(J_f(J_f + 1) - \Omega_f(\Omega_f \pm 1))^{1/2} \quad (22)$$

with $\xi = 1$ in a “regular” calculation. Changing ξ allows one to vary the effective Coriolis strength within the calculation with a fixed J_f and thus to stress the purely Coriolis effect. The black solid line in Fig. 8 shows β_{O1D} calculated with $\xi = 0$, i.e., without Coriolis coupling. In this case, the β parameter has a constant value of 1.83, which is close to β_{jac} estimated above in the impulsive model. Without Coriolis interaction, β is determined solely by the initial populations, $|T_{\alpha}(1, 0)|^2 \propto |\mu_z(FC)|^2$ and $|T_{\alpha}(1, 1)|^2 \propto |\mu_y(FC)|^2$, of states $\Omega_f = 0$ and $\Omega_f = 1$. These initial populations are given by the TDM components at the FC point, $|\mu_z(FC)|^2 \gg |\mu_y(FC)|^2$, and are virtually independent of the dynamics and thus of E_{ph} . The blue solid line in Fig. 8 is β for $\xi = 1$. The red solid line corresponds to β_{O1D} calculated with $\xi = \sqrt{2}$. The increase in the overall strength of the Coriolis interaction diminishes the anisotropy parameters and makes the β_{O1D} dependence on E_{ph} steeper. In our numerical experiment, varying the strength factor ξ between 0 and $\sqrt{2}$ directly amounts to varying the slope of the curve $\beta_{O1D}(E_{ph})$ (with indications of an eventual saturation). This observation might suggest that

the anisotropy parameter depends on E_{ph} because the Coriolis coupling strength does: Ozone becomes more “floppy” as its internal energy increases leading to an effective amplification of the Coriolis interaction and effective reduction of the anisotropy. This explanation implies that the slope of the $\beta_{O1D}(E_{ph})$ dependence is proportional to the effective strength of the Coriolis coupling in the dissociating molecule.

A word of warning is in order here. Coriolis coupling is a fictitious interaction which exists only in the rotating molecular frame, and the above explanation is strongly tied to the fact that the quantum mechanical calculations are performed in body fixed coordinates. The choice of the molecular frame for the calculations is a purely technical detail, and physical arguments constructed on the basis of Coriolis interaction lack generality. For example, the classical trajectory calculations, reported in Ref. 15 and shown to agree with experiment almost as accurately as the present quantum results in Fig. 8, are performed for $J_f = 0$. Clearly, there is no Coriolis interaction in non-rotating ozone and the dependence of β_{O1D} on E_{ph} can be given a different explanation.

Dylewsky *et al.* also report the anisotropy parameter and its dependence on the rotational quantum number j at long wavelengths around 305 nm, close to the dissociation threshold of the B state.⁶⁵ The measured $\beta_{O1D,v=0,j}$ grows from 0.13 for $j = 16$ to 1.7 for $j = 7$, reflecting the difference in the dissociation dynamics between the rotationally excited and the rotationally cold fragments. The calculated $\beta_{O1D,v=0,j}$ near 305 nm is consistent with this observation: It is small (and even slightly negative) at the high end of the j distribution, and becomes large, $\beta_{O1D,v=0,j} > 1.5$, as j decreases and approaches $j = 0$. This distinct anticorrelation between j and the calculated β is seen in both electronic channels. It provides an alternative explanation of the observed decline of β_{O1D} with growing E_{ph} : Larger photon energies correlate with a stronger rotational excitation and lower values of β . The anticorrelation between β and j is discussed in more detail in Sec. VB.

Another set of measurements in the immediate vicinity of the dissociation threshold, between $\lambda = 295$ nm and $\lambda = 320$ nm, was performed by Horrocks *et al.*^{66,67} in order to establish the wavelength dependence of $\beta_{O1D,v=0}$. A comparison between the experiment and our calculations is summarized in Appendix B.

B. Triplet channel

The triplet channel is reached from the B state via the adiabatic path through the CI and a relevant question here is whether signatures of the adiabatic passage through the degeneracy region are seen in the angular distribution. The rotational energy of the $O_2(^3\Sigma_g^-)$ fragments is large [see Fig. 4(a)], and the fragments are accelerated by a strong torque $\sim \partial V_{ad}/\partial\theta$ which shapes the angular distribution. However, this torque acts in the exit channel of the repulsive R state potential. At the CI, the torque is small—the angle θ is not the coupling mode (as, for example, is the case in water molecule⁶⁸ or in many heteroaromatic molecules⁶⁹), but the seam mode, and $\partial V_{ad}/\partial\theta$ is non-zero at the CI only because of the seam is slightly curved in the (r, θ) plane. For this

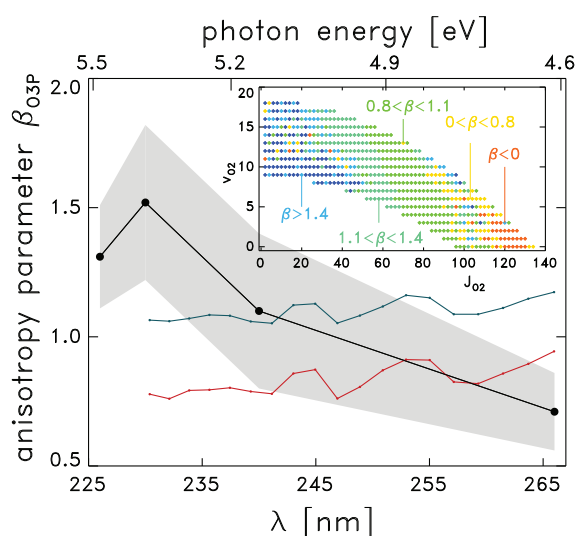


FIG. 9. Measured⁶⁵ (black) and calculated (blue and red) anisotropy parameters in the triplet channel. Experimental β_{O3P} values are shown only for the “fast” fragments with $E_{\text{kin}} \geq 1$ eV; extremely slow and vibrationally hot fragments are not included. Shaded area indicates the uncertainty of the experimental data. Blue line is a calculation with $J_p = 1$ and the Coriolis coupling “on”; red line is a calculation with the Coriolis coupling amplified by a factor of $\xi = \sqrt{2}$. Inset illustrates the dependence of β_{O3P} on the vibrational (v) and rotational (j) quantum numbers. The shown points are calculated for $E_{\text{ph}} = 5.5$ eV ($\lambda = 226$ nm) and refer to a limited range of translational energies, $1.5 \text{ eV} \leq E_{\text{trans}} \leq 2.7 \text{ eV}$. Different colors correspond to different values of β_{O3P} as indicated.

reason, the influence of the CI on the observed distribution is expected to be minor.

The calculated and the measured anisotropy parameters β_{O3P} are shown in Fig. 9. Only experimental values for the “fast” fragments⁵⁸ are shown (the contribution of slow and extremely vibrationally excited O_2 is omitted). Compared to singlet channel, the experimental β_{O3P} values are noticeably reduced and this effect is correctly captured by the calculation. Coriolis coupling has nearly the same effect on β_{O3P} as on β_{O1D} , suppressing the anisotropy of the angular distribution with increasing coupling strength.

The calculated β_{O3P} values show strong anticorrelation with the degree of rotational excitation of the $O_2(^3\Sigma_g^-)$ fragment. The inset of Fig. 9 illustrates how β_{O3P} depends on the vibrational v and the rotational j quantum numbers. This “map” is calculated for the photon energy of 5.5 eV and a translational energy window centered at $E_{\text{trans}} \approx 2.0$ eV [which is the average TKER in this channel, cf. Fig. 4(c)]; the dependence of β_{O3P} on E_{trans} within this window is weak. The main control parameter of the anisotropy of the calculated angular distributions is the rotational angular momentum j . Strongly rotationally excited diatoms with $j \geq 100$ have zero or even negative anisotropy parameters. With decreasing rotational excitation, β_{O3P} gradually grows, reaches 1.1 for $j \approx 60$ (which is the maximum of the rotational distribution for $v = 8$ at this energy), and finally climbs above 1.5 for $j < 30$. The dependence on the vibrational quantum number v is much less pronounced, and many different β values are found for a given v . Strong anticorrelation between β and j was previously observed in the photodissociation of N_2O in

the bent $2^1A'$ state⁷⁰ and shown to be qualitatively consistent with the predictions of an impulsive model.

The “maps” of β_{O3P} in the $j - v$ plane at longer wavelengths are qualitatively similar: The range of variation of j and v shrinks as E_{ph} decreases, but approximately the same values of β_{O3P} are found at approximately the same j 's. The “map” in Fig. 9 is in this sense universal. Moreover, a similar growth of β with decreasing j is found also for the singlet channel (see Sec. V A), albeit in the interval of $0 \leq j \leq 80$. This $\beta_{O3P}(j)$ dependence explains several characteristic trends observed in the calculation. For example, the growth of β_{O3P} with decreasing E_{ph} is due to cooling of the rotational excitation. The observed difference between the β parameters in the two electronic channels, $\beta_{O3P} < \beta_{O1D}$, is due to generally colder rotational distributions in the singlet channel. Finally, similar slopes of $\beta_{O3P}(E_{\text{ph}})$ and of $\beta_{O1D}(E_{\text{ph}})$ in the calculations can be understood using Fig. 4(a) which shows that the dependences of the average rotational excitations $\langle E_{\text{rot}} \rangle$ on E_{ph} in the two channels also have the same slopes.

At the same time, the calculated dependence of β_{O3P} on the photon energy differs substantially from experiment, the anisotropy parameter in which decreases as the photon energy decreases. This discrepancy might have two reasons: Either the dependence of β on j is different in experiment, or the rotational state distribution is different. An additional technical issue might be the accuracy, with which the “slow” and the “fast” fragments in the experimental signal, are distinguished at different photolysis wavelengths. Unfortunately, very little is known about the experimental rotational excitation in the triplet channel, and the present calculations indicate that this knowledge is crucial in understanding the angular distributions and their energy dependence.

VI. CONCLUSIONS

In this paper, the absorption spectrum and the internal state and angular photofragment distributions in the photodissociation of ozone are analyzed using quantum mechanics for nuclear dynamics in two coupled electronic states and *ab initio* SMB PESs of Schinke and McBane.¹⁴ The main results of this study are as follows:

1. The room temperature absorption spectrum, constructed as a Boltzmann average of many spectra corresponding to different initial rotational states of parent ozone, is in good agreement with experiment in terms of (a) the position and shape of the spectral envelope, (b) the widths and intensities of the weak diffuse structures, and (c) the times and intensities of recurrences in the autocorrelation function for times $t \leq 200$ fs.
2. The calculated vibrational, rotational, and kinetic energy distributions agree with experimental results in a broad range of wavelengths across Hartley band. The items (1.) and (2.) allow us to conclude that the SMB PESs provide an extremely accurate description of the near UV photodissociation of ozone.
3. The shape of the observed scalar distributions is related to the details of the vibrational energy exchange at the conical intersection between the two participating

electronic states. Analysis of quantum mechanical wave functions demonstrates that the strong vibrational excitation of the O₂ fragments in the triplet dissociation channel reflects a severely overstretched short O–O bond of parent ozone as the molecule passes through the CI along the adiabatic pathway.

4. The angular anisotropy parameters in the two electronic channels are in reasonable agreement with the experimental data. Agreement is especially good in the singlet channel. An anticorrelation is found between the values of β and the rotational state j of the O₂ fragment: Larger j values correspond to smaller β values. This anticorrelation is predicted to hold at different photolysis wavelength and in both electronic channels. It can explain the difference between β parameters in two channels and their dependence on photon energy.

This study illuminates a relation existing between the topography of the B/R conical intersection and the photofragment distributions in the vibrational and translational modes which map onto the branching space of the intersection. A simple FC mapping of the vibrational distributions in the adiabatic “triplet” channel can be used to reverse engineer the most probable O–O bond length, at which the electronic transition from B to R takes place. In fact, even more detailed information on the Massey parameter at the intersection is encoded in the vibrational and kinetic energy distributions. This additional information can be retrieved if the formation of products is tracked across the CI, and the analysis of the resulting local transient populations is given in a separate publication.⁶²

ACKNOWLEDGMENTS

The authors would like to thank Professor Paul Houston for many insightful comments. Financial support by the Deutsche Forschungsgemeinschaft is gratefully acknowledged. D.P. acknowledges support by a fellowship of the International Max-Planck Research School of Advanced Photon Science.

APPENDIX A: EVEN j PROPENSITY EFFECT IN THE SINGLET DISSOCIATION CHANNEL

Valentini *et al.*⁵⁶ observed a substantial depletion of the population of odd j states, as compared to the even j states, in the singlet channel. Experimental data in Fig. 3(a)–3(c) clearly illustrate this “even- j propensity” effect. The two sets of states have different parities with respect to the exchange of identical oxygen atoms in the fragment O₂. The authors of Ref. 56 attributed their observation to the fact that oxygen molecules O₂(³Σ_g⁻) in the *complementary* triplet channel are formed exclusively in the odd rotational states, so that the odd j population in the B state is drained through the B/R conical intersection making the even j population look artificially enriched. The effect was therefore considered as an example of a parity selective transition mediated by the conically intersecting electronic states. Indeed, the even j propensity disappeared⁵⁶ in isotopically substituted ozone dissociating into heteronuclear diatom ¹⁶O¹⁸O.

In the wave mechanics, the exchange symmetry of the identical nuclei in the fragment O₂ corresponds to the $\theta \rightarrow \pi - \theta$ symmetry of the wave function in Jacobi coordinates. Although this symmetry is globally imposed in our propagation, we found no even- j propensity in the calculations which combined the odd parity rotational states in the R state with the rotational states of a given parity (even or odd) in the B state. The reason for this is the potential energy profile along the Jacobi angle θ near the B/R CI. The CI crossing seam in one dissociation channel passes close to the minima of the B state, which are located at $\theta = 60^\circ$ and 120° and separated by a 1.2 eV high potential barrier [see Fig. 2(f)]. The bending energy of ~ 0.2 eV is much smaller than the barrier height, and the even and odd parity states are almost degenerate near the CI and strongly localized around 60° and 120° . In the terminology of Bunker,⁷¹ the exchange of identical nuclei near the B/R crossing is an “unfeasible” symmetry operation. The CI imposes no symmetry restrictions on the diabatic coupling $V_{BR}(\theta)$ along the seam mode, and the angular integral in the matrix element $\langle \psi_j^B(\theta) | V_{BR}(\theta) | \psi_j^R(\theta) \rangle$, essentially restricted to the vicinity of each minimum, is roughly the same for any combination of parities in the bending wave functions $\psi_j^B(\theta)$ and $\psi_j^R(\theta)$ in the B and R states. In other words, the odd j' states in R can form from both even or odd j states in B. As a result, the “unfeasible” symmetry operation has no effect on the calculated product state distributions.

The authors of Ref. 56 presented several pieces of strong experimental evidence relating the observed effect to the B/R crossing dynamics; our present calculations, although symmetry adapted, do not reproduce the parity effect. The origin of the discrepancy between theory and experiment is unclear at the moment. There exists one experimental observation, however, which seems to contradict our understanding of the dynamics of the transition from B to R. At all wavelengths studied in Ref. 56, the even j propensity is the strongest for $v = 0$ and gradually disappears as v increases (see their Figs. 7–9). It is shown in Sec. IV B and also recognized in Refs. 15, 21, and 27 that the transition probability between B and R states has the opposite v dependence: It is the *smallest* for $v = 0$ and grows as v grows. Qualitatively, this is due to the dependence of the Landau-Zener transition probability on the sojourn time $\bar{\tau}_x$ in Eq. (3). Should the conical intersection be indeed responsible for the observed depletion of the odd j states, one would expect the effect to be the strongest for the highly vibrationally excited O₂ fragments.

APPENDIX B: ANISOTROPY PARAMETER β_{O1D} NEAR 305 nm

An unusual feature of the anisotropy parameters measured in Horrock *et al.*^{66,67} between 295 nm and 320 nm is a pronounced minimum in the β_{O1D} parameter reached precisely at the dissociation threshold of the B state, $\lambda = 310$ nm (see Fig. 10). Horrocks *et al.* attributed the “dip” in the magnitude of β_{O1D} to the change in the alignment of the TDM between the ground electronic state \tilde{X} and the B state and to the pronounced contribution of a “perpendicular” transition to the near threshold photoexcitation. They went on to suggest that it is the antisymmetric stretch excitation in \tilde{X} which

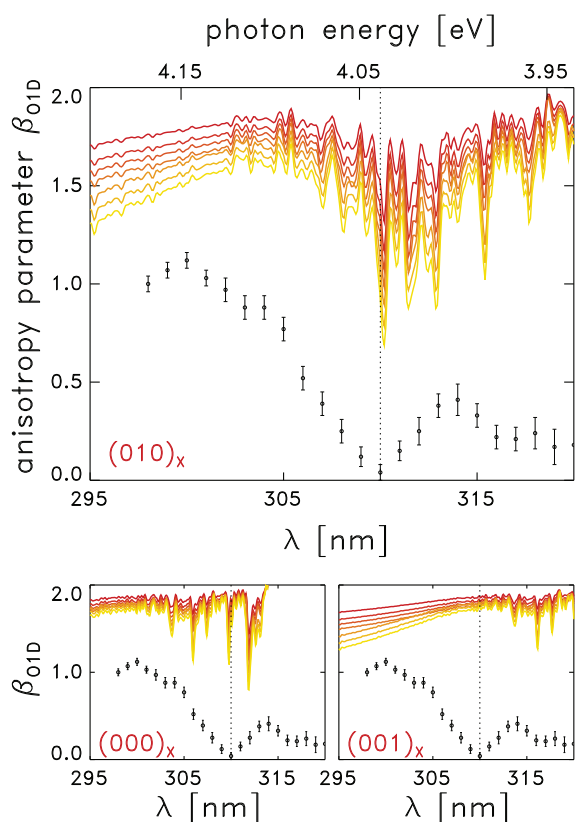


FIG. 10. Measured (open symbols, Ref. 66) and calculated (solid lines; $J_f = 1$) anisotropy parameters in the singlet channel near dissociation threshold of the B state. Results in different panels are calculated with a different initial state $(v_1, v_2, v_3)_X$ of the parent ozone, as indicated in each panel. The color of solid lines indicates different strength factors ξ of the Coriolis coupling: $\xi = 0.5$ for the dark red line (always the topmost curve) and $\xi = 1.7$ for the light yellow line (always the lowest curve), the increment between curves is $\Delta\xi = 0.2$. Vertical dashed line shows the position of threshold.

can—based on 1^1B_2 symmetry of the upper electronic state—lend the transition a perpendicular character, and the “dip” at 310 nm is due to photolysis of the parent ozone with one quantum of antisymmetric stretch.

The quantum mechanical β parameters, calculated near dissociation threshold of the B state for the parent ozone in several initial vibrational states $(v_1, v_2, v_3)_X$ are shown in Fig. 10; v_1 , v_2 , and v_3 denote quantum numbers of the symmetric stretch, the bend, and the antisymmetric stretch. The calculations were performed for several values of the Coriolis coupling strength factor ξ [see Eq. (22)] ranging from 0.5 (red lines) to 1.7 (yellow lines); this allowed us to approximately assess the (modest) effect of the overall rotation on the observed β values. The anisotropy parameter calculated for the ground vibrational state $(0, 0, 0)_X$ (lower left panel) exhibits several resonance-like structures, at which β sharply decreases. Narrow structures at the same energies were observed in the partial absorption spectrum calculated in Ref. 13 and attributed to a progression of long lived resonance states with excitations of the short bond stretching mode and located above the shallow C_s wells of the B state PES. Relatively small β values for these states are due to long lifetimes. Apart from these structures, the β_{OID} parameter for the initial state

$(0, 0, 0)_X$ is larger than 1.7 and shows little dependence on the photolysis wavelength. The same is true for the β_{OID} parameter calculated for the parent state $(0, 0, 1)_X$ with one quantum of antisymmetric stretch (lower right panel). The sharp structures, arising from the short bond stretch resonances, are now shifted to longer wavelengths, and the anisotropy parameter smoothly depends on λ between 312 nm and 295 nm. This contrasts with β_{OID} calculated for the initial state $(0, 1, 0)_X$ (a single bending excitation) shown in the upper panel. The resonance structures in this case are positioned around 310 nm, and the envelope of the β_{OID} vs. λ dependence shows a noticeable “dip” at threshold; the minimum value of β_{OID} at 310 nm shows a rather strong dependence on the strength of Coriolis coupling.

In view of the discussion in Sec. V A, it appears quite natural that the calculated angular anisotropy is sensitive to the pre-excitation in the bending mode: It is the bending mode which efficiently mediates the breakdown of the axial recoil approximation and leads to larger effective Coriolis coupling. The antisymmetric (or the symmetric) stretch pre-excitations contribute comparatively little to the Coriolis coupling and do not affect the β parameter much, except for the overall shift on the wavelength scale. The symmetry argument, advocated in Refs. 66 and 67, does not seem to be operative in our calculations: The B state PES has C_s symmetry and cannot be classified as B_2 . Physically this means that the electronic excitation from the state $(0, 0, 1)_X$ is accomplished with the same TDM as from the state $(0, 0, 0)_X$: The vibrational states in the B state are nearly degenerate symmetric/antisymmetric pairs, and the symmetry of the terminal state in the matrix element can always be “adjusted” in a given transition.

We presented the numerical evidence that the observed “dip” in the anisotropy parameter at 310 nm is due to parent bending states. However, it would be premature to claim that the “dip” is fully explained in these calculations: The agreement with experiment is at best qualitative, and the calculated β values consistently overestimate the ones measured in the threshold region. Moreover, the resonance structures due to the short bond excitations in the B state, clearly visible in the calculation for $J_f = 1$, are not observed in the experiment.

¹W. N. Hartley, *J. Chem. Soc.* **39**, 111 (1881).

²W. Huggins and M. Huggins, *Proc. R. Soc. Lond.* **48**, 216 (1890).

³D. E. Freeman, K. Yoshino, J. R. Esmond, and W. H. Parkinson, *Planet. Space Sci.* **32**, 239 (1984).

⁴N. J. Mason, J. M. Gingell, J. A. Davis, H. Zhao, I. C. Walker, and M. R. F. Siggel, *J. Phys. B.* **29**, 3075 (1996).

⁵R. Basic, A. J. Bouvier, and J. M. Flaud, *Spectrochim. Acta, Part A* **54**, 17 (1998).

⁶C. Parisse, J. Brion, and J. Malicet, *Chem. Phys. Lett.* **248**, 31 (1996).

⁷J. A. Joens, *J. Chem. Phys.* **100**, 3407 (1994).

⁸P. O’Keeffe, T. Ridley, K. P. Lawley, and R. J. Donovan, *J. Chem. Phys.* **115**, 9311 (2001).

⁹P. J. Hay, R. T. Pack, R. B. Walker, and E. J. Heller, *J. Phys. Chem.* **86**, 862 (1982).

¹⁰C. Leforestier, F. LeQuéré, K. Yamashita, and K. Morokuma, *J. Chem. Phys.* **101**, 3806 (1994).

¹¹Z.-W. Qu, H. Zhu, S. Yu. Grebenshchikov, R. Schinke, and S. Farantos, *J. Chem. Phys.* **121**, 11731 (2004).

¹²E. Baloitcha and G. G. Balint-Kurti, *J. Chem. Phys.* **123**, 014306 (2005).

¹³S. Yu. Grebenshchikov and S. Rosenwaks, *J. Phys. Chem. A* **114**, 9809 (2010).

- ¹⁴R. Schinke and G. C. McBane, *J. Chem. Phys.* **132**, 044305 (2010).
- ¹⁵G. C. McBane, L. T. Nguyen, and R. Schinke, *J. Chem. Phys.* **133**, 144312 (2010).
- ¹⁶B. R. Johnson and J. L. Kinsey, *Phys. Rev. Lett.* **62**, 1607 (1989).
- ¹⁷B. R. Johnson and J. L. Kinsey, *J. Chem. Phys.* **91**, 7638 (1989).
- ¹⁸B. R. Johnson, B.-Y. Chang, C. W. Hsiao, L. Le, and J. L. Kinsey, *J. Chem. Phys.* **108**, 7670 (1998).
- ¹⁹G. Parlant, *J. Chem. Phys.* **112**, 6956 (2000).
- ²⁰C. K. Ulrich, J. Chen, O. Tokel, P. L. Houston, and S. Yu. Grebenshchikov, *J. Phys. Chem. A* **117**, 12011 (2013).
- ²¹S. Yu. Grebenshchikov, Z.-W. Qu, H. Zhu, and R. Schinke, *Phys. Chem. Chem. Phys.* **9**, 2044 (2007).
- ²²Another ¹A' state, the so-called "A state" correlating with cyclic ozone, forms narrowly avoided crossings with both B and R states and lies in the range of excitation of the Hartley bands. However, the transition dipole moment with the \tilde{X} state is vanishingly small. Moreover, the *ab initio* and the trajectory surface hopping studies of Ref. 14, as well as our own test quantum mechanical calculations including this state, indicate that the non-adiabatic interactions with either B or R states are dynamically quenched so that the A state has hardly any impact on the UV photodissociation.
- ²³Z.-W. Qu, H. Zhu, M. Tashiro, R. Schinke, and S. Farantos, *J. Chem. Phys.* **120**, 6811 (2004).
- ²⁴Y. Matsumi and M. Kawasaki, *Chem. Rev.* **103**, 4767 (2003).
- ²⁵H. Zhu, Z.-W. Qu, M. Tashiro, and R. Schinke, *Chem. Phys. Lett.* **384**, 45 (2004).
- ²⁶E. E. Nikitin and L. P. Pitaevskii, *Phys. Rev. A* **49**, 695 (1994).
- ²⁷Z.-W. Qu, H. Zhu, S. Yu. Grebenshchikov, and R. Schinke, *J. Chem. Phys.* **122**, 191102 (2005).
- ²⁸E. Teller, *J. Phys. Chem.* **41**, 109 (1937).
- ²⁹J. C. Tully, *J. Chem. Phys.* **93**, 1061 (1990).
- ³⁰M. G. Sheppard and R. B. Walker, *J. Chem. Phys.* **78**, 7191 (1983).
- ³¹N. Balakrishnan and G. D. Billing, *J. Chem. Phys.* **101**, 2968 (1994).
- ³²S. Y. Lin, K. L. Han, and G. Z. He, *J. Chem. Phys.* **114**, 10651 (2001).
- ³³Z.-W. Qu, H. Zhu, S. Yu. Grebenshchikov, and R. Schinke, *J. Chem. Phys.* **123**, 074305 (2005).
- ³⁴H. Köppel, in *Conical Intersections*, edited by W. Domcke, D. R. Yarkony, and H. Köppel (World Scientific, Singapore, 2004).
- ³⁵J. Z. H. Zhang, *Theory and Application of Quantum Molecular Dynamics* (World Scientific, Singapore, 1999).
- ³⁶G. G. Balint-Kurti, *Adv. Chem. Phys.* **128**, 249 (2004).
- ³⁷D. J. Tannor, *Introduction to Quantum Mechanics. A Time-Dependent Perspective* (University Science Books, Sausalito, CA, 2007).
- ³⁸V. A. Mandelshtam and H. S. Taylor, *J. Chem. Soc., Faraday Trans.* **93**, 847 (1997).
- ³⁹G. G. Balint-Kurti and M. Shapiro, *Chem. Phys.* **61**, 137 (1981).
- ⁴⁰G. G. Balint-Kurti, R. N. Dixon, and C. C. Marston, *J. Chem. Soc., Faraday Trans.* **86**, 1741 (1990).
- ⁴¹R. N. Zare, *Angular Momentum* (Wiley, New York, 1988).
- ⁴²G. Jolicard and E. J. Austin, *Chem. Phys. Lett.* **121**, 106 (1985).
- ⁴³H. Tal-Ezer and R. Kosloff, *J. Chem. Phys.* **81**, 3967 (1984).
- ⁴⁴V. A. Mandelshtam and H. S. Taylor, *J. Chem. Phys.* **103**, 2903 (1995).
- ⁴⁵R. Schinke, *Photodissociation Dynamics* (Cambridge University Press, Cambridge, 1993).
- ⁴⁶J. C. Light and T. Carrington, *Adv. Chem. Phys.* **114**, 263 (2000).
- ⁴⁷J. Echave and D. C. Clary, *Chem. Phys. Lett.* **190**, 225 (1992).
- ⁴⁸B. Kirmse, B. Abel, D. Schwarzer, S. Yu. Grebenshchikov, and R. Schinke, *J. Phys. Chem. A* **104**, 10398 (2000).
- ⁴⁹M. Alacid and C. Leforestier, *J. Chem. Phys.* **114**, 1685 (2001).
- ⁵⁰H. Zhu, Z.-W. Qu, S. Yu. Grebenshchikov, R. Schinke, J. Malicet, J. Brion, and D. Daumont, *J. Chem. Phys.* **122**, 024310 (2005).
- ⁵¹The photoexcited vibrational levels primarily involve excitations in the long-bond stretching mode ν_1 and in the bending mode ν_2 . Because the long-bond stretch frequency (681 cm^{-1} in these calculations) is accidentally about twice as large as the bending one (375 cm^{-1}), the photoexcited states form multiplets (polyads) with the polyad quantum number $P = \nu_1 + 2\nu_2$. The sequence of polyads extends to the dissociation threshold of the B state.
- ⁵²A. Sinha, D. Imre, J. H. Goble, Jr., and J. L. Kinsey, *J. Chem. Phys.* **84**, 6108 (1986).
- ⁵³G. de Polavieja, F. Borondo, and R. M. Benito, *Phys. Rev. Lett.* **73**, 1613 (1994).
- ⁵⁴S. M. Ball, G. Hancock, and F. Winterbottom, *Faraday Discuss.* **100**, 215 (1995).
- ⁵⁵R. K. Talukdar, C. A. Longfellow, M. K. Gilles, and A. R. Ravishankara, *Geophys. Res. Lett.* **25**, 143, doi:10.1029/97GL03354 (1998).
- ⁵⁶J. J. Valentini, D. P. Gerrity, D. L. Phillips, J.-C. Nieh, and K. D. Tabor, *J. Chem. Phys.* **86**, 6745 (1987).
- ⁵⁷M. J. Daniels and J. R. Wiesenfeld, *J. Chem. Phys.* **98**, 321 (1993).
- ⁵⁸P. L. Houston, "Photodissociation dynamics of ozone in the Hartley band," in *Modern Trends in Chemical Reaction Dynamics: Experiment and Theory*, Advanced Series in Physical Chemistry, edited by X. Yang and K. Liu (World Scientific, Singapore, 2005).
- ⁵⁹R. Schinke, G. C. McBane, L. Shen, P. C. Singh, and A. G. Suits, *J. Chem. Phys.* **131**, 011101 (2009).
- ⁶⁰G. Herzberg, *Naturwissenschaften* **20**, 577 (1932).
- ⁶¹M. S. Child and M. Shapiro, *Mol. Phys.* **48**, 111 (1983).
- ⁶²D. Picconi and S. Yu. Grebenshchikov "Transient photofragment distributions as proxies for non-adiabatic dynamics: Applications to the Hartley band of ozone" (unpublished).
- ⁶³C. Jonah, *J. Chem. Phys.* **55**, 1915 (1971).
- ⁶⁴G. E. Busch and K. R. Wilson, *J. Chem. Phys.* **56**, 3626 (1972).
- ⁶⁵S. M. Dylewski, J. D. Geiser, and P. L. Houston, *J. Chem. Phys.* **115**, 7460 (2001).
- ⁶⁶S. J. Horrocks, P. J. Pearson, and G. A. D. Ritchie, *J. Chem. Phys.* **125**, 133313 (2006).
- ⁶⁷S. J. Horrocks, G. A. D. Ritchie, and T. R. Sharples, *J. Chem. Phys.* **126**, 044308 (2007).
- ⁶⁸K. Yuan, R. N. Dixon, and X. Yang, *Acc. Chem. Res.* **44**, 369 (2011).
- ⁶⁹M. N. R. Ashfold, G. A. King, D. Murdock, M. G. D. Nix, T. A. A. Oliver, and A. G. Sage, *Phys. Chem. Chem. Phys.* **12**, 1218 (2010).
- ⁷⁰D. W. Neyer, A. J. R. Heck, and D. W. Chandler, *J. Chem. Phys.* **110**, 3411 (1999).
- ⁷¹P. R. Bunker, *Molecular Symmetry and Spectroscopy* (Academic Press, San Diego, 1979).
- ⁷²J. Malicet, D. Daumont, J. Charbonnier, C. Parrisé, A. Chakir, and J. Brion, *J. Atmos. Chem.* **21**, 263 (1995).

Paper 2

Intermediate photofragment distributions as probes of non-adiabatic dynamics at conical intersections: application to the Hartley band of ozone. D. Picconi and S. Yu. Grebenschikov, *Phys. Chem. Chem. Phys.* **17**, 28931 (2015); <http://dx.doi.org/10.1039/c5cp04564a>.



Cite this: *Phys. Chem. Chem. Phys.*,
2015, 17, 28931

Intermediate photofragment distributions as probes of non-adiabatic dynamics at conical intersections: application to the Hartley band of ozone†

David Picconi and Sergy Yu. Grebenshchikov*

Quantum dynamics at a reactive two-state conical intersection lying outside the Franck–Condon zone is studied for a prototypical reaction of ultraviolet photodissociation of ozone in the Hartley band. The focus is on the vibrational distributions in the two electronic states at intermediate interfragment distances near the intersection. Such intermediate distributions of strongly interacting photofragments contain unique information on the location and shape of the conical intersection. Multidimensional Landau–Zener modeling provides a framework to reverse engineer the molecular geometry-dependent Massey parameter of the intersection from the intermediate distributions. The conceptual approach is demonstrated for the intermediate O–O bond stretch distributions which become strongly inverted on adiabatic passage through the intersection. It is further demonstrated that intermediate distributions can be reconstructed from the photoemission spectrum of the dissociating molecule. The illustration, given using quantum mechanical calculations of resonance Raman profiles for ozone, completes a practicable cycle of conversion of intermediate distributions into topographic features of the conical intersection.

Received 1st August 2015,
Accepted 28th September 2015

DOI: 10.1039/c5cp04564a

www.rsc.org/pccp

1 Introduction

Conical intersections of electronic states are a focus of extensive experimental and theoretical scrutiny in the domain of reaction dynamics: the presently accumulated evidence indicates that conical intersections are common in the excited electronic states and therefore are likely to be encountered as the excited molecule moves along the reaction coordinate.¹ Such reactive conical intersections are postulated to mediate ultrafast (femtosecond-scale) radiationless transitions and are recognized as natural molecular hubs, or generalized transition states, routing the reactive system towards specific final states or specific products.^{2,3} The knowledge of their energetic position and topography is often regarded as instrumental to the ability to control elementary reactive steps in, for example, organic photochemistry, photobiology, or molecular electronics.^{1,3} At a more fundamental level, reactive conical intersections represent molecular sites at which the characteristic time scales of electronic and nuclear motions become compatible, and the correlated electron–nuclear dynamics can be effectively probed.^{4,5} This paper demonstrates how to locate reactive conical intersections and to characterize their shape using excitation distributions in the modes transverse to the reaction path.

Recent years have seen a growing effort to detect reactive conical intersections experimentally.^{6,7} For a molecule with N_c nuclear degrees of freedom, a conical intersection is characterized (a) by an $(N_c - 2)$ dimensional space of coordinates $\{Z\}$, called seam space, in which the energies of the intersecting states stay equal, and (b) by a two dimensional branching space (X, Y) , in which the degeneracy is lifted. The familiar hourglass picture of a conical intersection, with ‘sand’ (*i.e.* the state population) flowing from the upper into the lower cone, refers to the branching space: The reaction complex switches electronic states only if it moves in the coordinates (X, Y) . This suggests that experimentally conspicuous reactive conical intersections arise if the reaction path lies in their branching space.⁸

The non-adiabatic molecular photodissociation provides an effective means to probe reactive conical intersections with a fully controlled initial state.^{1,7,9,10} A prototypical arrangement of electronic states is illustrated in Fig. 1(a) in a potential energy diagram. The photoexcitation from the ground electronic state \bar{X} brings the molecule into a single optically bright diabatic electronic state B shown with blue. The B state forms an intersection (marked with a circle) with another diabatic electronic state R shown in red. The coordinate X in this diagram is the tuning mode of the intersection: The energy difference between the B and R states along X changes the fastest. The second coordinate of the branching space, Y , is perpendicular to the plane of the figure—it is the coupling mode along which the interstate coupling grows

Department of Chemistry, Technische Universität München, Lichtenbergstr. 4,
85747 Garching, Germany. E-mail: Sergy.Grebenshchikov@ch.tum.de

† Electronic supplementary information (ESI) available. See DOI: 10.1039/c5cp04564a

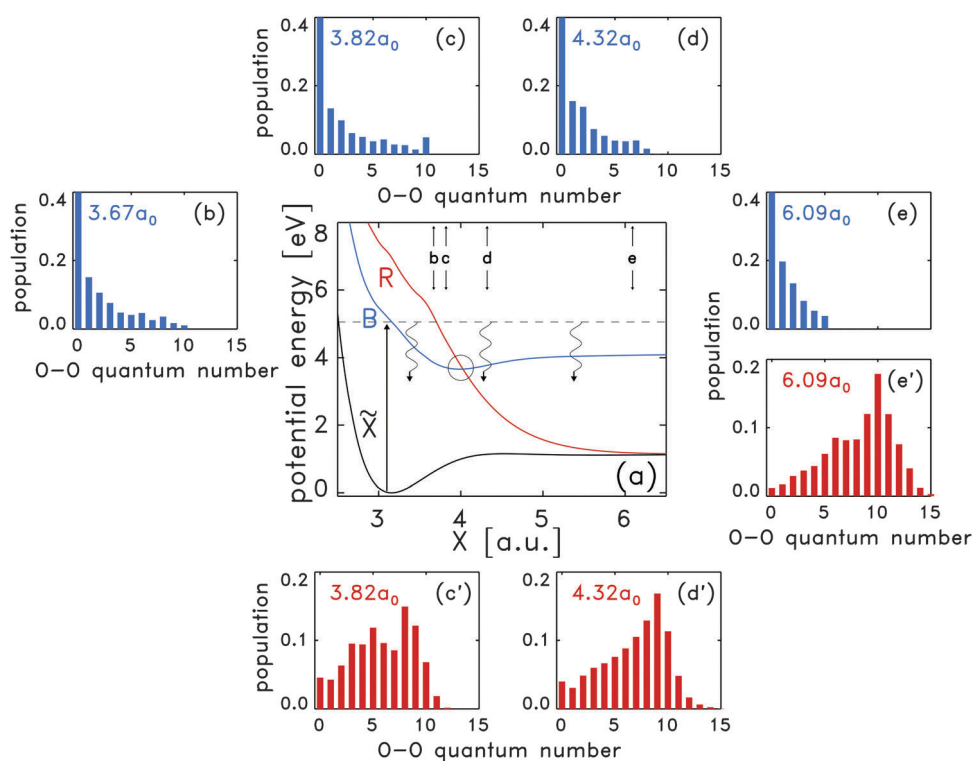


Fig. 1 (a) A one dimensional cut along the interfragment Jacobi distance X through the *ab initio* potential energy surfaces of the electronic states \tilde{X}^1A' (black; marked \tilde{X}), $3^1A'$ (blue; marked B), and $1^1A'$ (red; marked R), participating in the UV photodissociation of ozone. Two other Jacobi coordinates are optimized to give the minimum energy of the B state. The B/R conical intersection is marked with a circle. Straight line arrows indicate the distances X , at which the distributions in panels (b–e) and (c'–e') are evaluated. Curved arrows represent emission of the dissociating molecule. (b–e) The normalized vibrational distributions in the short O–O bond stretch in the B state at fixed distances X indicated in each frame. (c'–e') The same distributions, as in (c–e), but for the R state. The photon energy is $E_{\text{ph}} = 4.96$ eV (the photolysis wavelength $\lambda = 250$ nm).

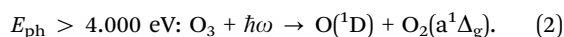
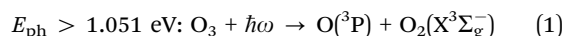
the fastest. The conical intersection is shifted halfway into the exit channel, and two distinct electronic dissociation channels emerge from the intersection. The dissociation coordinate in this example coincides with the tuning mode X . The state intersection pattern in Fig. 1(a) is characteristic of several broad classes of UV photodissociation reactions in which two fragments, an atom and a molecule, are formed. Examples of such exit channel intersections are found in the photodissociation of triatomic atmospheric trace gases (such as N_2O ,¹¹ CO_2 ,^{12,13} or O_3 ^{14,15}), photodissociation of halogenoalkanes (in particular, methyl halides^{16–19} CY_3I or CY_3Br , with $Y = \text{H}, \text{D},$ or F), and the currently much studied ultrafast decomposition of heteroaromatic molecules (such as pyrrole⁹ or phenol and its derivatives^{7,20,21}) into an H atom and a radical co-fragment. Although the exit channel conical intersections lie outside the Franck–Condon zone and are difficult to detect spectroscopically, they influence the separating photofragments. Clearly affected are the observables associated with the tuning mode X , e.g. the electronic branching ratios and the total kinetic energy release, but those associated with the coupling mode Y (for example, rovibrational or angular distributions) are influenced, too. The information content of the distributions associated with the branching space (X, Y) can be illustrated using a Landau–Zener-type estimate.^{15,22,23} The probability of a transition between the diabatic states B and R depends on the average²⁴ adiabatic energy gap $\overline{\Delta E^{\text{ad}}}$ and the average sojourn

time $\bar{\tau}_x$ in the crossing region, $w^{\text{LZ}}(\text{B} \rightarrow \text{R}) \approx 1 - \exp(-\overline{\Delta E^{\text{ad}}}\bar{\tau}_x)$. The more adiabatic the motion along X , the larger the gap between the adiabatic states, the longer the time spent near intersection, and the larger the transition probability $w^{\text{LZ}}(\text{B} \rightarrow \text{R})$. Molecules in the B state with no excitation in the coupling mode Y are moving fast through the region of small gap $\overline{\Delta E^{\text{ad}}}$; as a result they behave diabatically and end up in the upper dissociation channel B. Molecules, moving in the B state with the mode Y strongly excited, sample large gaps $\overline{\Delta E^{\text{ad}}}$ and move slowly along X ; as a result they are diverted into the lower dissociation channel R. The conical intersection acts as a ‘beam splitter’, sending the X -slow/ Y -excited fragments into one (adiabatic) channel and the X -fast/ Y -cold fragments into the other (diabatic) channel. The final photofragment distributions in the adiabatic and the diabatic channels, if simultaneously observed, reveal the presence of the reactive conical intersection.^{7,15,25} The major obstacle, however, are the post-intersection dynamics which are different in the two electronic channels and which distort the distributions arriving in the asymptotic region. The situation is somewhat similar to the one encountered in direct probing of a fleeting transition state in bimolecular reactions.²⁶ In the potential diagram in Fig. 1(a), an important source of such distortions is a nearly 3 eV difference in the dissociation energies of the two channels.

This work shows that intermediate distributions, recorded in the vicinity of the intersection, carry structural and dynamical

information about the shape of the conical intersection in the branching space. Our aim is to demonstrate how this information can be extracted from the vibrational distributions in the coupling mode Y , taken as the main example, and how the intermediate vibrational distributions themselves can be reconstructed from the emission spectrum of the dissociating molecule.

The ultraviolet (UV) photodissociation of ozone in the Hartley band serves as proof-of-principle application; this reaction is the key step in the protective function of the stratospheric ozone layer and the primary source of $O(^1D)$ oxygen in the atmosphere of Earth.^{14,15,27–31} The diagram in Fig. 1(a) depicts three singlet electronic states involved in the reaction:^{14,28,31} The ground electronic state \tilde{X}^1A' , the optically bright state $3^1A'$ ('B'), and the purely repulsive dark singlet state $^1A'$ ('R'). The two dissociation channels are spin-allowed and, combined, carry most of the reaction flux:^{27,29}



In the 'singlet' channel (2), reached diabatically along the B state, O and O_2 are electronically excited; this is the major reaction channel accounting for 90% of the products. In the 'triplet' channel (1), reached adiabatically by taking a hop to the R state, the fragments are formed in their ground electronic states; this is a minor channel with the quantum yield between 7% and 9%. Molecules, photoexcited into the B state, branch between the two channels at the B/R conical intersection. The tuning mode X is the O... O_2 distance; the coupling mode Y is the short (fragment) O–O bond length. Photodissociation in the Hartley band has been exhaustively described using quantum mechanics.¹⁵ The calculations with the *ab initio* potentials of ref. 31, accurately reproduce the temperature dependent³² Hartley absorption spectrum with its weak diffuse bands and the final rovibrational and angular photofragment distributions.

The diffuse absorption spectrum reflects early photodissociation dynamics in the Franck–Condon region; the asymptotic distributions are shaped by the integrated effect of all interactions acting along the dissociation path. In this work, we concentrate on intermediate dissociation distances near the conical intersection, and use quantum mechanical calculations to construct vibronic distributions of the emerging but still interacting photofragments over the local vibrational modes transverse to the dissociation path. The approach to calculation of intermediate distributions is described in Section 2. In Section 3, the intermediate distributions are used to track the non-adiabatic dynamics at the conical intersection with spatial and energy resolution, and to visualize the bond breaking and energy redistribution in the photoexcited ozone. This analysis reveals an unexpectedly active energy exchange in the branching space, with up to 6 vibrational quanta (corresponding to the vibrational energy of more than 1.0 eV) transferred to the coupling mode upon crossing the intersection. The modelling of the intermediate distributions in the framework of Landau–Zener theory in Section 4 allows one to reverse engineer the parameters of the conical intersection. Finally, the intermediate distributions are inferred from the amplitudes of

fluorescence into the ground electronic state in Section 5. Summary is given in Section 6. Technical information and numerical details are summarized in two Appendices and in the ESI.†

2 Vibronic distributions of interacting photofragments at intermediate interfragment distances

We shall consider the dissociation dynamics of the photoexcited ozone using the molecular Hamiltonian set in the quasi-diabatic representation:³³

$$\hat{H}^0 = \begin{pmatrix} \hat{T} & 0 \\ 0 & \hat{T} \end{pmatrix} + \begin{pmatrix} V_B & V_{BR} \\ V_{BR} & V_R \end{pmatrix}. \quad (3)$$

\hat{T} is the standard³⁴ kinetic energy operator for a non-rotating triatomic molecule, common for both electronic states and specified in the body fixed (BF) frame using the Jacobi coordinates $\mathbf{Q} = (X, Y, Z)$. The coordinate X (the tuning mode) is the distance between one oxygen atom and the center of mass of O_2 , Y is the O–O distance (the coupling mode), and Z is the angle between the vectors \mathbf{X} and \mathbf{Y} .

Internal electronic ($\gamma = B$ or R), vibrational (V) and rotational (J) states of the oxygen molecule label the asymptotic scattering channels (γ, J, V) whose populations give the asymptotic photofragment distributions $P_\gamma(J, V)$, defined in terms of the total and partial absorption cross sections. Meaningful and eventually observable vibronic distributions at intermediate interfragment separations X_* are constructed by smoothly continuing the channels (γ, J, V) into the inner region.

The photon energy dependent total absorption cross section is given by a Fourier transform of the autocorrelation function ($\hbar = 1$ hereafter),

$$\sigma_{\text{tot}}(E_{\text{ph}}) = \frac{\pi E_{\text{ph}}}{3c\epsilon_0} \int_0^\infty \langle \Phi_0 | e^{-i\hat{H}^0 t} | \Phi_0 \rangle e^{iE_{\text{ph}} t} dt. \quad (4)$$

The total cross section can be written in the equivalent form

$$\sigma_{\text{tot}}(E_{\text{ph}}) = \frac{E_{\text{ph}}}{3c\epsilon_0} \lim_{\lambda \rightarrow 0} \lambda \langle \Psi^\lambda(\mathbf{Q}|E_{\text{ph}}) | \Psi^\lambda(\mathbf{Q}|E_{\text{ph}}) \rangle, \quad (5)$$

which involves the stationary energy component of the wave packet in two electronic states,

$$\Psi^\lambda(\mathbf{Q}|E_{\text{ph}}) = \int_0^\infty e^{-i(\mathbf{H}^0 - i\lambda)t} \Phi_0 e^{-iE_{\text{ph}} t} dt. \quad (6)$$

The electronic components Ψ_γ^λ of the vector Ψ^λ contain purely outgoing waves along X . In practice, the infinitesimal damping λ , ensuring this asymptotic behaviour, enters the calculations as an absorbing potential described in Section I of the ESI.† Using the completeness relation for the energy-normalized scattering eigenstates $\{\psi_{\gamma JV}^-\}$, the total cross section can be written as a sum of partial cross sections,

$$\sigma_{\text{tot}}(E_{\text{ph}}) = \sum_{\gamma JV} \sigma_{\text{par}}(E_{\text{ph}} | \gamma JV), \quad (7)$$

$$\begin{aligned}\sigma_{\text{par}}(E_{\text{ph}}|\gamma JV) &= \frac{E_{\text{ph}}}{3c\epsilon_0} \lim_{\lambda \rightarrow 0} \lambda \left| \left\langle \psi_{\gamma JV}^- | \Psi_{\gamma}^{\lambda}(\mathbf{Q}|E_{\text{ph}}) \right\rangle \right|^2 \\ &= \frac{E_{\text{ph}}}{3c\epsilon_0} |T_{\gamma JV}(E_{\text{ph}})|^2,\end{aligned}\quad (8)$$

with the photodissociation matrix element – the central piece of the theory – given by

$$T_{\gamma JV}(E_{\text{ph}}) = \lim_{\lambda \rightarrow 0} \lambda \left\langle \psi_{\gamma JV}^- | \Psi_{\gamma}^{\lambda} \right\rangle \quad (9)$$

The normalized photofragment distributions $P_{\gamma}(J,V)$

$$P_{\gamma}(J, V) = \frac{1}{\mathcal{N}_{\gamma}} |T_{\gamma JV}(E_{\text{ph}})|^2, \quad (10)$$

are proportional to the squares of the T -matrix elements. The goal is to find a reliable continuation of the T -matrix elements to intermediate interfragment distances. Our approach extends the projection method of Balint-Kurti and coworkers,^{35,36} originally developed for large interfragment distances and based on the asymptotic factorization of the wave function $\Psi^{\lambda}(X; Y, Z|E_{\text{ph}})$ into the X - and the (Y, Z) -dependent part in each dissociation channel,

$$\begin{aligned}\Psi_{\gamma}^{\lambda}(X; Y, Z|E_{\text{ph}}) &\xrightarrow{X \rightarrow \infty} -i \sum_{JV} T_{\gamma JV}(E_{\text{ph}}) \sqrt{\frac{\mu_X}{k_{\gamma JV}}} e^{ik_{\gamma JV} X} \chi_{\gamma JV}(Y, Z) \\ &\equiv \sum_{JV} f_{\gamma JV}(X) \chi_{\gamma JV}(Y, Z),\end{aligned}\quad (11)$$

where μ_X is the O/O₂ reduced mass, $\chi_{\gamma JV}(Y, Z)$ is the eigenfunction of the fragment state (γ, J, V) , $\epsilon_{\gamma JV}$ is its eigenenergy, and $k_{\gamma JV} = \sqrt{2\mu_X(E_{\text{ph}} - \epsilon_{\gamma JV})}$ is the channel momentum (atomic units $\hbar = 1$ are used).

In the asymptotic region, at the analysis line $X = X_{\infty}$, the fragment eigenstates form an orthogonal set, and the T -matrix element can be projected out of eqn (11):

$$|T_{\gamma JV}(X_{\infty})|^2 = \frac{k_{\gamma JV}}{\mu_X} \left| \left\langle \chi_{\gamma JV}(Y, Z) | \delta(X - X_{\infty}) | \Psi_{\gamma}^{\lambda}(X; Y, Z) \right\rangle \right|^2. \quad (12)$$

In terms of the velocity operator $\hat{v}_X = \hat{p}_X/\mu_X$ and its real eigenvalues $\dot{X}_{\gamma JV} = k_{\gamma JV}/\mu_X$, eqn (12) can be re-written as

$$|T_{\gamma JV}(X_{\infty})|^2 = f_{\gamma JV}^*(X_{\infty}) \dot{X}_{\gamma JV} f_{\gamma JV}(X_{\infty}). \quad (13)$$

An alternative formulation for the T -matrix element, developed by Manolopolous, Rist and Alexander^{37,38} in the context of time-independent close coupling method and adapted by Zhang³⁴ for wave packet propagation, is based directly on the flux operator,

$$|T_{\gamma JV}(X_{\infty})|^2 = \text{Re}[f_{\gamma JV}^*(X_{\infty}) \hat{v}_X f_{\gamma JV}(X_{\infty})]. \quad (14)$$

The eqn (13) and (14) are equivalent in the asymptotic region. Either of them can be used to continue the T -matrix elements to arbitrary interfragment distances, $X^* < X_{\infty}$, and to define the intermediate populations $P_{\gamma}(j, \nu)$. The corresponding continued channels (γ, j, ν) are denoted with lowercase letters,

with j standing for the local OOO bending and ν for the short O–O bond stretching quantum numbers; the corresponding local eigenstates $\chi_{\gamma j\nu}(Y, Z|X^*)$ have eigenenergies $\epsilon_{\gamma j\nu}(X^*)$. The wave functions $\chi_{\gamma j\nu}$ are calculated at a fixed intermediate distance X^* in the plane (Y, Z) transverse to the reaction path, and the wave function Ψ^{λ} is expanded in terms of the complete set of these eigenstates:

$$\Psi_{\gamma}^{\lambda}(\mathbf{Q}|E_{\text{ph}}) = \sum_{j\nu} f_{\gamma j\nu}(X - X^*) \chi_{\gamma j\nu}(Y, Z|X^*). \quad (15)$$

The functions $\{\chi_{\gamma j\nu}(Y, Z|X^*)\}$ are the local transverse eigenstates, adiabatic in the vibrational and diabatic in the electronic degrees of freedom,³⁸ evaluated as eigenstates of the intermediate Hamiltonian with a fixed value of $X = X^*$. In the limit $X \rightarrow \infty$ they converge to the eigenstates of the free O₂.

The functions $f_{\gamma j\nu}(X - X^*)$ describe the relative motion of the fragments along the reaction coordinate near X^* with the velocity $\dot{X}_{\gamma j\nu}$. They can be used to construct the intermediate T -matrix elements either *via* the expression

$$|T_{\gamma j\nu}(X^*)|^2 = f_{\gamma j\nu}^*(0) \dot{X}_{\gamma j\nu} f_{\gamma j\nu}(0), \quad (16)$$

which is analogous to eqn (13), or *via*

$$|T_{\gamma j\nu}(X^*)|^2 = \text{Re}[f_{\gamma j\nu}^*(0) \hat{v}_X f_{\gamma j\nu}(0)], \quad (17)$$

which is analogous to eqn (14).

This gives the total cross section as a sum of partial components proportional to $|T_{\gamma j\nu}(X^*)|^2$ and thus defines local vibrational populations in the transverse vibrationally adiabatic modes. The absolute squares of the T -matrix elements sum up to the same total absorption cross section for any X^* . Alexander and co-workers used the eqn (17) to define local reactive fluxes.^{37,38} Intermediate distributions in this work are calculated using the eqn (16). In principle, the two definitions lead to different results, because the functions $f_{\gamma j\nu}(X - X^*)$ contain both incoming and outgoing waves and are no longer eigenfunctions of \hat{v}_X . Eqn (17) is more physically sound: Due to flux conservation the reactive flux can be evaluated across arbitrary (closed) surface. On the other hand, the less rigorous eqn (16) is easier to implement within an iterative propagation scheme, because it amounts to calculating only the projection integral

$$\langle \chi_{\gamma j\nu}(Y, Z|X^*) | \delta(X - X^*) | \Psi_{\gamma}^{\lambda}(X; Y, Z|E_{\text{ph}}) \rangle$$

at the analysis line $X = X^*$. The calculation with eqn (17) involves taking the derivative of this integral with respect to X . The distributions obtained using the two expressions are compared in Fig. S3 of the ESI;† they turn out to be nearly indistinguishable. The definition of eqn (16) is also used in Section 5 to relate the T -matrix elements to resonance Raman amplitudes.

In practice, the normalized intermediate distributions in the electronic state γ ,

$$P_{\gamma}(j, \nu) = \frac{1}{\mathcal{N}_{\gamma}} |T_{\gamma j\nu}(E_{\text{ph}}|X^*)|^2 \quad (18)$$

are calculated by overlapping the evolving wave packet with the local projection eigenstates $\chi_{\gamma j\nu}$. The photodissociation matrix elements $T_{\gamma j\nu}$ are calculated as half-Fourier transforms of the

overlaps $C_{\gamma\nu}(t|X_*)$ of the wave packet $\Phi_\gamma(t)$ with the local projection states $\chi_{\gamma\nu}(Y,Z|X_*)$ at the analysis line X_* :

$$C_{\gamma\nu}(t|X_*) = [\chi_{\gamma\nu}|\Phi_\gamma(t)]_{X_*}$$

$$|T_{\gamma\nu}(E_{\text{ph}}|X_*)|^2 = \frac{k_{\gamma\nu}(X_*)}{\mu_X} \left| \int_0^\infty C_{\gamma\nu}(t|X_*) \exp(iE_{\text{ph}}t) dt \right|^2 \quad (19)$$

Here $k_{\gamma\nu}(X_*) = \sqrt{2\mu_X(E_{\text{ph}} - \varepsilon_{\gamma\nu}(X_*))}$ is the local channel momentum. Integration in square brackets $[\cdot]_{X_*}$ is carried out only over the coordinates (Y, Z) at $X = X_*$.

3 Intermediate distributions in photodissociating ozone

Calculations on ozone are performed with the initial state

$$\Phi_0(\mathbf{Q}) = |\mu(\mathbf{Q})|\Psi_X(\mathbf{Q}), \quad (20)$$

which is the wave function of the ground vibrational state of non-rotating ozone in the ground electronic state \tilde{X} , multiplied by the transition dipole moment (TDM) between the states B and \tilde{X} . Such initial state, violating the optical selection rules and corresponding to a $J_i = 0 \rightarrow J_f = 0$ transition, is often used in calculations of absorption spectra and partial cross sections, and it is demonstrated in ref. 15 that this choice does not affect the product states distributions. In the photon energy range studied in this work, $4.5 \text{ eV} < E_{\text{ph}} < 5.5 \text{ eV}$, only the B state can be initially populated (the vertical excitation energy to the R state is $\approx 9 \text{ eV}$). The *ab initio* coordinate dependent TDM components are taken from ref. 39.

The intermediate distributions discussed below are calculated in two steps. First the non-stationary initial state of ozone in the optically bright B state is prepared according to eqn (20). Next, this initial excitation in B is propagated under the influence of the molecular Hamiltonian of eqn (3) describing the motion in the coupled *ab initio* potential energy surfaces B and R. Computational details are given in Section I of the ESI.†

The absolute squares of the *T*-matrix elements are calculated before and after the conical intersection (see Fig. 1), in the dynamically relevant region in which most of the population transfer from B to R takes place (see Section III of the ESI,† for a definition of the intersection region and, in particular, Fig. S1 and S2 (ESI†) showing the intersection topography including the minimum energy intersection).

Vibrational distributions in the short O–O bond stretch describe the energy content of the coupling mode Y and their variation across the B/R intersection is remarkably different in the two electronic states. This is illustrated in panels (b)–(e) and (c′)–(e′) of Fig. 1. The panel (b) shows the local vibrational distribution $P_B(\nu)$ in the B state at $X_* = 3.67a_0$, *i.e.* to the left of the intersection region: The molecule is in the B state, the R state is unpopulated. This intermediate distribution is the ‘initial condition’ for the coupled state dynamics at the conical intersection. It peaks at $\nu = 0$ and rapidly falls off with growing ν : molecules in the B state arrive at the intersection region with only modestly excited short O–O bond. This incident distribution is preserved as ozone moves along the

adiabatic path across the intersection region [panels (c), (d), and (e)]. The only noticeable change with growing O··O₂ separation is a slight cooling off of the high- ν tail adjusting itself to the rising potential energy of the fragments climbing towards the asymptotic singlet channel.

The shape of the incident distribution changes dramatically along the adiabatic path (c′)–(d′)–(e′) across the intersection. Only molecules with substantial excitation in the short O–O bond, sieved out of the tail of the incident distribution, emerge in the R state, and the vibrational distribution inverts in the intersection region and peaks at $\nu \approx 6$ –8. The distance $X_* \approx 4.0a_0$, at which the distribution becomes detectable (*e.g.*, *via* emission to the ground electronic state, see Section 5), approximately marks the location of the conical intersection. The post-intersection R state dynamics broaden this distribution and shift its maximum to higher ν values. The mismatch in the local equilibria of the O₂ moieties in B and R states is negligible and cannot explain the difference in the distributions.

The strongly inverted asymptotic vibrational distributions in the triplet channel (1), exemplified in panel (e′), have been measured in ref. 40 (a detailed comparison between calculated and measured asymptotic vibrational distributions can be found in ref. 15). The above analysis demonstrates that they are formed in the immediate vicinity of the conical intersection. Physically, the distributions are inverted because only the molecules with an over-stretched O–O bond emerge in the R state, following an adiabatic passage through the intersection. R state components of the stationary scattering wave functions, filtered out of the wave packet at fixed photon energies,¹⁵ are peaked close to $Y \approx 2.9a_0$, which is $0.6a_0$ longer than the equilibrium O–O bond length in molecular oxygen.

4 Landau–Zener modelling and reverse engineering of the parameters of a conical intersection

The presented picture is qualitatively consistent with the Landau–Zener estimation: Molecules with a strongly excited high frequency O–O vibration lack translational energy in the tuning O··O₂ mode, spend long time in the intersection region, and make a transition from B to R state with large probability. This has previously been noticed in the Landau–Zener-based surface hopping trajectory calculations performed in ref. 14, 23, and 31. The efficiency with which the O₂ bond is excited is astonishing: The intermediate distributions in panels (b) and (c′) reveal that 6–8 vibrational quanta are transferred to the tuning mode on the adiabatic path, and more than 1.0 eV of vibrational energy is relocated over an interfragment displacement of $\sim 0.5a_0$. This energy has to be compared with the transfer of a single vibrational quantum ($\sim 0.17 \text{ eV}$), commonly expected in models based on the popular linear vibronic coupling Hamiltonian.⁴¹ The origin of the active energy redistribution in the branching space is a strong superlinear dependence of the *ab initio* diabatic coupling element V_{BR} on the O–O bond distance. In a separate numerical experiment, the upper adiabatic surface has been removed from the calculation (see Appendix A). The resulting asymptotic O–O distributions

in the R-channel differ drastically from the above two-state case: They are cold and peak sharply at $\nu = 0$.

The Landau–Zener approach can also serve as a basis for quantitative modelling of the direct dissociation through an exit channel conical intersection.^{16,43–45} Suppose that the system moves in the vicinity of the intersection along a straight line trajectory $X(t) = X_* + \dot{X}_\nu(t - t_*)$ in the B state, and the coupling mode Y and the seam mode Z are in a local quantum state $|\chi_{Bj\nu}\rangle$; the velocity along the tuning mode is $\dot{X}_\nu = \{2(E_{\text{ph}} - \epsilon_{Bj\nu}(X_*))/\mu_X\}^{1/2}$. The average^{24,46} transition probability $w_{j\nu}^{\text{LZ}}(\text{B} \rightarrow \text{R})$ between the diabatic states B and R can be expressed in terms of the local Massey parameter $\xi_{j\nu}(X_*)$,

$$w_{j\nu}^{\text{LZ}}(\text{B} \rightarrow \text{R}) = 1 - \exp(-\xi_{j\nu})$$

$$\xi_{j\nu}(X_*) = \frac{2\pi(V_{\text{BR}}^2)_{j\nu}}{\dot{X}_\nu(\Delta F)_{j\nu}} \quad (21)$$

$\xi_{j\nu}(X_*)$ characterizes the local shape of the intersecting states, probed in the transverse quantum state $|\chi_{Bj\nu}\rangle$ in terms of the two key parameters, namely the expectation values of the diabatic coupling, $(V_{\text{AB}}^2)_{j\nu} = |\chi_{Bj\nu}|V_{\text{AB}}^2|\chi_{Bj\nu}\rangle_X$, and the difference of slopes of the diabatic potentials along X , $(\Delta F)_{j\nu} = |\chi_{Bj\nu}|\Delta F|\chi_{Bj\nu}\rangle_X$. Small

$\xi_{j\nu} \rightarrow 0$ implies small transition probability $w_{j\nu}^{\text{LZ}}(\text{B} \rightarrow \text{R})$; dissociating molecules tend to stay in the diabatic B state as they pass through the conical intersection. Large $\xi_{j\nu}$ corresponds to larger $w_{j\nu}^{\text{LZ}}(\text{B} \rightarrow \text{R})$, with more molecules diverted into the R state and dissociating adiabatically.

Estimates, based on the ‘diagonal’ (in j and ν) state-averaged Landau–Zener model of eqn (21), are remarkably accurate for ozone. For example, the population of the R state, evaluated near the conical intersection at $X_* = 3.9a_0$ as a sum of all Landau–Zener transition probabilities $\sum_j 1 - \exp(-\xi_{j\nu})$, amounts to 0.040; the quantum mechanical value is 0.035 (the cited yields are for $E_{\text{ph}} = 4.96$ eV). Another example is provided by the inverted vibrational distributions in the local O–O vibration in the R state. Their Landau–Zener counterparts are given by a convolution of the transition probability with the incident distribution $P_{\text{B}}(j, \nu)$ in the B state:

$$P_{\text{R}}^{\text{LZ}}(\nu) = \sum_j w_{j\nu}^{\text{LZ}}(\text{B} \rightarrow \text{R})P_{\text{B}}(j, \nu). \quad (22)$$

The ν dependence of $P_{\text{B}}(j, \nu)$ is shown in panel (a) of Fig. 2, and the Landau–Zener approximation $P_{\text{R}}^{\text{LZ}}(\nu)$ is compared with the quantum

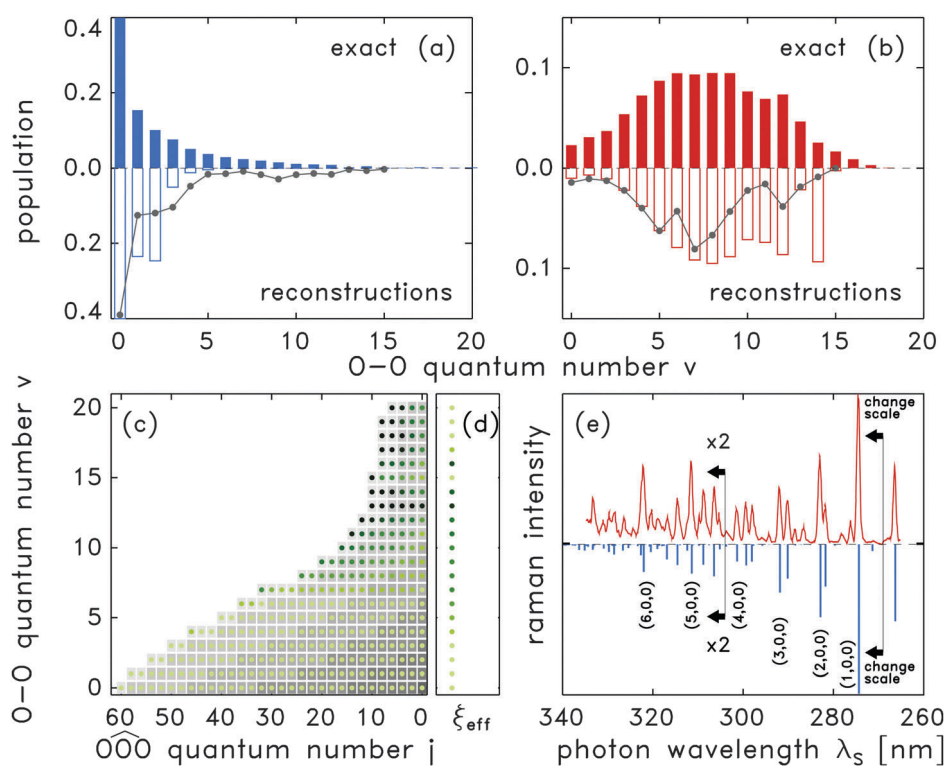


Fig. 2 (a) The normalized quantum vibrational distribution in the short O–O bond stretch in the B state evaluated at $X_* = 3.9a_0$ (filled histograms). The same distribution reconstructed from the emission amplitudes α_{k0}^{B} into the bound states of \tilde{X} is shown with empty histograms. Gray line depicts the reconstruction including emission into both bound and continuum states of \tilde{X} . (b) The normalized quantum vibrational distribution in the short O–O bond stretch in the R state evaluated at $X_* = 3.9a_0$ (filled histograms). The same distribution reconstructed using the Landau–Zener eqn (22) is shown with empty histograms. Gray line depicts the reconstruction based on the emission amplitudes α_{k0}^{B} into both bound and continuum states of \tilde{X} . (c) Two dimensional map of the Massey parameter $\xi_{j\nu}(X_*)$ at $X_* = 3.9a_0$ in the plane of the local quantum numbers ν and j ; light green color corresponds to $\xi_{j\nu} \leq 0.05$, black marks $\xi_{j\nu} \geq 1.40$. The respective translational energies in the B state are shown with gray shading (light gray for $E_{\text{trans}} \leq 0.15$ eV; dark gray for $E_{\text{trans}} \geq 2.00$ eV). (d) The Massey parameter $\xi_{\text{eff}}(\nu)$ as a function of ν calculated from the quantum distributions in (a) and (b) (filled histograms) using eqn (23). The photon energy in panels (a–d) is $E = 5.49$ eV (the photolysis wavelength $\lambda = 226$ nm). (e) Experimental (red) and calculated (blue) photoemission spectrum of ozone photoexcited at 266 nm as function of the scattered photon wavelength λ_s . The experimental emission spectrum is redrawn from Fig. 1 of ref. 42. The intensities of the first and the third calculated peaks are set equal to their experimental counterparts. Pure symmetric stretch excitations in \tilde{X} are assigned.

intermediate distribution at $X_* = 3.9a_0$ in panel (b). The agreement is good for $\nu \leq 13$; higher vibrational quantum numbers are weakly populated in the incident distribution and the reconstruction becomes less accurate. Extensions of the LZ model, which include non-diagonal matrix elements $j \rightarrow j'$ and $\nu \rightarrow \nu'$, are discussed in Section IV of ESL.[†]

The local Massey parameter $\xi_{j\nu}(X_*)$ links the shape of the potentials near the conical intersection with the intermediate distributions in the local transverse modes. The dependence of $\xi_{j\nu}(X_*)$ on the quantum numbers j and ν , shown in Fig. 2(c) for $X_* = 3.9a_0$, can be regarded as a two dimensional dynamical map of the intersection as seen by the separating fragments. Each (j, ν) state is colored according to the value of the Massey parameter; the underlying gray shading shows the corresponding translational energy along X , $E_{\text{trans}} = \mu_X \dot{X}_{j\nu}^2/2$; the fastest fragments are located near the origin ($j = 0, \nu = 0$), and E_{trans} decreases as one moves towards the outer edge of the two dimensional map. As expected, $\xi_{j\nu}(X_*)$ gradually increases with decreasing E_{trans} and with growing vibrational excitation: The dot color is generally darker at the outer edge than near the origin. However, the Massey parameter is influenced by the local stretch and bend differently. The impact of the short O–O bond quantum number is strong, and $\xi_{j\nu}$, as well as the transition probability $w_{j\nu}^{\text{LZ}}(\text{B} \rightarrow \text{R})$, quickly grow with ν ; as one moves along the ν axis, the dot color noticeably darkens. The reason is the simultaneous growth of the coupling strength $(V_{\text{AB}})_{j\nu}$ and the decrease of the velocity $\dot{X}_{j\nu}$. In contrast, $\xi_{j\nu}(X_*)$ is only weakly dependent on the bending quantum number j , and the dot color barely changes along the j axis: the coupling strength is approximately independent of the seam coordinate Z and the Landau–Zener transition probability is mainly determined in the branching space rather than in the seam space. In the coordinate space (Y, Z) , the energy difference between adiabatic states near conical intersection follows a similar pattern: It depends strongly on the coupling mode Y and is independent of the seam mode Z . The influence of the gradient factor in the local Massey parameter on the transition probability appears to be far weaker than the influence of either the coupling or the velocity factors. This is further illustrated in Appendix A which shows that the coupling mode gradient of the lower adiabatic surface is insufficient to create an inverted vibrational distribution along the adiabatic path.

Extraction of Massey parameter is equivalent to mapping out the key topographic characteristics of a conical intersection, and this task can be accomplished using the Landau–Zener relation (22) between the incident, $P_{\text{B}}(j, \nu)$, and the transmitted, $P_{\text{R}}(\nu)$, distributions. Because $\xi_{j\nu}$ is nearly independent of the seam quantum number j , the sum over j on the right-hand side of eqn (22) can be evaluated, giving the incident distribution $P_{\text{B}}(\nu)$ in the O–O stretch shown in Fig. 2(a). The equation can now be inverted to give the effective Massey parameter in terms of the two intermediate distributions:

$$\xi_{\text{eff}}(\nu) = -\ln\left(1 - \frac{P_{\text{R}}(\nu)}{P_{\text{B}}(\nu)}\right) \quad (23)$$

In Fig. 2(d), the approximate Massey parameter $\xi_{\text{eff}}(\nu)$ is reconstructed from the quantum mechanical intermediate distributions

in panels (a) and (b) as a function of ν . The agreement with the ν dependence of $\xi_{j\nu}$ in panel (c) is fair for $\nu \leq 15$; for larger ν the B state population is very small and eqn (23) becomes unreliable. Thus, an ‘experiment’ detecting intermediate vibrational distributions in the coupling mode Y is capable of delivering the effective Massey parameter for the nearby conical intersection.

5 Intermediate distributions from the Raman emission amplitudes

Emission spectroscopy^{16,47} might be potentially applicable to detection of the intermediate distributions of interacting photofragments. The cross correlation function $C_{\gamma j\nu}(t|X_*)$ in eqn (19) can be represented as a full-space overlap integral,

$$C_{\gamma j\nu}(t|X_*) = \langle \chi_{\gamma j\nu}(Y, Z|X_*) g(X - X_*) | \Phi_{\gamma}(t) \rangle, \quad (24)$$

of the wave packet $\Phi_{\gamma}(t)$, moving on the electronic surface γ , with the projection state $\chi_{\gamma j\nu}(Y, Z|X_*) g(X - X_*)$. Integration in angular brackets $\langle \cdot | \cdot \rangle$ is carried out over all three coordinates (X, Y, Z) ; $g(X - X_*)$ is a function localized near X_* . Strictly speaking, $g(X - X_*)$ is a delta function $\delta(X - X_*)$ [see eqn (19)], but in practical calculations any function sufficiently localized around $X = X_*$ will lead to a similar $C_{\gamma j\nu}(t|X_*)$. Now the cross correlation function—and consequently the intermediate distributions—can be expressed in terms of the resonance Raman amplitudes⁴⁸

$$\alpha_{k0}^{\gamma}(E_{\text{ph}}) = \int_0^{\infty} \langle \phi_k | \Phi_{\gamma}(t) \rangle \exp(iE_{\text{ph}}t) dt \quad (25)$$

for emission into the vibrational states ϕ_k of the ground electronic states \tilde{X} . This is achieved by expanding the localized projection state in terms of complete set of bound states ϕ_k ,

$$\chi_{\gamma j\nu}(Y, Z|X_*) g(X - X_*) \approx \sum_k a_k^{\gamma}(X_*) \phi_k(X, Y, Z) \quad (26)$$

With this expansion, the cross correlation function $C_{\gamma j\nu}(t|X_*)$ in eqn (24) and the T -matrix elements in eqn (19) become linear combinations of α_{k0}^{γ} :

$$\begin{aligned} |T_{\gamma j\nu}(E_{\text{ph}}|X_*)|^2 &= \frac{k_{\gamma j\nu}(X_*)}{\mu_X} \left| \int_0^{\infty} C_{\gamma j\nu}(t|X_*) e^{iE_{\text{ph}}t} dt \right|^2 \\ &= \frac{k_{\gamma j\nu}(X_*)}{\mu_X} \left| \sum_k \int_0^{\infty} \langle \chi_{\gamma j\nu} g | \phi_k \rangle \langle \phi_k | \Phi_{\gamma}(t) \rangle e^{iE_{\text{ph}}t} dt \right|^2 \\ &= \frac{k_{\gamma j\nu}(X_*)}{\mu_X} \left| \sum_k (a_k^{\gamma}(X_*))^* \alpha_{k0}^{\gamma}(E_{\text{ph}}) \right|^2. \end{aligned} \quad (27)$$

In order to elicit the accuracy of eqn (27), a complete set $\{\phi_k\}$ of about 250 bound vibrational states in one potential well of the \tilde{X} state is calculated. For these states, the complex Raman amplitudes α_{k0}^{γ} are evaluated for ozone dissociating in the coupled B and R states. Technical details of these calculations are summarized in Appendix B. The emission spectrum $\sigma_{\text{ram}}(E_{\text{ph}}, E_{\text{S}}) \sim E_{\text{ph}} E_{\text{S}}^3 \sum_k |\alpha_{k0}^{\text{B}} + \alpha_{k0}^{\text{R}}|^2 \delta(E_{\text{S}} - E_k)$, for the

incident photon wavelength of 266 nm ($E_{\text{ph}} = 4.66$ eV) is compared with the experimental spectrum of ref. 42 in Fig. 2(e). The calculated spectrum stems mainly from the B state, agrees with experiment over a broad range of scattered photon wavelengths λ_s , and quantitatively reproduces the rapidly decreasing intensity with growing λ_s , the multiplet structure of the emission, and the intensity patterns within multiplets. In particular, the enhanced emission intensity into pure symmetric stretch overtones in \tilde{X} is excellently reproduced. This is the first calculated spectrum demonstrating a one-to-one comparison in the measured emission band intensities up to $\lambda_s = 320$ nm and it clearly points out the emission lines stemming directly from the molecule undergoing an ultrafast dissociation on the time scale of 200 fs. The basis set $\{\phi_k\}$ in \tilde{X} is next used to represent the projection states and to calculate the expansion coefficients $a_k^{\tilde{X}}(X^*)$. The function $g(X - X^*)$ in the projection states is chosen as a rectangle $X^* - 0.1a_0 \leq X \leq X^* + 0.1a_0$ localized at $X^* = 3.9a_0$. Finally, the amplitudes $\alpha_{k0}^{\tilde{X}}$ and the coefficients $a_k^{\tilde{X}}(X^*)$ are used in eqn (27) to calculate the intermediate distributions.

The O–O vibrational distribution in the B state, reconstructed from the Raman amplitudes α_{k0}^{B} , is shown in Fig. 2(a) with empty histograms. The exact quantum mechanical distribution peaking at $\nu = 0$ is clearly well reproduced. The very long- ν tail of the distribution is missing because most of the bound states $\{\phi_k\}$ capable of representing the corresponding projection states do not extend to large interfragment distances of $X^* = 3.9a_0$.

Detection of emission from the R state and converting it into intermediate vibrational distributions along the electronically adiabatic path is required in order to locate the intersection along the tuning mode¹⁶ and to characterize its shape. However, both the detection and the conversion steps are challenging. Indeed, the emission is strongly quenched, because the dipole moment of the $\tilde{X} \leftarrow \text{R}$ transition (~ 0.04 D) is much smaller than that for the B state, and $|\alpha_{k0}^{\text{R}}| \ll |\alpha_{k0}^{\text{B}}|$ (however, the polarization directions of the emitted photons in the two transitions are orthogonal, see Appendix B). Moreover, the R state is purely repulsive, and the corresponding molecular eigenstates are scattering states with vanishing amplitude at small interfragment distances. As a result, most of the R state emission is into the dissociation continuum of the \tilde{X} state (the so-called wing emission⁴⁹). The R state distributions can therefore be reliably calculated only from the continuum part of the emission spectrum. We illustrate this point by augmenting the bound basis $\{\phi_k\}$ with $\sim 10^5$ scattering states spanning a 2.5 eV wide energy range above the first dissociation threshold of \tilde{X} . Most of the emission from the R state falls into this energy interval. The quasi-continuum basis functions are constructed as products of the asymptotic fragment eigenstates and the X -dependent functions as described in Appendix B.

The O–O vibrational distribution in the R state, reconstructed using both bound and scattering states, is shown in Fig. 2(b) with a gray solid line. The reconstruction properly captures the overall shape of the exact quantum mechanical distribution and the extent of the O–O bond excitation. It is worth noting that the main effect of the scattering quasi-

continuum on the reconstructed distribution in the B state in Fig. 2(a) is to slightly enhance the population in the high- ν tail bringing it in a better agreement with the exact result.

6 Conclusions

In this paper, we investigate a reactive exit channel conical intersection in the UV photodissociation of ozone, in which the tuning mode X is aligned along the reaction coordinate. Two findings emerge from the exact quantum mechanical calculations combined with a Landau–Zener type analysis of the interacting photofragments:

1. Intermediate vibrational distributions in the ‘transverse’ coupling mode Y allow one to reverse engineer the local Massey parameter and to delineate the key parameters of the intersection in the branching space. The unique structural information about the shape of the conical intersection carried by the intermediate distributions is mapped out in the framework of a three-dimensional Landau–Zener model. For ozone, the intermediate distributions in the O–O vibration become strongly inverted as the molecule crosses the intersection adiabatically, and more than 1.0 eV of vibrational energy is transferred into the coupling mode.

2. Intermediate distributions can be reconstructed from the emission spectra of the two intersecting states. For ozone, the resonance Raman spectrum quantitatively agreeing with experiment has been calculated for the first time. A complete set of Raman amplitudes is then used to evaluate the O–O vibrational distributions near conical intersection. Reconstruction of intermediate distributions in the repulsive dark R state, populated *via* non-adiabatic transitions in the exit channel, requires the continuum wing emission to be taken into account.

Appendix A product state distributions on a single adiabatic potential energy surface

In this Appendix, a single adiabatic state calculation for the photodissociation in the triplet dissociation channel is described. The final vibrational state distributions are calculated using the lower adiabatic potential

$$V_{\text{ad}}(X, Y, Z) = \frac{V_{\text{B}} + V_{\text{R}}}{2} - \sqrt{\left(\frac{V_{\text{B}} - V_{\text{R}}}{2}\right)^2 + V_{\text{BR}}^2}.$$

A cut through this potential along X is shown in Fig. 4 (thick blue and red lines). The simulation allows one to separate the impact of the topology of the lower adiabatic potential energy surface and the impact of the two state dynamics on the shape of the vibrational distributions in the triplet channel. The one-state calculation is performed using the same settings and the same initial state as those in the two-state calculation.

The final vibrational state distributions are calculated using eqn (13) and the populations for $E_{\text{ph}} = 5.49$ eV are given in Fig. 3

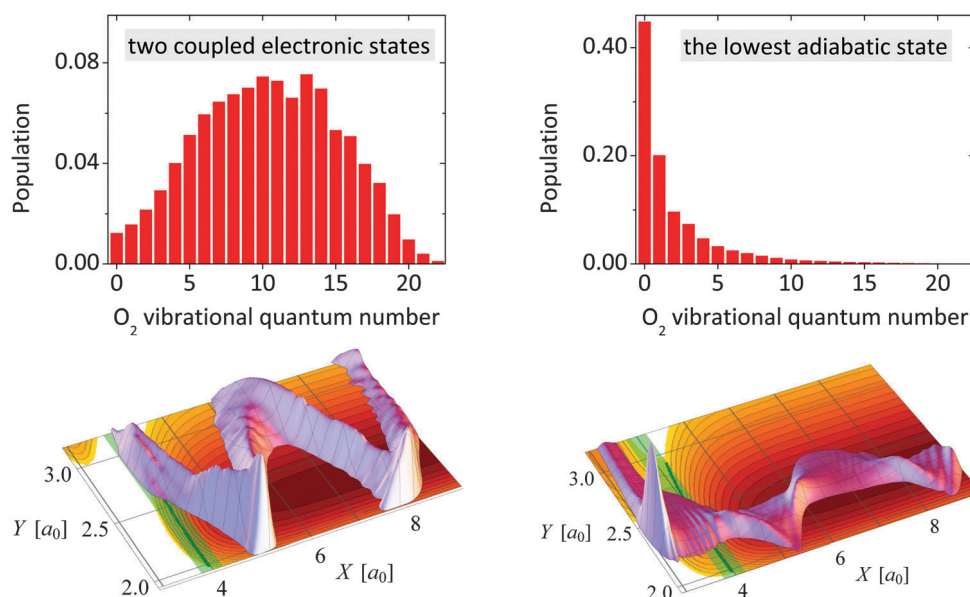


Fig. 3 Final vibrational state distribution in the R channel for $E_{\text{ph}} = 5.49$ eV: (left panel) the two-state system (full Hamiltonian); (right panel) arising from the dynamics on the lower adiabatic potential energy surface (single state Hamiltonian). The bottom panels show the squares of the energy components of the wave packets in the (X, Y) -plane, integrated over Z .

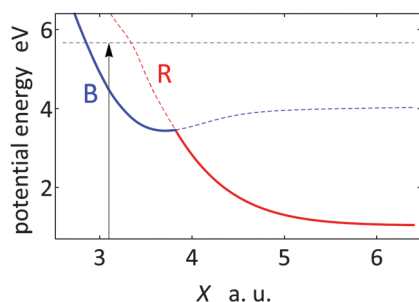


Fig. 4 Cut of the adiabatic potentials along the dissociation coordinate X . The coordinates (Y, Z) are fixed to the minimum of the diabatic B state. The lower adiabatic potential, used in the one-state calculation is marked with a thick line (blue for $X < X_{\text{Cl}}$, red for $X > X_{\text{Cl}}$). It is close to V_{B} (blue) at short distances and to V_{R} (red) at long distances. The dashed black line indicates the energy corresponding to the excitation with $\lambda = 226$ nm, for which the final vibrational distribution is shown in Fig. 3.

(top-right panel). The corresponding populations in the two-state problem are shown in the top-left panel. As discussed in the main text, this distribution, created in the $\text{B} \rightarrow \text{R}$ transition, is vibrationally hot, peaking around $V \approx 10\text{--}13$. On the contrary, the distribution calculated using the lower adiabatic state has a maximum at $V = 0$, and the population decreases quickly with increasing V , resembling the distribution on the B channel in the two-state problem.

Fixed energy components of the wave packets are shown in the lower panels of Fig. 3 for the one-state (right panel) and the two-state (left panel) calculations. They illustrate a dramatic change which the photodissociation dynamics in the R channel undergoes upon removing the upper electronic state. In particular, the large amplitude vibrations of the emerging molecular fragment are completely suppressed in the one-state calculation.

Appendix B calculation of the Raman spectrum and reconstruction of the intermediate distributions

The resonance Raman amplitudes $\alpha_{k_0}^{\gamma}$ (or: elements of the molecular polarizability tensor) for the emission from an electronic state γ into the vibrational states $\{\phi_k(\mathbf{Q})\}$ of the ground electronic states $\tilde{\text{X}}$ are given by half-Fourier transforms of the cross correlation functions of the evolving wave packet $\Phi_{\gamma}(t)$ with the functions ϕ_k via eqn (25). The emission of a (scattered) photon with energy E_{S} follows the absorption from the vibrational ground state of $\tilde{\text{X}}$ at a fixed incident photon energy E_{ph} ; such emission spectrum was measured in the experiments of Kinsey and co-workers.⁴² This spectrum is efficiently simulated using the stationary energy component $\Psi^{\gamma}(\mathbf{Q}|E_{\text{ph}})$ [eqn (6)], which in the present context is often referred to as a Raman wave function. With $\Psi^{\gamma}(\mathbf{Q}|E_{\text{ph}})$, the emission amplitudes are given by the overlap⁵⁰

$$\alpha_{k_0}^{\gamma}(E_{\text{ph}}, E_{\text{S}}) = \langle \phi_k | \Psi_{\gamma}^{\gamma}(E_{\text{ph}}) \rangle. \quad (28)$$

The ingredients leading to the emission amplitudes of eqn (28) include (a) the function $\Psi_{\gamma}^{\gamma}(E_{\text{ph}})$, (b) the basis states $\{\phi_k(\mathbf{Q})\}$, and (c) the transition dipole moments (TDMs) $\mu_{\text{B}\tilde{\text{X}}}$ and $\mu_{\text{R}\tilde{\text{X}}}$ between the $\tilde{\text{X}}$ state and the B and R states, respectively. Raman wavefunctions (see for example Fig. 3, bottom-left panel) are briefly discussed in the ESI.† The items (b) and (c) are discussed below.

Note that the emission spectrum $\sigma_{\text{ram}}^{\gamma} \sim \sum_k |\alpha_{k_0}^{\gamma}(E_{\text{ph}}, E_{\text{S}})|^2 \delta(E_k - E_{\text{S}})$ can be evaluated⁵⁰ as a Fourier transform of the autocorrelation function generated via a propagation of $\Psi_{\gamma}^{\gamma}(E_{\text{ph}})$ in the ground electronic state $\tilde{\text{X}}$ with the Hamiltonian $\hat{H}_{\tilde{\text{X}}}$:

$$\sigma_{\text{ram}}^{\gamma}(E_{\text{ph}}, E_{\text{S}}) \sim E_{\text{ph}} E_{\text{S}}^3 \int_0^{\infty} \left\langle \Psi_{\gamma}^{\gamma} \left| e^{-i\hat{H}_{\tilde{\text{X}}}t} \right| \Psi_{\gamma}^{\gamma} \right\rangle e^{i(E_{\text{ph}} - E_{\text{S}})t} dt. \quad (29)$$

An explicit construction of the basis states $\{\phi_k\}$ can be avoided in this case.

B.1 Basis states in the ground electronic state

The vibrational basis states $\{\phi_k(\mathbf{Q})\}$ have been calculated using the potential energy surface of the ground electronic state as described in the ESI.† All calculated eigenstates were either symmetric or antisymmetric with respect to the interchange of the two end atoms. A total of 244 states (138 symmetric and 106 antisymmetric states) were found.

Transitions terminating on the bound states $\{\phi_k\}$ constitute the main part of the emission spectrum of ozone dissociating in the B state. In order to calculate the contribution to the emission spectrum from the R state, the set $\{\phi_k\}$ has to be augmented with the continuum basis states $\{\phi_n^-(E_S)\}$ lying above the ground-state dissociation threshold. Indeed, the R state is purely repulsive, and the corresponding molecular eigenstates, populated from the B state at relatively large interfragment distances near the conical intersection, are scattering states with vanishing amplitude at small interfragment distances. Under these circumstances, the wing emission into the dissociation continuum of the \tilde{X} state is expected to be dominant. In many molecules, the wing emission corresponds to a broad featureless spectral region.⁴⁹ In ozone, emission into relatively narrow resonance states lying *ca.* 0.25 eV above the dissociation threshold has also been observed.⁵¹

In order to illustrate the shape of the wing emission from the R state, scattering basis states $\phi_n^-(E_S)$ in \tilde{X} are constructed in Jacobi coordinates (X, Y, Z) in a given arrangement dissociation channel. For each scattered photon energy E_S (*i.e.*, for each energy in the \tilde{X} state $E_{\tilde{X}} = E_{\text{ph}} - E_S$), approximate basis states are constructed as products of X - and (Y, Z) -dependent functions. The (Y, Z) -dependent factor is a rovibrational state $\chi_n(Y, Z)$ of the $\text{O}_2(^3\Sigma_g^-)$ fragment with energy ε_n . The X -dependent factor is a scattering solution of a one-dimensional Schrödinger equation, with an effective vibrationally adiabatic potential, for the translational energy $E_{\text{trans}} = k_n^2/2\mu_X = E_{\tilde{X}} - \varepsilon_n$. Although this procedure produces distorted wave functions, it gives a large (and ideally a complete) set of both resonance and purely scattering basis states.⁵² The energies E_S form an equidistant grid of 500 points in the energy interval [2.0–5.0] eV; for each E_S , all open channels are included. This results in about 100 000 mutually orthogonal scattering basis states. The spectra shown below demonstrate that most of the emission from the R state falls into the chosen energy window.

B.2 Ab initio transition dipole moments

The TDM $|\mu_{B\tilde{X}}|$ between B and \tilde{X} is a spline interpolation of the *ab initio* data of ref. 39. The TDM $\mu_{R\tilde{X}}$ between R and \tilde{X} has been calculated with an AVTZ basis set of Dunning at the CASSCF level of theory over a range of bond distances covering a broad vicinity of the conical intersection. It is shown in Fig. 5 as a function of one O–O bond length. In the spectral calculations, it is set to a constant value of $\mu_{R\tilde{X}} = 0.02$ a.u.

Near the conical intersection, the TDM $\mu_{B\tilde{X}}$ is close to 0.06 a.u. which is three times larger than $\mu_{R\tilde{X}}$, implying that the molecules staying in the B state and following the diabatic

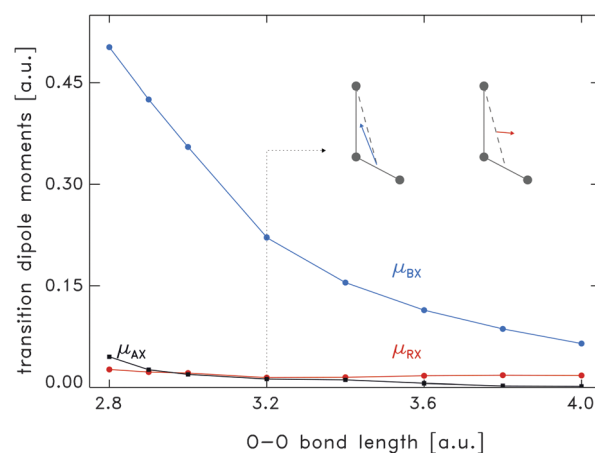


Fig. 5 Diabatic transition dipole moments of the three lowest singlet excited states with the ground electronic state \tilde{X} shown as functions of one O–O bond distance. The other bond distance is fixed at $2.30a_0$ and the valence angle is fixed at 117° . The diabatic states are labelled B, R, and A. Two molecular diagrams illustrate the direction of the TDM vectors for the B state (blue) and the R state (red) for the bond distance of $3.2a_0$, close to the B/R conical intersection. The dashed line in the two diagrams is the Jacobi distance X , *i.e.* the dissociation coordinate.

path through the intersection dominates the emission spectrum. At the same time, photons emitted from the two states have different polarizations. Indeed, although both B and R states are of A' symmetry and their TDM vectors lie in the molecular plane, the directions of the vectors $\mu_{B\tilde{X}}$ and $\mu_{R\tilde{X}}$ in this plane are different (see Fig. 5). For the B state, the vector $\mu_{B\tilde{X}}$ is mainly aligned along the dissociation coordinate X . For the R state, the vector $\mu_{R\tilde{X}}$ is essentially perpendicular to the dissociation direction. Thus, the emission along the diabatic path (B state) is parallel whereas the adiabatic path (R state) produces photons *via* a perpendicular TDM. The situation turns out to be similar to that encountered in the photodissociation of CH_3I .¹⁶

We note in passing that the photofragments heading into the diabatic and the adiabatic dissociation channels can also be distinguished by the anisotropy parameters⁵³ β of their intermediate angular distributions. A large positive β is expected for the OOO_2 complexes moving diabatically in the B state, while a substantially reduced or even negative β is expected for fragments dissociating along the adiabatic path. These expectations are actually confirmed by the direct quantum mechanical calculations of rotating ozone.¹⁵

B.3 Raman spectra

The photoemission spectra of the B state, $\sigma_{\text{ram}}^B(E_{\text{ph}}, E_S) \sim E_{\text{ph}} E_S^3 \sum_k |\alpha_{k0}^B|^2 \delta(E_S - E_k)$, for the excitation wavelengths $\lambda_1 = 266$ nm and $\lambda_1 = 226$ nm are shown in Fig. 2(e) and 6(a), respectively, as function of the scattered photon wavelength λ_s .

There is no published experimental spectrum at this wavelength; comparison with experiment is made for $\lambda_1 = 266$ nm in Fig. 2. The overall structure of the emission is similar for these two excitation wavelengths. Characteristic are the quick decrease of the emission intensity with growing λ_s , as the

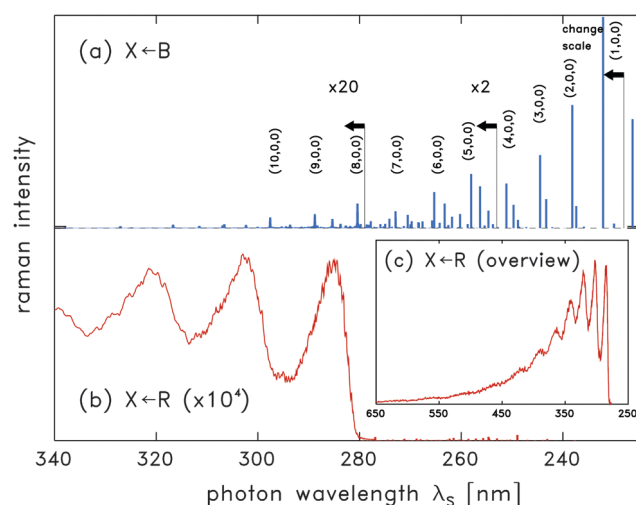


Fig. 6 The calculated photoemission spectrum of ozone photoexcited at 226 nm as function of the scattered photon wavelength λ_s . (a) Emission from the B state. The intensities of the first and the third calculated peaks are scaled as in Fig. 2 of the main article. The wavelength at which the intensities are multiplied by a factor of 20 marks the position of dissociation threshold in \tilde{X} ($\lambda_s \geq 280$ nm). Pure symmetric stretch excitations are assigned below and above dissociation threshold. (b) Emission from the R state. The emission intensity is 10^4 times weaker than that from the B state. Panel (c) shows the R state emission over a much broader wavelength interval of $230 \text{ nm} \leq \lambda_s \leq 650 \text{ nm}$.

progressively more excited vibrational states of the ground-state ozone are reached, and the polyad structure of the emission spectrum, with the intensity noticeably enhanced for the pure symmetric stretch excitations in \tilde{X} . The contribution of wing emission, observed above the dissociation threshold of the \tilde{X} state for $\lambda_s \geq 280$ nm, is small for the B state. However, a progression of narrow resonance states can be clearly isolated in the calculated emission spectrum for $\lambda_s \geq 280$ nm. Their wave functions correspond to pure symmetric stretch excitations and are assigned (8,0,0), (9,0,0), and (10,0,0) in Fig. 6(a). A quantitatively similar above-threshold emission progression has been detected in ref. 51 for $\lambda_1 = 266$ nm.

The photoemission spectrum for the R state, $\sigma_{\text{ram}}^{\text{R}}(E_{\text{ph}}, E_{\text{S}}) \sim E_{\text{ph}} E_{\text{S}}^3 \sum_k |\alpha_{k0}^{\text{R}}|^2 \delta(E_{\text{S}} - E_k)$, is shown in panel (b). Two features distinguish it from the emission from the B state. First, the R-state emission is about 10^4 times weaker than the B-state emission. This is partly because of difference in the TDMs for the two states and partly because the R state is populated only *via* non-adiabatic transitions from the B state; the non-adiabatic transition probability lies below 10% at this E_{ph} . Second, the dependence of the R-state emission intensity on λ_s is very different from that observed for the B state and has a pronounced threshold. There is essentially no emission into the bound states, and the intensity abruptly rises by about two orders of magnitude as the dissociation threshold of \tilde{X} is crossed. The emission maximum is reached approximately 0.5 eV above threshold, but a structured emission tale extends far into the visible range up to $\lambda_s \approx 600$ nm (see panel (c) of Fig. 6). The present calculations predict that the long wavelength

limit of the emission spectrum of ozone is dominated by the R state emission.

Acknowledgements

Financial support by the Deutsche Forschungsgemeinschaft is gratefully acknowledged. The authors would like to thank P. Houston for advice and a careful reading of the manuscript, W. Domcke for numerous discussions of the dynamics at conical intersections, and A. R. Ravishankara for a thought provoking discussion on the emission spectrum of the photodissociating ozone.

References

- 1 *Conical Intersections*, ed. W. Domcke, D. R. Yarkony and H. Köppel, World Scientific, Singapore, 2012.
- 2 B. G. Levine and T. J. Martinez, *Annu. Rev. Phys. Chem.*, 2007, **58**, 613.
- 3 N. J. Turro, V. Ramamurthy and V. C. Scaiano, *Principles of Molecular Photochemistry: An Introduction*, University Science Books, USA, 2000.
- 4 H. J. Worner, J. B. Bertrand, B. Fabre, J. Higuette, H. Ruf, A. Dubrouil, S. Patchkovskii, M. Spanner, Y. Mairesse, V. Blanchet, E. Mevel, E. Constant, P. B. Corkum and D. M. Villeneuve, *Science*, 2011, **334**, 208.
- 5 J. Krčmář, M. F. Gelin, D. Egorova and W. Domcke, *J. Phys. B: At., Mol. Opt. Phys.*, 2014, **47**, 124019.
- 6 D. Polli, P. Altoe, O. Weingart, K. M. Spillane, C. Manzoni, D. Brida, G. Tomasello, G. Orlandi, P. Kukura, R. A. Mathies, M. Garavelli and G. Cerullo, *Nature*, 2010, **467**, 440.
- 7 J. S. Lim and S. K. Kim, *Nat. Chem.*, 2010, **2**, 627.
- 8 The impact of motion in the seam space on the rate of a non-adiabatic reaction is discussed in the review by M. Robb in ref. 1 (p. 3), where several examples of the reaction coordinate running parallel to the intersection seam are considered.
- 9 M. N. R. Ashfold, G. A. King, D. Murdock, M. G. D. Nix, T. A. A. Oliver and A. G. Sage, *Phys. Chem. Chem. Phys.*, 2010, **12**, 1218.
- 10 M. L. Hause, Y. H. Yoon, A. S. Case and F. F. Crim, *J. Chem. Phys.*, 2008, **128**, 104307.
- 11 M. N. Daud, G. G. Balint-Kurti and A. Brown, *J. Chem. Phys.*, 2005, **122**, 054305.
- 12 S. Yu. Grebenshchikov, *J. Chem. Phys.*, 2013, **138**, 224106.
- 13 S. Yu. Grebenshchikov, *J. Chem. Phys.*, 2013, **138**, 224107.
- 14 S. Yu. Grebenshchikov, Z.-W. Qu, H. Zhu and R. Schinke, *Phys. Chem. Chem. Phys.*, 2007, **9**, 2044.
- 15 D. Picconi and S. Yu. Grebenshchikov, *J. Chem. Phys.*, 2014, **141**, 074311.
- 16 K. Q. Lao, M. D. Person, P. Xayariboun and L. J. Butler, *J. Chem. Phys.*, 1990, **92**, 823.
- 17 Y.-J. Jung, M. S. Park, Y. S. Kim, K.-H. Jung and H.-R. Volpp, *J. Chem. Phys.*, 1999, **111**, 4005.
- 18 R. de Nalda, J. Durá, A. García-Vela, J. G. Izquierdo, J. González-Vázquez and L. Banares, *J. Chem. Phys.*, 2008, **128**, 244309.

- 19 C. R. Evenhuis and U. Manthe, *J. Phys. Chem. A*, 2011, **115**, 5992.
- 20 A. L. Sobolewski, W. Domcke, C. Dedonder-Lardeux and C. Jouvet, *Phys. Chem. Chem. Phys.*, 2002, **4**, 1093.
- 21 A. S. Chatterley, J. D. Young, D. Townsend, J. M. Zurek, M. J. Paterson, G. M. Roberts and V. G. Stavros, *Phys. Chem. Chem. Phys.*, 2013, **15**, 6879.
- 22 L. D. Landau and E. M. Lifshitz, *Quantum Mechanics. Non-relativistic Theory*, Pergamon, New York, 1976.
- 23 Z.-W. Qu, H. Zhu, S. Yu. Grebenshchikov and R. Schinke, *J. Chem. Phys.*, 2005, **122**, 191102.
- 24 E. Teller, *J. Phys. Chem.*, 1937, **41**, 109.
- 25 A. L. Devine, M. G. D. Nix, R. N. Dixon and M. N. R. Ashfold, *J. Phys. Chem. A*, 2008, **112**, 9563.
- 26 Y.-T. W. S. Yan and K. Liu, *Proc. Natl. Acad. Sci. U. S. A.*, 2008, **105**, 12667.
- 27 A. R. Ravishankara, G. Hancock, M. Kawasaki and Y. Matsumi, *Science*, 1998, **280**, 60.
- 28 P. J. Hay, R. T. Pack, R. B. Walker and E. J. Heller, *J. Phys. Chem.*, 1982, **86**, 862.
- 29 Y. Matsumi and M. Kawasaki, *Chem. Rev.*, 2003, **103**, 4767.
- 30 S. Yu. Grebenshchikov and S. Rosenwaks, *J. Phys. Chem. A*, 2010, **114**, 9809.
- 31 R. Schinke and G. C. McBane, *J. Chem. Phys.*, 2010, **132**, 044305.
- 32 B. R. Johnson, B. Chang, C. Hsiao, L. Le and J. L. Kinsey, *J. Chem. Phys.*, 1998, **108**, 7670.
- 33 H. Köppel, in *Conical Intersections*, ed. W. Domcke, D. R. Yarkony and H. Köppel, World Scientific, Singapore, 2004.
- 34 J. Zhang, *Theory and Application of Quantum Molecular Dynamics*, World Scientific, Singapore, 1999.
- 35 G. G. Balint-Kurti, R. N. Dixon and C. C. Marston, *J. Chem. Soc., Faraday Trans.*, 1990, **86**, 1741.
- 36 G. G. Balint-Kurti, *Adv. Chem. Phys.*, 2004, **128**, 249.
- 37 D. E. Manolopoulos and M. H. Alexander, *J. Chem. Phys.*, 1992, **97**, 2527.
- 38 M. H. Alexander, C. Rist and D. E. Manolopoulos, *J. Chem. Phys.*, 1992, **97**, 4836.
- 39 E. Baloitcha and G. G. Balint-Kurti, *J. Chem. Phys.*, 2005, **123**, 014306.
- 40 S. M. Dylewski, J. D. Geiser and P. L. Houston, *J. Chem. Phys.*, 2001, **115**, 7460.
- 41 H. Köppel, W. Domcke and L. S. Cederbaum, *Adv. Chem. Phys.*, 1984, **57**, 59.
- 42 D. G. Imre, J. L. Kinsey, R. W. Field and D. H. Katayama, *J. Phys. Chem.*, 1982, **86**, 2564.
- 43 X.-P. Zhang, W.-B. Lee and K.-C. Lin, *J. Phys. Chem. A*, 2009, **113**, 35.
- 44 J. Malhado and J. Hynes, *Chem. Phys.*, 1995, **347**, 39.
- 45 A. Piryatinsky, M. Stepanov, S. Tretiak and V. Chernyak, *Phys. Rev. Lett.*, 2005, **95**, 223001.
- 46 R. R. Dogonadze and Z. D. Urushadze, *J. Electroanal. Chem.*, 1971, **32**, 235.
- 47 B. R. Johnson, C. Kittrell, P. B. Kelly and J. L. Kinsey, *J. Phys. Chem.*, 1996, **100**, 7743.
- 48 S. Y. Lee and E. J. Heller, *J. Chem. Phys.*, 1979, **71**, 4777.
- 49 D. G. Imre, J. L. Kinsey, A. Sinha and J. Krenos, *J. Phys. Chem.*, 1984, **88**, 3956.
- 50 E. J. Heller, R. L. Sundberg and D. Tannor, *J. Phys. Chem.*, 1982, **86**, 1822.
- 51 B.-Y. Chang, C.-Y. Kung, C. Kittrell, C.-W. Hsiao, B. R. Johnson, S. G. Glogover and J. L. Kinsey, *J. Chem. Phys.*, 1994, **101**, 1914.
- 52 M. Ivanov, S. Yu. Grebenshchikov and R. Schinke, *J. Chem. Phys.*, 2004, **120**, 10015.
- 53 R. N. Zare, *Angular Momentum*, Wiley, New York, 1988.

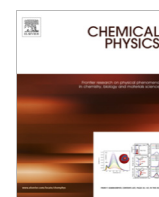
Paper 3

Partial dissociative emission cross sections and product state distributions of the resulting photofragments. D. Picconi and S. Yu. Grebenshchikov, *Chemical Physics* **481**, 231 (2016);
<https://doi.org/10.1016/j.chemphys.2016.08.011>.



Contents lists available at ScienceDirect

Chemical Physics

journal homepage: www.elsevier.com/locate/chemphys

Partial dissociative emission cross sections and product state distributions of the resulting photofragments

David Picconi, Sergy Yu. Grebenshchikov*

Department of Chemistry, Technische Universität München, Lichtenbergstr. 4, 85747 Garching, Germany

ARTICLE INFO

Article history:
Available online xxx

ABSTRACT

This paper relates the partial cross section of a continuous optical emission into a given scattering channel of the lower electronic state to the photofragment population. This allows one to infer partial emission cross sections ‘non-optically’ from product state distributions; in computations, explicit construction of exact scattering states is therefore avoided. Applications to the emission spectra of NaI, CO₂, and pyrrole are given. It is also demonstrated that a similar relationship holds between partial cross sections of dissociative photoionization and distributions of ionic fragments over final product channels.

© 2016 Elsevier B.V. All rights reserved.

1. Introduction

Light induced molecular dynamics in excited electronic states is an active field of interdisciplinary research [1] extending from fundamental questions of photostability of biochromophores [2,3] to the design of molecular photoswitches [4] and all the way to the utilization of carbon dioxide [5,6]. Emission – in particular optical emission – spectroscopy is a widely recognized tool for studying reaction pathways in excited electronic states [7–9,4]. Indeed, electronically excited molecules undergoing fast radiationless reactions (e.g. photodissociation or electronic relaxation via conical intersections [10–12]) can emit light as they move along the reaction path [13]. Even though the emission efficiency $\sim \tau_{\text{reac}}/\tau_{\text{rad}}$ is small because the characteristic reaction times τ_{reac} are often much shorter than the radiative lifetime τ_{rad} , the emission spectra carry detailed information on the topography and dynamics of the excited electronic state [9].

One generally distinguishes emission by the nature of the initial and final states either of which can be bound or dissociative. The possibilities, illustrated in Fig. 1, include bound initial and final states [panel (a) showing CO₂ molecule], dissociative initial and final states [panels (c) and (d), showing NaI and pyrrole], as well as respective mixed flavors. Discrete emission spectrum (bound final states) is especially convenient to analyze, allowing for example extraction of equilibrium geometry of the excited electronic state. The analysis of discrete emission capitalizes on the simplicity of the spectrum and the wave functions of final bound vibrational states, in particular the low lying ones [9,14]. Examples of discrete

emission spectra are given in Fig. 2(a) for the spin-forbidden transitions $\tilde{X}^1\Sigma_g^+ \leftarrow {}^3A_2$ and $\tilde{X}^1\Sigma_g^+ \leftarrow {}^3B_2$ originating from the lowest bent triplet states of CO₂ and terminating in the linear ground electronic state \tilde{X} (see Appendix for the computational details). Bent-to-linear emission transitions excite polyads (multiplets) of combined bending/symmetric stretch vibrational excitations; in \tilde{X} , these two modes are strongly coupled via the anharmonic 1:2 Fermi resonance [15]. The spectra are sensitive to the equilibrium valence angle α_{OCO}^0 : Emission from the state 3B_2 with $\alpha_{\text{OCO}}^0 = 118^\circ$ terminates in higher lying polyads and – within each polyad – in the levels with more bending character than emission from the state 3A_2 with $\alpha_{\text{OCO}}^0 = 127^\circ$. Polyad structure of the emission of bent CO₂ was first analyzed by Dixon [16] who gave accurate estimates of equilibrium bending angles.

Discrete emission from repulsive excited states has been studied in the context of dissociative resonance Raman spectroscopy [7,8]. This approach provides a sensitive probe of early stages of photodissociation in the excited electronic states [9]. The emission spectrum of CO₂ in Fig. 2(b) gives an example. Emission proceeds from a 180 cm⁻¹ wide resonance state located in the vibronically coupled singlet states $2, 3^1A'$ and belonging to a progression forming the vibrationally resolved optical absorption band around 134 nm [17]. In Ref. [17], this progression was assigned to a sequence of concerted stretching excitations winding about the closed seam of multiple conical intersections [18] and labelled by a ‘pseudorotational’ quantum number. The inner portion of the resonance wave function emits vacuum ultraviolet (VUV) light (emission wavelengths $\lambda_s \leq 155$ nm) and ends up in the low lying levels with combined symmetric and antisymmetric stretch excitations. The same resonance state emits strongly in the near

* Corresponding author.

E-mail address: Sergy.Grebenshchikov@ch.tum.de (S.Yu. Grebenshchikov).

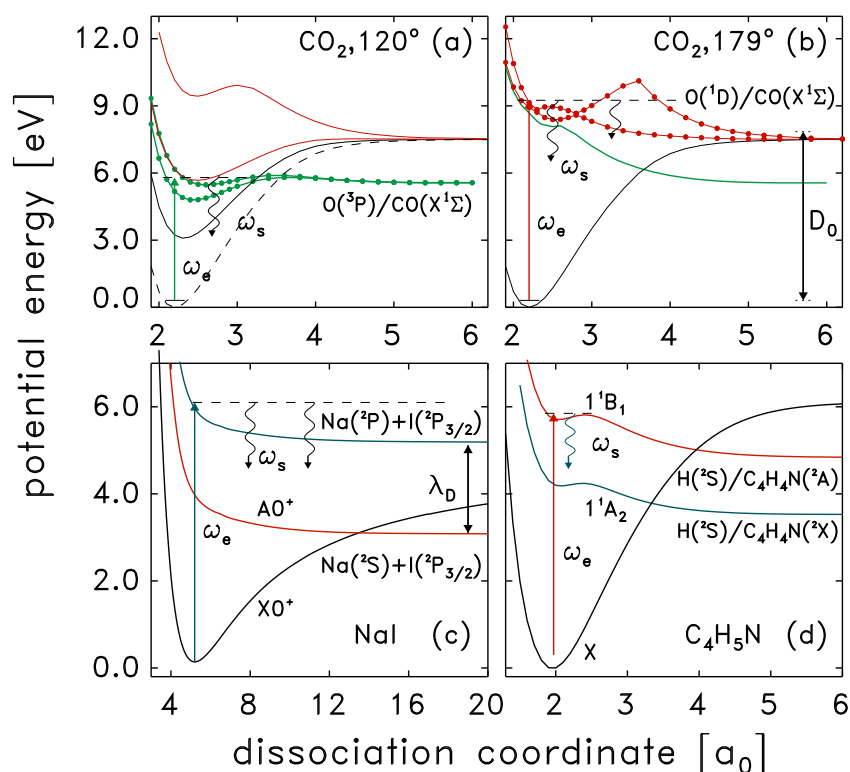


Fig. 1. Electronic states of molecules emission of which is discussed in this work. Photoexcitation (vertical arrows) proceeds with frequency ω_e ; emitted light (wavy arrows) has frequency ω_s . (a) Potentials of CO_2 for the ground electronic state (solid and dashed black curves), excited singlet states $2, 3^1A'$ (red) and the lowest bent triplet states $1^3A'$ and $1^3A'$ (green) as functions of one CO bond length. Spin-forbidden excitation to the bound states in the triplet potentials is shown with a green arrow. The valence angle is fixed at 120° , and the second CO bond is $2.2 a_0$. (b) The same curves as in (a) but for the valence angle of 179° . Excitation to the singlet metastable states is shown with a red arrow, and singlet dissociation threshold D_0 is indicated. (c) Potentials of the ionic (black) and covalent (red and blue) electronic states of NaI as functions of the interatomic distance. Excitation to the covalent state correlating with the excited $\text{Na}(^3P)$ fragment atoms is shown with a blue arrow. (d) Potentials of the ground electronic state of pyrrole (black) as well as of the excited electronic states 1^1A_2 (blue) and 1^1B_1 (red) as functions of the NH distance. Excitation of a metastable level in the 1^1B_1 state is shown with a red arrow. Blue wavy arrow indicates emission into the repulsive 1^1A_2 state. C_{2v} symmetry of pyrrole is preserved along the shown dissociative cut. For each NH distance, the energy of the 1^1A_2 state is optimized with respect to vibrations of pyrrolyl. (For interpretation of the references to colour in this figure legend, the reader is referred to the web version of this article.)

UV range, between 250 nm and 400 nm. This emission stems from the dissociative portion of the resonance wave function, with O–CO distance exceeding $3.5a_0$, and includes transitions into bound levels with antisymmetric stretch and bending excitations. Recently, we demonstrated that the corresponding Raman emission amplitudes can be utilized to accurately reconstruct intermediate stretching/bending distributions of the molecule moving across the conical intersection seam [14].

Finally, continuum emission into dissociative states of the final electronic state can be employed in the analysis. A prominent example is the emission spectrum of the photoexcited NaI – one of the first examples of the transition state spectroscopy [13,19]. The excitation/emission scheme is sketched in Fig. 1(c), while the corresponding calculated emission spectrum is given in Fig. 2(c). The dominant transition corresponds to the characteristic emission D-line λ_D of free electronically excited product Na^* atoms. Weak emission of the still interacting Na–I system into the bound NaI states is seen on the blue side of the atomic D line for $\lambda_s < \lambda_D$, while emission into the dissociative continuum of the low lying electronic states gives rise to a pronounced wing extending to the red for $\lambda_s > \lambda_D$. In principle, continuous emission contains a wealth of dynamical information on the excited electronic states [14,20] and – in polyatomic molecules – can be instrumental in the analysis of conical intersections shifted away from the Franck–Condon region into the exit dissociation channel [14]. However, the diffuse and often featureless continuous emission spectra are more difficult to interpret than the well resolved discrete emission into

bound levels. Moreover, a comprehensive analysis requires partial photoemission amplitudes into specific scattering channels of the final electronic state [14], and these are generally difficult to quantify either experimentally or computationally [21,22]. The aim of the present work is to close this gap and to provide theoretical means for the analysis of continuous emission spectra.

In this paper, partial cross sections for continuous emission are considered. It is demonstrated that the emission cross section in a given scattering channel is closely related to the photofragment population in this channel. Thus, photofragment populations can be used as proxies for efficient computation of the corresponding emission cross section. In fact, the two sets of data carry very similar information and can effectively complement each other. The rest of the paper is organized as follows: theory and illustrative computations are presented in Section 2. Conclusions are given in Section 3 and an extension to the case of dissociative photoelectron emission is discussed. Appendix summarizes the computational aspects of the presented emission spectra.

2. Partial emission cross sections and photofragment distributions

Relevant excitation/emission schemes are sketched in Fig. 1. Incident light with frequency ω_e promotes the system, originally residing in the ground electronic state \tilde{X} , into an electronically excited state or states, which we denote by B , and creates an initial excitation

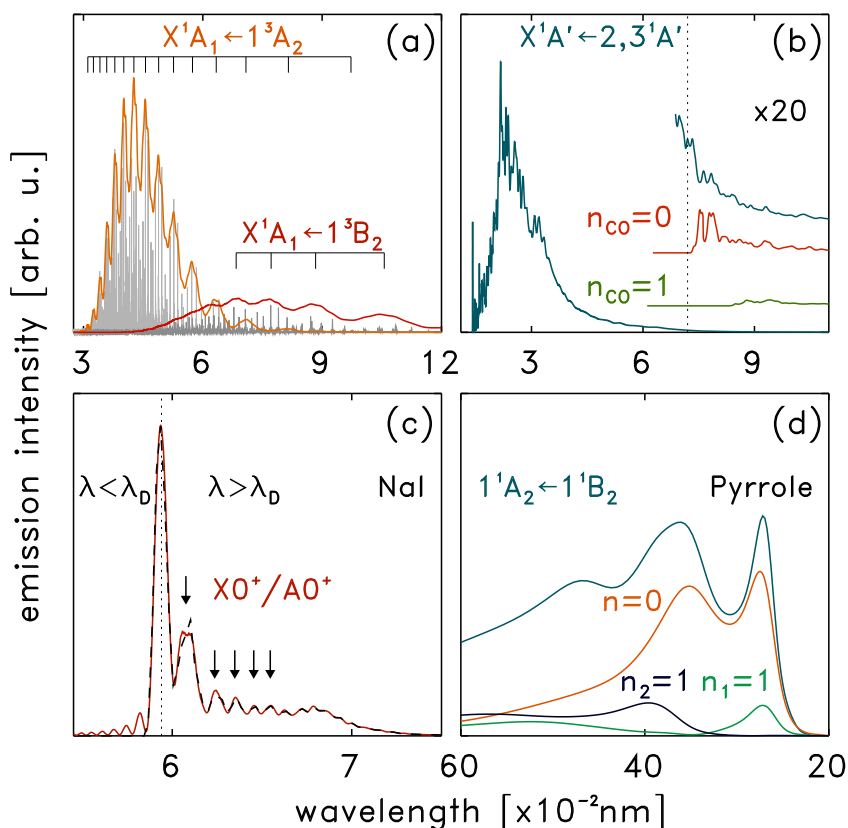


Fig. 2. Optical emission spectra shown as functions of the emission wavelength λ_s . (a) Emission of bent triplet states of CO_2 into bound levels (gray sticks) of the ground electronic state. Combs indicate vibrational states carrying maximum intensities inside each Fermi polyad. (b) Emission from linear singlet states of CO_2 into the ground electronic state. Most of the emission is into the bound levels. Continuous emission region is enhanced; vertical dotted line marks D_0 . Red and green lines show partial emission cross sections into the ground ($n_{\text{CO}} = 0$) and the first excited ($n_{\text{CO}} = 1$) vibrational states of the CO fragment. (c) Emission into the vibronically coupled $X0^+/A0^+$ states of NaI. Vertical dotted line marks emission at the sodium D-line λ_D . Arrows indicate positions of vibronic resonances in $X0^+/A0^+$. Dashed line is inferred from the kinetic energy spectrum of recoiling fragments. (d) Emission between the two $\pi\sigma^*$ states of pyrrole (solid blue line). Also shown are partial emission cross sections into the vibrationless pyrrolyl fragment ($n = 0$; orange) as well as the pyrrolyl fragment with one-quantum excitations in the A_1 modes with frequencies 939 cm^{-1} ($n_1 = 1$; green) and 1089 cm^{-1} ($n_2 = 1$; black). (For interpretation of the references to colour in this figure legend, the reader is referred to the web version of this article.)

$$\Phi_B = (\boldsymbol{\mu} \cdot \boldsymbol{\epsilon}_e)_{\text{BX}} \Phi_0, \quad (1)$$

where $(\boldsymbol{\mu} \cdot \boldsymbol{\epsilon}_e)_{\text{BX}}$ is the transition dipole moment (TDM) along the polarization direction $\boldsymbol{\epsilon}_e$ of the incident light, and Φ_0 is a vibrational state in \tilde{X} ; in what follows we shall apply the Condon approximation and neglect the coordinate dependence of the TDM (generalization to coordinate dependent TDMs is straightforward). Once in B , the molecule undergoes excited state dynamics and emits light with frequency ω_s , landing in the lower electronic state (e.g. \tilde{X}) with dissociation energy D_0 . For $\hbar(\omega_e - \omega_s) > D_0$, the emission is continuous. In a typical case of a UV excitation and emission into the ground state \tilde{X} with D_0 of the order of a few eV, the continuous emission falls into visible range and extends to near infrared.

Central for the analysis of the molecular photoresponse involving formation of separated fragments is the Franck-Condon-like matrix element $\langle \psi_{\gamma,n}^- | \Psi_\gamma \rangle$ [23], where $\psi_{\gamma,n}^-$ is an energy normalized scattering eigenstate in the electronic state γ with an outgoing wave in the scattering channel labelled by a collective index n (comprising e.g. rotational and/or vibrational quantum numbers of polyatomic products); Ψ_γ is the molecular wave function in the state γ prepared by absorption or emission of a photon, and its particular form depends on the experimental situation.

For example, in a one-photon photodissociation of a molecule excited into the state $\gamma = B$ with a narrow bandwidth laser pulse, the wave function $\Psi_{\gamma=B}(\omega_e)$ is a fixed energy component filtered out of the initial excitation Φ_B via

$$\Psi_B(\omega_e) \sim \int_0^\infty \exp(-i\hat{H}_B t) \Phi_B \exp(+i\omega_e t) dt. \quad (2)$$

\hat{H}_B is the excited state Hamiltonian augmented with a coordinate dependent complex absorbing potential in order to impose radiation boundary conditions for large interfragment separations $R \rightarrow \infty$ (hereafter, atomic units $\hbar = 1$ are used). The matrix element $\langle \psi_{B,n}^-(\omega_e) | \Psi_B(\omega_e) \rangle$ describes the *partial photodissociation* amplitude $\tau_B(\omega_e, n)$ in channel n , and the asymptotic form of $\Psi_B(\omega_e)$, containing purely outgoing waves along R , is given by

$$\Psi_B(\omega_e) \xrightarrow{R \rightarrow \infty} -i \sum_n \tau_B(\omega_e, n) \sqrt{\frac{\mu_R}{k_{B,n}}} e^{ik_{B,n} R} \chi_{B,n}(q). \quad (3)$$

In each channel n , the wave function is asymptotically factorized into a translational R -dependent part and the part depending on the internal degrees of freedom q of the fragment; $\tau_B(\omega_e, n)$ plays the role of a channel amplitude; μ_R is the reduced mass associated with R , $\chi_{B,n}(q)$ is the eigenfunction of the fragment state (B, n) , $\epsilon_{B,n}$ is its eigenenergy, and $k_{B,n} = \sqrt{2\mu_R(\omega_e - \epsilon_{B,n})}$ is the channel momentum.

This asymptotic factorization is the basis of the projection method developed by Balint-Kurti and co-workers [24,25], in which $\tau_B(\omega_e, n)$ is extracted out of the evolving molecular wave packet at the *analysis line* $R = R_\infty$ in the asymptotic region. The time independent version of this projection method reads as [14,23,26]

$$|\tau_B(\omega_e, n; R_\infty)|^2 = \frac{k_{B,n}}{\mu_R} \left| \langle \chi_{B,n}(q) | \delta(R - R_\infty) | \Psi_B(\omega_e) \rangle \right|^2. \quad (4)$$

If the electronically excited molecule in the state $\Psi_B(\omega_e)$ emits light and makes a transition into the dissociation continuum of, say, ground electronic state \tilde{X} , the matrix element $\langle \psi_{X,n}^- | \Psi_{\gamma=X}(\omega_e, \omega_s) \rangle$ describes the *partial photoemission* amplitude $\alpha_X(\omega_e, \omega_s, n)$ in the scattering channel n in \tilde{X} . The function Ψ_B is then the Raman wave function introduced by Lee and Heller [27], and the corresponding radiative transition generates a resonance Raman signal. The wave function $\Psi_X(\omega_e, \omega_s)$ is a fixed energy component, this time extracted from the state $\Psi_B(\omega_e)$ using the ground state Hamiltonian \hat{H}_X (also augmented with an absorbing potential) [27,28]:

$$\Psi_X(\omega_e, \omega_s) = \int_0^\infty \exp(-i\hat{H}_X t) \Psi_B(\omega_e) \exp(i(\omega_s - \omega_e)t) dt. \quad (5)$$

The asymptotic form of this wave function in each scattering channel of the terminal electronic state is again given by a factorized expression akin to Eq. (3):

$$\Psi_X(\omega_e, \omega_s) \xrightarrow{R \rightarrow \infty} -i \sum_n \alpha_X(\omega_e, \omega_s, n) \sqrt{\frac{\mu_R}{k_{X,n}}} e^{ik_{X,n}R} \chi_{X,n}(q). \quad (6)$$

All quantities describing fragments now refer to \tilde{X} . The channel amplitudes in Eq. (6) turn out to be the emission amplitudes $\alpha_X(\omega_e, \omega_s, n)$, and they can be quantified by measuring photofragment fluxes at an asymptotic analysis line:

$$|\alpha_X(\omega_e, \omega_s, n)|^2 = \frac{k_{X,n}}{\mu_R} \left| \langle \chi_{X,n}(q) | \delta(R - R_\infty) | \Psi_X(\omega_e, \omega_s) \rangle \right|^2. \quad (7)$$

This is the main result of this work: The photoemission intensity into a given scattering channel in the dissociation continuum of the lower electronic state is given by the emission induced population of this channel. This relation allows a straightforward computation of partial amplitudes of continuous emission without the need for explicit construction of exact scattering states $\{\psi_{X,n}^-\}$. Once the partial emission amplitudes are quantified they can be used to infer the excited state dynamics as described in Ref. [14]. The total photoemission cross section is related to the partial cross emission amplitudes via [28] $\sigma_R(\omega_e, \omega_s) \sim \omega_e \omega_s^3 \sum_n |\alpha_X(\omega_e, \omega_s, n)|^2$.

An effective iterative implementation for the integral in Eq. (7) is provided by the recursive construction of Krylov vectors $\xi_k(\omega_e) = Q_k \Psi_B(\omega_e)$, based on a sequence of modified Chebyshev polynomials $Q_k(\hat{H}_X)$ introduced by Mandelshtam and Taylor [29]:

$$\langle \chi_{X,n} | \delta(R - R_\infty) | \Psi_X \rangle = \sum_{k=1}^{N_{\text{iter}}} b_k \left[\chi_{X,n} | \xi_k \right]_{R=R_\infty}. \quad (8)$$

Here the integration in square brackets is carried out only over the fragment coordinates q ; b_k are the usual [30] energy dependent expansion coefficients for the propagator, and the expansion length N_{iter} is a convergence parameter of the computation. Examples below illustrate the calculation of partial emission cross sections via Eq. (7) for the molecular systems in Fig. 1(b,c,d) dissociating after emitting a photon. Computational details are given in the Appendix.

Application 1: NaI. Sodium iodide photoexcited at the wavelength of $\lambda_e \sim 220$ nm into a high lying repulsive covalent state dissociates in $\text{Na}(^2\text{P}) + \text{I}(^2\text{P}_{3/2})$ [see Fig. 1(c)] [13]. Free sodium atoms emit via a transition $\text{Na}(^2\text{S} \leftarrow ^2\text{P})$ at the D-line of $\lambda_D = 589$ nm [Fig. 2(c)]. As long as Na–I are still interacting, radiative transitions can also terminate in the low lying covalent state A0^+ which is vibronically coupled to the continuum of the ionic ground electronic state X0^+ at an avoided crossing [19,31]. These transitions

give rise to an appreciable wing emission for $\lambda_s > \lambda_D$. According to Eq. (7), the emission spectrum can be recorded ‘non-optically’, by detecting the kinetic energies of the recoiling atoms in the lowest electronic channel $\text{Na}(^2\text{S}) + \text{I}(^2\text{P}_{3/2})$ (rovibrational channels n are absent for atomic fragments). This is demonstrated in Fig. 2(c) which compares the emission spectrum, obtained from the kinetic energy release evaluated at the analysis line of $R_\infty = 25 a_0$, with the emission spectrum calculated directly by propagating the wave packet $\Psi_B(\omega_e)$ in the lower lying coupled $\text{A0}^+/\text{X0}^+$ states [27,28]. The agreement is excellent for the wing emission with $\lambda_s > \lambda_D$; peaks in this wavelength range are spaced by about 260 cm^{-1} and correspond to a progression of metastable resonances in the $\text{A0}^+/\text{X0}^+$ states. These resonances have been analyzed in detail by Alekseyev et al. [31] in the context of the absorption spectrum of NaI.

Application 2: CO₂. Discrete emission spectrum of carbon dioxide photoexcited into a pseudorotational vibronic resonance in the absorption band around 134 nm has already been discussed in the Introduction. As illustrated in the magnified portion of the spectrum in Fig. 2(b), the same state gives rise to a weak continuous emission into scattering states of the ground electronic state $\tilde{X}^1\Sigma_g^+$ correlating with the singlet dissociation threshold $\text{CO}(^1\Pi) + \text{O}(^1\text{D})$. The continuous emission extends to wavelengths longer than 620 nm, and its spectrum can be decomposed into partial components using Eq. (7) and the CO vibrational distributions. Most of the emission is into the vibrationless ($n = 0$) channel of carbon monoxide [red line in panel (b)]. Partial contribution from the first excited state $n = 1$ is also seen, but it is weak in the shown wavelength range: Emission induced CO vibrational state distributions are very cold. Higher vibrational channels are effectively populated via emission only for $\lambda_s > 1200$ nm (not shown).

Application 3: Pyrrole. Mechanisms of photodissociation of heteroaromatic chromophores – such as pyrrole $\text{C}_4\text{H}_4\text{NH}$ – are currently under investigation in several experimental and theoretical groups [32–36]. Of particular interest are photofragment distributions in the mixed Rydberg/valence $\pi\sigma^*$ states mediating fast direct dissociation of the NH bond. In Fig. 1(d), these states are denoted 1^1A_2 and 1^1B_1 according to the irreps of the C_{2v} symmetry group of the parent molecule. In the Franck–Condon region, the state 1^1B_1 features a local minimum lying 5.03 eV above the equilibrium of \tilde{X} and separated from the asymptotic channel by a 2145 cm^{-1} high potential barrier. The reported emission spectrum arises via a transition from the upper (1^1B_1) to the lower (1^1A_2) $\pi\sigma^*$ state following direct photoexcitation of the vibrational ground state in the local minimum of 1^1B_1 ; photoexcitation is dipole allowed (TDM between 1^1B_1 and \tilde{X} at the Franck–Condon point is 0.1 D). The emission transition $1^1\text{A}_2 \leftarrow 1^1\text{B}_1$ is also allowed, and the corresponding TDM of 0.75 D is large. The final state is repulsive and the emission spectrum is purely continuous.

The spectrum is evaluated using the recently constructed model potential energy surfaces comprising all 24 vibrational degrees of freedom of pyrrole [37]. The present calculations include the N–H dissociation coordinate and the eight totally symmetric (a_1) modes of the pyrrolyl ring. The resulting emission spectrum, covering the near to mid infrared range, is shown in Fig. 2. Diffuse spectral structures are due to a progression of broad resonance states built on consecutive excitations of the NH stretch in the final state 1^1A_2 . Partial emission cross sections into scattering channels corresponding to different vibrational states of pyrrolyl radical $\text{C}_4\text{H}_4\text{N}(^2\tilde{X})$ are also calculated from the product state distributions according to Eq. (7). They have the same characteristic shape as the total emission spectrum. For $\lambda < 5500$ nm, the strongest emission is into the channel $n = 0$ in which pyrrolyl is in the vibrational ground state. At longer wavelengths, channels with one-quantum

excitations of the low frequency pyrrolyl vibrations ($n_1 = 1$ and $n_2 = 1$) gradually become dominant.

3. Conclusions and outlook

This paper relates the partial cross sections of continuous emission to the resulting photofragment distributions over the open scattering channels. This is the main conclusion of this work. In computations, this opens a way to reconstruct partial emission cross sections by analyzing the flux of photofragments without the need to explicitly construct the exact scattering states. This reconstruction is in principle possible in a photodissociation experiment, too – if the detected photofragments in a given electronic channel predominantly originate from the emission transition. Finally, information on the emission intensities can be utilized to reconstruct transient dynamics in the excited electronic state [14].

Similar relationships can be found in other photoinduced reactions leading to an unstable final state. One promising application which deserves a more detailed study in the future is dissociative photoionization, a sensitive instrument in studies of the electronic relaxation of nucleobases [38,39]. Ionizing pulse prepares an unstable cationic state, and partial photoelectron cross sections, in which fragment ions are generated in specific electronic and vibrational states, can be related to the product state distributions in these channels. Indeed, the cross section of dissociative photoionization for a certain electron kinetic energy eKE is given by the familiar Franck–Condon like matrix element $\langle \psi_{\gamma,n}^- | \Psi_{\gamma} \rangle$ discussed in connection with Eqs. (3) and (6) and can be represented as a sum over partial cross sections in all electronic (F) and rovibrational (n) dissociation/ionization channels:

$$\sigma(\epsilon_{\text{ph}}, eKE|\tau) \sim \sum_n \sum_F \left| \left(\sum_s d_{ks} x_{FI}^s \right) \langle \psi_{Fn}^- | \Psi_1 \rangle \right|^2. \quad (9)$$

Here ψ_{Fn}^- are scattering states in the dissociation continuum of the unstable cation; Ψ_1 is the wave function of neutral molecule analogous to Ψ_B or Ψ_X above. If – as often done in the context of a ‘sudden’ approximation [40] – the ‘spectroscopic factors’ x_{FI}^s (i.e. the matrix elements of the electronic annihilation operator between states I and F) and the amplitudes d_{ks} (i.e. the bound-free one-electron dipole integrals) are ignored, the partial photoelectron emission cross sections are given by the Franck–Condon elements $\langle \psi_{Fn}^- | \Psi_1 \rangle$. These can again be evaluated in terms of partial photodissociation fluxes of the (this time ionic) fragments at the analysis line $R = R_{\infty}$. In other words, partial photoelectron cross sections can be found from the asymptotic detection of recoiling ionized molecular fragments.

Acknowledgement

Financial support by the Deutsche Forschungsgemeinschaft is gratefully acknowledged. Authors thank Samuel Markson for sending his version of the diabatic potential matrix of NaI. We dedicate this paper to Volodya Chernyak.

Appendix A. Quantum mechanical calculations of the emission spectra

1. Spectral calculations. For each molecule discussed in the main text, the total and – where applicable – the partial emission cross sections are calculated in two steps. In the first step, the molecular wave function $\Psi_B(\omega_e)$ is generated in the excited state manifold. For the emission of NaI and of singlet CO_2 , this is done by propagating the ground vibrational state of \tilde{X} under the influence of the molecular Hamiltonian of excited state(s) using the discrete

version of Eq. (2) [see, for example, Eq. (8)]. Bound vibrational states in the bent triplet potentials are found by applying Filter Diagonalization [41] to the respective Hamiltonians. The vibrational ground state in the local minimum of the 1^1B_1 state of pyrrole is calculated within the harmonic approximation for all vibrational degrees of freedom. In the second step, the initial state $\Psi_B(\omega_e)$ is iteratively propagated under the influence of the molecular Hamiltonian of the lower electronic states. The total emission cross section is proportional [28] to the Fourier Transform of the discrete Chebyshev autocorrelation function. The partial emission cross sections are evaluated with Eq. (7) using the discrete cross-correlation functions of Eq. (8) for each rovibrational channel.

2. Potential energy functions. Diabatic potential energy functions and off-diagonal coupling for the lowest two states of NaI are from Ref. [31]. The uppermost covalent state correlating with the dissociation channel $\text{Na}(^2P) + \text{I}(^2P_{3/2})$ is constructed as suggested in Ref. [13]. Potential energy surfaces of the singlet states of CO_2 are taken from Ref. [42]. The calculations of the two lowest bent triplet states are described in Ref. [6].

The potential energy surfaces of the two lowest $\pi\sigma^*$ states of pyrrole are constructed from CASSCF/CASPT2 ab initio calculations as described in Ref. [37]. In particular, the potential energy surface of the lower $\pi\sigma^*$ state 1^1A_2 is a quadratic function of the pyrrolyl normal modes $\{q_1 \dots q_8\}$ and has the form

$$V(R, \{q_1, \dots, q_8\}) = V_{1D}(R) + \sum_{i=1}^8 \kappa_i(R) q_i + \frac{1}{2} \sum_{ij=1}^8 \gamma_{ij}(R) q_i q_j. \quad (A1)$$

The zeroth-order term, the gradient, and the matrix elements of the Hessian depend on the dissociation coordinate R chosen to be the Jacobi distance of the departing H atom to the center of mass of the pyrrolyl moiety. By construction, the Hessian becomes diagonal for $R \rightarrow \infty$ and the gradient term vanishes.

3. Quantum mechanical calculations. Spectral calculations of NaI and CO_2 are performed using the program package ‘PolyWave’ [43]. For NaI, 1024 equidistant grid points spanning interatomic NaI distances between $3.0 a_0$ and $30.0 a_0$ are used. Grid parameters and propagation settings for CO_2 are described in Refs. [37,17]. Emission spectra of pyrrole are calculated using the MCTDH package [44]. The primitive grid in R consists of 97 sine DVR grid points chosen between $3.4 a_0$ and $13.0 a_0$; for each pyrrolyl normal mode q_i , 21 harmonic oscillator DVR grid points are used. The MCTDH wave function is expressed using five combined modes $\{R, (q_1, q_2), (q_3, q_4), (q_5, q_6), (q_7, q_8)\}$ with the scheme of $\{6, 5, 4, 3, 2\}$ single-particle functions for each combined mode.

References

- [1] T. Nelson, S. Fernandez-Alberti, V. Chernyak, A.E. Roitberg, S. Tretiak, J. Phys. Chem. B 115 (2011) 5402.
- [2] A.L. Sobolewski, W. Domcke, Phys. Chem. Chem. Phys. 12 (2010) 4897.
- [3] G. Féraud, M. Broquier, C. Dedonder-Lardeux, G. Grégoire, S.S. Soorkia, C. Jouvet, Phys. Chem. Chem. Phys. 16 (2011) 5250.
- [4] M. Sauer, Proc. Natl. Acad. Sci. 102 (2005) 9433.
- [5] G.J. van Rooij, D.C.M. van den Bekerom, N. den Harder, T. Minea, G. Berden, W. A. Bongers, R. Engeln, M.F. Graswinckel, E. Zoethout, M.C.M. van de Sanden, Faraday Discuss. 183 (2015) 233.
- [6] S. Yu. Grebenshchikov, J. CO_2 Utilization (2016), <http://dx.doi.org/10.1016/j.jcou.2016.02.007>.
- [7] D.G. Imre, J.L. Kinsey, A. Sinha, J. Krenos, J. Phys. Chem. 88 (1984) 3956.
- [8] K.Q. Lao, M.D. Person, P. Xayariboun, L.J. Butler, J. Chem. Phys. 92 (1990) 823.
- [9] B.R. Johnson, C. Kittrell, P.B. Kelly, J.L. Kinsey, J. Phys. Chem. 100 (1996) 7743.
- [10] R. Schinke, Photodissociation Dynamics, Cambridge University Press, Cambridge, 1993.
- [11] D.R. Yarkony, in: W. Domcke, D.R. Yarkony, H. Köppel (Eds.), Conical Intersections, World Scientific, Singapore, 2004.
- [12] A. Piryatinski, M. Stepanov, S. Tretiak, V. Chernyak, Phys. Rev. Lett. 95 (2005) 223001.
- [13] H. Foth, J.C. Polanyi, H.H. Telle, J. Phys. Chem. 86 (1982) 5027.
- [14] D. Picconi, S.Yu. Grebenshchikov, Phys. Chem. Chem. Phys. 17 (2015) 28931.

- [15] E. Fermi, *Z. Phys.* 71 (1931) 250.
- [16] R.N. Dixon, *Proc. R. Soc. A* 275 (1963) 431.
- [17] S.Yu. Grebenshchikov, *J. Chem. Phys.* 138 (2013) 224107.
- [18] S.Yu. Grebenshchikov, R. Borrelli, *J. Phys. Chem. Lett.* 3 (2012) 3223.
- [19] A.H. Zewail, *Science* 242 (1988) 1645.
- [20] B. Hartke, W. Kiefer, E. Kolba, J. Manz, J. Stempel, *J. Chem. Phys.* 96 (1992) 5636.
- [21] S.Y. Lee, *Chem. Phys. Lett.* 245 (1995) 620.
- [22] Z.W. Feng, S.Y. Lee, *J. Raman Spectrosc.* 32 (2001) 447.
- [23] J.Z.H. Zhang, *Theory and Application of Quantum Molecular Dynamics*, World Scientific, Singapore, 1999.
- [24] G.G. Balint-Kurti, R.N. Dixon, C.C. Marston, *J. Chem. Soc. Faraday Trans.* 86 (1990) 1741.
- [25] G.G. Balint-Kurti, *Adv. Chem. Phys.* 128 (2004) 249.
- [26] D.E. Manolopoulos, M.H. Alexander, *J. Chem. Phys.* 97 (1992) 2527.
- [27] S.Y. Lee, E.J. Heller, *J. Chem. Phys.* 71 (1979) 4777.
- [28] D.J. Tannor, *Introduction to Quantum Mechanics. A Time-Dependent Perspective*, University Science Books, Sausalito, California, 2007.
- [29] V.A. Mandelshtam, H.S. Taylor, *J. Chem. Phys.* 103 (1995) 2903.
- [30] H. Tal-Ezer, R. Kosloff, *J. Chem. Phys.* 81 (1984) 3967.
- [31] A.B. Alekseyev, H.-P. Liebermann, R.J. Buenker, N. Balakrishnan, H.R. Sadeghpour, S.T. Cornett, M.J. Cavagnero, *J. Chem. Phys.* 113 (2000) 1514.
- [32] M.N.R. Ashfold, G.A. King, D. Murdock, M.G.D. Nix, T.A.A. Oliver, A.G. Sage, *Phys. Chem. Chem. Phys.* 12 (2010) 1218.
- [33] G.M. Roberts, V.G. Stavros, *Chem. Sci.* 5 (2014) 1698.
- [34] X. Xu, J. Zheng, K.R. Yang, D.G. Truhlar, *J. Am. Chem. Soc.* 136 (2014) 16378–16386.
- [35] D.V. Makhov, K. Saita, T.J. Martinez, D.V. Shalashilin, *Phys. Chem. Chem. Phys.* 17 (2015) 3316–3325.
- [36] M. Barbatti, K. Sen, *Int. J. Quant. Chem.* 116 (2015) 762.
- [37] D. Picconi, S. Yu. Grebenshchikov, in preparation, 2016.
- [38] M. Kotur, T.C. Weinacht, C. Zhou, K.A. Kistler, S. Matsika, *J. Chem. Phys.* 134 (2011) 184309.
- [39] M. Ryszka, R. Pandey, C. Rizk, J. Tabet, B. Barc, M. Dampc, N.J. Mason, S. Eden, *Int. J. Mass Spectrom.* 396 (2016) 48.
- [40] W. Domcke, *Phys. Rep.* 208 (1991) 97.
- [41] V.A. Mandelshtam, T.P. Grozdanov, H.S. Taylor, *J. Chem. Phys.* 103 (1995) 10074.
- [42] S.Yu. Grebenshchikov, *J. Chem. Phys.* 138 (2013) 224106.
- [43] 'PolyWave' is a package of FORTRAN90 programs for iterative quantum mechanical calculations of bound states, dissociative resonance states, photoabsorption or photoemission spectra, as well as product state distributions in molecules with up to six internal degrees of freedom and $N \leq 100$ coupled electronic states.
- [44] M.H. Beck, A. Jäckle, G.A. Worth, H.-D. Meyer, *Phys. Rep.* 324 (2000) 1.

Paper 4

Photodissociation dynamics and photofragment distributions in the first absorption band of pyrrole: I. Vibronic Franck-Condon Herzberg-Teller excitation of the ${}^1A_2(\pi\sigma^*) \leftarrow \tilde{X}{}^1A_1(\pi\pi)$ transition. D. Picconi and S. Yu. Grebenshchikov, in preparation.

Photodissociation dynamics and photofragment distributions in the first absorption band of pyrrole: I. Vibronic Herzberg-Teller excitation of the ${}^1A_2(\pi\sigma^*) \leftarrow \tilde{X}{}^1A_1(\pi\pi)$ transition

David Picconi and Sergy Yu. Grebenschikov*

Department of Chemistry, Technical University of Munich,

Lichtenbergstr. 4, 85747 Garching, Germany

Photodissociation of pyrrole, following the excitation to the low-lying ${}^1A_2(\pi\sigma^*)$ state is studied quantum mechanically. A new set of 24-dimensional diabatic potential energy surfaces are constructed using high level ab initio calculations. The excitation is described using coordinate-dependent transition dipole moment functions which are constructed as Herzberg-Teller expansions. The calculated observables are absorption spectra and photofragment translational energy distributions (frequency-resolved properties) and the dissociation time scales and the resonance lifetimes (time-resolved properties). Simulations are performed including a different number of degrees of freedom (6, 11 and 15), and the different spectroscopic features ascribed to totally symmetric and non-totally symmetric modes are analyzed in detail. Approximate methods, involving a minimum computational effort, are developed to calculate the absorption spectrum and the photofragment distributions. These approaches, whose validity is demonstrated for pyrrole, are promising for the study of photodissociation of $\pi\sigma^*$ states in broad classes of biochromophores.

I. INTRODUCTION

The atomistic mechanisms of non-radiative decay of the initial electronic excitation in aromatic molecules, serving as models of broad classes of ultraviolet (UV) biochromophores, are actively studied using experiment and theory (see Refs. 1–22 and references therein). In the gas phase, the internal energy of the molecules, excited with UV light, allows dissociation into several kinetically competing channels. One group of channels is populated on

* Emails: Sergy.Grebenshchikov@ch.tum.de and sgreben@gwdg.de

a nanosecond time scale²³ and is reached via electronic relaxation to the ground electronic state \tilde{X} along the ring-deformation and ring-opening pathways.^{12,14,15,18,24,25} In contrast, dissociation into a hydrogen atom and a radical co-fragment via $^1\pi\sigma^*$ excited states occurs on a sub-picosecond time scale.^{7,8,11,13,14} The $^1\pi\sigma^*$ states often lack oscillator strength (especially if compared to the optically ‘bright’ $^1\pi\pi^*$ states), but the topography of their potential energy surfaces allows them to control ultrafast electronic relaxation pathways.^{13,14,16}

The $^1\pi\sigma^*$ -mediated H-atom detachment in heteroaromatic molecules, such as pyrrole, is an actively expanding research field in which a range of powerful spectroscopic techniques, both high-resolution frequency-resolved¹³ and ultrafast time-resolved,^{12,14,26} are used to monitor the reaction fragments. They are combined with ab initio theoretical calculations,^{4,16,17,21} which provide a convincing interpretation in terms of the electronic structure and quantum dynamics simulations.

The molecule of pyrrole, whose structure is present in a number of biomolecules (as for example the amino acid tryptophan, and porphyrin compounds), is a characteristic example of a chromophore which exhibits $\pi\sigma^*$ photochemistry. Its low-lying $^1\pi\sigma^*$ states are known to be predissociative with respect to the N–H bond.¹⁶

The first absorption band of pyrrole (see Fig. 1(a)), extending from 5.5 eV to 6.5 eV, was extensively studied in the past. While the complete electronic assignment of the band remains a subject of hot discussions, most researchers currently agree that the two lowest excited states of the molecule in the Franck-Condon (FC) range are of $^1\pi\sigma^*$ character. The first excited singlet state $^1A_2(\pi\sigma^*)$ (with the vertical excitation energy T_e of about 5.0 eV) arises mainly from the promotion of an electron from the $1a_2(\pi)$ to the $10a_1(3s/\sigma^*)$ molecular orbital; the transition from the ground electronic state $\tilde{X}^1A_1(\pi\pi)$ (hereafter referred to as \tilde{X}) is electric dipole forbidden and is accomplished via the vibronic intensity borrowing. The second $\pi\sigma^*$ state, located ~ 0.7 eV above A_2 , is the state $^1B_1(\pi\sigma^*)$. It originates mainly from the $2b_1(\pi) \rightarrow 10a_1(3s/\sigma^*)$ orbital excitation and, although its excitation from \tilde{X} is electric dipole allowed, the oscillator strength of this transition is weak. As a result, the absorption cross section of pyrrole below 5.6 eV (218 nm on the wavelength scale) is small, of the order of 10^{-18} cm².

The one-dimensional potential energy curves of the three lowest electronic states of pyrrole along the dissociation coordinate are illustrated in Fig. 2(a) and (b). Both states are repulsive with respect to the extension of the N–H bond; the state $^1A_2(\pi\sigma^*)$ correlates

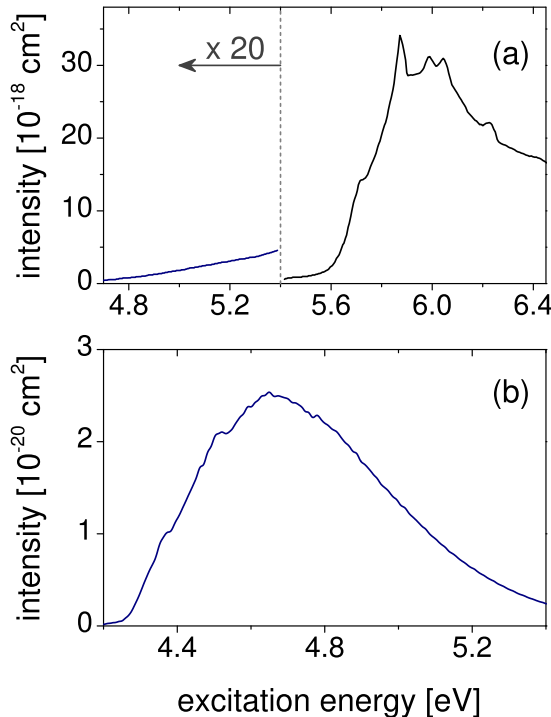


FIG. 1: (a) Overview of the experimental absorption spectrum in the first absorption band of pyrrole (see Refs. 27 and 28). (b) Theoretical absorption spectrum due to the transition ${}^1A_2 \leftarrow \tilde{X}$ calculated as described in Sect. V. (c) Theoretical spectrum of Roos et al. (Ref. 29), calculated using Herzberg-Teller transition dipole moments and a globally harmonic approximation (i. e. not including the broadening due to the dissociation).

with the photofragments in the electronic ground states, $H({}^1S) + \text{pyrrolyl}({}^2A_2)$, while the state ${}^1B_1(\pi\sigma^*)$ correlates with the pyrrolyl's first excited state 1B_1 . Both $\pi\sigma^*$ states feature shallow local minima in the FC zone separated from the asymptotic region by low barriers, indicating that a tunneling contribution to the dissociation can be expected.¹⁶

The two $\pi\sigma^*$ states in Fig. 2 form conical intersections (CIs) with the ground electronic state in the exit channel, away from the FC zone. These intersections, predicted by Sobolewsky, Domcke and co-workers on the basis of general symmetry arguments,¹⁶ are the most salient features of the $\pi\sigma^*$ states of pyrrole and, as argued in Refs. 7,13,14, are also expected to be the intrinsic properties of the $\pi\sigma^*$ states in many model biochromophores. Due to their location in the exit dissociation channel, these intersections are expected to influence the vibrational state distributions and the kinetic energy release of the photofrag-

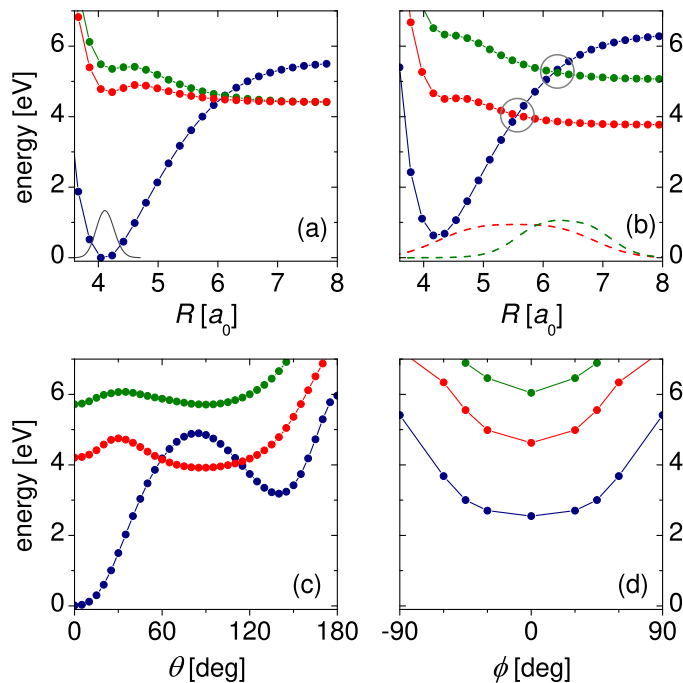


FIG. 2: One-dimensional potential energy cuts of the 1A_1 (blue), 1A_2 (red), 1B_1 (green) electronic states as a function of the pyrrolyl–H Jacobi distance R . For each electronic state a cut at the ground state pyrrole equilibrium [panel (a)] and a cut at the pyrrolyl fragment equilibrium [panel (b)] are shown. Conical intersections are marked with circles, and the respective local diabatic couplings are exemplified with dashed lines: The red line corresponds to ten times the \tilde{X}/A_2 coupling induced by a displacement by 1 along the mode $Q_{a_2}(2)$; the green line corresponds to twice the \tilde{X}/B_1 coupling induced by a displacement by 30° along the out-of-plane H bending. Shown in panel (c) are the potential energy cuts along the polar angle θ for $\phi = 0^\circ$; vibrational modes of pyrrolyl are fixed at the MEP defined in Sect. II for $R = 4.15 a_0$. Shown in panel (d) are the potential energy cuts along the azimuthal angle ϕ for $\theta = 40^\circ$; vibrational modes of pyrrolyl are fixed at the MEP defined in Sect. II for $R = 4.15 a_0$.

ments, but they can also have an unexpected impact on the absorption spectra.³⁰ The CIs are encountered at C_{2v} geometries and involve states belonging to different irreps of the C_{2v} point group. They are symmetry allowed, and the dissociation coordinate R acts as a tuning mode. The coupling modes have a_2 symmetry for the \tilde{X}/A_2 intersection and b_1 symmetry for the \tilde{X}/B_1 intersection.

The CIs between the repulsive $\pi\sigma^*$ states and the attractive ground state \tilde{X} are expected

to have a strong impact on the photoreactivity of the model biochromophores. Incidentally, these CIs are the primary reason why the weakest part of the first absorption band at the longest wavelength has been probed by many experimental and theoretical groups.^{28,29,31–34} Indeed, the photodissociation of pyrrole in the lowest $^1\pi\sigma^*$ states below 5.7 eV has been extensively studied in the frequency- and time domain. The H-atom Rydberg tagging photofragment translational spectroscopy studies of Ashfold and co-workers^{13,32,35} interrogated the formation of the fragment hydrogen atom for a series of photolysis wavelengths λ between 254 nm and 190 nm. Their key observable is the total kinetic energy release (TKER) in the photodissociation reaction. In the two fragment channels H+pyrrolyl, the TKER spectra are equivalent to the rovibrational distributions of the pyrrolyl radical. The observed kinetic energy distributions are bimodal,³² with the fast (average $E_{\text{kin}} \geq 4000 \text{ cm}^{-1}$) and slow (average $E_{\text{kin}} \sim 1000 \text{ cm}^{-1}$) components well resolved for most wavelengths. The angular distributions of the fast fragments are typically anisotropic (non-zero recoil anisotropy parameter), while the slow components correspond to isotropically distributed fragments. These observations lead experimentalists^{13,31,32} to associate the fast products with direct dissociation in the excited electronic states and to assume that the slow products emerge as a result of statistical decomposition in the ground electronic state reached via internal conversion. The principal observation regarding the fast component of the TKER distributions is that the $^1\pi\sigma^*$ photodissociation entails selective population of a limited number of vibrational levels of pyrrolyl.³² For this reason, the photodissociation of pyrrole in the long wavelength tail of the first absorption band system has been characterized by a high degree of vibrational adiabaticity in the modes orthogonal to the dissociation path.³² In fact, the vibrationally adiabatic dynamics was found to be a characteristic property of the photodissociation in the $^1\pi\sigma^*$ states of several model biochromophores.⁷

Early time-resolved pump-probe measurements performed at $\lambda = 250 \text{ nm}$, established two well separated dissociation time constants, $\tau_d = 110 \text{ fs}$ and $\tau_d = 1.1 \text{ ps}$.³⁶ The radical co-fragments can be formed in either ground (correlating with $\pi\sigma^*$) or excited (correlating with \tilde{X}) electronic states, and it appears reasonable to associate the fast fragments with the electronically excited channel and the slow fragments with the ground-state radicals. However, the experimental evidence is controversial, and the formation of the electronically excited pyrrolyl has never been confirmed. Recent ultrafast time-resolved experiments at the photolysis wavelength of 250 nm detected the fast dissociation time of $\tau_d = 126 \text{ fs}$ and

associated it with the tunneling lifetime.²⁸ The same group found a much shorter dissociation time of $\tau_d = 46$ fs for $\lambda = 238$ nm. Even shorter dissociation time constants of 12 fs and 19 fs for $\lambda = 242$ nm and 236 nm, respectively, were found in the time resolved photoelectron measurements of Wu et al.³⁷

Theoretical studies of the electronic structure, spectroscopy, and photochemistry of pyrrole are numerous. Accurate ab initio calculations of vertical excitation energies clarified the ordering of the low-lying valence and Rydberg excited states.^{29,33,34,38-40} The branching ratios of several arrangement channels including ring deformation and ring opening reactions were simulated using classical trajectory surface hopping algorithm.^{34,40} Multi-dimensional multi-state quantum dynamics investigations of the ultrafast electronic population dynamics in the excited states of pyrrole was performed by Köppel, Lischka, and co-workers³⁸ and, very recently, by Neville and Worth⁴¹ who constructed an ab initio Hamiltonian, based on an extension of the quadratic vibronic coupling model, including the first seven electronic states and valid from the Franck-Condon region to the asymptotic dissociation channels. These studies yielded important insight into the radiationless decay dynamics of pyrrole, provided new vibronic assignments of the intense features in the first absorption band between 5.5 eV and 6.5 eV, and gave an estimation of the dissociation time constants in the $1^1A_2(\pi\sigma^*)$ state between 35 fs and 133 fs, in a general agreement with various experimental results.^{37,41}

The final state analysis was reported in the quantum mechanical reduced-dimensionality calculations of Domcke and co-workers who employed complete-active-space self-consistent field (CASSCF) and multi-reference configuration-interaction (MRCI) methods and constructed diabatic potential energy models including the N-H stretching coordinate as well as the most important coupling modes at the exit channel CIs.^{16,17,33,42} These authors performed three-dimensional time dependent wave packet calculations and concentrated on the dependence of the branching ratios of the electronic dissociation channels on the initial vibrational state of the system. The formation of photofragments has been recently analyzed using the Ehrenfest algorithm within the framework of the classical mechanical ‘direct dynamics’ with all 24 degrees of freedom included.⁴³ Both the TKER and the angular distributions were calculated without the construction of global potential energy surfaces of the lowest four electronic states, and some qualitative features of the experimental distributions were successfully reproduced. The numerical accuracy is difficult to estimate, however, as the calculations were performed at a CASSCF level with a modest active space and a limited

atomic basis set.

Several key questions require further investigation going beyond the previous extensive experimental and theoretical analysis. In the frequency domain, the absorption spectrum of the two lowest $\pi\sigma^*$ states of pyrrole remains virtually unexplored; the only published spectra were calculated by Roos et al. 15 years ago.²⁹ Furthermore, the TKER distributions measured by Ashfold and co-workers at specific photolysis wavelengths¹³ have never been completely assigned nor reproduced theoretically. The actual extent of vibrational adiabaticity, postulated by the experimentalists for the photodissociation in the $\pi\sigma^*$ states, remains unknown. In the time domain, the tunnelling contribution to the sub-picosecond dissociation in the $1^1A_2(\pi\sigma^*)$ state is not quantified.

This is the first of two papers which explore in detail the dissociation of pyrrole photoexcited into the states $1^1A_2(\pi\sigma^*)$ and $1^1B_1(\pi\sigma^*)$. New high level ab initio calculations have been performed on a coordinate grid which uniformly covers the inner FC zone and the asymptotic region of separated H-atom and pyrrolyl. These calculations serve as a basis for constructing a 24 dimensional (24D) molecular Hamiltonian in a local quasi-diabatic representation in which quantum dynamical calculations are performed. The Hamiltonian utilizes the reaction path formalism⁴⁴ extended to three electronic states and the constructed diagonal quasi-diabatic potentials are chosen harmonic only in the degrees of freedom of the pyrrolyl fragment. The coordinate dependence of the transition dipole moment (TDM) vectors is explicitly included within the Herzberg-Teller framework⁴⁵ in order to allow direct excitation of these optically dark states. The primary goal of this work is to provide a comprehensive picture of the photodissociation in the $\pi\sigma^*$ states: To investigate the weak diffuse absorption bands, to assign them vibrational quantum numbers, to explore the photodissociation time scales, and to analyze the features of the resulting TKER distributions. The emphasis in the present paper is on the dissociation in the state $1^1A_2(\pi\sigma^*)$. Its coupling to other electronic states is relatively weak,³⁰ and it is justified to treat it in isolation. However, the dissociation in the coupled states $\tilde{X}/1^1A_2(\pi\sigma^*)$ is briefly considered for completeness. It is the second paper of the series which extensively deals with the multistate effects in connection with the photodissociation dynamics in the second excited state $1^1B_1(\pi\sigma^*)$.

The second goal of this study is the development of a simplified computational scheme within which the diffuse absorption in the repulsive $\pi\sigma^*$ states and the subsequent sub-picosecond formation of the photofragments can be quantitatively analyzed. Two approxi-

mation schemes are introduced, one for the absorption spectra (approximated as a convolution of the absorptions due to the departing H-atom and due to the pyrrolyl ring) and one for the TKER distributions (obtained via the adiabatic mapping of the FC excitation onto the vibrational states of the free pyrrolyl). The principal methodological aim is to propose methods which require a minimal ab initio input and a numerical effort not exceeding that of a FC factor calculation for a polyatomic molecule. The methods explicitly base on the vibrational adiabaticity of the dissociation dynamics.^{7,28}

The remainder of the paper is organized as follows: The design of the 24D molecular Hamiltonian comprising the states \tilde{X} , $1^1A_2(\pi\sigma^*)$, and $1^1B_1(\pi\sigma^*)$, including the details of the electronic structure calculations, is presented in Sect. II. The methodology of the calculations of the absorption spectrum using the quantum dynamics and the convolution approximation is summarized in Sect. III and in the Appendix, while the approach to the photofragment distributions is described in Sect. IV. The results of the calculations of the photodissociation dynamics are given in Sects. V and VI. The emphasis here is on the dissociation in the isolated state $1^1A_2(\pi\sigma^*)$; the dissociation in the coupled pair $\tilde{X}/1^1A_2(\pi\sigma^*)$ is also considered and the intriguing effects arising in the two-state dynamics are discussed. The results are summarized in Sect. VII.

II. CONSTRUCTION OF THE MOLECULAR HAMILTONIAN

A. The form of the 24 dimensional Hamiltonian

The molecular Hamiltonian,

$$\hat{H} = \begin{pmatrix} \hat{T} & 0 & 0 \\ 0 & \hat{T} & 0 \\ 0 & 0 & \hat{T} \end{pmatrix} + \begin{pmatrix} V^X & V^{XA_2} & V^{XB_1} \\ V^{XA_2} & V^{A_2} & V^{A_2B_1} \\ V^{XB_1} & V^{A_2B_1} & V^{B_1} \end{pmatrix}, \quad (1)$$

is set in the basis of three locally diabatic electronic states $\tilde{X}A_1$ (abbreviated as X or A_1), A_2 , and B_1 ; the labels denote the state symmetries at C_{2v} geometries. Pyrrole is described using (a) 3 Jacobi coordinates $\mathbf{R} \equiv (R, \theta, \phi)$ of the dissociating H-atom with respect to the center of mass of the pyrrolyl fragment (the so-called ‘disappearing modes’; see Fig. 3) and (b) 21 dimensionless normal modes \mathbf{Q} of pyrrolyl, calculated at the equilibrium geometry of the fragment (the so-called ‘non-disappearing modes’). The normal modes \mathbf{Q}

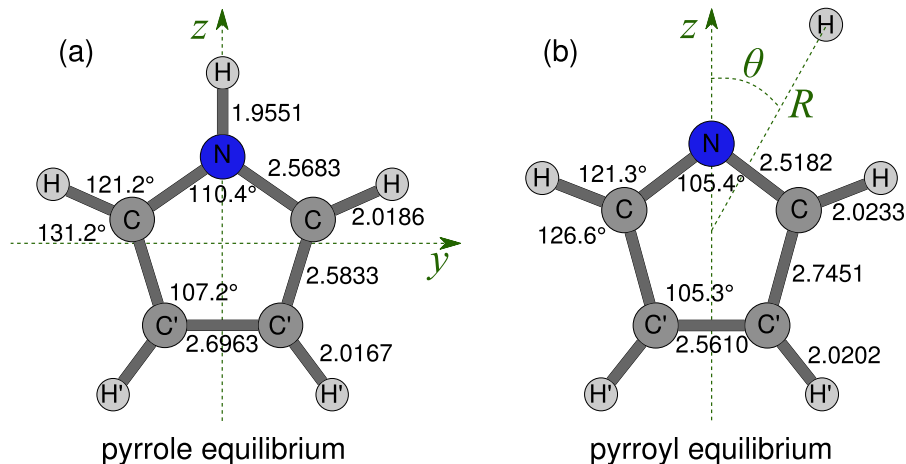


FIG. 3: The SA-CASSCF(8,7)/CASPT2/aug-cc-pVTZ+ equilibrium geometries of the ground states of pyrrole and pyrrolyl are shown in panel (a) and (b). Bond distances are reported in a_0 . Also shown are the Cartesian coordinate system used in the calculation of the TDMs [panel (a); axis x is perpendicular to the molecular plane] and the definition of the disappearing modes R and θ [panel (b); the azimuthal angle ϕ is defined relative to the y axis in the yz plane].

are partitioned into four blocks according to the irreducible representations Γ of the C_{2v} point group, $\mathbf{Q} = \{\mathbf{Q}_{a_1}, \mathbf{Q}_{a_2}, \mathbf{Q}_{b_1}, \mathbf{Q}_{b_2}\}$.

The kinetic energy operator in Eq. (1) is set in the body-fixed principal axis frame for the zero total angular momentum of pyrrole (atomic units are used hereafter):

$$\begin{aligned} \hat{T} &= \hat{T}_R + \hat{T}_Q \\ &= -\frac{1}{2\mu} \frac{\partial^2}{\partial R^2} + \frac{\mathbf{j}^2}{2\mu R^2} + \frac{1}{2} \left(\frac{j_x^2}{I_x} + \frac{j_y^2}{I_y} + \frac{j_z^2}{I_z} \right) - \frac{1}{2} \sum_{\substack{\Gamma=a_1, a_2, \\ b_1, b_2}} \sum_i^\Gamma \omega_\Gamma(i) \frac{\partial^2}{\partial Q_\Gamma(i)^2}. \end{aligned} \quad (2)$$

The first three terms refer to the kinetic energy of the disappearing modes \hat{T}_R : The kinetic energy of the relative motion of H-atom and pyrrolyl (μ is the corresponding reduced mass), the orbital motion of the H-atom, and the rotational motion of the rigid pyrrolyl ring, respectively ($\mathbf{j} = (j_x, j_y, j_z)$ is the pyrrolyl angular momentum operator and the inertia constants I_x , I_y and I_z are evaluated at pyrrolyl equilibrium). The term \hat{T}_Q refers to pyrrolyl vibrations; the sum \sum_i^Γ is over the vibrational modes i belonging to an irrep Γ . The C_{2v} symmetric pyrrolyl ring lies in the yz -plane, with z being the C_2 axis (see Fig. 3).

All the elements of the quasi-diabatic potential energy matrix in Eq. (1) are constructed

as sums of two groups of terms:

$$\mathbf{V}(\mathbf{R}, \mathbf{Q}) = \mathbf{W}_R(\mathbf{R}) + \mathbf{W}_Q(\mathbf{Q}|R) \quad (3)$$

The matrix elements $\mathbf{W}(\mathbf{R})$ depend on the three disappearing modes (R, θ, ϕ) only. The corresponding three-dimensional (3D) functions are spline interpolations of the quasi-diabatic energies on a dense ab initio coordinate grid in \mathbf{R} . The matrix elements $\mathbf{W}(\mathbf{Q}|R)$ depend on the 21 non-disappearing modes \mathbf{Q} . These 21D functions are constructed in the spirit of the vibronic coupling model,⁴⁶ with the pyrrolyl treated as a semirigid ring using quadratic Hamiltonians, and the model parameters depending on the interfragment distance R . The structure of the resulting Hamiltonian is similar to that chosen in the work of Neville and Worth.⁴¹ The difference is in the choice of the disappearing modes \mathbf{R} (here: three Jacobi coordinates), in the choice of the coordinate grids (here: a coordinate grid uniformly covering the complete dissociation path), and in the construction of the matrices $\mathbf{W}(\mathbf{R})$ and $\mathbf{W}(\mathbf{Q}|R)$ (here: spline interpolations on the uniform grid, no switching functions).

The diagonal elements of the potential matrix have the form ($\alpha = X, A_2, B_1$):

$$\begin{aligned} V^\alpha(R, \theta, \phi, \mathbf{Q}) &= W_R^\alpha(\mathbf{R}) + W_Q^\alpha(\mathbf{Q}|R) \\ &= V_{1D}^\alpha(R) + V_{\text{ang}}^\alpha(R, \theta, \phi) \\ &\quad + \sum_i^{a_1} \kappa_i^\alpha(R) Q_{a_1}(i) + \frac{1}{2} \sum_\Gamma \sum_{i,j}^\Gamma \gamma_{\Gamma,ij}^\alpha(R) Q_\Gamma(i) Q_\Gamma(j). \end{aligned} \quad (4)$$

$V_{1D}^\alpha(R)$ is the one-dimensional potential energy function along R at the fragment equilibrium geometry $\theta, \phi = 0$ and $\mathbf{Q} = \mathbf{0}$; $V_{\text{ang}}^\alpha(R, \theta, \phi)$ are distance-dependent angular potentials, set to zero at $\theta, \phi = 0$; $\kappa_i^\alpha(R)$ and $\gamma_{ij}^\alpha(R)$ are the R -dependent gradients (vanishing for all modes but a_1), and the R -dependent Hessians with respect to the normal modes, evaluated at $\mathbf{Q} = \mathbf{0}$. Hessian matrices γ^α are four-block diagonal: $\gamma^\alpha = \gamma_{a_1}^\alpha \oplus \gamma_{a_2}^\alpha \oplus \gamma_{b_1}^\alpha \oplus \gamma_{b_2}^\alpha$.

The off-diagonal diabatic coupling elements $V^{\alpha\beta}$ are

$$\begin{aligned} V^{\alpha\beta}(R, \theta, \phi, \mathbf{Q}) &= W_R^{\alpha\beta}(\mathbf{R}) + W_Q^{\alpha\beta}(\mathbf{Q}|R) \\ &= V_{\text{ang}}^{\alpha\beta}(R, \theta, \phi) + \sum_i^{\Gamma_\alpha \times \Gamma_\beta} \lambda_i^{\alpha\beta}(R) Q_{\Gamma_\alpha \times \Gamma_\beta}(i), \end{aligned} \quad (5)$$

The elements $V_{\text{ang}}^{\alpha\beta}(R, \theta, \phi)$ are constructed on the coordinate grid by applying the regularized diabaticization procedure of Köppel et al.⁴⁷ to the raw adiabatic ab initio energies. Next, the matrix elements are spline interpolated. While they do not have an analytical

representation, near CIs the construction algorithm ensures that they follow the lowest allowed orders in the symmetry-adapted spherical harmonics, namely $V_{\text{ang}}^{A_1A_2} \sim \sin^2 \theta \sin(2\phi)$, $V_{\text{ang}}^{A_1B_1} \sim \sin \theta \cos \phi$. The \mathbf{Q} -dependent couplings are linear in the vibrational modes, and the X/A_2 and X/B_1 coupling terms are promoted by modes of a_2 and b_1 symmetry, respectively. The matrix element $V^{A_2B_1}$ between the states A_2/B_1 is not included in the quantum mechanical calculations.

The quasi-diabatic representation used in the Hamiltonian Eq. (1) is local, i.e. a given off-diagonal matrix element is non-zero only in the vicinity of the respective conical intersection, where a non-vanishing transition probability between quasi-diabatic states is expected. For the second term in Eq. (5), this is achieved by using the following functional form for the coupling strength $\lambda_i^{\alpha\beta}$:

$$\lambda_i^{\alpha\beta}(R) = \lambda_{\text{CI},i}^{\alpha\beta} \exp\left(-\left|\frac{R - R_{\text{CI}}^{\alpha\beta}}{\Delta}\right|^n\right), \quad (6)$$

where $R_{\text{CI}}^{\alpha\beta}$ is the position of a CI between $\alpha/\beta = X/A_2$ or X/B_1 . The parameters $\lambda_{\text{CI},i}^{\alpha\beta}$, Δ and n are tuned ‘by eye’ in order to obtain smooth diabatic Hessians for the coupled states. Similar attenuation functions are applied to the mixing angles of the regularized adiabatic-to-diabatic transformation in (R, θ, ϕ) .

B. Ab initio parameterization of the molecular Hamiltonian

1. Quantum chemical calculations

The matrix elements of the molecular Hamiltonian, Eqs. (1) and (4)–(6), are found from the electronic structure calculations performed using the aug-cc-pVTZ (AVTZ) basis set of Dunning⁴⁸ further supplemented with the diffuse s and p functions added to the N and H atoms of the dissociating bond (one set of s and p functions for N and two sets for H). The exponents of these functions are derived in an even tempered manner from the most diffuse s and p functions of the AVTZ basis by dividing the exponents successively by a factor of 3.0.³³ This extension is necessary to correctly describe the Rydberg character of the A_2 and B_1 states, and the resulting basis set is referred to as AVTZ+.

Calculations are performed at the CASPT2 level of theory. The reference wavefunctions are obtained from the state-averaged CASSCF calculations including the \tilde{X} , 1A_2 and 1B_1

states. The active space (eight electrons in seven orbitals) comprises five π valence molecular orbitals, three of b_1 and two of a_2 symmetry, the $9a_1(\sigma)$ and the $10a_1(3s/\sigma^*)$ orbitals. Electronic structure calculations are performed using the highest possible symmetry. In particular, the a_1 , a_2 , b_1 and b_2 blocks of the Hessian matrices are calculated separately using C_{2v} , C_2 , C_s and C'_s symmetries, respectively. Coordinate-dependent transition dipole moment functions, necessary to properly describe the optical excitation of the $\pi\sigma^*$ states from the ground electronic state, are calculated at the CASSCF level.

The construction of the Hamiltonian starts with the calculation of the minimum energy path (MEP) for the hydrogen detachment from the N-H group along the Jacobi coordinate R in the lowest excited $\pi\sigma^*$ state of the molecule, the state 1A_2 . 28 grid points in R are used between $R_{\min} = 3.5 a_0$ and $R_{\max} = 8.3 a_0$. Along this path, the molecule is constrained to C_{2v} geometries (i.e., $\theta, \phi = 0$). In the next steps, the full dimensional quasi-diabatic representation is constructed using this ‘relaxed’ path as a reference. This makes the resulting molecular Hamiltonian conceptually similar to the reaction path (or reaction surface) Hamiltonian of Miller and coworkers,⁴⁹ with the difference that a single fixed set of normal modes is used along the relaxed path.

The optimized structures of pyrrole and pyrrolyl are shown in Fig. 2. The main geometrical displacements in going from the parent to the fragment structure are an increase of the C – C' bond length (by $0.16 a_0$) and a decrease of the C' – C' distance (by $0.14 a_0$). Fig. 2 reports the one-dimensional potential energy cuts of the A_1 , A_2 and B_1 states calculated at the pyrrole and the pyrrolyl ring geometries, as a function of the Jacobi distance R . The ground state minimum is located at $R \approx 4.1 a_0$. The one-dimensional potentials for the A_2 and B_1 states show local minima at short dissociation distances, followed by barriers before the repulsive descent. The local minima are at $R = 4.23 a_0$ for the A_2 and at $R = 4.14 a_0$ for the B_1 state.

Table I summarizes the characteristic features of the three calculated electronic states of pyrrole and compares them with the available experimental data. Compared to experimental values, the present calculations underestimate the absorption origin (T_0) and the dissociation threshold (D_0) of the 1A_2 state by ~ 0.55 eV and ~ 0.65 , respectively. For the 1B_1 state, T_0 is also underestimated by ≈ 0.6 eV. The results of additional calculations and previous ab initio studies^{29,41,50,51} are reported in Table II. In multi-reference methods, the excitation energies are very sensitive to the active space and to the number of states included in the

Diabatic state	T_0	T_0 (exp)	Dissociation channel	D_0	D_0 (exp.)
$\tilde{X}^1A_1(\pi\pi)$	0.0	0.0	H(1S)/pyrrolyl(1^2A_1)	5.09	—
$1^1A_2(\pi\sigma^*)$	4.32	$<4.88^a$	H(1S)/pyrrolyl(1^2A_2)	3.40	4.07^a
$1^1B_1(\pi\sigma^*)$	5.30	5.86^b	H(1S)/pyrrolyl(1^2B_1)	3.96	$4.62 - 4.67^c$

^aRef. 32.

^bRef. 50.

^cDFT⁵² and MRCI⁵³ methods estimate the difference in the threshold energies $D_0(1^2B_1) - D_0(1^2A_2)$ to be in the range of 0.55 eV—0.60 eV.

TABLE I: Properties of the CASPT2 potential energy surfaces of the three lowest electronic states of pyrrole compared with the available experimental data: Band origins T_0 which include zero-point energies of the ground and the excited electronic states and the quantum mechanical thresholds D_0 for the diabatically correlating electronic channels. Energies are in eV.

state-averaging. Accurate energies can be obtained by performing MRCI calculations based on CASSCF wavefunctions obtained with a relatively small active space, and reducing the number of frozen orbitals in the configuration interaction. Such calculations would make the construction of the global PESs very time-consuming. On the other hand, our CASPT2 surfaces predict with good accuracy the $^1B_1 - ^1A_2$ energy gap, the difference between vertical excitation energies and dissociation energies, and the position of the conical intersections, therefore they are reliable to simulate excited state quantum dynamics with a good accuracy.

2. 3D diabatic potentials for the disappearing modes

The CASPT2 calculations of the energies of the lowest three electronic states as functions of the disappearing modes are performed using C_1 symmetry group on a three-dimensional grid (R_i, θ_j, ϕ_k) , with the nodes R_i being grid points on the relaxed path. The grid points θ_j in the polar angle cover the range $[0^\circ, 90^\circ]$ with a step of 5° ; energies for $\theta > 90^\circ$ are extrap-

TABLE II: Computed vertical excitation energies T_v and diabatic dissociation thresholds D_e of the states $1^1A_2(\pi\sigma^*)$ and $1^1B_1(\pi\sigma^*)$ compared with the previously published theoretical data (references are given in square brackets). Energies are in eV.

State	Property	CASSCF ($8_e, 7_o$) AVDZ+	CASPT2 ($8_e, 7_o$) AVTZ+	CASPT2 ($8_e, 9_o$) AVTZ+	CASPT2 ($8_e, 8_o$) AVDZ+	MRCI ($8_e, 9_o$) AVTZ+	MRCI (<i>Barbat</i>) DAVQZ	MRCI ($6_e, 5_o$) AVDZ	EOM-CCSD AVTZ+	EOM-CCSD [54]	ADC(2) [55]
$1^1A_2(\pi\sigma^*)$	T_v	4.45	4.80	4.87	5.06	4.92	5.09	5.33	5.21	5.18	4.99
	D_e	3.96	3.82	3.90	3.17	4.00	-	-	-	-	-
	T_v	5.03	5.45	5.67	5.86	5.53	5.86	6.12	5.96	5.84	5.99
$1^1B_1(\pi\sigma^*)$	D_e	4.09	4.31	5.11	-	4.70	-	-	-	-	-

olated. The grid in the azimuthal angle ϕ ranges from 0° (H-atom in the σ'_v plane) to 90° (H-atom in the σ_v plane) with a step of 15° ; energies for larger ϕ are reconstructed using C_{2v} symmetry of the pyrrolyl ring. The angular modes do not couple states \tilde{X} and A_2 at either $\phi = 0^\circ$ or 90° , and the impact of the angular modes on the dissociation dynamics of the A_2 state is exceedingly weak. For this reason, these two states can be diabaticized by a straightforward relabelling the adiabatic energies. Finally, an explicit functional form is assumed for the coupling matrix element for $\phi \neq 0, 90^\circ$, $V^{XA_2}(R, \theta, \phi) = \lambda_{\text{ang}}^{XA_2}(R) \sin^2 \theta \sin(2\phi)$, with the function $\lambda_{\text{ang}}^{XA_2}(R) = c[1 - \text{atan}((R - R_0)/\Delta R)]$. The parameters in this function are chosen ‘by eye’ in order to give smooth diabatic curves for a full range of ϕ . The energies of the states \tilde{X} and B_1 are subsequently transformed to the diabatic representation using the regularized diabatic state method of Köppel et al.⁴⁷ The function $V^{XB_1}(R_i, \theta_j, \phi_k)$ is constructed on the angular grid, with the polar angle θ being the most important coupling mode. As shown in Fig. 2(a), the shape of the V^{XB_2} coupling function is localized in proximity of the \tilde{X}/B_1 intersection.

Finally, all matrix elements set on the grid are interpolated using cubic splines. It is ensured that all potential functions become independent of the disappearing angles θ and ϕ as R goes to infinity.

Potential energy cuts along the out-of-plane Jacobi bending and the torsional angle ϕ are shown in Fig. 2(c) and (d). Accidental conical intersections between the states \tilde{X} and 1A_2 are found for quite large bending angles, $\theta \approx 60^\circ$ and $\theta \approx 115^\circ$. In the 1A_2 surface, these intersection are separated by a ~ 0.6 eV barrier from the $\theta = 0^\circ$ zone, therefore they are not easily accessible: In the quantum mechanical calculations of Sect. V, the width of initial wavefunction along θ is $\approx 5^\circ$, and there is no strong force driving the H atom across the barrier. Varying ϕ for $\theta \neq 0^\circ$, the potentials show a strong nearly parallel increase in going from $\phi = 0^\circ$ to $\phi = 90^\circ$. Indeed, the in-plane ($\phi = 90^\circ$) H-bending frequency is almost three time larger than the out-of-plane ($\phi = 0^\circ$) H-bending frequency.

Fig. 4 shows the PESs in the (R, θ) plane for $\phi = 0^\circ$ (H-atom bends out of the pyrrolyl plane; irrep b_1) and $\phi = 90^\circ$ (H-atom bends in the pyrrolyl plane; irrep b_2). The modes \mathbf{Q} are set, for each R , to the relaxed geometries in the state A_2 . The minimum of the ground electronic state is found at $R = 4.15 a_0$ and $\theta = 0^\circ$. The Jacobi coordinates R and θ are seen to be strongly mixed in the FC zone, especially at $\phi = 0^\circ$, and the potential minimum has a characteristic ‘banana’ shape indicating that the equilibrium R shifts to shorter distances

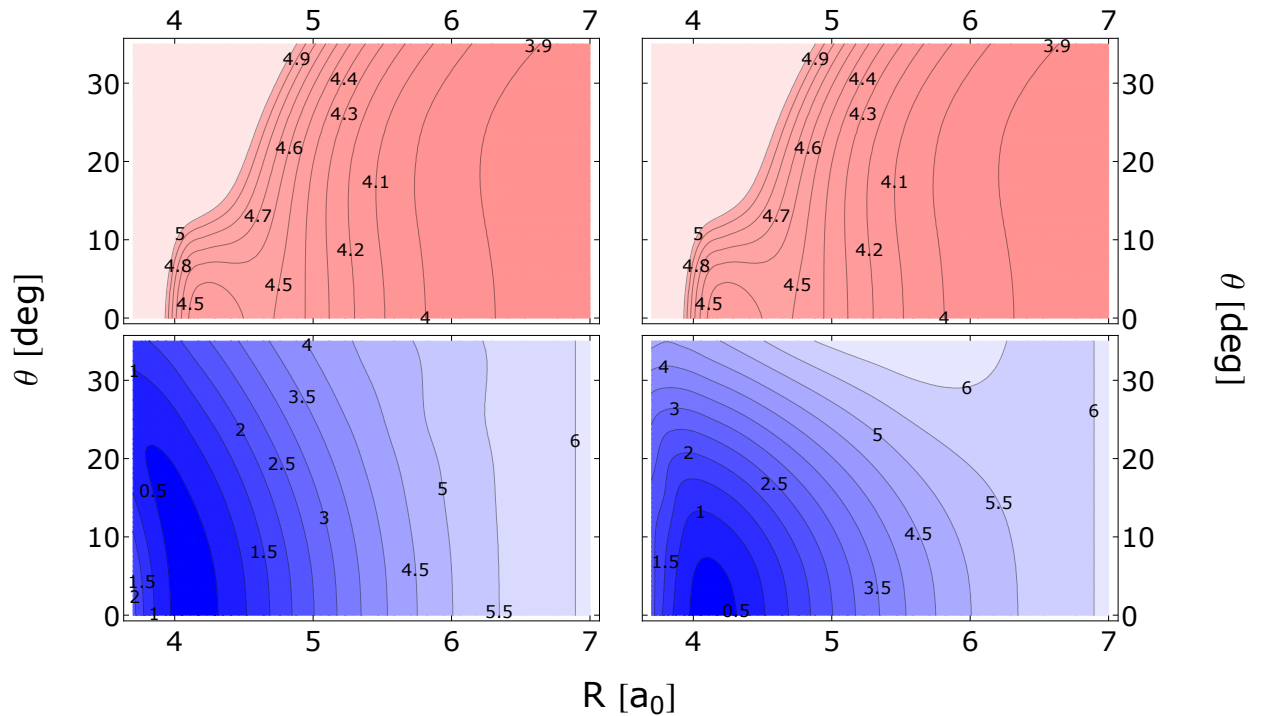


FIG. 4: Model potential energy surfaces for the states A_1 (blue, bottom) and A_2 (red, top) in the (R, θ) plane. For each distance, the normal modes are set to the relaxed values $\mathbf{Q} = \mathbf{Q}_{\text{Relax}}$. The angle ϕ is set to 0° (left panels) and 90° (right panels). Energies are reported in eV on the contour lines.

as the H-atom moves out of the pyrrolyl plane. The out-of-plane bending frequency in \tilde{X} is lower than the in-plane bending frequency: The lowest excited vibrational eigenstates in the potential $W_R^X((R, \theta, \phi))$ lie 406 cm^{-1} (one quantum of the out-of-plane bending) and 1281 cm^{-1} (one quantum of the in-plane bending) above zero-point energy.

In the A_2 state, R and θ are also mixed, and the height of the dissociation barrier, seen around $R \approx 4.7 a_0$, depends on the angle θ . However, the barrier along the straight line dissociation path with $\theta = 0$ is always lower than the barriers encountered for $\theta \neq 0$. For this reason, the H-atom departing in the A_2 state can be hardly subject to a torque along θ in the initial stages of photodissociation.

3. 21D diabatic potentials for the non-disappearing modes

The parameters of the \mathbf{Q} -dependent part of the Hamiltonian are calculated as first and second derivatives with respect to deviations from the relaxed path (MEP) in the lowest excited state A_2 . The following sequence of *ab initio* calculations was applied:

- Geometry optimization and frequency calculation for the normal modes of pyrrolyl ground state (A_2). In this way the coordinates \mathbf{Q} are defined. The pyrrolyl normal modes \mathbf{Q} are related to the Cartesian coordinates \mathbf{X} via the rectangular matrix transformation

$$Q_i = \sum_r \sqrt{\frac{\omega_i M_r}{\hbar}} U_{ir} X_r = \sum_r L_{ir} X_r, \quad i = 1, 21 \text{ and } r = 1, 27 \quad (7)$$

where M_r is the mass of the atom associated with the coordinate X_r , ω_i is the frequency of the normal mode Q_i , and $\{U_{ir}\}$ is the matrix of the eigenvectors of the mass-weighted Cartesian Hessian, after the removal of the rows corresponding to Wilson translations and rotations.

- A relaxed scan (in C_{2v} symmetry) for the A_2 state along a grid in the Jacobi distance R . This yields a set of relaxed geometries $\mathbf{Q} = \mathbf{Q}_{\min}(R)$ and the corresponding energies $V_{\text{Relax}}^\alpha(R)$ for the states A_1 , A_2 and B_1 .
- Cartesian gradient ($\{\bar{g}_i^\alpha\}$) and Hessian ($\{\bar{\gamma}_{ij}^\alpha\}$) calculations for the three states in correspondence of the points on the A_2 relaxed scan. The gradient and the Hessian are then expressed with respect to the dimensionless fragment normal modes \mathbf{Q} using the transformations

$$g_i^\alpha = \sum_r (\mathbb{L}^{-1})_{ri} \bar{g}_r^\alpha \quad (8)$$

$$\gamma_{ij}^\alpha = \sum_{rs} (\mathbb{L}^{-1})_{ri} (\mathbb{L}^{-1})_{sj} \bar{\gamma}_{rs}^\alpha, \quad (9)$$

where the variables with and without overbar refer to Cartesian coordinates and normal modes, respectively. The Hessian matrix $\{\gamma_{ij}^\alpha\}$ is directly obtained (for some blocks of $\{\gamma^\alpha\}$ a diabaticization is necessary, see below). The gradient $\mathbf{g}^\alpha(R)$, computed at $\mathbf{Q} = \mathbf{Q}_{\min}(R)$, vanishes for the A_2 states and differs from zero for the A_1 and B_1

states. $\mathbf{g}^\alpha(R)$ is used to calculate the gradient at $\mathbf{Q} = \mathbf{0}$ and the function V_{1D}^α via the equations:

$$\boldsymbol{\kappa}^\alpha(R) = \mathbf{g}^\alpha(R) - \boldsymbol{\gamma}^\alpha(R)\mathbf{Q}_{\min}(R), \quad (10a)$$

$$V_{1D}^\alpha(R) = V_{\text{Relax}}^\alpha(R) - \mathbf{Q}_{\min}^T(R)\mathbf{g}^\alpha(R). \quad (10b)$$

The quantities $V_{1D}^\alpha(R)$, $\{\kappa_i^\alpha(R)\}$ and $\{\gamma_{ij}^\alpha(R)\}$ were calculated on the grid in R and interpolated with a cubic spline. A remark is important here: In most quantum dynamical studies of photodissociation of aromatic molecules, the distance-dependent parameters are fitted with Morse, avoided crossing, or switching functions.^{33,41} Here we directly interpolate the parameters on the ab initio points, without performing any fitting procedure.

- A local diabatic representation is used for the $V^{A_1A_2}$ and the $V^{A_1B_1}$ matrix elements. The former depend linearly on the vibrational modes of a_2 symmetry, and the latter depend linearly on the vibrational modes of b_1 symmetry. Since R is a tuning mode for the A_1/A_2 and A_1/B_1 conical intersections, the a_2 block of the A_2 adiabatic Hessian and the b_1 block of the B_1 adiabatic Hessian diverge as R approaches the respective crossings. The R -dependent *diabatic* Hessians $\{\gamma_{ij}^\alpha(R)\}$ [Eq. (4)] are related to the ab initio *adiabatic* Hessians $\{\tilde{\gamma}_{ij}^\alpha(R)\}$ by the relations

$$\begin{aligned} \gamma_{ij}^{A_1}(R) &= \tilde{\gamma}_{ij}^{A_1}(R) + 2 \frac{\lambda_i^{A_1A_2}(R)\lambda_j^{A_1A_2}(R)}{V_{1D}^{A_1}(R) - V_{1D}^{A_2}(R)}, \quad \Gamma_i, \Gamma_j = a_2 \\ \gamma_{ij}^{A_1}(R) &= \tilde{\gamma}_{ij}^{A_1}(R) + 2 \frac{\lambda_i^{A_1B_1}(R)\lambda_j^{A_1B_1}(R)}{V_{1D}^{A_1}(R) - V_{1D}^{B_1}(R)}, \quad \Gamma_i, \Gamma_j = b_1 \\ \gamma_{ij}^{A_2}(R) &= \tilde{\gamma}_{ij}^{A_2}(R) - 2 \frac{\lambda_i^{A_1A_2}(R)\lambda_j^{A_1A_2}(R)}{V_{1D}^{A_1}(R) - V_{1D}^{A_2}(R)}, \quad \Gamma_i, \Gamma_j = a_2 \\ \gamma_{ij}^{B_1}(R) &= \tilde{\gamma}_{ij}^{B_1}(R) - 2 \frac{\lambda_i^{A_1B_1}(R)\lambda_j^{A_1B_1}(R)}{V_{1D}^{A_1}(R) - V_{1D}^{B_1}(R)}, \quad \Gamma_i, \Gamma_j = b_1. \end{aligned} \quad (11)$$

When the electronic energies are large compared to the coupling strength, the differences between the adiabatic and the diabatic Hessian are negligible. In the intersection region, the terms $\lambda_i\lambda_j/\Delta V$ in Eq. (11) compensate the divergence of the adiabatic Hessian, making the diabatic matrix elements smooth functions of R . The local character of the diabatic functions is expressed in the R -dependence of the coupling coefficients λ_i given in Eq. (6).

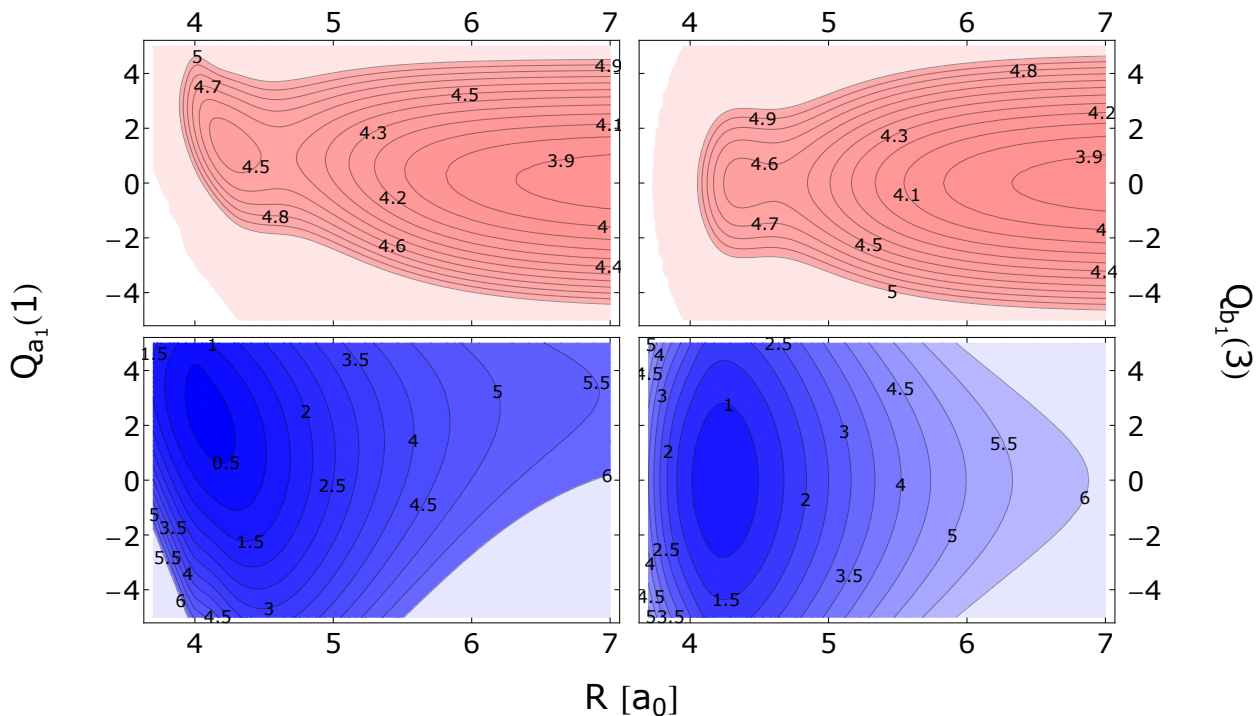


FIG. 5: Model potential energy surfaces for the states A_1 (blue, bottom) and A_2 (red, top) in the $(R, Q_1^{a_1})$ plane (left panels) and in the $(R, Q_3^{b_1})$ plane (right panels). All the other normal modes are set to the value of zero ($\mathbf{Q} = \mathbf{0}$), corresponding to the pyrrolyl A_2 equilibrium. Energies are reported in eV on the contour lines.

Vibrational frequencies calculated at the A_1 minimum, at the A_2 optimized local minimum and at the pyrrolyl ground state geometry are reported in Table III. The normal modes at the ground state pyrrolyl minimum are listed in order of increasing frequency. The frequencies at the A_1 minimum and excited states local minima are ordered according to the pyrrolyl normal mode to which they correlate. This does not always correspond to an increasing frequency order, because of the Duschinsky mixing, especially between modes of similar frequencies. Three pyrrole normal modes, of symmetries a_1 , b_1 and b_2 , disappear into inter-fragment translation and rotations, so they are not present in pyrrolyl.

Table IV gives the dimensionless coupling strength parameters $\kappa = \lambda/\omega$ for the coupling modes of a_2 and b_1 symmetries, respectively. The frequency ω is taken to be the frequency calculated at the respective conical intersections.

Fig. 5 shows two cuts of the PESs for A_1 and A_2 . The cuts include R and a normal

a_1 modes				b_2 modes									
Mode	pyrrolyl minimum	pyrrole local 1A_2 minimum	pyrrole minimum	$\mu_{x,i}^{B_1}$	$\mu_{y,i}$	$\mu_{z,i}$	Mode	pyrrolyl minimum	pyrrole local 1A_2 minimum	pyrrole minimum	$\mu_{x,i}^{A_2}$	$\mu_{y,i}$	$\mu_{z,i}$
$Q_{a_1}(1)$	932	908	939 (881)	0.0074	-	-	$Q_{b_2}(1)$	710	783	930 (865)	-0.0223	-	-
$Q_{a_1}(2)$	1106	1124	1230 (1144)	0.0042	-	-	$Q_{b_2}(2)$	997	1045	1143 (1048)	-0.0041	-	-
$Q_{a_1}(3)$	1163	1155	1089 (1016)	0.0066	-	-	θ $\phi=90^\circ$	-	1029	1200 (1134)	-0.3349	-	-
$Q_{a_1}(4)$	1268	1255	1164 (1074)	0.0004	-	-	$Q_{b_2}(3)$	1156	1321	1585 (1422)	0.0311	-	-
$Q_{a_1}(5)$	1558	1659	1615 (1467)	-0.0127	-	-	$Q_{b_2}(4)$	1408	1421	1420 (1287)	0.0015	-	-
$Q_{a_1}(6)$	1655	1584	1509 (1382)	-0.0192	-	-	$Q_{b_2}(5)$	1474	1545	1670 (1530)	0.0166	-	-
$Q_{a_1}(7)$	3369	3385	3383 (3129)	-0.0002	-	-	$Q_{b_2}(6)$	3362	3382	3383 (3129)	-0.0111	-	-
$Q_{a_1}(8)$	3396	3409	3417 (3145)	0.0045	-	-	$Q_{b_2}(7)$	3376	3395	3404 (3145)	0.0102	-	-
R	-	2608	3915 (3531)	-0.1202	-	-							

b_1 modes				a_2 modes									
Mode	pyrrolyl minimum	pyrrole local 1A_2 minimum	pyrrole minimum	$\mu_{y,i}^{A_2}$	$\mu_{z,i}^{B_1}$	$\mu_{x,i}$	Mode	pyrrolyl minimum	pyrrole local 1A_2 minimum	pyrrole minimum	$\mu_{x,i}$	$\mu_{y,i}^{B_1}$	$\mu_{z,i}^{A_2}$
θ $\phi=0^\circ$	-	616	362 (474)	-0.33	-0.35	-	$Q_{a_2}(1)$	533	543	636 (618)	-	0.0046	-0.0231
$Q_{b_1}(1)$	586	533	634 (601)	-	0.0016	-0.0360	$Q_{a_2}(2)$	861	895	715 (710)	-	0.0033	0.0258
$Q_{b_1}(2)$	757	785	763 (721)	-	-0.0263	-0.0364	$Q_{a_2}(3)$	932	969	909 (869)	-	0.0095	0.0340
$Q_{b_1}(3)$	867	941	878 (826)	-	-0.0223	0.0186							

TABLE III: CASPT2 frequencies (cm^{-1}) of the vibrational modes $Q_{\Gamma}(i)$ in the pyrrolyl minimum in increasing order for four irreps of the C_{2v} group. Also shown are the frequencies of pyrrole in the FC zone including the local minimum of the state ${}^1A_2(\pi\sigma^*)$ and the global minimum of the state \tilde{X} . Entries denoted R , θ , $\phi = 0^\circ$, and θ , $\phi = 90^\circ$ refer to the disappearing modes of pyrrole [stretching vibration; out-of-plane bending, and in-plane bending]. Available experimental values, taken from Ref. ?, are shown in parenthesis. Herzberg-Teller coefficients of the TDMs with \tilde{X} in the FC zone, $\mu_{x,y,z}^{A_2}$ and $\mu_{x,y,z}^{B_1}$, are given in the last three columns for each symmetry block.

Mode	λ_c	ω_c	κ_c
$\tilde{X}/^1A_2$ intersection			
$Q_{a_2}(1)$	574.0	551.8	1.04
$Q_{a_2}(2)$	759.0	895.7	0.85
$Q_{a_2}(3)$	213.0	940.3	0.23
$\tilde{X}/^1B_1$ intersection			
θ	19751.00	854.00	23.12
$Q_{b_1}(1)$	1151.00	823.6	1.40
$Q_{b_1}(2)$	600.00	765.2	0.78
$Q_{b_1}(3)$	265.00	875.3	0.30

TABLE IV: Vibrational frequencies $\omega(i)$ (in cm^{-1}), coupling strengths λ_i (in cm^{-1}), and the dimensionless coupling strength parameters $\kappa_c = \lambda_c/\omega_c$ for the vibrational modes of a_2 symmetry at the $\tilde{X}/^1A_2$ conical intersection, and for the vibrational modes of b_1 symmetry at the $\tilde{X}/^1B_1$ conical intersection. For the angle θ , λ_θ is evaluated as a gradient $\partial V/\partial(\sin \theta)$ at the intersection.

mode, totally symmetric in the left panels ($Q_{a_1}(1)$, 932 cm^{-1}) and non-totally symmetric in the right panels ($Q_{b_1}(3)$, 867 cm^{-1}). All the other modes are set to the pyrrolyl A_2 minimum, $\mathbf{Q} = \mathbf{0}$. The $Q_{a_1}(1)$ mode is the most displaced mode between the parent and the fragment equilibrium geometries. For a given electronic state, as R moves, the position of the minimum along R changes strongly. The relaxed PES for a state can be obtained from the $\mathbf{Q} = \mathbf{0}$ cut, after displacements along a_1 modes only. In the $(R, Q_{a_1}(1))$ cut, the minimum of the A_1 state is located at $Q_{a_1}(1) = 2.24$. Classically speaking, this is the initial point for the dynamics on the A_2 surface, and it is quite displaced from the relaxed path. Therefore, a large degree of correlation can be expected between the motions along R and along $Q_{a_1}(1)$ (and, more in general, between R and the a_1 modes).

In contrast, the coupling between the totally symmetric R and the non-totally symmetric modes is weak [Fig. 4 (right panel)]. The contour plot shows the diabatic potential in the space spanned by R and the mode $Q_{b_1}(2)$. At the C_{2v} FC geometry, the non totally symmetric modes are not displaced upon vertical excitation, the potential of the excited state is stationary relative to the non-totally symmetric distortions, and the Hessian at

$\mathbf{Q}^\Gamma = \mathbf{0}$ ($\Gamma \neq a_1$) is positive definite. Thus, following the excitation of the A_2 state, the initial wave packet is exposed to the forces acting only along the a_1 coordinates.

C. Ab initio transition dipole moment functions

The transition dipole moment function $\boldsymbol{\mu}(\mathbf{R}, \mathbf{Q})$ for the ${}^1A_2 \leftarrow \tilde{X}$ excitation was approximated using a Herzberg-Teller expansion in which the coordinate dependence of $\boldsymbol{\mu}(\mathbf{R}, \mathbf{Q})$ is truncated at linear deviations from the FC geometry:

$$\boldsymbol{\mu}(\mathbf{R}, \mathbf{Q}) \approx \boldsymbol{\mu}_R(\mathbf{R}) + \boldsymbol{\mu}_Q(\mathbf{Q}). \quad (12)$$

The symmetry properties of $\boldsymbol{\mu}^{A_2}$ are crucial for calculating and understanding the absorption spectra and the photofragment distributions discussed in this work.

The ${}^1A_2 \leftarrow \tilde{X}$ transition is forbidden by symmetry at C_{2v} geometries. In order to vibronically allow x -, y - and z -polarized transitions, the molecule has to undergo distortions of b_2 , b_1 and a_2 symmetry, respectively. Note that the b_1 and b_2 distortions include also the displacements along θ at $\phi = 0$ and $\phi = 90^\circ$, respectively. The lowest order expansion of the components of $\boldsymbol{\mu}^{A_2}(\mathbf{R}, \mathbf{Q})$ around the minimum of S_0 , compatible with Eq. (12), reads as

$$\mu_x^{A_2}(\mathbf{R}, \mathbf{Q}) = \mu_{x,\theta}^{A_2}(R_{\text{FC}}) \sin(\theta) \sin(\phi) + \sum_{\Gamma_i=b_2} \mu_{x,i}^{A_2}(R_{\text{FC}}) Q_{b_2}(i), \quad (13a)$$

$$\mu_y^{A_2}(\mathbf{R}, \mathbf{Q}) = \mu_{y,\theta}^{A_2}(R_{\text{FC}}) \sin(\theta) \cos(\phi) + \sum_{\Gamma_i=b_1} \mu_{y,i}^{A_2}(R_{\text{FC}}) Q_{b_1}(i), \quad (13b)$$

$$\mu_z^{A_2}(\mathbf{R}, \mathbf{Q}) = \sum_{\Gamma_i=a_2} \mu_{z,i}^{A_2}(R_{\text{FC}}) Q_{a_2}(i). \quad (13c)$$

The angular functions are chosen to coincide with the real spherical harmonics p_x and p_y . The coefficients in these equations are essentially the derivatives of the TDM components with respect to the pyrrolyl normal modes. Their dependence on the interfragment distance R is suppressed: All coefficients, given in Tables IV–VI, are evaluated at the FC point R_{FC} at the CASSCF level of theory. The modes which significantly mediate the excitation of the state ${}^1A_2(\pi\sigma^*)$ are the bending mode θ for μ_x and μ_y , as well as the out of plane mode $Q_{a_2}(3)$ of a_2 symmetry.

Strictly speaking, the Herzberg-Teller expansion in Eqs. (12) and (13) is applicable to the adiabatic rather than diabatic states. In the globally diabatic representations, the TDMs

are often taken coordinate independent, with different diabats distinguished by their having ‘negligible TDM’ or ‘large TDM’;^{56,57} such diabaticization scheme was employed by Neville and Worth.⁴¹ Its consistent realization requires, however, that all important intensity lending bright electronic states are included in the calculation. Only the lowest $\pi\sigma^*$ states are considered in this work, and the $\pi\pi^*$ states — carrying the oscillator strength at the FC geometry — are missing. Moreover, the CI $1^1A_2(\pi\sigma^*)/\tilde{X}$ is located outside the FC zone and is diabaticized locally: The 2×2 adiabatic-to-diabatic matrix parametrized by the coordinate dependent mixing angle smoothly becomes diagonal as the interfragment distance R moves away from intersection. In the locally diabatic representation, the adiabatic and the diabatic states in the FC zone nearly coincide, and the Herzberg-Teller expansion, with the coefficients obtained directly from the electronic structure calculations, is justified.

III. CALCULATIONS OF THE ABSORPTION SPECTRA

A. Quantum mechanical calculations

The linear absorption spectrum for the transition $1^1A_2(\pi\sigma^*) \leftarrow \tilde{X}^1A_1(\pi\pi)$ is calculated quantum mechanically. The calculations are performed using the molecular Hamiltonian of Eq. (1). Up to 12 vibrational modes are simultaneously included in the dynamics, in addition to the disappearing coordinates; the remaining degrees of freedom are frozen.

The initial state of the parent molecule, $\Psi_0(\mathbf{R}, \mathbf{Q})$, is the ground vibrational state of the Hamiltonian $\hat{T} + V^X$ with energy E_0 ; this Hamiltonian refers to the lowest locally diabatic electronic state. The wave function $\Psi_0(\mathbf{R}, \mathbf{Q})$ is strongly localized near $R = R_{\text{FC}} \approx 4.1 a_0$, and the off-diagonal diabatic coupling matrix elements $V^{\alpha\beta}$ can be safely neglected. The molecular state immediately after photoexcitation is given by

$$\Phi_\epsilon(0) = (\boldsymbol{\mu}^{A_2}(\mathbf{R}, \mathbf{Q}) \cdot \hat{\epsilon}) \Psi_0(\mathbf{R}, \mathbf{Q}), \quad (14)$$

where $\hat{\epsilon}$ is the polarization vector of the electric field of the incident laser. At time $t = 0$, only the state A_2 is populated.

The absorption spectra are calculated using the MCTDH code.^{58,59} First, the autocorrelation function,

$$S_\epsilon(t) = \langle \Phi_\epsilon(0) | \exp(-i\hat{H}t) | \Phi_\epsilon(0) \rangle, \quad (15)$$

is evaluated via a propagation on a discrete time grid. Next, the spectrum is calculated using the Fourier transform of $S_\epsilon(t)$:

$$\sigma_\epsilon(E_{\text{ph}}) = \frac{E_{\text{ph}}}{2\epsilon_0 c} \int_{-\infty}^{\infty} S_\epsilon(t) e^{iE_{\text{ph}}t} dt. \quad (16)$$

The photon energy is measured relative to the energy E_0 of the state $\Psi_0(\mathbf{R}, \mathbf{Q})$. Averaging over the orientations of the electric field gives the total absorption spectrum

$$\sigma_{\text{tot}}(\omega) = \frac{1}{3} \sum_{\epsilon=x,y,z} \sigma_\epsilon(E_{\text{ph}}) \quad (17)$$

The parameters of the quantum mechanical calculations discussed below are summarized in Table V. The active vibrational coordinates, the vertical excitation energy, the initial state and the intensity at the absorption maximum are indicated. Table VI reports the parameters of the MCTDH calculation.

B. Absorption spectrum as a convolution

The quantum mechanical calculations described in Sect. III A can be considerably simplified because the dissociation dynamics in the $\pi\sigma^*$ states is mainly direct, and the initial stages of the time evolution in the excited state reveal the shape of the absorption spectrum. The N—H stretching frequency in the ground electronic state is large, $\sim 3915 \text{ cm}^{-1}$, and the wave function $\Psi_0(\mathbf{R}, \mathbf{Q})$ of the parent molecule is localized within a narrow interval $\Delta R \approx 0.13 a_0$ around R_{FC} . This has two consequences. First, $\Psi_0(\mathbf{R}, \mathbf{Q})$ is accurately approximated by a product of an \mathbf{R} - and a \mathbf{Q} -dependent factor,

$$\Psi_0(\mathbf{R}, \mathbf{Q}) \approx \Psi_R(\mathbf{R})\Psi_Q(\mathbf{Q}). \quad (18)$$

Indeed, the Hessian matrix near R_{FC} is approximately block diagonal, and the coupling between three coordinates of the dissociating H-atom on the one hand and the coordinates of the pyrrolyl unit on the other hand is vanishingly small. The photoexcited state $\Phi_\epsilon(0)$ with the TDM from the Herzberg-Teller expansion of Eq. (12) has the same product form,

$$\Phi_\epsilon(0) \approx F_R(\mathbf{R})f_Q(\mathbf{Q}), \quad (19)$$

(if $\mu_Q^{A_2}$ vanishes) or is a sum of several such product terms (if $\mu_R^{A_2}$ and $\mu_Q^{A_2}$ are nonzero). Second, the diabatic potential matrix $\mathbf{W}_Q(\mathbf{Q}|R)$ in Eq. (3) and, in particular, the functions

	Included normal modes	T_v [eV]	Initial state	Max. intensity [10 ⁻²⁰ cm ²]
6D	$Q_{b_1}(1, 2, 3)$	4.19	$\Phi_x = \mu_{x,\theta}^{A_2}(R_{\text{FC}}) \sin \theta \sin \phi \Psi_0$ $\Phi_y = \left(\mu_{y,\theta}^{A_2}(R_{\text{FC}}) \sin \theta \cos \phi + \sum_{i=1,2,3} \mu_{y,i}^{A_2}(R_{\text{FC}}) Q_{b_1}(i) \right) \Psi_0$	4.0
11D	$Q_{a_1}(1, \dots, 8)$	4.80	$\Phi_x = \mu_{x,\theta}^{A_2}(R_{\text{FC}}) \sin \theta \sin \phi \Psi_0$ $\Phi_y = \mu_{y,\theta}^{A_2}(R_{\text{FC}}) \sin \theta \cos \phi \Psi_0$	1.0
15D	$Q_{a_1}(1, 2, 5)$ $Q_{a_2}(1, 2, 3)$ $Q_{b_1}(1, 2, 3)$ $Q_{b_2}(1, 3, 5)$	4.72	$\Phi_x = \left(\mu_{x,\theta}^{A_2}(R_{\text{FC}}) \sin \theta \sin \phi + \sum_{i=1,3,5} \mu_{x,i}^{A_2}(R_{\text{FC}}) Q_{b_2}(i) \right) \Psi_0$ $\Phi_y = \left(\mu_{y,\theta}^{A_2}(R_{\text{FC}}) \sin \theta \cos \phi + \sum_{i=1,2,3} \mu_{y,i}^{A_2}(R_{\text{FC}}) Q_{b_1}(i) \right) \Psi_0$ $\Phi_z = \left(\sum_{i=1,2,3} \mu_{z,i}^{A_2}(R_{\text{FC}}) Q_{a_2}(i) \right) \Psi_0$	2.5

TABLE V: Summary of the quantum mechanical calculations for the photodissociation of pyrrole. Different models are denoted by the total number coordinates. The coordinates of the departing H atom (R, θ, ϕ) are part of all the calculations. For each case, the Table shows the list of included normal modes, the vertical excitation energy T_v of the resulting PES, the initial states Φ_s for the nonzero TDM components ($s = x, y, z$), and the maximum intensity of the calculated spectrum. In all the calculations, Ψ_0 is the ground state of the N -dimensional Hamiltonian, with $N = 6, 11, 15$.

$\kappa_i^\alpha(R)$ and $\gamma_{ij}^\alpha(R)$ in Eq. (4), can be fixed to their values at a distance $R \approx R_{\text{FC}}$ chosen near the equilibrium of the state \tilde{X} . The dynamics of the initial wave packet in the FC zone is therefore governed by the Hamiltonian

$$\hat{H}_0 \approx \hat{H}_R + \hat{H}_Q(\mathbf{Q}|R_{\text{FC}}), \quad (20)$$

represented as a sum of the commuting operators $\hat{H}_R = \hat{T}_R + \mathbf{W}_R(\mathbf{R})$ and $\hat{H}_Q(\mathbf{Q}|R_{\text{FC}}) = \hat{T}_Q + \mathbf{W}_Q(\mathbf{Q}|R_{\text{FC}})$. As a result, the vibrational motion of the ring is decoupled from the dissociative dynamics along \mathbf{R} . In the locally diabatic representation, this separable representation is valid for any number of electronic states included in the dynamics: In the FC zone, the off-diagonal matrix elements of $\mathbf{W}(\mathbf{R}, \mathbf{Q})$ vanish by construction.

Particle	DVR type	N_i, N_j, N_k	n_X, n_{A_2}
6D			
R	sine	98	5
(θ, ϕ)	2D Legendre	71, 21	5
$Q_{b_1}(1, 2, 3)$	HO, HO, HO	17	4
11D			
R	sine	98	9
(θ, ϕ)	2D Legendre	71, 21	7
$Q_{a_1}(1, 2)$	HO, HO	37, 29	7
$Q_{a_1}(3, 4)$	HO, HO	21, 21	5
$Q_{a_1}(5, 6)$	HO, HO	25, 21	4
$Q_{a_1}(7, 8)$	HO, HO	21, 21	2
15D			
$R, Q_{a_1}(1)$	sine, HO	65, 37	23, 9
(θ, ϕ)	2D Legendre	61, 19	19, 6
$Q_{a_1}(2, 5)$	HO, HO	29, 25	16, 5
$Q_{a_2}(1, 2, 3)$	HO, HO, HO	17, 17, 17	7, 4
$Q_{b_1}(1, 2, 3)$	HO, HO, HO	17, 17, 17	4, 3
$Q_{b_2}(1, 3, 5)$	HO, HO, HO	17, 17, 17	5, 3

TABLE VI: Computational details of the MCTDH calculations. The DVR type HO stands for the harmonic oscillator DVR. N_i, N_j, N_k are the number of primitive DVR functions used for each particle. n_X and n_{A_2} are the number of single-particle functions used for the \tilde{X} and 1A_2 states. The 6D and 11D include only the 1A_2 state.

The separability of the dissociative and the vibrational dynamics, underlined in Eqs. (19) and (20), allows one to express the total absorption spectrum as a convolution of the spectra originating from the \mathbf{R} - and \mathbf{Q} -subspaces. Let us specifically consider the case of dissociation in the isolated state $1^1A_2(\pi\sigma^*)$ photoexcited in a z -polarized transition mediated by the TDM $\mu_z^{A_2}$ depending on a single a_2 -symmetric mode $Q_{a_2}(3)$. In fact, the convolution approximation can be extended to the TDMs obeying the general Herzberg-Teller expansion (Appendix A)

and to the situations in which off-diagonal coupling matrix elements are retained either in \hat{H}_R or in \hat{H}_Q .

The autocorrelation function $S(t)$, defined in Eq. (15), is approximated by a product (the polarization index $\epsilon = z$ is omitted)

$$S(t) \approx \langle F_R | \exp(-i\hat{H}_R t) | F_R \rangle_R \cdot \langle f_Q | \exp(-i\hat{H}_Q t) | f_Q \rangle_Q \equiv s_R(t)s_Q(t), \quad (21)$$

where the spatial integration variables are explicitly indicated for each set of angular brackets. Next, the Fourier integral in Eq. (16) is transformed into a convolution of the Fourier integrals over the functions $s_R(t)$ and $s_Q(t)$ via a standard transformation (introduce an integration over the second time variable $\delta(t - \tau) d\tau$, replace the δ -function with an integral $\exp[i(t - \tau)\omega] d\omega$, and isolate the individual Fourier integrals). Defining ‘spectral functions’ without the energy prefactor,

$$\begin{aligned} \bar{\sigma}_R(E) &= \int_{-\infty}^{\infty} s_R(t) e^{iEt} dt, \\ \bar{\sigma}_Q(E) &= \int_{-\infty}^{\infty} s_Q(t) e^{iEt} dt, \end{aligned} \quad (22)$$

the absorption cross section can be written as

$$\sigma(E_{\text{ph}}) = \frac{E_{\text{ph}}}{2\epsilon_0 c} \int_{-\infty}^{\infty} \bar{\sigma}_R(E_{\text{ph}} - \omega) \bar{\sigma}_Q(\omega) d\omega. \quad (23)$$

In the \mathbf{R} -space, the motion of the wave packet is (directly or indirectly) dissociative, while the motion in the quadratic potentials of the \mathbf{Q} -space is bound. Thus, the absorption spectrum in Eq. (23) consists of a series of excitations of the pyrrolyl ring broadened by the dissociation of the hydrogen atom. As shown in Appendix A, more convolution terms are needed to approximate the absorption spectrum of the A_2 state if the transition is induced by a TDM in the Herzberg-Teller form of Eq. (12). The accuracy of the approximation is illustrated in Sect. V.

The convolution approach to the absorption spectrum can be considered as an extension of the familiar FC computations of bound–bound transitions^{60,61} to the case of dissociative spectra. This extension has several computational advantages. For example, the method reduces the amount of ab initio computations needed to evaluate $\bar{\sigma}_R(E)$: While a 3D potential energy surface of the excited state in the disappearing modes (R, θ, ϕ) is required, the \mathbf{Q} space is described only using Hessians in the ground and the excited electronic states

at $R = R_{\text{FC}}$, because the bound vibrational spectrum $\bar{\sigma}_Q(E)$ is given by the FC overlap integrals,

$$\bar{\sigma}_Q(E) = \sum_m |\langle \varphi_m(\mathbf{Q}) | f_Q(\mathbf{Q}) \rangle|^2 \delta(E - E_m), \quad (24)$$

between the eigenfunctions $\varphi_m(\mathbf{Q})$ (with energies E_m) of the non-disappearing modes in the FC zone and the initial state f_Q . Note that the harmonic stick spectrum in the \mathbf{Q} -space can be efficiently calculated analytically using the techniques developed for the FC factors in polyatomic molecules.^{62,63} The convolution calculations are further simplified if the $\pi\sigma^*$ state is purely repulsive. In this case, the absorption spectrum $\bar{\sigma}_R(E)$ can be accurately reconstructed using the reflection principle⁶⁴ which only requires the gradient of the 3D potential at the FC point. In the most optimistic scenario, a convolution calculation of the diffuse absorption spectrum becomes purely analytical, while the ab initio input refers to a single molecular geometry, namely the FC point.

IV. CALCULATIONS OF THE PHOTOFRAGMENT DISTRIBUTIONS

A. Quantum mechanical calculations

The quantum mechanical calculations of the rovibrational photofragment distributions in the electronic channel H + pyrrolyl(2A_2), diabatically correlating with the state $1^1A_2(\pi\sigma^*)$, are performed using the projection method of Balint-Kurti and coworkers,^{65,66} which we formulate in the time-independent framework.⁶⁷⁻⁶⁹ The partial photodissociation cross section for the formation of pyrrolyl in a vibrational state \mathbf{n} is given by:⁶⁶

$$\sigma(E_{\text{ph}}, \mathbf{n}) = \frac{E_{\text{ph}}}{3c\epsilon_0} \lim_{\lambda \rightarrow 0} \lambda |\langle \psi_{\mathbf{n}}^- | \Psi^\lambda(E_{\text{ph}}) \rangle|^2 = \frac{E_{\text{ph}}}{3c\epsilon_0} |T_{\mathbf{n}}(E_{\text{ph}})|^2; \quad (25)$$

the rotational motion of pyrrolyl, described by the coordinates θ and ϕ , is not explicitly included here, although it is taken into account in the actual calculations. The scattering state $\psi_{\mathbf{n}}^-(E_{\text{ph}})$ in the dissociation continuum describes the atom and the radical with photon energy E_{ph} recoiling into the channel \mathbf{n} . The wave function $\Psi^\lambda(E_{\text{ph}})$ is a stationary energy component of the initial excitation $\Phi(0)$ [Eq. (14)] in the state A_2 :

$$\Psi^\lambda(E_{\text{ph}}) = \hat{G}^+(E_{\text{ph}})\Phi(0); \quad (26)$$

Here $\hat{G}^+(E)$ is the advanced Green's function,

$$\hat{G}^+(E_{\text{ph}}) = -i \int_0^\infty e^{-i(\hat{H}-i\lambda)t} e^{iE_{\text{ph}}t} dt, \quad (27)$$

and λ in the above equations signifies the asymptotic absorbing potential. At large inter-fragment distances $R \rightarrow \infty$, the state $\Psi^\lambda(E_{\text{ph}})$ contains purely outgoing waves along R :

$$\Psi^\lambda(E_{\text{ph}}) \rightarrow - \sum_{\mathbf{n}} T_{\mathbf{n}}(E_{\text{ph}}) \sqrt{\frac{\mu}{k_{\mathbf{n}}}} e^{ik_{\mathbf{n}}R} \chi_{\mathbf{n}}(\mathbf{Q}). \quad (28)$$

The wave functions $\chi_{\mathbf{n}}(\mathbf{Q})$ are the vibrational eigenstates of pyrrolyl with energies $E_{\mathbf{n}}$ and $k_{\mathbf{n}} = \sqrt{2\mu(E_{\text{ph}} - E_{\mathbf{n}})}$ is the channel momentum.⁷⁴

The amplitudes in each channel are the photodissociation matrix elements $T_{\mathbf{n}}(E_{\text{ph}})$ [see Eq. (25)] which contain all dynamical information on the dissociation process.⁶⁶ They are found by introducing projection operators onto $\chi_{\mathbf{n}}$,

$$\hat{\mathcal{P}}_{\mathbf{n}} = \delta(R - R_\infty) |\chi_{\mathbf{n}}(\mathbf{Q})\rangle, \quad (29)$$

at the analysis line $R = R_\infty$ located in the asymptotic region, and applying them to the state $\Psi^\lambda(E)$:

$$|T_{\mathbf{n}}(E_{\text{ph}})|^2 \sim \frac{k_{\mathbf{n}}}{\mu} \left| \hat{\mathcal{P}}_{\mathbf{n}}^* |\Psi^\lambda(E_{\text{ph}})\rangle \right|^2. \quad (30)$$

The matrix elements $|T_{\mathbf{n}}(E_{\text{ph}})|^2$ are, with a proper normalization, the vibrational photofragment distributions; summation of the partial cross sections over all quantum numbers \mathbf{n} gives the total absorption cross section of Eq. (17). The TKER spectrum^{13,32} $P(E_{\text{kin}}|E_{\text{ph}})$ is obtained via transforming the internal energy distributions to the photofragment kinetic energy scale:

$$P(E_{\text{kin}}|E_{\text{ph}}) = \sum_{\mathbf{n}} \frac{k_{\mathbf{n}}}{\mu} |T_{\mathbf{n}}(E_{\text{ph}})|^2 \delta(E_{\text{ph}} - D_0 - E_{\mathbf{n}} - E_{\text{kin}}), \quad (31)$$

where D_0 is the lowest quantum mechanical dissociation threshold of pyrrole.

Our calculation of the photofragment distributions makes use of the time-dependent wavefunction $\Phi(t) = \exp(-i\hat{H}t - \lambda t) \Phi(0)$ calculated using the MCTDH method. Once the time propagation has terminated, the T -matrix elements are calculated as follows:

- For each pyrrolyl eigenstate $|\chi_{\mathbf{n}}(\mathbf{Q})\rangle$, the projection function of Eq. (29) is generated in the same MCTDH form used in the wave packet calculation. Since the Hamiltonian is set in the normal modes of pyrrolyl, it becomes separable as $R \rightarrow \infty$. Therefore, the eigenstate wavefunctions are straightforwardly obtained as a single configuration.

- State-dependent cross-correlation functions are calculated as

$$S_{\mathbf{n}}(t) = \langle \chi_{\mathbf{n}}(\mathbf{Q}) | \delta(R - R_{\infty}) | \Phi(t) \rangle .$$

- The photon energy-dependent T -matrix elements are obtained as half-Fourier transform of the cross-correlation functions,

$$T_{\mathbf{n}}(E_{\text{ph}}) \sim \sqrt{\frac{k_{\mathbf{n}}}{\mu}} \int_0^{\infty} S_{\mathbf{n}}(t) e^{iE_{\text{ph}}t} dt . \quad (32)$$

B. Overlap integral-based mapping calculations of the photofragment distributions

The convolution introduced in Sect. III B for the absorption spectra can be used as a starting point for an approximate calculation of the T -matrix elements and the photofragment distributions using adiabatic mapping. The spectral convolution in Eq. (23), based on the separable Hamiltonian [Eq. (20)] and a product form of the initial state $\Phi(0)$ [Eq. (19)], is valid for the Green's function $\hat{G}^+(E_{\text{ph}})$, too:

$$\hat{G}^+(E_{\text{ph}}) \approx \hat{G}_0^+(E_{\text{ph}}) = -(2\pi i)^{-1} \int_{-\infty}^{\infty} \hat{G}_R^+(E_{\text{ph}} - \omega) \hat{G}_Q^+(\omega) d\omega , \quad (33)$$

where the Green's functions $\hat{G}_R^+(E) = (E - \hat{H}_R(\mathbf{R}) + i\lambda)^{-1}$ and $\hat{G}_Q^+(E) = (E - \hat{H}_Q(\mathbf{Q}|R_{\text{FC}}) + i\lambda)^{-1}$ refer to the three disappearing modes and the pyrrolyl normal modes, respectively. For the bound vibrational spectrum of Eq. (24), one can specify

$$\hat{G}_Q^+(\omega) = \sum_{\mathbf{m}} \frac{|\varphi_{\mathbf{m}}\rangle \langle \varphi_{\mathbf{m}}|}{\omega - E_{\mathbf{m}} + i\lambda} , \quad (34)$$

insert this Green's function into the convolution integral of Eq. (33), and apply it to the initial state $\Phi(0)$. This gives the stationary energy component $\Psi^\lambda(E_{\text{ph}})$ in the form

$$\Psi^\lambda(E_{\text{ph}}) \approx \hat{G}_0^+(E_{\text{ph}}) \Phi(0) = \sum_{\mathbf{m}} \left[\hat{G}_R^+(E_{\text{ph}} - E_{\mathbf{m}}) F_R(\mathbf{R}) \right] \langle \varphi_{\mathbf{m}} | f_Q \rangle \varphi_{\mathbf{m}}(\mathbf{Q}) . \quad (35)$$

The Green's function $\left[\hat{G}_R^+ F_R \right]$ acting on the initial state in the \mathbf{R} space generates an outgoing wave along R , and the form of the above expression is similar to the channel representation of $\Psi^\lambda(E_{\text{ph}})$ in Eq. (28). Although the derivation uses separability of the Hamiltonian in the FC zone $R \approx R_{\text{FC}}$, the expansion $\sum_{\mathbf{m}}$ in Eq. (35) is approximately valid for all R if the eigenstates $\varphi_{\mathbf{m}}(\mathbf{Q})$ smoothly vary with the dissociation coordinate R and commute with the kinetic energy \hat{T}_R — i.e. if the evolution in the coordinates orthogonal to the reaction path

is adiabatic. The states $\varphi_{\mathbf{m}}$ go over into the free vibrational states $\chi_{\mathbf{n}}$ as $R \rightarrow \infty$, and the asymptotic form of Eq. (35) can be written as

$$\Psi^\lambda(E_{\text{ph}}) \rightarrow - \sum_{\mathbf{n}} [\bar{\sigma}_R(E_{\text{ph}} - E_{\mathbf{m}})]^{1/2} e^{i\alpha} \langle \varphi_{\mathbf{m}} | f_Q \rangle \sqrt{\frac{\mu}{k_{\mathbf{n}}}} e^{ik_{\mathbf{n}}R} \chi_{\mathbf{n}}(\mathbf{Q}), \quad (36)$$

where $[\bar{\sigma}_R(E_{\text{ph}} - E_{\mathbf{m}})]^{1/2} e^{i\alpha}$ stands for the (semiclassical) complex amplitude of the outgoing wave of $[\hat{G}_R^+ F_R]$ along the reaction coordinate. Application of the projector $\hat{\mathcal{P}}_{\mathbf{n}}$ gives the vibrational state distributions in the mapping approximation:

$$|t_{\mathbf{n}}(E_{\text{ph}})|^2 \sim \frac{k_{\mathbf{n}}}{\mu} |\langle \varphi_{\mathbf{m}}(\mathbf{Q}) | f_Q(\mathbf{Q}) \rangle|^2 \bar{\sigma}_R(E_{\text{ph}} - E_{\mathbf{m}}). \quad (37)$$

They are proportional to the FC overlap integrals in the \mathbf{Q} -space, taken at the excitation point R_{FC} and weighted with the ‘radial factor’ $\bar{\sigma}_R = \lim_{\lambda \rightarrow 0} \lambda \langle \hat{G}_R^+ F_R | \hat{G}_R^+ F_R \rangle$. The physical interpretation in view of Eq. (24) is that the population of a given product state $\chi_{\mathbf{n}}$ is controlled by the intensity $|\langle \varphi_{\mathbf{m}} | f_Q \rangle|^2$ of excitation of the adiabatically connected state $\varphi_{\mathbf{m}}$ in the FC zone, multiplied by the probability $\bar{\sigma}_R(E_{\text{ph}} - E_{\mathbf{m}})$ of excitation of the radial dissociative motion with the translational energy $E_{\text{kin}} = E_{\text{ph}} - E_{\mathbf{m}}$. In other words, the harmonic populations of the non-disappearing modes in the FC zone are adiabatically translated to the infinite interfragment separation and mapped onto product states. The expression for the product state distributions in the overlap integral-based adiabatic mapping is similar to the semiclassical FC mapping expression familiar in the context of triatomic photodissociation (see, for example, Refs. 64,70,71). The FC mapping is recovered if the spectral amplitudes $\langle \varphi_{\mathbf{m}} | f_Q \rangle$ are replaced with the projections $\langle \chi_{\mathbf{n}} | f_Q \rangle$ of the initial wave function directly onto the asymptotic product states.

In the actual application of the adiabatic mapping approximation, we associate each normal mode in the FC region with the pyrrolyl mode with the largest squared Duschinsky overlap. In this way, we could establish a one-to-one mapping between short- and long-distance normal modes. Given a vibrational state in the FC region, the corresponding asymptotic state is readily obtained by assigning the quantum numbers \mathbf{m} of the FC modes to the corresponding pyrrolyl modes (whose quantum numbers are denoted by \mathbf{n} in the Equations above).

V. RESULTS: PHOTOABSORPTION

Absorption spectra for the ${}^1A_2(\pi\sigma^*) \leftarrow \tilde{X}$ transition are calculated using the Hamiltonian of Eq. (1). Three calculations are discussed below, in which the following degrees of freedom are included: (i) $R, \theta, \phi, Q_{b_1}(1, 2, 3)$; (ii) $R, \theta, \phi, Q_{a_1}(1, 2, 3, 4, 5, 6, 7, 8)$; and (iii) $R, \theta, \phi, Q_{a_1}(1, 2, 5), Q_{a_2}(1, 2, 3), Q_{b_1}(1, 2, 3), Q_{b_2}(1, 3, 5)$. The settings of the three calculations are summarized in Table V.

Calculations (i) and (ii) are performed for the isolated 1A_2 electronic state and highlight the specific absorption features due to totally symmetric (irrep a_1) and non-totally symmetric (irrep b_1) modes. The a_1 modes in FC region of the A_2 state are displaced relative to the equilibrium geometries of pyrrole and pyrrolyl. All displacements for the b_1 modes vanish by symmetry for both species regardless of the electronic state. The focus in (i) and (ii) is on the dissociative absorption spectra in the isolated 1A_2 state and the accuracy of the convolution approximation. Considering dynamics in the isolated A_2 state is justified: The coupling $V_{\text{ang}}^{XA_2}$, involving the angular coordinates (θ, ϕ) , is small. The (minor) differences with the two-state dynamics are discussed in the Supporting Information.

Calculation (iii) is performed for the coupled pair \tilde{X}/A_2 and provides a realistic absorption spectrum of pyrrole in the long wavelength limit which is close to the full-dimensional spectrum. Included are all modes of a_2 and b_1 symmetry, as well as three a_1 modes with the largest displacement between the minima of pyrrole and pyrrolyl, and three b_2 modes along which the TDM has the largest gradient [Eq. (13c)]. This calculation accounts for the impact of the CI on the photodissociation dynamics.

Since the $A_2 \leftarrow \tilde{X}$ transition is Franck-Condon forbidden, the absorption cross sections are small, of the order of 10^{-20} cm^{-1} . For this reason, the shape of the corresponding absorption band could not be reliably measured: The absorption of the lowest $\pi\sigma^*$ state is overlaid by the intense band of a neighbouring $\pi\pi^*$ state.²⁸ The experimental characterization of the photodissociation in the A_2 state is more advanced in the time domain.^{28,31,36,37} For this reason, the absorption spectra are discussed together with the autocorrelation functions, which provide information about the dissociation lifetimes.

A. 6D absorption spectrum: Coordinates $R, \theta, \phi, Q_{b_1}(1, 2, 3)$

The calculation is performed for the isolated A_2 state. The modes not included in the calculation are set equal to $\mathbf{Q}_{\min}(R)$ for each R (i.e., they follow the relaxed scan on the A_2 surface, as described in Sect. II B 3).

The A_2 state is excited via the TDMs μ_x and μ_y creating molecular states of B_2 and B_1 symmetry, respectively. The initial wavefunctions $\Phi_x(0)$ and $\Phi_y(0)$ are reported in Table V.

The total absorption spectrum is a sum of two contributions, $\frac{1}{3}\sigma_x$ and $\frac{1}{3}\sigma_y$ [see Eq. (17)]. The spectra and the autocorrelation functions are shown in Fig. 6(a).

Both spectral components peak close to the vertical excitation energy of 4.19 eV, and the peak intensity of the total absorption does not exceed $4 \cdot 10^{-20}$ cm². The spectra σ_x and σ_y consist of a main peak and a shoulder on the high energy side. For the σ_x spectrum the maximum intensity is at $E_{\max} = 4.15$ eV and the standard deviation of the absorption profile is $\Delta = 0.17$ eV. For σ_y the maximum is shifted to lower energies, $E_{\max} = 4.10$ eV, and $\Delta = 0.15$ eV. The only geometrical change between the (local) minima of V^X and V^{A_2} is the elongation of the N–H bond by $0.12 a_0$. This shift along R determines the spectral width, and suggests that the main peak corresponds to the ground vibrational state (a short-lived resonance) in the A_2 state, and the shoulder is a resonance state with one quantum of N–H stretch.

The component σ_y makes the main contribution to the total spectrum. The reason is that the TDM μ_y grows mostly along the out-of-plane H bending mode. Since this mode has a low frequency in the ground electronic state (see Table III), the wavefunction $\Psi_0(\mathbf{R}, \mathbf{Q}_{b_1})$ is broadened along this coordinate and the sampled TDM is large. Moreover, both the out-of-plane H bending and the Q_{b_1} modes contribute to the y -polarized excitation, whereas the x -polarized excitation is promoted only by the in-plane H bending mode.

The autocorrelation functions S_x and S_y further help to interpret the spectra σ_x and σ_y . Their absolute values are depicted in Fig. 6(b). For both polarizations, the autocorrelation functions decay monotonically and no neat recurrences are observed. In the first 10 fs the amplitude of $S_x(t)$ and $S_y(t)$ decreases to $\approx 30\%$ of its initial value, indicating a fast direct dissociation of a substantial fraction of the initial wave packet. Slower decays, recognizable in $|S_x(t)|$ and $|S_y(t)|$ in the range 10–40 fs, are probably due to a tiny recurrence around ≈ 25 fs, associated to the high energy shoulder of σ_y .

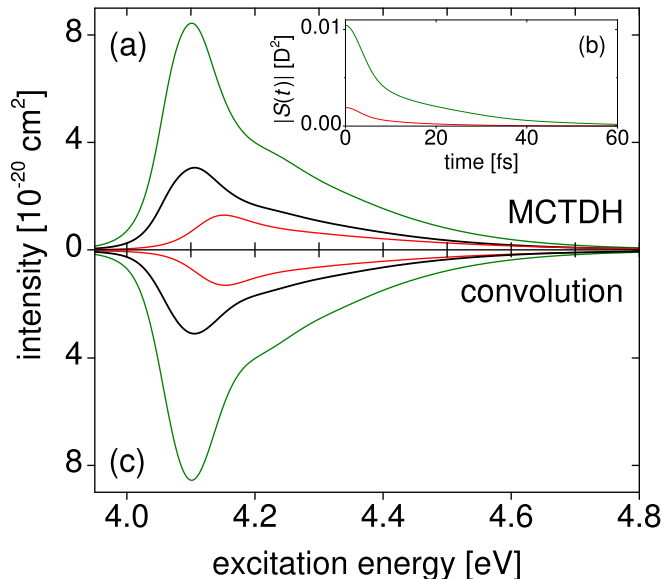


FIG. 6: (a) Absorption spectra for the isolated 1A_2 state of pyrrole calculated using three disappearing modes (R, θ, ϕ) of the detaching H atom and three b_1 modes of the pyrrolyl ring. The spectra are calculated exactly using MCTDH propagation on the 6D potential. The profiles σ_x and σ_y corresponding to the x - and y -polarizations are shown in red and green, respectively. The total spectrum $(\sigma_x + \sigma_y)/3$ is shown in black. (b) Autocorrelation function amplitudes $|S_x|$ (red) and $|S_y|$ (green) as a function of time for the spectra of panel (a). (c) The same spectra as in (a) evaluated using the convolution approximation.

The autocorrelation function was processed using the low storage filter diagonalization method of Mandelshatm and Taylor.⁷² The intense resonance peaks were found at 4.14 eV in the σ_x spectrum, and at 4.07 eV and 4.11 eV in the σ_y spectrum; the lifetimes are 5.6 fs (for σ_x) and 8 fs (for σ_y). The difference between the energies of these resonances, compared with the frequencies of Table III (second column), suggests the assignment to states with one vibrational quantum respectively in the in-plane H-bending mode ($\omega \sim 0.13$ eV), in the out-of-plane H-bending mode ($\omega \sim 0.08$ eV) and in the $Q_{b_1}(3)$ mode ($\omega \sim 0.12$ eV).

This assignment could have been anticipated: it is these modes which one expects to become excited in the initial wave packets Φ_x and Φ_y via the coordinate dependence of the TDMs. The lifetimes, in the range 5–8 fs are mode-specific and are close to the experimental dissociation lifetime of 12 fs reported in Ref. 37. Our lifetimes are shorter, which indicates that the height of the potential barrier in the FC region, 0.09 eV, is probably slightly

underestimated.

More short lived resonance states are found at higher energies correlating with the spectral shoulders. In the σ_x spectrum a resonance is found at 4.44 eV and attributed to a state with one vibrational quantum in both the in-plane H bending and the N–H stretch (R coordinate, $\omega \sim 0.32$ eV). In the spectrum σ_y , we find another resonance state at 4.21 eV and attribute it to the third overtone of the out-of-plane H bending.

Figure 6(c) shows the spectra calculated using the convolution approximation of Eq. (23). The convolution is done separately for each polarization and the agreement with MCTDH calculations is excellent. The approximation of (21) is good because the b_1 modes are not displaced in the minima of either \tilde{X} or A_2 states, so that the coordinates \mathbf{R} and \mathbf{Q}_{b_1} are largely decoupled, and the separation (20) is fully valid.

For the x -polarization, the vibrational wavefunction $f_Q(\mathbf{Q}_{b_1})$ of the initial state [Eq. (19)] is a Gaussian function which significantly overlaps only with the ground vibrational level of the A_2 state. As a consequence, the convoluted spectrum [Eq. (23)] has the same shape of the dissociative profile $\bar{\sigma}_R(E)$.

For the y -polarization, both the out-of-plane H bending and the b_1 modes contribute to the TDM function. Three vibrational states of A_2 make the largest contribution to the vibrational convolution factor $\bar{\sigma}_Q(E)$ [Eq. (24)]: The ground vibrational state, associated with the excitation of the out-of-plane H bending, and the states with one quantum on the modes $Q_{b_1}(2)$ and $Q_{b_1}(3)$. The mode $Q_{b_1}(1)$ has a small coefficient in the Herzberg-Teller TDM function, and is not excited in the ${}^1A_2 \leftarrow \tilde{X}$ transition.

B. 11D absorption spectrum: Coordinates $R, \theta, \phi, Q_{a_1}(1, 2, 3, 4, 5, 6, 7, 8)$

The calculation is performed for the isolated 1A_2 state. The non totally-symmetric modes are fixed to their equilibrium values. The 11D potentials V^X and V^{A_2} include the equilibrium geometries of pyrrole and pyrrolyl, the local minimum in the FC region of the 1A_2 state, as well as the small barrier to dissociation (see Table I).

The ${}^1A_2 \leftarrow \tilde{X}$ excitation is promoted by the TDMs μ_x and μ_y , which create molecular states of B_2 and B_1 symmetry. The corresponding initial wave packets $\Phi_x(0)$ and $\Phi_y(0)$ are defined in Table V. The total spectrum $\sigma = (\sigma_x + \sigma_y)/3$ has a maximum intensity of $\approx 10^{-20}$ cm² [see Fig. 7(a)]. The spectrum consists of a series of diffuse vibrational bands

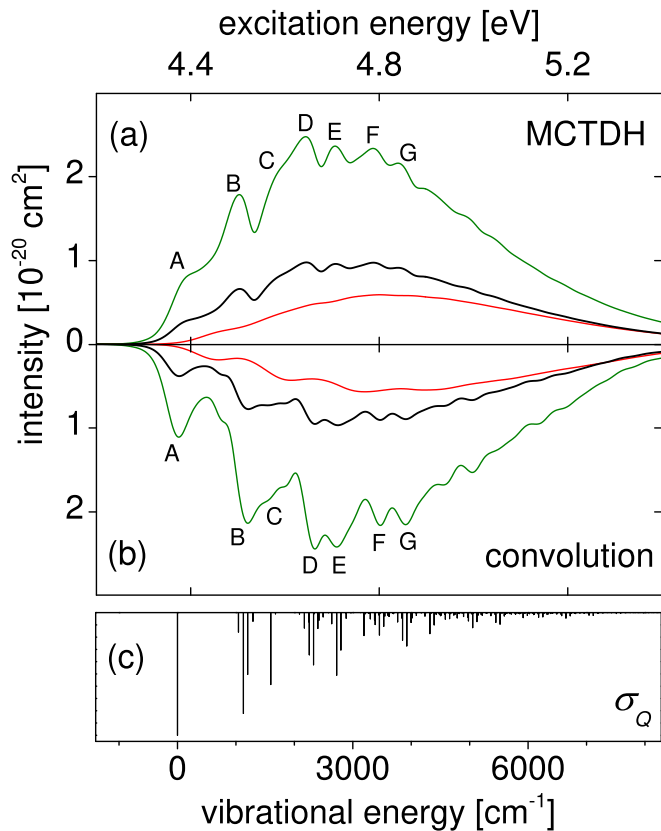


FIG. 7: (a) Absorption spectra for the isolated 1A_2 state of pyrrole calculated using three disappearing modes (R, θ, ϕ) of the detaching H atom and eight a_1 modes of the pyrrolyl ring. The spectra are calculated exactly using MCTDH propagation on the 11D potential. The profiles σ_x and σ_y corresponding to the x - and y -polarizations are shown in red and green, respectively. The total spectrum $(\sigma_x + \sigma_y)/3$ is shown in black. (b) The same spectra as in (a) evaluated using the convolution approximation. The assigned vibrational bands in (a) and (b) are marked with letters A–G. (c) Vibrational stick spectrum σ_Q , used in the convolution method. Vibrational levels are denoted using the set of vibrational quantum numbers of the a_1 modes $n_{a_1}(i)$, $i = 1, 8$. The states mostly contributing to each peak are: (A) $n_{a_1}(i) = 0$, for $i = 1, \dots, 8$; (B) $(n_{a_1}(1) = 1)$, $(n_{a_1}(2) = 1)$, $n_{a_1}(3) = 1$; (C) $(n_{a_1}(5) = 1)$; (D) $(n_{a_1}(2) = 2)$, $(n_{a_1}(2) = 1, n_{a_1}(3) = 1)$; (E) $(n_{a_1}(2) = 1, n_{a_1}(5) = 1)$, $(n_{a_1}(3) = 1, n_{a_1}(5) = 1)$; (F) $(n_{a_1}(2) = 2, n_{a_1}(3) = 1)$; (G) $(n_{a_1}(2) = 1, n_{a_1}(3) = 1, n_{a_1}(5) = 1)$, $(n_{a_1}(2) = 2, n_{a_1}(5) = 1)$.

structuring the 0.6 eV wide absorption envelope. The vibrational peaks are poorly resolved because they are broadened by the fast dissociation.

The structures in the absorption profile, as well as the recurrences in the autocorrelation function, are best interpreted using the normal modes $\tilde{\mathbf{Q}}_{a_1}$, calculated for the pyrrolyl ring at the local minimum on the A_2 surface. The spectral width is determined mostly by the vibrational excitations of the $\tilde{\mathbf{Q}}_{a_1}$ modes and, to a lesser extent, by the broadening induced by dissociation. The convolution approximation discussed below allows one to make this distinction quantitative. The larger shift δQ of a particular mode between the minima of V^X and V^{A_2} , the more vibrational overtones of this mode are excited in the absorption spectrum. These geometrical changes were described in Sect. II B 1 and illustrated in Fig. 3. The largest displacements are found for the modes $\tilde{Q}_{a_1}(1)$ ($\delta Q = 0.54$), $\tilde{Q}_{a_1}(2)$ ($\delta Q = 1.32$), $\tilde{Q}_{a_1}(3)$ ($\delta Q = 1.03$) and $\tilde{Q}_{a_1}(5)$ ($\delta Q = 1.15$). These modes show up in the absorption spectrum, while the remaining modes $\tilde{Q}_{a_1}(4, 6, 7, 8)$ are minimally shifted, and behave as ‘spectators’.

The spectra σ_x and σ_y have maxima close to the vertical excitation energy of 4.80 eV. This value is higher in the 11D than in the 6D calculation of Sect. V A, because the 6D PES is relaxed on the 1A_2 , but not on the \tilde{X} state, and the potential minimum in \tilde{X} is elevated by ~ 0.6 eV. With all eight a_1 modes included in the calculation, the \tilde{X} state relaxes to its global minimum, and the vertical excitation energy increases. The spectrum σ_x (red line) has a maximum at $E_{\max} = 4.80$ eV and a FWHM of 0.64 eV. The maximum intensity is $6 \cdot 10^{-21}$ cm². Although many vibrational states are excited, their peaks are considerably broadened due to fast dissociation and the vibrational progressions remain unresolved.

Similarly to the 6D calculation, the spectrum σ_y (green line) has a higher intensity than σ_x , with a maximum of $\sim 2.5 \cdot 10^{-20}$ cm², peaking at $E_{\max} = 4.64$ eV. The vibrational bands are well resolved against the 0.59 eV broad background, and are recognizable in the total absorption spectrum, too. They are labelled with letters A–G in Fig. 7(a). The vibrational ground state in the A_2 state (band A) is seen as a weak shoulder. The assignment of the vibrational peaks B–G is elucidated below with the help of the convolution approach.

The autocorrelation functions S_x and S_y help to rationalize the differences between σ_x and σ_y . Figure 8(a) shows the absolute values $|S_x|$ and $|S_y|$ for the first 250 fs, plotted on a logarithmic scale in order to highlight vibrational recurrences. In the short time scale, $|S_x|$ and $|S_y|$ decay to half their initial value in $T = 2.9$ fs and $T = 3.1$ fs, respectively. The spectral widths of σ_x and σ_y are related to such fastest time scales by the energy-time uncertainty principle, $\text{FWHM} = 4\hbar \ln 2/T$.⁷³ In $|S_x|$ the initial decay is followed by

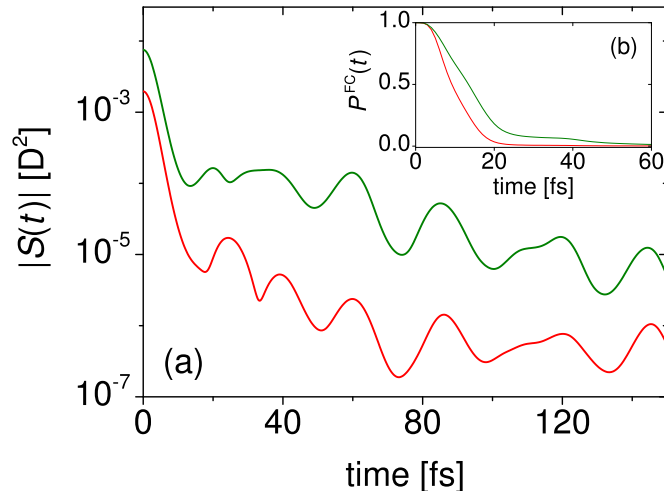


FIG. 8: (a) Autocorrelation function amplitudes $|S_x|$ (red) and $|S_y|$ (green) as a function of time for the spectra of Fig. 7. (b) Populations in the Franck-Condon region P_x^{FC} (red) and P_y^{FC} (green) as a function of time.

two recurrences, whose periods are 24.5 fs and 39 fs, corresponding to the frequencies of 1361 cm^{-2} and 855 cm^{-2} , and attributed to the second overtone of the out-of-plane H bending and the one quantum excitation on $\tilde{Q}_{a_1}(1)$, respectively. In $|S_y|$, the shortest recurrence time of 20 fs corresponds to the frequency of 1668 cm^{-2} , associated with the $\tilde{Q}_{a_1}(5)$ mode: The vibrational state with one quantum on $Q_{a_1}(5)$ gives rise to the shoulder C at $E_{\text{ph}} = 4.60 \text{ eV}$. Additional recurrences are visible in the range 30–36 fs and are associated with the low-frequency a_1 modes, which span the frequency range $900\text{--}1150 \text{ cm}^{-2}$: The vibrational states with one quantum on $Q_{a_1}(1, 2, 3)$ fall under the band B, peaking at $E_{\text{ph}} = 4.50 \text{ eV}$.

The spectral resolution is related to the dissociation-induced damping of the recurrences in the autocorrelation function. The TDMs μ_x and μ_y create the initial wavefunctions having one vibrational quantum in the in-plane and the out-of-plane H bending modes, respectively (see Table V). According to Table III, the frequency of the in-plane bending is lower in the A_2 state than in the \tilde{X} state. Therefore the wave packet $\Phi_x(0)$, initially narrow along θ , experiences a reduced frequency on the A_2 state and widens. As a consequence, the recurrence amplitude decreases rapidly, and the resulting spectrum σ_x is broad and unresolved. In contrast, the out-of-plane bending has a higher frequency in the excited state, so that no broadening along θ occurs at short times, the amplitude of the recurrences

remains large for a longer time (the first three recurrence peaks have almost the same height), and the vibrational peaks in σ_y are pronounced.

The dissociation time scales in the spectra σ_x and σ_y are found from the time dependence of the population

$$P_i^{\text{FC}}(t) = \frac{\langle \Phi_i(t) | \Theta(R_b - R) | \Phi_i(t) \rangle}{\langle \Phi_i(0) | \Phi_i(0) \rangle}, \quad i = x, y, \quad (38)$$

in the FC region, where $\Theta(x)$ is the Heaviside step function, and $R_b = 4.6 a_0$ is the position of the barrier maximum on the A_2 PES. The functions $P_x^{\text{FC}}(t)$ and $P_y^{\text{FC}}(t)$ are plotted in Fig. 8(b). In order to determine dissociation lifetimes, we fitted the functions $P_i^{\text{FC}}(t)$ to the model

$$f(t) = \Theta(t_0 - t) + \Theta(t - t_0) \left[a \exp\left(-\frac{(t - t_0)^2}{T_1^2}\right) + (1 - a) \exp\left(-\frac{t - t_0}{T_2}\right) \right], \quad (39)$$

in which the Gaussian decay is attributed to the direct dissociation with the time constant T_1 , and the exponential with lifetime T_2 accounts for the tunneling through the A_2 potential barrier (0.09 eV). The parameter t_0 indicates the time in which the wave packet reaches the distance R_b , and it is determined in the range 1–2 fs. $P_x^{\text{FC}}(t)$ is best fitted setting $a = 1$ and $T_1 = 10.3$ fs. The time constants for P_y^{FC} are $T_1 = 13.4$ fs and $T_2 = 47.2$ fs, and $a = 0.91$. The shorter time constants agree with the experimental value of 12 fs,³⁷ obtained by time-resolved photoelectron spectroscopy measurements, which are sensitive to the excited state population in the FC region. The longer time constant agrees with the value of 46 fs reported by Stavros and coworkers²⁸, obtained by time-resolved pyrrolyl yield measurements, with a time resolution of 30 fs. The resonance states, calculated near the absorption maximum and carrying the largest intensities, have lifetimes ranging from 20 fs to 60 fs, in agreement with the above analysis.

The decay rate and the recurrence pattern after 100 fs are identical for the functions $|S_x|$ and $|S_y|$. This suggests that the same vibrational progressions, built on the TDM-induced H bending excitations, are active in the two spectra. Indeed, the same vibrational spectrum σ_Q is used for the two polarizations in the convolution equations Eqs. (22) and (23).

The 11D calculation including all a_1 vibrational modes is the most stringent test for the convolution method (Sect. III B), because the a_1 modes are strongly coupled to the totally symmetric dissociation coordinate R . The two convolution factors $\bar{\sigma}_R$ and $\bar{\sigma}_Q$ [Eq. (22)] are calculated as follows.

For the \mathbf{R} -space, the initial 3D wavefunction $\Psi_R(\mathbf{R})$ of Eq. (18) is defined as the ground state of the \tilde{X} state Hamiltonian, with the \mathbf{Q}_{a_1} modes fixed at the \tilde{X} minimum. $\Psi_R(\mathbf{R})$ is then multiplied by the TDM functions μ_x and μ_y , and propagated with the Hamiltonian $\hat{H}_R = \hat{T}_R + W_R(\mathbf{R})$ thus giving the factor $\bar{\sigma}_R$. The function $W_R(\mathbf{R})$ is the potential along the MEP on the 1A_2 state. The convolution factors $\bar{\sigma}_R$ have shapes similar to the 6D spectra, i. e. a main peak and a high energy shoulder. The FWHM for $\bar{\sigma}_R$ are 0.18 eV and 0.12 eV for μ_x and μ_y . The width of the $\bar{\sigma}_R$ convolution factor represents the contribution to the spectral broadening due to dissociation. Since the total spectral width (≈ 0.6 eV) is approximately four times larger than the width of $\bar{\sigma}_R$, most of the spectral broadening is due to the extension of the a_1 progressions, define by the convolution factor $\bar{\sigma}_Q$.

The profile $\bar{\sigma}_Q$ is a harmonic Franck-Condon spectrum, calculated using the Hamiltonians of the states \tilde{X} and 1A_2 , $\hat{H}_Q = \hat{T}_Q + W^\alpha(\mathbf{Q}|R_{\text{FC}})$, and $\alpha = X, A_2$. For each electronic state, the value of R_{FC} is fixed at the respective (local) minimum: $R_{\text{FC}} = 4.10 a_0$ for \tilde{X} , and $R_{\text{FC}} = 4.23 a_0$ for A_2 . The width of σ_Q is ≈ 0.4 eV, larger than the FWHM of $\bar{\sigma}_R$

Fig. 7(b) depicts the spectra σ_x and σ_y , calculated using the convolution approach. The absorption profiles agree well with the exact MCTDH calculation: The approximated spectra are correctly positioned on the energy scale and the moments of the spectral envelope (width, asymmetry, etc.) are well reproduced. The lower resolution of the σ_x profile, compared to σ_y , is reproduced by the convolution approach, and it is traced back to the broader $\bar{\sigma}_R$ profile.

In the σ_y spectrum, many similarities in the sequence of vibrational peaks are recognizable between the exact and the approximated calculation. An advantage of the convolution method is that the approximated spectrum is automatically assigned, because the vibrational convolution factor $\bar{\sigma}_Q$ – the same for all the calculations – is a stick spectrum, and the individual contributions of Eq. (24) can be isolated. The intense peaks in the two spectral profiles are matched by visual inspection, and the corresponding bands are labelled with the same letters in Figs. 7(a) and (b). The spectrum σ_Q is shown in Fig. 7(c). The bands A–G correspond to peaks in σ_Q and their assignment is reported in the figure caption.

The most intense peaks involve excitations in the modes which are mostly displaced between the \tilde{X} and A_2 minima: $\tilde{Q}_{a_1}(2)$, $\tilde{Q}_{a_1}(5)$, which give rise to the most intense progressions, and $\tilde{Q}_{a_1}(3)$, which produces slightly weaker peaks. Since the vibrational couplings between R and the a_1 modes are neglected, the mode frequencies used in the convolution spectrum do

not perfectly coincide with the effective frequencies emerging from the MCTDH calculation. This is the price to be paid for using the separable approximation in the convolution. The band B involves one quantum excitation on the modes $Q_{a_1}(2)$ and $Q_{a_1}(3)$ and appears to be shifted to higher energy by $\sim 120 \text{ cm}^{-1}$. On the contrary, the frequency of the $Q_{a_1}(5)$ mode, whose excitation gives rise to the shoulder C, is underestimated by $\sim 130 \text{ cm}^{-1}$ in the approximation.

C. 15D absorption spectrum: Coordinates

$$R, \theta, \phi, Q_{a_1}(1, 2, 5), Q_{a_2}(1, 2, 3), Q_{b_1}(1, 2, 3), Q_{b_2}(1, 3, 5)$$

The calculation includes the coupled $\tilde{X}/^1A_2$ diabatic states. The 15D diabatic potentials V^X and V^{A_2} depend on the disappearing modes, and on three modes of each symmetry. All the other modes are set to the pyrrolyl equilibrium. The diabatic coupling V^{XA_2} depends on the coordinates R and $Q_{a_2}(1, 2, 3)$ [see Eqs. (5) and (6)].

The TDMS μ_x , μ_y and μ_z , promoting the $^1A_2 \leftarrow \tilde{X}$ excitation, create initial states of B_2 , B_1 and A_2 symmetry, respectively. The initial wavefunctions $\Phi_x(0)$, $\Phi_y(0)$ and $\Phi_z(0)$ are reported in Table V. The spectra for the individual x -, y - and z -polarizations and the total spectrum $\sigma = (\sigma_x + \sigma_y + \sigma_z)/3$ are shown in Fig. 9. This calculation provides the most reliable value for the absorption cross section, because all the modes which strongly induce the $^1A_2 \leftarrow \tilde{X}$ excitation are included. The weak absorption intensity does not exceed $2.5 \cdot 10^{-20} \text{ cm}^2$. The absorption envelope has a FWHM of 0.61 eV.

The spectra σ_x , σ_y and σ_z are characterized by a broad background, structured by a number of weak narrow peaks, emerging as ‘ripples’ on the spectral profile. The background envelope features several diffuse vibrational bands, similarly to the spectra in the 11D calculation for the isolated 1A_2 state (see Sect. V B). The narrow peaks are overlayed on the broad profile, and are due to the Fano interference of two diabatic dissociation pathways: The direct dissociation pathway in the A_2 state and the second one, which involves a temporary sojourn in the \tilde{X} state. The implications of this interference for the absorption spectrum and the photofragment distributions are discussed elsewhere.[?] As shown in Fig. 9(d), the narrow structures disappear if only the diabatic A_2 state is included in the calculation: They are the signature of coupling at the $\tilde{X}/^1A_2$ conical intersection.

In our calculations, the extent of $A_2 \rightarrow \tilde{X}$ transfer is less than 10% for the three polariza-

tions, and the effects of the conical intersection is small. The diffuse bands are not affected by the state crossing, and can be assigned to vibrational states on the isolated A_2 surface. As in the 11D calculation, the spectral width is mostly due the geometry changes between the (local) minima of V^X and V^{A_2} , conveniently expressed by the shifts (δQ) with respect to the a_1 modes \tilde{Q}_{a_1} , calculated for pyrrolyl at the local A_2 minimum. $\delta Q = 0.37$ for the $\tilde{Q}_{a_1}(1)$ mode, $\delta Q = 1.58$ for $\tilde{Q}_{a_1}(2)$, and $\delta Q = 1.04$ for $\tilde{Q}_{a_1}(5)$. The local mode frequencies are 1052 cm^{-1} for $\tilde{Q}_{a_1}(1)$, 1190 cm^{-1} for $\tilde{Q}_{a_1}(2)$ and 1609 cm^{-1} for $\tilde{Q}_{a_1}(5)$. The displaced modes $\tilde{Q}_{a_1}(1, 2, 5)$ included in the 15D calculation, are sufficient to reproduce the same spectral width of the 11D calculation, which includes all the a_1 coordinates. The vertical excitation energy, 4.72 eV, is also similar for the two calculations, and the resulting spectra span the same excitation energy range.

A number of vibrational bands, although not very pronounced, are recognizable in the spectra for the individual polarizations, and marked with letters in Fig. 9. Similarly to the 11D calculation, the vibrational states contributing to each band have been assigned with the help of the convolution method.

The spectrum σ_x originates from the excitation promoted by the b_2 modes and the in-plane H bending, and has a maximum intensity of $1.7 \cdot 10^{-20} \text{ cm}^2$ at $E_{\text{ph}} = 4.75 \text{ eV}$. The diffuse vibrational structures are poorly resolved.

The y -polarized excitation is promoted by the b_1 modes and the out-of-plane H bending. The maximum intensity of the σ_y profile is $3.7 \cdot 10^{-20} \text{ cm}^2$, corresponding to a vibrational band peaking around 4.65 eV, and coinciding with the maximum of the average profile σ . Another intense band stands out at 4.50 eV, and also persists in the total spectrum.

The profile σ_z originates from the excitation promoted by the a_2 modes. Its maximum intensity is $2.3 \cdot 10^{-20} \text{ cm}^2$, intermediate between σ_x and σ_y . Although the vibrational structure is not very pronounced, the approximate energies of several vibrational bands can be identified: 4.38 eV, 4.50 eV, 4.60 eV, 4.70 eV (the profile maximum) and 4.78 eV.

The energy of the first vibrational peaks increases in the order $A < A' < A''$. Since the spectral width and the low-resolution envelope are similar for the three polarizations, the corresponding absorption maxima are also shifted in the order $\sigma_y < \sigma_z < \sigma_x$. The peaks A, A' and A'' are associated with vibrational states having one quantum in the modes promoting the ${}^1A_2 \leftarrow \tilde{X}$ transition. In the σ_y , σ_z and σ_x spectra, the modes with the largest Herzberg-Teller coefficient are the out-of-plane H bending ($\omega = 616 \text{ cm}^{-1}$), $Q_{a_2}(3)$ ($\omega = 969 \text{ cm}^{-1}$)

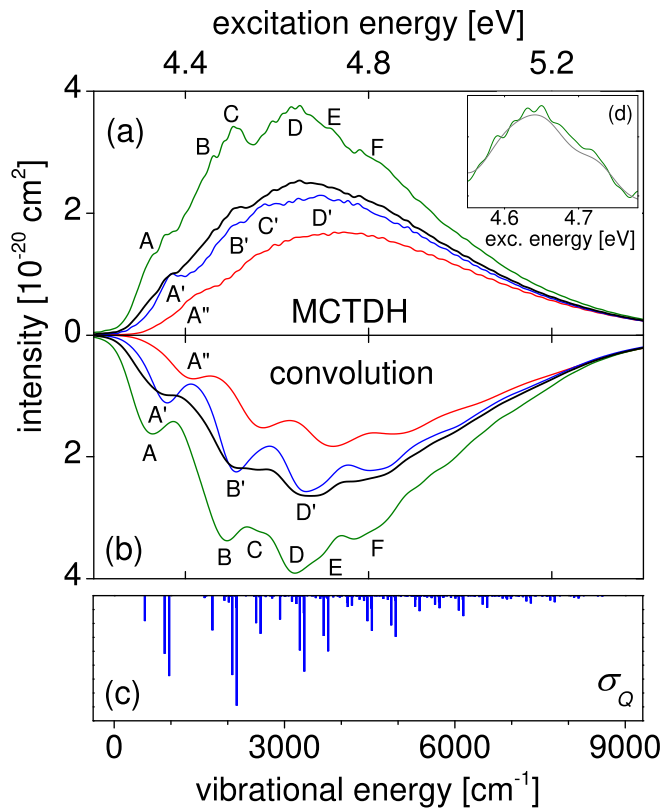


FIG. 9: (a) Absorption spectra for the coupled $\tilde{X}/^1A_2$ states of pyrrole calculated using three disappearing modes (R, θ, ϕ) of the detaching H atom and three modes for each symmetry (a_1, a_2, b_1, b_2). The spectra are calculated exactly using MCTDH propagation on the 15D potential. The profiles σ_x, σ_y and σ_z , corresponding to the x -, y - and y -polarizations are shown in red, green and blue respectively. The total spectrum $(\sigma_x + \sigma_y + \sigma_z)/3$ is shown in black. (b) The same spectra as in (a) evaluated using the convolution approximation. The assigned vibrational bands in (a) and (b) are marked with letters: A – F for σ_y , A' – D' for σ_z , and A'' for σ_x . (c) Vibrational stick spectrum σ_Q , used in the convolution method for the calculation of the σ_z profile. (d) Details of the MCTDH σ_y profiles, calculated using either the isolated 1A_2 state (gray line) and the coupled \tilde{X}/A_2 states (green line). In the assignment, the vibrational levels are denoted using the set of vibrational quantum numbers of the modes $n_\Gamma(i)$ belonging to the irrep Γ . The states mostly contributing to each peak are: (A) $n_{a_1}(i) = 0, n_{b_1}(2) = 1, n_{b_1}(3) = 2$, and the fundamental excitation of the out-of-plane H bending; (A') $n_{a_1}(i) = 0, n_{a_2}(i) = 1$, for $i = 1, 2, 3$; (A'') $n_{a_1}(i) = 0, n_{b_2}(i) = 1$, for $i = 1, 3, 5$, and the fundamental excitation of the in-plane H bending; (B, B') the states of the bands A, A' with $n_{a_1}(2) = 1$; (C, C') the states in A, A' with $n_{a_1}(5) = 1$; (D, D') the states in A, A' with $n_{a_1}(2) = 2$; (E) the states in A with $(n_{a_1}(2) = 1, n_{a_1}(5) = 1)$; (F) the states in A with $n_{a_1}(2) = 3$, and the states in A with $(n_{a_1}(2) = 2, n_{a_1}(5) = 1)$.

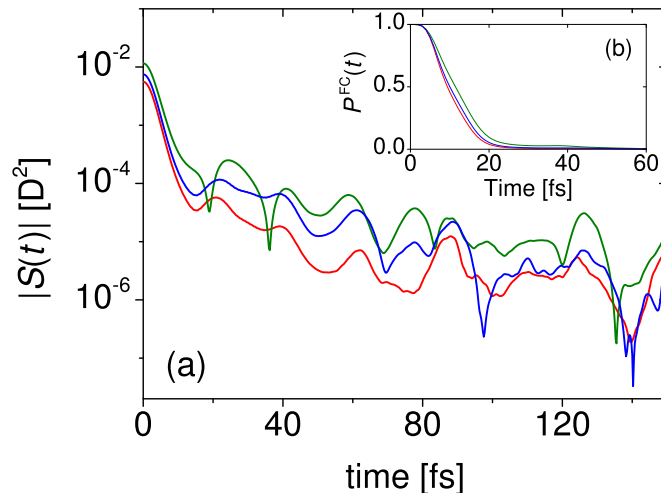


FIG. 10: (a) Autocorrelation function amplitudes $|S_x|$ (red), $|S_y|$ (green) and $|S_z|$ (blue) as a function of time for the spectra of Fig. 9. (b) Populations in the Franck-Condon region P_x^{FC} (red), P_y^{FC} (green) and P_z^{FC} (blue) as a function of time.

and $Q_{b_2}(3)$ ($\omega = 1321 \text{ cm}^{-1}$), respectively: The larger the frequency of the excited modes, the higher the absorption origin.

Fig. 10 shows the autocorrelation functions S_x , S_y and S_z for the first 150 fs of dynamics. The qualitative behaviour is similar for the three polarizations. Similarly to the 6D and 11D calculation, the functions $|S(t)|$ decay rapidly, reaching half of their initial value in the time $T \sim 3$ fs. This initial falloff is due to the initial wave packet motion away from the excitation region, and determines the overall spectral breadth, $\text{FWHM} = 4\hbar \ln 2/T \sim 0.6 \text{ eV}$. In the range 15–100 fs the autocorrelation functions decay more slowly and exhibit a sequence of weak vibrational recurrences. The damping of the recurrences is faster for S_x than for S_y and S_z , therefore the σ_x profile is the least resolved. The recurrence peaks are broader than in the 11D calculation, and have a similar pattern for the three polarizations. The shorter recurrence time is 21 fs and correlates with a frequency of $\approx 1600 \text{ cm}^{-1}$, which matches the vibrational period of the $Q_{a_1}(5)$ mode. A second recurrence follows at 38–39 fs, corresponding to a frequency of $\approx 870 \text{ cm}^{-1}$, associated to the $Q_{a_1}(1)$ mode. A shoulder is visible in $|S_y|$ around 15.5 fs, and is possibly associated to the high frequency N–H stretch. Additional recurrence peaks, not shown in Fig. 10, appear in the range 150 – 300 fs, and are responsible for the narrow peaks on the absorption envelope. Indeed, the evaluation of the

autocorrelation functions up to 300 – 350 fs is needed to ensure that the ‘ripples’ emerge.

Dissociation lifetimes are determined for σ_x , σ_y and σ_z by the time-dependent populations $P_i^{\text{FC}}(t)$, $i = x, y, z$, shown in Fig. 10(b). Time constants T_1 , accounting for the direct dissociations, are obtained by fitting P_i^{FC} to the function of Eq. (39). The resulting values for T_1 are 10.1 fs, 11.8 fs and 10.9 fs for the x -, y - and z -polarizations, respectively. These dissociation lifetimes agree with the results for the 6D and the 11D calculations, and with the experiment of Ref. 37. A second time constant $T_2 = 48.8$ fs is found for $P_y^{\text{FC}}(t)$ (in this case $a = 0.95$): This value is in agreement with the measurements of Ref²⁸, and it is attributed to population which dissociates via tunnelling through the barrier on the A_2 PES.

The spectra calculated using MCTDH quantum dynamics are compared with the convolution approximation in Fig. 9(b). The convolution approach is applied for the dissociation in the single state A_2 using the methodology described in Sect. III B. In this formulation the convolution spectrum provides the assignment of the main diffuse bands, but gives no information on the Fano resonances.

The convolution factors $\bar{\sigma}_R$ and $\bar{\sigma}_Q$ are calculated using the same protocol of the 11D calculation. Since the TDMS μ_x and μ_y depend on the coordinates of either the \mathbf{R} -space and the \mathbf{Q} -space, two convolution terms are needed to approximate the spectra σ_x and σ_y , as shown in Appendix A. The width of the convolution profiles $\bar{\sigma}_R$ and $\bar{\sigma}_Q$ are ~ 0.15 eV and ~ 0.4 eV, respectively: As in the 11D case, the width of 0.65 eV is mainly due to the progression in the a_1 modes, whereas the dissociation induces a smaller broadening.

The convoluted spectra compare well enough with the MCTDH calculation: The position on the energy scale, the shapes of the absorption profile and the differences in the vibrational resolutions are nicely reproduced. The approximated σ_x and σ_z profiles overestimate the vibrational resolution, so that the diffuse bands are more pronounced. The peaks of the convolution spectra are matched to the bands in the MCTDH profiles, and associated with the vibrational states in the local A_2 minimum. The assignment of the most relevant peaks is reported in the Figure caption.

The bands A, A' and A'' in the spectra σ_y , σ_z and σ_x include the symmetry-allowed vibrational states with the lowest energies. In the σ_x profile these states have one vibrational quantum on one the b_2 modes or on the in-plane H bending; in σ_y the lowest energy states are excited in one of the b_1 modes or in the out-of-plane H bending; in σ_z the band A' includes the states with one quantum on one of the a_2 modes. The vibrational states contributing to

the peaks B – F (in σ_y) and B' – D' (in σ_z) arise from the progressions on the modes $Q_{a_1}(2)$ and $Q_{a_1}(5)$, built on the lowest excitations falling under the bands A and A'.

Fig. 10(c) shows the convolution spectrum σ_Q used to calculate the σ_z profile. The stick spectrum includes only the vibrational states of A_2 symmetry. The comparison between the MCTDH profile, the convolution approximation and the σ_Q spectrum reveals some inaccuracies in the harmonic intensities, which are mainly related to the geometry shifts between the minima of V^X and V^{A_2} . The approximated intensities for the excitations on the modes $Q_{a_1}(2)$ and $Q_{a_1}(5)$ (associated with the bands B'' and C'') are respectively too high and too low. The reason is that in the approximation the coupling between the modes $Q_{a_1}(2)$ and $Q_{a_1}(5)$ and the dissociation coordinate R is neglected. As a consequence, the shift used in the convolution method is overestimated for $Q_{a_1}(2)$ and underestimated for $Q_{a_1}(5)$, so that the peak intensities are slightly inaccurate.

VI. RESULTS: PRODUCT STATE DISTRIBUTIONS AND TKER

Pyrryl internal state distributions are evaluated in the 6D, 11D, and 15D calculations, using the procedure of Sect. IV, and shown as TKER spectra [Eq. (31)]. The T -matrix elements of Eq. (30) are calculated using the vibrational eigenstates of the pyrrolyl fragment $\chi_{\mathbf{n}}(\mathbf{Q})$, where \mathbf{n} is the vector of vibrational quantum numbers for the modes \mathbf{Q} . The rotational eigenstates of pyrrolyl are described using symmetry-adapted combinations of spherical harmonics $Y_{jm}(\theta, \phi)$, where (j, m) are the quantum numbers for the operators \mathbf{j}^2 and j_z .

In the TKER spectrum, the individual states peak at the translational energy $\text{TKER} = E_{\text{ph}} - D_0 - E_{\mathbf{n},j,m}$, where E_{ph} is the excitation energy, D_0 is the dissociation energy (calculated including the zero-point energies of pyrrole and pyrrolyl), and $E_{\mathbf{n},j,m}$ is the internal pyrrolyl energy. When the photon energy is increased, the vibrational peaks shift by the same amount on the TKER scale.

In the actual calculations, the δ -function of Eq. (31) is replaced with a Gaussian with a standard deviation of 10 cm^{-1} . As a consequence, the closely spaced rotational states are not resolved in the reported TKER spectra, and only the vibrational peaks are assigned, as in the experimental measurements.

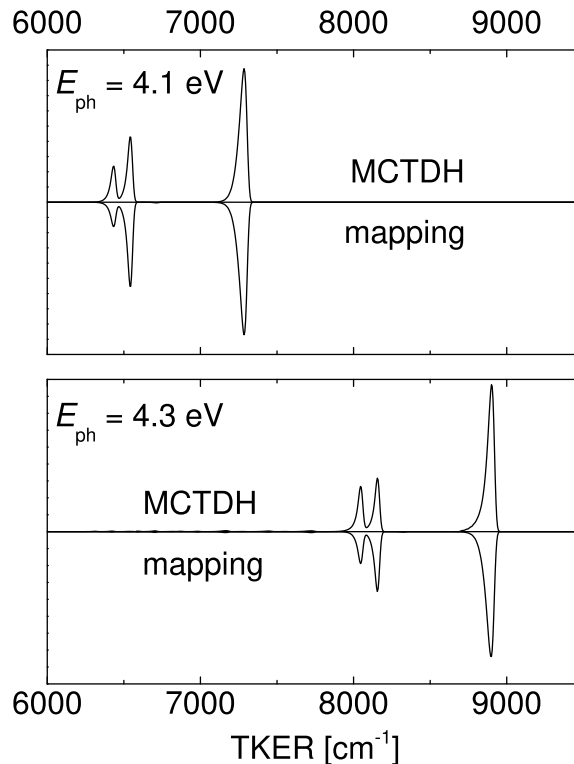


FIG. 11: TKER calculated for the 6D spectra of Fig. 6 at the excitation energies $E_{\text{ph}} = 4.1$ eV and $E_{\text{ph}} = 4.3$ eV. The exact profiles, calculated using the MCTDH wavefunction, are compared to the profiles obtained by adiabatic mapping.

A. 6D product state distributions: Coordinates $R, \theta, \phi, Q_{b_1}(1, 2, 3)$

In this calculation the ${}^1A_2 \leftarrow \tilde{X}$ excitation is induced by the TDM components μ_x and μ_y . The x -polarized excitation is promoted by the disappearing in-plane H bending and leads to the formation of pyrrolyl in vibrational states of A_1 symmetry (associated with angular states of B_2 symmetry). The TDM μ_y excites either the out-of-plane H bending or the b_1 normal modes, so that pyrrolyl is formed in vibrational states of A_1 and B_1 symmetry, respectively (the total symmetry-allowed rovibrational states belong to the irrep B_1). It is worth to emphasize that such symmetry considerations apply because: i) The calculation is performed for total angular momentum $J = 0$; ii) only one electronic state is included; iii) the harmonic Hamiltonian for the \mathbf{Q} -space, based on a block diagonal Hessian, prevents the exchange of vibrational excitation between degrees of freedom of different symmetry.

The TKERs calculated from the MCTDH wavefunction are shown in Fig. 11 for the excitation energies $E_{\text{ph}} = 4.1 \text{ eV}$ and $E_{\text{ph}} = 4.3 \text{ eV}$, corresponding to the maximum and the shoulder of the total spectrum, shown in black in Fig. 6(a). The spectra are averaged over the field polarizations and consist of three peaks. The fastest peak corresponds to the vibrational ground state, and the two slower peaks are assigned to the fundamental excitations on the modes $Q_{b_1}(2)$ and $Q_{b_1}(3)$. Overtones and combination states are scarcely populated.

The vibrational ground state is formed because the TDM components μ_x and μ_y excite the in- and out-of-plane bending modes of the detaching H atom, which disappear into the free rotations of pyrrolyl. The states with one quantum on the b_1 modes are formed for the excitation induced by the TDM component μ_y . The peak intensities for the different modes are determined by the magnitude of the Herzberg-Teller coefficients: The mode $Q_{b_1}(1)$ contributes negligibly to the TDM, therefore it is not populated in the fragment.

The line shapes of the vibrational peaks are given by rotational distributions and have a FWHM of $\approx 60 \text{ cm}^{-1}$. Since the dissociating wave packets experience a weak torque along θ , the rotational excitation is modest (the highest population is obtained for $j \approx 10$).

The exact TKER spectra are compared with the distributions obtained using the adiabatic mapping approximation described in Sect. IV B. Each pyrrolyl mode adiabatically correlates with a specific mode at the 1A_2 minimum in the FC range. According to Eq. (37), the populations of the fragment states are approximated as products of a FC overlap (for the \mathbf{Q} -space) and a radial factor $\bar{\sigma}_R$ evaluated at the corresponding translational energy. The rotational line shapes are calculated from the rotational distributions obtained from the wave packet propagation in the \mathbf{R} -space.

The approximated spectra agree almost perfectly with the exact MCTDH calculation. This proves that the 6D potential V^{A_2} , involving only undisplaced modes, has a high degree of vibrational adiabaticity. Therefore the initial vibrational state distribution, created in the excitation region, is carried over to the fragments without any energy redistribution.

B. 11D product state distributions: Coordinates $R, \theta, \phi, Q_{a_1}(1, 2, 3, 4, 5, 6, 7, 8)$

In the 11D calculation the TDM components μ_x and μ_y induce the ${}^1A_2 \leftarrow \tilde{X}$ transition exciting the in- and out-of-plane H bending modes, respectively. Since the initially excited

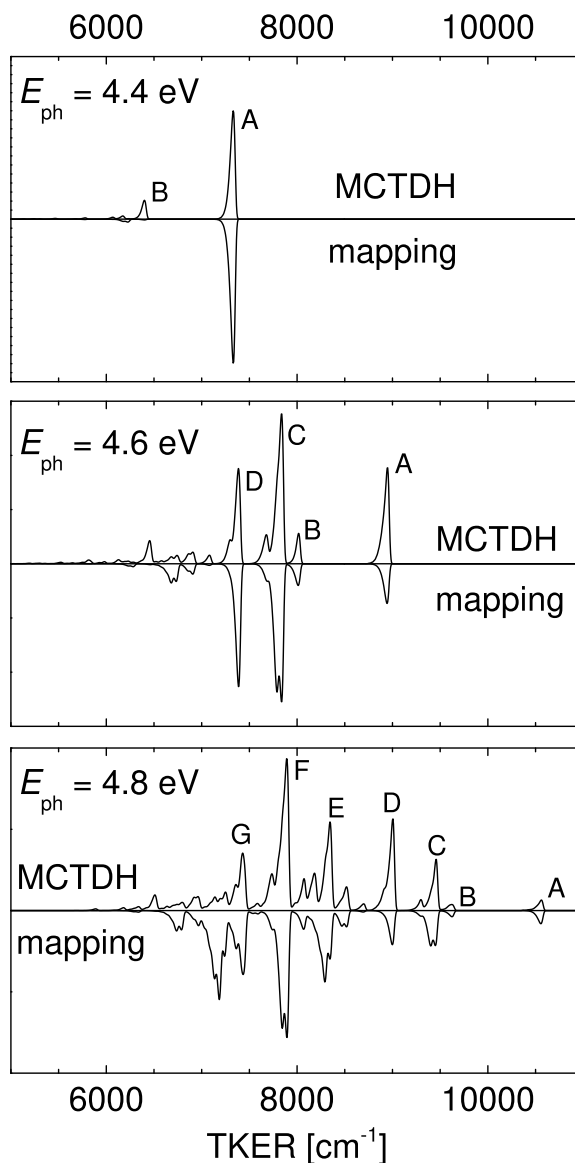


FIG. 12: TKER calculated for the 11D spectra of Fig. 7 at the excitation energies $E_{\text{ph}} = 4.4 \text{ eV}$, $E_{\text{ph}} = 4.6 \text{ eV}$ and $E_{\text{ph}} = 4.8 \text{ eV}$. The exact profiles, calculated using the MCTDH wavefunction, are compared to the profiles obtained by adiabatic mapping. Following the notation of Fig. 9, the vibrational states are assigned as follows: (A) ground state; (B) $n_{a_1}(1) = 1$; (C) $n_{a_1}(2) = 1$; (D) $n_{a_1}(5) = 1$; (E) $n_{a_1}(2) = 2$; (F) ($n_{a_1}(2) = 1, n_{a_1}(5) = 1$); (G) $n_{a_1}(2) = 3$.

coordinates are disappearing modes, pyrrolyl is formed in vibrational states of A_1 symmetry, associated with rotational states of either B_1 or B_2 symmetry.

The polarization-averaged TKER profile, corresponding to the spectrum shown in black

in Fig. 7(a), is plotted in Fig. 12 for the excitation energies $E_{\text{ph}} = 4.4 \text{ eV}$, $E_{\text{ph}} = 4.6 \text{ eV}$ and $E_{\text{ph}} = 4.8 \text{ eV}$. A number of vibrational peaks are visible, and the rotational line shapes are very similar to the ones discussed in Sect. VI A.

Differently from the 6D calculation, the vibrational state populations depend strongly on the photon energy. The total spectrum is a sum of partial cross sections, each one being associated to a particular vibrational state of the fragment: The vibrational state populations are given by the intensities of the partial cross sections at a given photon energy. The partial cross sections for the states in the vibrational progression of a a_1 mode are displaced by the mode frequency. With increasing photon energy, the most populated state changes from the ground state to a state with a gradually higher degree of vibrational excitation.

The excitation energy of $E_{\text{ph}} = 4.4 \text{ eV}$ is close to the origin of the absorption. At this energy only the ground state (peak A) and the state with one quantum on the low frequency $Q_{a_1}(1)$ mode (peak B) are significantly populated. The states with excitations on higher frequency modes have low initial intensities, therefore their population is negligible.

At $E_{\text{ph}} = 4.6 \text{ eV}$ the states with zero or one vibrational quantum are the most populated. The peak C corresponds to the state with one quantum on the mode $Q_{a_1}(2)$. The peak D is the fundamental excitation of the $Q_{a_1}(5)$ mode. The most populated pyrrolyl modes, $Q_{a_1}(2,5)$, correlate adiabatically with the modes $\tilde{Q}_{a_1}(2,5)$ in the FC zone, which give rise to the most extended progressions in the absorption spectrum (see Sect. V B).

At $E_{\text{ph}} = 4.8 \text{ eV}$ the most populated states are overtones and combination states. The most intense peaks correspond to the state with two quanta on $Q_{a_1}(2)$ (peak E), the state with one quantum on both $Q_{a_1}(2)$ and $Q_{a_1}(5)$ (peak F), and the state with three quanta on $Q_{a_1}(2)$ (peak G).

In Fig. 12, the exact TKER are compared with the distributions obtained by the adiabatic mapping approach. The approximation makes use of the convolution factors $\bar{\sigma}_R$ and $\bar{\sigma}_Q$, discussed in Sect. V B. Each mode at the local A_2 minimum is associated with the mostly overlapping fragment mode. In this way, each vibrational state in the excitation zone is mapped onto a fragment state. Excitation energy dependent vibrational state populations are calculated as the product of a FC factor (taken from the spectrum $\bar{\sigma}_Q$) and the $\bar{\sigma}_R$ intensity at the given translational energy [see Eq. (37)].

The approximated TKER profiles agree nicely with the distributions calculated using

wave packet propagation. The adiabatic mapping proves to be a good method to estimate the final state distributions using a minimum number of ab initio calculations. The good quality of the approximation is justified by a high degree of vibrational adiabaticity. The most populated states involve excitations in the modes mapped to the most displaced modes between the minima of V^X and V^{A_2} , which have the longest progressions. The excitation created in the FC zone is then propagated to the fragments.

Some discrepancies between the MCTDH calculation and the adiabatic mapping can be analyzed. For $E_{\text{ph}} = 4.4 \text{ eV}$, the population of the $Q_{a_1}(1)$ mode is highly underestimated. The reason is that the $Q_{a_1}(1)$ mode is not very displaced in the excitation region, but it is the most displaced mode between pyrrole and pyrrolyl. Therefore, the $Q_{a_1}(1)$ mode develops the excitation along the dissociation pathway, but not in the FC zone.

Another inaccuracy is the overestimation of the population of the $Q_{a_1}(3)$ mode. The excitations of this mode do not appear in the MCTDH calculation, whereas they are visible as a ‘bifurcation’ in the peak C (which involves also the excitation of the $Q_{a_1}(2)$ mode). The mode $Q_{a_1}(3)$ undergoes a substantial Duschinsky mixing between the FC zone and the pyrrolyl. The short-distance pyrrole modes having the highest overlap with $Q_{a_1}(3)$ are the modes $\tilde{Q}_{a_1}(3)$, which has an extended FC progression, and $\tilde{Q}_{a_1}(4)$, whose FC progression is narrow. In the approximation, $Q_{a_1}(3)$ is mapped only to $\tilde{Q}_{a_1}(3)$, and not to the nearly undisplaced $\tilde{Q}_{a_1}(4)$. Therefore, the extent of its progression, as well as its final population, are overestimated.

C. 15D product state distributions: Coordinates

$$R, \theta, \phi, Q_{a_1}(1, 2, 5), Q_{a_2}(1, 2, 3), Q_{b_1}(1, 2, 3), Q_{b_2}(1, 3, 5)$$

TKER spectra are calculated for the photodissociation in the coupled ${}^1A_2/\tilde{X}$ states. The higher electronic channel, diabatically correlating with the \tilde{X} state, is closed at the excitation energies of the calculation. Since the $A_2 \rightarrow \tilde{X}$ internal conversion involves less than 10% of the population, the effect of the conical intersection on the TKER spectra is expected to be relevant only at the energies of strong Fano resonances, not observed here.

The ${}^1A_2 \leftarrow \tilde{X}$ transition is induced by the three TDM components, which create initial states of different symmetries, and are associated with different product states. The symmetry of the fragment vibrational-rotational states is given as the direct product $\Gamma_Q \times \Gamma_{\text{ang}}$,

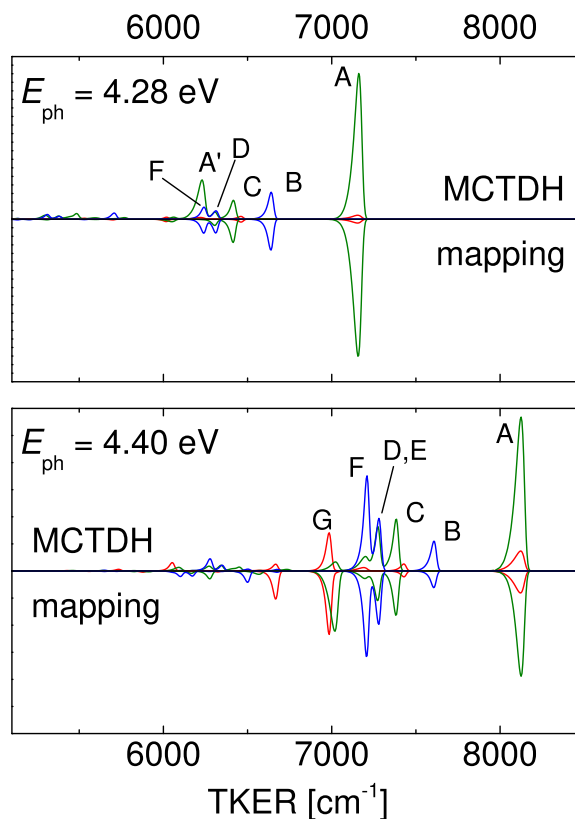


FIG. 13: TKER calculated for the 15D spectra of Fig. 9 at the excitation energies $E_{\text{ph}} = 4.28$ eV, and $E_{\text{ph}} = 4.40$ eV. The profiles obtained for the ${}^1A_2 \leftarrow \tilde{X}$ promoted by the TDM components μ_x , μ_y and μ_z are shown in red, green and blue, respectively. The exact profiles, calculated using the MCTDH wavefunction, are compared to the profiles obtained by adiabatic mapping. Following the notation of Fig. 9, the vibrational states are assigned as follows: (A) ground state; (B) $n_{a_2}(1) = 1$; (C) $n_{b_1}(2) = 1$; (D) $n_{a_2}(2) = 1$; (E) $n_{b_1}(3) = 2$; (F) $n_{a_2}(3) = 1$; (G) $n_{b_2}(3) = 1$.

where Γ_Q and Γ_{ang} are the irreducible representations of the vibrational and rotational eigenfunctions, respectively. For the μ_x -induced transition, the symmetry-allowed vibrational-rotational states have B_2 symmetry and can be formed with the following combinations: (i) $\Gamma_Q = A_1$, $\Gamma_{\text{ang}} = B_2$; (ii) $\Gamma_Q = B_2$, $\Gamma_{\text{ang}} = A_1$; (iii) $\Gamma_Q = A_2$, $\Gamma_{\text{ang}} = B_1$; (iv) $\Gamma_Q = B_1$, $\Gamma_{\text{ang}} = A_2$. For the y -polarization, the total symmetry is B_1 and the possible combinations are: (v) $\Gamma_Q = A_1$, $\Gamma_{\text{ang}} = B_1$; (vi) $\Gamma_Q = B_1$, $\Gamma_{\text{ang}} = A_1$; (vii) $\Gamma_Q = A_2$, $\Gamma_{\text{ang}} = B_2$; (viii) $\Gamma_Q = B_2$, $\Gamma_{\text{ang}} = A_2$. For the μ_z -induced transition the total symmetry is A_2 and the allowed states are: (ix) $\Gamma_Q = A_2$, $\Gamma_{\text{ang}} = A_1$; (x) $\Gamma_Q = A_1$, $\Gamma_{\text{ang}} = A_2$. The combinations (i), (ii), (v), (vi) and (ix) are associated to the five different terms in the TDM expression of

Eq. (13). The combinations (iii), (iv), (vii), (viii) and (x), cannot be populated in a single state dissociation, but they are theoretically allowed by the conical intersection. Consider, as an example, a wave packet in the state (i), initially on the V^{A_2} surface, which undergoes a first transfer to the \tilde{X} state induced by a a_2 coupling mode, and a second back transfer induced by the angular term $\sim \sin^2 \theta \sin(2\phi)$: The final state would be in the form (iii). Although such states are in principle allowed, they are not populated in our simulations, probably due to the weak diabatic coupling induced by the angular coordinates.

The TKER spectra for the three polarizations, $P_i(E_{\text{kin}}|E_{\text{ph}})$, with $i = x, y, z$, are shown in Fig. 13 for the excitation energies $E_{\text{ph}} = 4.28$ eV and $E_{\text{ph}} = 4.40$ eV, corresponding to the low energy side of the absorption spectrum (see Fig. 9), in which a relatively low number of vibrational channels is open. At higher excitation energies, the number of populated states greatly increases, so that the detailed analysis of the TKER spectra becomes cumbersome.

For $E_{\text{ph}} = 4.28$ eV, the TKER profile is dominated by the peaks associated with the y -polarization, because the intensities of σ_x and σ_z are low at this excitation energy. The peak A is the most intense, and corresponds to the ground vibrational state, which is formed after the initial ${}^1A_2 \leftarrow \tilde{X}$ excitation, induced by the out-of-plane H bending (a disappearing mode). This is the lowest frequency mode, therefore it is the first to be excited while scanning the spectrum from the origin to higher energies. The second highest peak (A') corresponds to the fundamental excitation of the $Q_{a_1}(1)$ mode. The peak C is associated with the state with one quantum on the $Q_{b_1}(2)$ mode, which is the b_1 mode with the highest Herzberg-Teller coefficient. The peaks corresponding to the fundamental excitations on the three a_2 modes are visible in the $P_z(E_{\text{kin}}|E_{\text{ph}})$ profile, and marked with the letters B, D and F. The weak structures appearing at $\text{TKER} < 5800 \text{ cm}^{-1}$ are given by vibrational states, obtained by adding a quantum on $Q_{a_1}(1)$ to the states peaking between 6000 cm^{-1} and 6700 cm^{-1} .

In the TKER profile for $E_{\text{ph}} = 4.40$ eV, the dominating peak (A) is still the vibrational ground state, arising mostly from the y -polarization. However, the ground state population decreases with increasing excitation energy, and the peaks corresponding to states with one vibrational quantum (between 6600 cm^{-1} and 7700 cm^{-1}) become more intense. The peaks C and E in the $P_y(E_{\text{kin}}|E_{\text{ph}})$ TKER spectrum correspond to the fundamental excitations on the modes $Q_{b_1}(2)$ and $Q_{b_1}(3)$. The mode $Q_{b_1}(1)$ has a tiny Herzberg-Teller coefficient, therefore it is not populated. The three states with one quantum on the a_2 modes are visible in the TKER profile for the z -polarization (peaks B, D and F). Their intensities

increase in the order $Q_{a_2}(1) < Q_{a_2}(2) < Q_{a_2}(3)$, in agreement with the magnitude of the Herzberg-Teller coefficients. The most intense peaks in the $P_x(E_{\text{kin}}|E_{\text{ph}})$ profile are also due to the modes with the largest coefficients in the TDM function μ_x : The disappearing in-plane H bending, associated with the ground state peak, and the $Q_{b_2}(3)$ coordinate, whose fundamental excitation is associated with peak G. The peaks for $\text{TKER} < 6600 \text{ cm}^{-1}$ are obtained from the states B–G, with an additional quantum on the $Q_{a_1}(1)$.

The correlation between the magnitude of the Herzberg-Teller coefficients and the final mode populations, observed in the TKER profiles, is the basic assumption for the validity of the adiabatic mapping approach. Fig. 13 illustrates the comparison between the TKER spectra, obtained from the MCTDH calculation, and the profiles calculating using the mapping. The approximation follows the same protocol described in Sect. IV B, applied to the dissociation in the isolated V^{A_2} PES.

The mapping approach is successful in predicting the vibrational pattern in the TKER spectra. In a similar way to the 6D and 11D calculations, the good quality of the approximation implies a picture in which the initial vibrational excitation, created by the TDM function, is propagated along the reaction pathway in a vibrationally adiabatic manner.

The only substantial difference between the adiabatic mapping and the exact MCTDH calculation, is the intensity of the A' peak, associated with the fundamental excitation of the $Q_{a_1}(1)$ mode. The population of this vibrational state is underestimated at $E_{\text{ph}} = 4.28 \text{ eV}$ and overestimated at $E_{\text{ph}} = 4.40 \text{ eV}$. This inaccuracy was discussed in Sect. VI B, and it is due to a high degree of coupling between the $Q_{a_1}(1)$ mode and the coordinate R , which reduces the validity of the separable approximation of Eq. (20).

VII. CONCLUSIONS

This paper analyzes the mechanism of the photodissociation of pyrrole, following the excitation to the low-lying ${}^1A_2(\pi\sigma^*)$ state. The absorption spectrum, the dissociation lifetimes and the total kinetic energy release distributions are calculated. To this purpose, 24-dimensional potential energy surfaces of the \tilde{X} state and the two lowest $\pi\sigma^*$ states are constructed using CASPT2 calculations and a local diabaticization in proximity of the $\tilde{X}/\pi\sigma^*$ intersections. Nuclear dynamics are studied at the quantum mechanical level, using the MCTDH method with high-dimensional PESs for the \tilde{X} and 1A_2 states. The exact absorp-

tion spectra and photon energy-dependent TKER distributions are compared with approximated profiles, obtained by a convolution approach and an adiabatic mapping method, whose application requires a modest amount of ab initio calculations. The main results of this investigation are as follows:

1. The photoabsorption profile for the ${}^1A_2 \leftarrow \tilde{X}$ excitation, forbidden at C_{2v} geometries, is predicted to have a weak cross section, not exceeding $3 \cdot 10^{-20} \text{ cm}^2$. The spectrum cannot be reasonably measured, because it is overlaid by the $\approx 2 \cdot 10^{-18} \text{ cm}^2$ intense band of a neighbouring $\pi\pi^*$ state.⁵⁰ The width of the absorption profile is due to vibrational progressions involving the a_1 modes of the pyrrolyl ring. Non-totally symmetric modes are excited by the geometry-dependent transition dipole moment functions. Different modes are excited for different electric field polarizations. The vibrational bands are highly broadened by the fast dissociation.
2. Photodissociation occurs on a time scale of $\approx 10 \text{ fs}$, in agreement with the recent time-resolved photoelectron spectroscopy measurements of Stolow and coworkers.³⁷ A second time constant of $\approx 45 \text{ fs}$ is associated to dissociation via tunneling through the $\sim 0.9 \text{ eV}$ potential barrier on the A_2 PES.
3. The convolution approximation is capable of reproducing the main features of the exact absorption spectra. The agreement is excellent for the bands of the undisplaced non-totally symmetric modes. In the progressions for the a_1 modes, small inaccuracies are found for the mode frequencies, the relative peak intensities for different modes, and the spectral resolution. Nevertheless, the convolution method is proved to be a valid tool to assign the diffuse vibrational bands, using a small amount of ab initio calculations.
4. The TKER spectra consist in a number of peaks, corresponding to the vibrational levels of the pyrrolyl fragment. States of different symmetries are populated for different electric field polarizations. The PES of the 1A_2 state, quadratic in the normal modes, has a high degree of vibrational adiabaticity. Such property was already pointed out by Ashfold and coworkers³², and implies that TKER profiles are largely defined by the initial wave packet, created by the TDM functions. Therefore, the most populated states are the ground vibrational level and the fundamental excitation of the modes

which strongly induce the ${}^1A_2 \leftarrow \tilde{X}$ excitation.

5. The adiabatic mapping approximation successfully reproduces the exact TKER distribution, and their dependence on the excitation energy. The good quality of the approximation is ascribed to the vibrational adiabaticity. The convolution and adiabatic mapping methods can be applied together, without the necessity of constructing high-dimensional potential energy surfaces. Therefore they are valuable for a systematic study of photodissociation in large classes of polyatomic aromatic molecules, in which vibrationally adiabatic dynamics are expected.

Although the CASPT2 calculations underestimate the vertical excitation energy and the dissociation energy, the results obtained from the nuclear quantum dynamics, compare well with most of the experimental observations on the low energy photodissociation of pyrrole.

APPENDIX A: CONVOLUTION APPROXIMATION FOR A GENERAL FORM OF THE HERZBERG-TELLER TDM

In this Appendix, the convolution approximation described in Section III B is developed for a more general TDM function,

$$\mu(\mathbf{R}, \mathbf{Q}) = \sum_i \mu_R^i(\mathbf{R}) \mu_Q^i(\mathbf{Q}) , \quad (\text{A1})$$

which includes Eq. (13) as a special case.

The initial state of the parent molecules is taken as in Eq. (18), $\Psi_0(\mathbf{R}, \mathbf{Q}) \approx \Psi_R(\mathbf{R})\Psi_Q(\mathbf{Q})$, and the photoexcited state $\Phi(\mathbf{R}, \mathbf{Q})$ is obtained by applying the TDM function of Eq. (A1),

$$\begin{aligned} \Phi(\mathbf{R}, \mathbf{Q}) &= \mu(\mathbf{R}, \mathbf{Q})\Psi_0(\mathbf{R}, \mathbf{Q}) \\ &= \sum_i (\mu_i^R(\mathbf{R})\Psi_R(\mathbf{R})) (\mu_i^Q(\mathbf{Q})\Psi_Q(\mathbf{Q})) \\ &= \sum_i F_R^i(\mathbf{R})f_Q^i(\mathbf{Q}) . \end{aligned} \quad (\text{A2})$$

Eq. (A2) is a generalization of the Eq. (19) for the initial state.

Using the separability approximation of Eq. (20), an expression akin to Eq. (21) is

obtained for the autocorrelation function:

$$\begin{aligned} S(t) &\approx \sum_{ij} \langle F_R^i | \exp(-i\hat{H}_R t) | F_R^j \rangle_R \langle f_Q^i | \exp(-i\hat{H}_Q t) | F_Q^j \rangle_Q \\ &= \sum_{ij} s_R^{ij}(t) s_Q^{ij}(t) . \end{aligned} \quad (\text{A3})$$

The cross-correlation functions $s_R^{ij}(t)$ and $s_Q^{ij}(t)$ are used to define the spectral functions

$$\begin{aligned} \bar{\sigma}_R^{ij}(E) &= \int_{-\infty}^{\infty} s_R^{ij}(t) e^{iEt} dt \\ \bar{\sigma}_Q^{ij}(E) &= \int_{-\infty}^{\infty} s_Q^{ij}(t) e^{iEt} dt . \end{aligned} \quad (\text{A4})$$

The approximated absorption spectrum, given by the Fourier transform of the autocorrelation function of Eq. (A3), is finally given as

$$\sigma(E_{\text{ph}}) = \frac{E_{\text{ph}}}{2\epsilon_0 c} \sum_{ij} \int_{-\infty}^{\infty} \bar{\sigma}_R^{ij}(E_{\text{ph}} - \omega) \bar{\sigma}_Q^{ij}(\omega) d\omega . \quad (\text{A5})$$

Eq. (A5) is the extension of Eq. (23) to the TDM in the general form of Eq. (A1).

In order to apply Eq. (A5), the initial functions $F_R^i(\mathbf{R})$ are propagated in the \mathbf{R} -space, under the action of the Hamiltonian \hat{H}_R , and used to evaluate the cross-correlation functions $s_R^{ij}(t)$, whose Fourier transform gives the spectral functions $\bar{\sigma}_R^{ij}(E)$. The profiles $\bar{\sigma}_Q^{ij}(E)$ can be calculated analytically for the harmonic Hamiltonian \hat{H}_Q , and are given as an expression akin to Eq. (24):

$$\bar{\sigma}_Q^{ij}(E) = \sum_m \langle f_Q^i(\mathbf{Q}) | \phi_m(\mathbf{Q}) \rangle \langle \phi_m | f_Q^j(\mathbf{Q}) \rangle \delta(E - E_m) . \quad (\text{A6})$$

ACKNOWLEDGMENTS

S.Yu.G. acknowledges the financial support by the Deutsche Forschungsgemeinschaft.

¹ A. L. Devine, B. Cronin, M. G. D. Nix, and M. N. R. Ashfold. *J. Chem. Phys.*, 125:184302, 2006.

² D. J. Hadden, K. L. Wells, G. M. Roberts, L. T. Berhendahl, M. J. Paterson, and V. G. Stavros. *Phys. Chem. Chem. Phys.*, 13:10342, 2011.

- ³ R. Montero, A. P. Conde, V. Ovejas, M. Fernandez-Fernandez, F. Castaño, and A. Longarte. *J. Phys. Chem. A*, 116:10752, 2012.
- ⁴ R. Crespo-Otero, M. Barbatti, H. Yu, N. K. Evans, and S. Ullrich. *ChemPhysChem*, 12:3365, 2011.
- ⁵ G. M. Roberts, C. A. Williams, M. J. Paterson, S. Ulrich, and V. G. Stavros. *Chem. Sci.*, 5:1698, 2014.
- ⁶ M. N. R. Ashfold, A. L. Devine, R. N. Dixon, G. A. King, M. G. D. Nix, and T. A. A. Oliver. *Proc. Natl. Acad. Sci. U. S. A.*, 105:12701, 2008.
- ⁷ M. N. R. Ashfold, B. Cronin, A. L. Devine, R. N. Dixon, and M. G. D. Nix. *Science*, 312:1637, 2006.
- ⁸ M. G. D. Nix, A. L. Devine, B. Cronin, R. N. Dixon, and M. N. R. Ashfold. *J. Chem. Phys.*, 125:133318, 2006.
- ⁹ M. G. D. Nix, A. L. Devine, B. Cronin, and M. N. R. Ashfold. *Phys. Chem. Chem. Phys.*, 8:2610, 2006.
- ¹⁰ T. J. Godfrey, H. Yu, M. S. Biddle, and S. Ullrich. *Phys. Chem. Chem. Phys.*, 17:25197, 2015.
- ¹¹ T. A. A. Oliver, G. A. King, and M. N. R. Ashfold. *Phys. Chem. Chem. Phys.*, 13:14646, 2011.
- ¹² M. M. Zawadzki, J. O. F. Thompson, E. A. Burgess, M. J. Paterson, and D. Townsend. *Phys. Chem. Chem. Phys.*, 17:26659, 2015.
- ¹³ M. N. R. Ashfold, G. A. King, D. Murdock, M. G. D. Nix, T. A. A. Oliver, and A. G. Sage. *Phys. Chem. Chem. Phys.*, 12:1218, 2010.
- ¹⁴ G. M. Roberts and V. G. Stavros. *Chem. Sci.*, 5:1698, 2014.
- ¹⁵ B. Marchetti, T. N. V. Karsili, M. N. R. Ashfold, and W. Domcke. *Phys. Chem. Chem. Phys.*, 18:20007, 2016.
- ¹⁶ A. L. Sobolewski, W. Domcke, C. Dedonder-Lardeux, and C. Jouvet. *Phys. Chem. Chem. Phys.*, 4:1093, 2002.
- ¹⁷ Z. Lan, W. Domcke, V. Vallet, A. L. Sobolewski, and S. Mahapatra. *J. Chem. Phys.*, 122:224315, 2005.
- ¹⁸ M. Barbatti, H. Lischka, S. Salzmann, and C. M. Marian. *J. Chem. Phys.*, 130:034305, 2009.
- ¹⁹ K. R. Yang, X. Xu, J. J. Zheng, and D. G. Truhlar. *Chem. Sci.*, 5:4661, 2014.
- ²⁰ X. Zhu and D. R. Yarkony. *J. Chem. Phys.*, 144:024105, 2016.
- ²¹ C. Xie, J. Ma, X. Zhu, D. Yarkoni, S. Xie, and H. Guo. *J. Am. Chem. Soc.*,

- doi 10.1021/jacs.6b03288*, 2016.
- ²² C. Brand, J. Küpper, D. W. Pratt, W. L. Meerts, D. Krüger, J. Tatchen, and M. Schmitt. *Phys. Chem. Chem. Phys.*, 12:4968, 2010.
- ²³ J. Michl and V. Bonacic-Koutecky. *Electronic Aspects of Organic Photochemistry*. Wiley, New York, 1990.
- ²⁴ D. A. Blank, S. W. North, and Y. T. Lee. *Chem. Phys.*, 187:35, 1994.
- ²⁵ J. Wei, A. Kuczmann, J. Riedel, F. Renth, and F. Temps. *Phys. Chem. Chem. Phys.*, 5:315, 2003.
- ²⁶ T. Suzuki. *J. Phys. B: At. Mol. Opt. Phys.*, 47:124001, 2014.
- ²⁷ M. H. Palmer and P. J. Wilson. *Mol. Phys.*, 101:2391, 2003.
- ²⁸ G. M. Roberts, C. A. Williams, H. Yu, A. S. Chatterley, J. D. Young, S. Ullrich, and V. G. Stavros. *Faraday Discuss.*, 163:95, 2013.
- ²⁹ B. O. Roos, P.-A. Malmqvist, V. Molina, L. Serrano-Andres, and M. Merchan. *J. Chem. Phys.*, 116:7526, 2002.
- ³⁰ S. Yu. Grebenshchikov and D. Picconi. Fano resonances in the photoinduced h-atom elimination dynamics in the $\pi\sigma^*$ states of pyrrole. *submitted*.
- ³¹ J. Wei, J. Riedel, A. Kuczmann, F. Renth, and F. Temps. *J. Chem. Soc. Faraday Disc.*, 127:267, 2004.
- ³² B. Cronin, M. G. D. Nix, R. H. Qadiri, and M. N. R. Ashfold. *Phys. Chem. Chem. Phys.*, 6:5031, 2004.
- ³³ V. Vallet, Z. Lan, S. Mahapatra, A. L. Sobolewski, and W. Domcke. *J. Chem. Phys.*, 123:144307, 2005.
- ³⁴ M. Barbatti, M. Vazdar, A. J. A. Aquino, M. Eckert-Maksic, and H. Lischka. *J. Chem. Phys.*, 125:164323, 2006.
- ³⁵ B. Cronin, A. L. Devine, M. G. D. Nix, and M. N. R. Ashfold. *Phys. Chem. Chem. Phys.*, 8:3440, 2006.
- ³⁶ H. Lippert, H.-H. Ritze, L. V. Hertel, and W. Raqdlhoff. *Chem. Phys. Chem.*, 5:1423, 2004.
- ³⁷ G. Wu, S. P. Neville, O. Schalk, T. Sekikawa, M. N. R. Ashfold, G. A. Worth, and A. Stolow. *J. Chem. Phys.*, 142:074302, 2015.
- ³⁸ S. Faraji, M. Vazdar, V. S. Reddy, M. Eckert-Maksic, H. Lischka, and H. Köppel. *J. Chem. Phys.*, 135:154310, 2011.

- ³⁹ P. Celani and H. J. Werner. *J. Chem. Phys.*, 119:5044, 2003.
- ⁴⁰ B. Sellner, M. Barbatti, and H. Lischka. *J. Chem. Phys.*, 131:024312, 2009.
- ⁴¹ S. P. Neville and G. A. Worth. *J. Chem. Phys.*, 140:034317, 2014.
- ⁴² O. P. J. Vieuxmaire, Z. Lan, A. L. Sobolewski, and W. Domcke. *J. Chem. Phys.*, 129:224307, 2008.
- ⁴³ D. V. Makhov, K. Saita, T. J. Martinez, and D. V. Shalashilin. *Phys. Chem. Chem. Phys.*, 17:3316–3325, 2015.
- ⁴⁴ W. H. Miller, N. C. Handy, and J. E. Adams. *J. Chem. Phys.*, 72:99, 1980.
- ⁴⁵ P. R. Bunker and P. Jensen. *Molecular Symmetry and Spectroscopy*. NRC Research Press, Ottawa, 2006.
- ⁴⁶ H. Köppel, W. Domcke, and L. S. Cederbaum. *Adv. Chem. Phys.*, 57:59, 1984.
- ⁴⁷ H. Köppel, J. Gronki, and S. Mahapatra. *J. Chem. Phys.*, 115:2377, 2001.
- ⁴⁸ T. H. Dunning. *J. Chem. Phys.*, 90:1007, 1989.
- ⁴⁹ W. H. Miller, N. C. Handy, and J. E. Adams. *J. Chem. Phys.*, 72:99, 1979.
- ⁵⁰ M. H. Palmer, I. C. Walker, and M. F. Guest. *Chem. Phys.*, 238:179, 1998.
- ⁵¹ M. Pastore, C. Angeli, and R. Cimiraglia. *Chem. Phys. Lett.*, 422:522, 2006.
- ⁵² A. J. Gianola, T. Ichino, R. L. Hoenigman, S. Kato, V. M. Bierbaum, and W. C. Lineberger. *J. Phys. Chem. A*, 108:10326, 2004.
- ⁵³ A. Motzke, Z. Lan, C. Woywod, and W. Domcke. *Chem. Phys.*, 329:50, 2006.
- ⁵⁴ X. Li and J. Paldus. *J. Phys. Chem. A*, 114:8591, 2010.
- ⁵⁵ A. B. Trofimov and J. Schirmer. *Chem. Phys.*, 214:153, 1997.
- ⁵⁶ H.-J. Werner and W. Meyer. *J. Chem. Phys.*, 74:5802, 1981.
- ⁵⁷ H. Köppel. In W. Domcke, D. R. Yarkony, and H. Köppel, editors, *Conical Intersections*. World Scientific, Singapore, 2004.
- ⁵⁸ M. H. Beck, A. Jäckle, G. A. Worth, and H.-D. Meyer. *Phys. Rep.*, 324:1, 2000.
- ⁵⁹ G. A. Worth, M. H. Beck, A. Jäckle, and H.-D. Meyer. The MCTDH Package. H.-D. Meyer, Version 8.3 (2002), Version 8.4 (2007). O. Vendrell and H.-D. Meyer, Version 8.5 (2011). see <http://mctdh.uni-hd.de/>.
- ⁶⁰ S. Schumm, M. Gerhards, and K. Kleinermanns. *J. Phys. Chem. A*, 104:10648, 2000.
- ⁶¹ J. P. Götze, B. Karasulu, and W. Thiel. *J. Chem. Phys.*, 139:234108, 2013.
- ⁶² A. Toniolo and M. Persico. *J. Comp. Chem.*, 22:968, 2001.

- ⁶³ M. Biczysko, J. Bloino, F. Santoro, and Vincenzo Barone. In V. Barone, editor, *Computational Strategies for Spectroscopy*. Wiley, New Jersey, 2012.
- ⁶⁴ M. S. Child and M. Shapiro. *Mol. Phys.*, 48:111, 1983.
- ⁶⁵ G. G. Balint-Kurti, R. N. Dixon, and C. C. Marston. *J. Chem. Soc. Faraday Trans.*, 86:1741, 1990.
- ⁶⁶ G. G. Balint-Kurti. *Adv. Chem. Phys.*, 128:249, 2004.
- ⁶⁷ D. E. Manolopoulos and M. H. Alexander. *J. Chem. Phys.*, 97:2527, 1992.
- ⁶⁸ M. H. Alexander, C. Rist, and D. E. Manolopoulos. *J. Chem. Phys.*, 97:4836, 1992.
- ⁶⁹ D. Picconi and S. Yu. Grebenshchikov. *Phys. Chem. Chem. Phys.*, 17:28931, 2015.
- ⁷⁰ G. G. Balint-Kurti. *J. Chem. Phys.*, 84:4443, 1986.
- ⁷¹ D. Häusler, P. Andresen, and R. Schinke. *J. Chem. Phys.*, 87:3949, 1987.
- ⁷² V. A. Mandelshtam and H. S. Taylor. *J. Chem. Phys.*, 106:5085, 1997.
- ⁷³ R. Schinke. *Photodissociation Dynamics*. Cambridge University Press, Cambridge, 1993.
- ⁷⁴ The rotational motion of free pyrrolyl, treated as a rigid rotor, is described by the Wigner D -functions D_{k0}^j . In order to account for it, each channel carries additional indices j and k corresponding to pyrrolyl angular momentum and its body-fixed projection; the sum extends over j and k , and the definition of the channel momentum includes the total rotational energy of the radical.

Paper 5

Fano resonances in the photoinduced H-atom elimination dynamics in the $\pi\sigma^*$ states of pyrrole. S. Yu. Grebenshchikov and D. Picconi, submitted to *Phys. Chem. Chem. Phys.*

Cite this: DOI: 10.1039/xxxxxxxxxx

Fano Resonances in the Photoinduced H-Atom Elimination Dynamics in the $\pi\sigma^*$ States of Pyrrole[†]

 Sergy Yu. Grebenshchikov^{a*} and David Picconi^a

Received Date

Accepted Date

DOI: 10.1039/xxxxxxxxxx

www.rsc.org/journalname

Fano resonances are predicted to be prominent features of the $\pi\sigma^*$ photochemistry of pyrrole. The Fano interference leads to distorted absorption bands and internally hot photofragments. The interference, studied using high level ab initio theory and quantum mechanics, is supported by two distinct dynamical scenarios controlled by two exit channel conical intersections between the $\pi\sigma^*$ states and the ground electronic state \tilde{X} . For the lowest state ${}^1A_2(\pi\sigma^*)$, the coupling at the conical intersection is weak, and the interfering dissociation pathways are diabatic; for the higher lying ${}^1B_1(\pi\sigma^*)$ state, the coupling at the conical intersection is strong, and the interfering dissociation pathways are adiabatic. Both scenarios persist with increasing number of degrees of freedom included in the dynamic modelling. They are expected to be operative in the $\pi\sigma^*$ photochemistry of a broad class of model UV biochromophores.

We often visualize the course of a chemical reaction as a classical mechanical motion of heavy atoms or functional groups ('billiard balls') leading to a rearrangement of chemical bonds ('springs'); the quantum mechanical description is reserved solely for light electrons.¹ Because exceptions to this picture promise rich chemical insights, there is much interest in predicting and observing quantum effects in chemical dynamics.^{1–3} Prominent examples include tunneling reactions (e.g. photoinduced excited state H-atom transfer in the hydrogen-bonded organic π -systems^{4–8}), non-adiabatic transitions at conical intersections encountered e.g. in the photodissociation of heteroaromatic chromophores^{5,7,9–13}, and resonance phenomena in reactive scattering.^{3,14} All these phenomena are various manifestations of the quantum interference in reacting molecules. The archetype of interference-driven dynamics are Fano resonances whose asym-

metric lineshapes manifest that the final state is formed via two interfering pathways, one direct and one involving an intermediate bound state.¹⁵

While Fano resonances are ubiquitous in the spectroscopy of real¹⁶ and artificial¹⁷ molecules, their observations in chemical reactions are scarce. Photodissociation reactions with a precisely controlled initial state provide a convenient framework for detection of Fano effect^{18,19} — which, indeed, has been observed in photodissociating di- and triatomic molecules.^{20–22} The interference patterns are often believed to be too fragile to survive in larger molecules. An illuminating counterexample has recently been provided: Fano resonances were detected in the photofragment excitation (PHOFEX) spectrum of 5-atomic diarizine²³ suggesting that there is still more to learn about the fundamental interference mechanisms in photoreactive polyatomics.

In this Communication we analyze the near ultraviolet (UV) photodissociation of the 10-atomic pyrrole C_4H_4NH , and predict strong Fano interference effects. Our electronic structure and quantum dynamical calculations focus on the dissociation of the NH bond in the lowest ${}^1A_2(\pi\sigma^*)$ and ${}^1B_1(\pi\sigma^*)$ electronic states interacting with the ground electronic state $\tilde{X}{}^1A_1(\pi\pi)$ [see Fig. 1(a)]. Ultrafast dissociation in the $\pi\sigma^*$ states and the formation of H + pyrrolyl (C_4H_4N) on the time scale of merely ≤ 20 fs²⁴ gives rise to a smooth structureless spectral background [Fig. 1(b,c)]. The interaction with the \tilde{X} state distorts this background absorption: For the pair ${}^1A_2(\pi\sigma^*)/\tilde{X}$, it creates a series of narrow asymmetric Fano resonances; for the pair ${}^1B_1(\pi\sigma^*)/\tilde{X}$, it transforms the continuous absorption into clear progressions of intense asymmetric lines. The impact on the photofragment distributions is also strong, and the internally hot pyrrolyl radicals are formed.

The Fano interference in pyrrole is rooted in the relative arrangement of the potential curves of the $\pi\sigma^*$ states and the \tilde{X} state [Fig. 1(a)] yielding two conical intersections located in the exit channel, well outside the Franck-Condon zone. Very general chemical arguments predict conical intersections with \tilde{X} to be inherent features of $\pi\sigma^*$ states.⁵ In pyrrole, the intersections are well documented and have often been invoked by experimentalists to explain a substantial (up to 50%) population of the \tilde{X}

^a Department of Chemistry, Technische Universität München, Lichtenbergstr. 4, 85747 Garching, Germany

* Sergy.Grebenshchikov@ch.tum.de

[†] Electronic Supplementary Information (ESI) available: Form and ab initio determination of the molecular Hamiltonian, details of quantum chemical calculations, and vibrational state distributions. See DOI: 10.1039/b000000x/

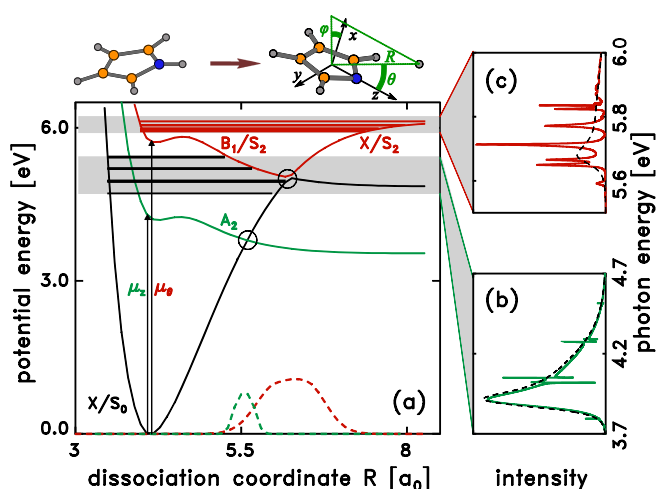


Fig. 1 (a) Ab initio potential energy curves of the ground electronic state $\tilde{X}^1A_1(\pi\pi)$ and the first two $^1\pi\sigma^*$ states of pyrrole as functions of the interfragment Jacobi distance R . The diabatic state $^1A_2(\pi\sigma^*)$ is shown with a green line; the adiabatic state S_2 , which coincides $^1B_1(\pi\sigma^*)$ for $R \leq 5.5a_0$, is shown red. Conical intersections are marked with circles, and the respective local diabatic couplings are exemplified with dashed lines. The tuning mode in both cases is mainly R . The coupling modes for the $^1A_2(\pi\sigma^*)/\tilde{X}$ intersection comprise three out of plane ring deformation coordinates $Q_{a2}(i = 1, 2, 3)$ of a_2 symmetry; the coupling modes for the $^1B_1(\pi\sigma^*)/\tilde{X}$ intersection comprise four vibrational coordinates $Q_{b1}(i = 1, 2, 3, 4)$ of b_1 symmetry, with the out of plane bending θ of the NH group providing the strongest coupling. Also sketched are vibrational levels in \tilde{X} and in the upper adiabatic potential S_2 (black and red horizontal lines). (b) The absorption spectrum of the coupled states $^1A_2(\pi\sigma^*)/\tilde{X}$ (solid green line) calculated using the coordinates R and $Q_{a2}(3)$. The diabatic state $^1A_2(\pi\sigma^*)$ is populated via the transition dipole moment μ_z directed along the NH bond and proportional to $Q_{a2}(3)$. The positions of Fano resonances coincide with the vibrational levels in the \tilde{X} state shown in panel (a). The spectrum of the isolated state $^1A_2(\pi\sigma^*)$ is shown with a dashed line. (c) The absorption spectrum of and the coupled states $^1B_1(\pi\sigma^*)/\tilde{X}$ (solid red line) calculated using the coordinates R and θ . The transition dipole moment is proportional to $\mu_\theta \sim \sin \theta$. The positions of Fano resonances agree well with the vibrational levels in the S_2 state shown in panel (a). The spectrum of the isolated $^1B_1(\pi\sigma^*)$ state is shown with a dashed line.

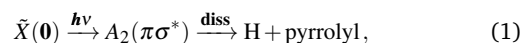
state leading to the formation of slow H-atoms.^{7,25} However, it went hitherto unnoticed that the intersections effectively create a molecular interferometer in which two competing reaction pathways produce stable interference patterns. Two opposite vibronic coupling regimes are realized at these isolated²⁶ intersections, as illustrated by the dimensionless coupling parameter²⁷ $\kappa_c = \lambda_c/\omega_c$ (ω_c is the vibrational frequency and λ_c is the gradient of the off-diagonal diabatic coupling at the intersection). The coupling is small, $\kappa_c \leq 1$, for the $^1A_2(\pi\sigma^*)/\tilde{X}$ pair, and large, $\kappa_c \sim 20$, for the $^1B_1(\pi\sigma^*)/\tilde{X}$ pair [numerical details are given in the Supporting Information (SI)]. In keeping with this distinction, we find two different Fano interference mechanisms in pyrrole, one involving diabatic and the other adiabatic reaction paths.

Electronic structure of pyrrole has been extensively studied and hotly discussed.^{26,28–32} At present, most researchers agree that the first two excited singlet states have the $\pi\sigma^*(3s)$ char-

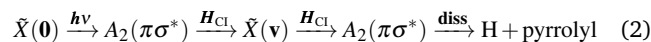
acter and are of A_2 and B_1 symmetry. Definitive assignments of the higher lying absorption bands, including the strongest ones, have begun to emerge only recently.^{24,33} In this study we concentrate on the weak low energy absorption of the $\pi\sigma^*$ states (photon energy $E_{ph} \leq 6.5$ eV) and the resulting photofragment distributions.^{34,35} To this end, new high level electronic structure calculations have been performed for all 24 vibrational degrees of freedom on a coordinate grid uniformly covering the H-atom elimination path from the Franck-Condon zone to the separated H + pyrrolyl. Based on these calculations, a molecular Hamiltonian comprising three electronic states $\tilde{X}^1A_1(\pi\pi)$, $^1A_2(\pi\sigma^*)$, and $^1B_1(\pi\sigma^*)$ is constructed in the local quasi-diabatic³⁶ representation. Off-diagonal diabatic couplings, sketched in Fig. 1(a), are localized at state intersections in the exit channel. With this Hamiltonian, the Fano interference is studied using quantum mechanical calculations. Optical transitions from \tilde{X} are mediated by the coordinate dependent transition dipole moments. Calculations, performed using the program package PolyWave³⁷ and the Heidelberg MCTDH package,³⁸ reproduce the known characteristics of the $\pi\sigma^*$ states in the frequency and time domains (see SI for details).

Conical intersection $\tilde{X}/^1A_2(\pi\sigma^)$: Diabatic dynamics.* The absorption spectrum in Fig. 1(b) is calculated using only two coordinates of the branching space, the tuning mode R and the coupling mode $Q_{a2}(3)$. The narrow spikes of Fano resonances are observed at energies E_X of the vibrationally excited states $|\tilde{X}(\mathbf{v})\rangle$ of the ground electronic state [black horizontal lines in panel (a)]. The one-to-one correspondence between the diabatic states $|\tilde{X}(\mathbf{v})\rangle$ and the Fano resonances is confirmed by direct visual inspection of the wave functions. Note that the states $|\tilde{X}(\mathbf{v})\rangle$ are optically dark. Only the scattering states $|\pi\sigma^*(E)\rangle$ of the repulsive diabatic state $^1A_2(\pi\sigma^*)$ are initially excited. The dark states borrow intensity at the conical intersection via the diabatic coupling matrix element $\mathbf{H}_{Cl} = \langle \tilde{X}(\mathbf{v}) | \hat{H}_{Cl} | \pi\sigma^*(E) \rangle$. This coupling is weak, the resonances are narrow, and the dissociation occurs in the diabatic regime.

The photofragments H + C₄H₄N(²A₂) are formed via two interfering diabatic reaction pathways, both starting from the ground vibrational state $|\tilde{X}(\mathbf{0})\rangle$:



in which the products are formed directly in the $\pi\sigma^*$ state, and



with the products formed via virtual transitions from continuum to the diabatic bound state $|\tilde{X}(\mathbf{v})\rangle$ and back. The absorption cross section $\sigma(E_{ph})$ is given by the photodissociation matrix element $|\langle \tilde{X}(\mathbf{0}) | \mu | \Psi(E_{ph}) \rangle|^2$ involving the exact vibronic state $|\Psi(E_{ph})\rangle$:

$$\sigma(E_{ph}) \sim \left| \langle \tilde{X}(\mathbf{0}) | \mu | \pi\sigma^* \rangle \frac{E_{ph} - E_X}{E_{ph} - E_{res}} + \langle \tilde{X}(\mathbf{0}) | \mu | \pi\sigma^* \rangle \mathbf{H}_{Cl}^* \frac{(-i\pi)}{E_{ph} - E_{res}} \mathbf{H}_{Cl} \right|^2, \quad (3)$$

where $E_{\text{res}} = E_X - i\Gamma_X/2$ is the complex energy of the Fano resonance. The first term in $|\dots|^2$ corresponds to the direct reaction of Eq. (1), the second term corresponds to the indirect reaction of Eq. (2), and optical excitation of the bound states $|\tilde{X}(\mathbf{v})\rangle$ is forbidden. The widths of Fano resonances are small, $\Gamma_X \leq 1 \text{ cm}^{-1}$, for several reasons. First, the weak diabatic coupling is localized near $R_{\text{CI}} = 5.5 a_0$, so that \mathbf{H}_{CI} vanishes unless the state $|\tilde{X}(\mathbf{v})\rangle$ is strongly excited along the N–H bond and can reach R_{CI} (the quantum number $\nu_R \gg 1$). Second, only a small portion of all decay channels $|\pi\sigma^*(E)\rangle$ is accessible to a given bound state: The diabatic coupling, linear in $Q_{a2}(3)$, links only such states $|\tilde{X}(\mathbf{v})\rangle$ and $|\pi\sigma^*(E)\rangle$ which differ by one quantum in this mode, $\nu_{a2} \pm 1$. As a result, the resonance lifetimes reach 1 ps while the direct diabatic dissociation takes about 20 fs.²⁴

The calculation using two degrees of freedom is merely a convenient vehicle to expose the diabatic interference mechanism of Eqs. (1) and (2). In fact, the same mechanism is operative in many dimensions. This is illustrated in a calculation including three coordinates (R, θ, ϕ) of the dissociating hydrogen atom, two coupling modes $Q_{a2}(1)$ and $Q_{a2}(3)$, and an additional in-plane mode $Q_{a1}(5)$ of a_1 symmetry. Figure 2(a) compares the absorption spectrum of the coupled states $\tilde{X}/^1A_2(\pi\sigma^*)$ (solid line) with the hypothetical spectrum calculated for the isolated state $^1A_2(\pi\sigma^*)$ (dashed line). The mode $Q_{a1}(5)$ in the $\pi\sigma^*$ state is strongly displaced relative to the ground state, and the three broad maxima, separated by 1560 cm^{-1} and indicated with arrows, are consecutive excitations in this mode. As in the two dimensional case, the smooth spectral envelope, corresponding to the reaction of Eq. (1), is spiked by intense Fano resonances originating from the bound states in \tilde{X} . Their origin is confirmed by comparison with the spectrum of the \tilde{X} state, as well as by the resonance wave functions whose diabatic components are iden-

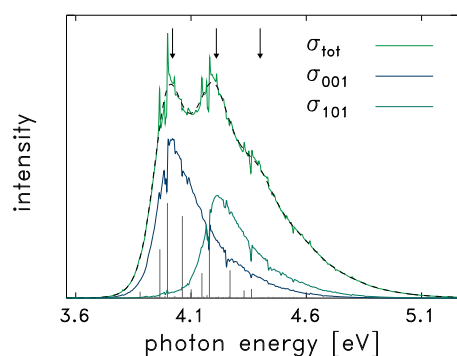


Fig. 2 The total absorption spectrum of the coupled states $^1A_2(\pi\sigma^*)/\tilde{X}$ (solid green line) calculated using three disappearing modes (R, θ, ϕ) of the departing hydrogen, two coupling modes $Q_{a2}(1)$ and $Q_{a2}(3)$, and one mode $Q_{a1}(5)$ of a_1 symmetry. The diabatic state $^1A_2(\pi\sigma^*)$ is populated via the transition dipole moment μ_x directed along the NH bond and proportional to $Q_{a2}(1)$ and $Q_{a2}(3)$. Consecutive excitations of the mode $Q_{a1}(5)$ are marked with arrows. Prominent Fano resonances are emphasized with a stick spectrum. Spiked curves under the total spectrum are the PHOFEX spectra calculated for two final vibrational states of pyrrolyl including 0 or 1 quanta in the mode $Q_{a1}(5)$, 0 or 1 quanta in the mode $Q_{a2}(1)$, and 1 quantum in the mode $Q_{a2}(3)$. The total absorption spectrum of the isolated $^1A_2(\pi\sigma^*)$ state is shown with a dashed line.

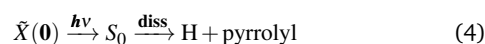
tical with the bound wave functions in \tilde{X} . The added degrees of freedom induce resonance broadening ($\Gamma_X \sim 10 \text{ cm}^{-1}$) because the number of pyrrolyl vibrational modes (i.e. the number of open dissociation channels) increases. Nevertheless, the spacing between the dark states $|\tilde{X}(\mathbf{v})\rangle$ is still much larger than the resonance width Γ_X , and the Fano interference is clearly seen.

Passage through the conical intersection, represented by the term $\mathbf{H}_{\text{CI}}^*(E_{\text{ph}} - E_{\text{res}})^{-1}\mathbf{H}_{\text{CI}}$ in the photodissociation amplitude in Eq. (3), imprints the vibrational structure of the dark state $|\tilde{X}(\mathbf{v})\rangle$ onto the photofragment distributions. Figure 2 illustrates the variation of the yield of pyrrolyl radical in two specific vibrational states with increasing photolysis energy. These PHOFEX spectra (i.e., the partial cross sections) exhibit clear Fano profiles which closely follow the absorption spectrum. There is a one-to-one correspondence between the peaks in the PHOFEX spectra and the excitations of the dark states $|\tilde{X}(\mathbf{v})\rangle$. This is because the \tilde{X}/A_2 conical intersection is located in the reaction exit channel allowing the nodal patterns acquired at the intersection to be carried over onto the dissociated fragment nearly intact (this also leads to a near resonance enhancement of the pyrrolyl vibrational excitation; see SI). The spectral patterns of the photofragment yield spectra sensitively reflect the narrow Fano peaks making PHOFEX a method of choice for detecting the interference effects in the photoproducts.^{22,23}

Conical intersection $\tilde{X}/^1B_1(\pi\sigma^)$: Adiabatic dynamics.* The absorption spectrum of the vibronically coupled states, calculated using the coordinates (R, θ, ϕ) is shown in Fig. 3(a). The smooth absorption envelope, corresponding to fast dissociation in the isolated state $^1B_1(\pi\sigma^*)$, is almost entirely suppressed, the resonances are intense and substantially broadened ($\Gamma_{S_2} \sim 80 \text{ cm}^{-1}$), and line shapes are asymmetric. All this suggests that the Fano interference is again operative in the reaction, but its mechanism is different from the above case of the $^1A_2(\pi\sigma^*)/\tilde{X}$ states.

Indeed, peaks in Fig. 3(a) can no longer be associated with the zeroth order bound states in the \tilde{X} potential. The resonances are best analyzed in the adiabatic, rather than diabatic, representation in terms of the lower adiabatic (S_0) and the upper adiabatic (S_2) surfaces [see Fig. 1(a)]. Taken isolated, the state S_2 is bound up to about 6.5 eV; at the Franck-Condon geometry it coincides with the locally diabatic state $^1B_1(\pi\sigma^*)$ and is optically bright. The state S_0 coincides with \tilde{X} at the Franck-Condon point but correlates with the open channel $\text{H} + \text{pyrrolyl}(^2B_1)$; its oscillator strength is small. Spacings between resonance energies in Fig. 3(a) correlate with progressions of vibrational states $|S_2(\mathbf{v})\rangle$ in the upper adiabatic state (so-called Slonczewski resonances³⁹). The upper adiabatic components of the resonance wave functions, illustrated in panels (d) and (e), identify the two main progressions built on zero and one quantum of the out-of-plane NH bending excitation. Resonances dissociate via the lower adiabatic surface S_0 , and the transition $S_2 \rightarrow S_0$ is mediated by the non-adiabatic derivative coupling \mathbf{A}_{CI} .²⁷

Photodissociation, triggered by the optical excitation from the ground state $|\tilde{X}(\mathbf{0})\rangle$, follows two interfering adiabatic pathways, one involving dissociation in S_0 :



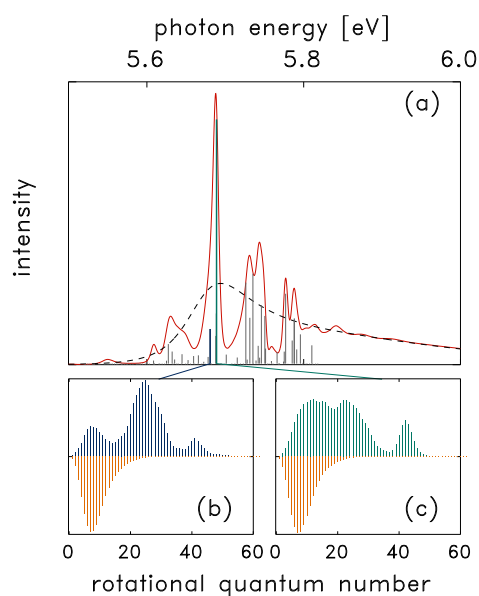
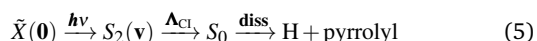


Fig. 3 (a) The absorption spectrum of the coupled states ${}^1B_1(\pi\sigma^*)/\tilde{X}$ (solid red line), calculated using three disappearing modes (R, θ, ϕ) of the departing hydrogen. The diabatic state ${}^1B_1(\pi\sigma^*)$ is populated via the transition dipole moment component proportional to $\sim \sin\theta \cos\phi$. Prominent Fano resonances are shown with a stick spectrum. The spectrum of the isolated ${}^1B_1(\pi\sigma^*)$ state is shown with a dashed line. (b) The rotational state distribution of pyrrolyl calculated at the Fano resonance marked blue in panel (a). The distribution calculated at the same energy for the isolated ${}^1B_1(\pi\sigma^*)$ state is shown with orange color. (c) The same as in (b), but for the resonance marked green in panel (a).

and the other proceeding via optically bright states in S_2 :



Adiabatic reaction dynamics at a conical intersection has been previously analyzed in the visible Chappuis band of ozone.⁴⁰ The photoabsorption cross section is given by

$$\sigma(E_{\text{ph}}) \sim \left| \langle \tilde{X}(\mathbf{0}) | \mu | S_0 \rangle \frac{E_{\text{ph}} - E_{\tilde{X}}}{E_{\text{ph}} - E_{\text{res}}} + \langle \tilde{X}(\mathbf{0}) | \mu | S_2(\mathbf{v}) \rangle \frac{\Lambda_{\text{Cl}}}{E_{\text{ph}} - E_{\text{res}}} \right|^2 \quad (6)$$

The first term corresponds, as in Eq. (3), to the direct dissociation pathway. In this case, this term is small compared to the second one which describes the direct optical excitation of the states $|S_2(\mathbf{v})\rangle$, and the spectrum develops pronounced absorption bands at (complex) resonance energies $E_{\text{res}} = E_{S_2} - i\Gamma_{S_2}/2$.

The S_0/S_2 conical intersection has a profound impact on the rotational distributions of the pyrrolyl fragment. This is illustrated in Fig. 3(b) and (c) comparing the distributions in the coupled S_2/S_0 states calculated near two indicated Fano resonances with the reference case of the isolated diabatic state ${}^1B_1(\pi\sigma^*)$. The non-resonant diabatic distributions (orange lines) are unimodal, the rotational quantum number J does not exceed 20, and the average rotational energy is less than 50 cm^{-1} . These distributions merely reflect^{41,42} the rotational content of the initial state $\mu|\tilde{X}(\mathbf{0})\rangle$ and are commonly assumed in the analysis if the rota-

tional structure remains unresolved in the experiment.⁷ In contrast, the true rotational distributions in the S_0/S_2 dissociation (blue/green lines) are multimodal, extend up to $J \leq 50$, and carry large average rotational energy of 400 cm^{-1} comparable with the low frequency vibrational quanta of pyrrolyl. The impact of the S_0/S_2 conical intersection is not simply quantitative, as in the case of the weakly coupled ${}^1A_2(\pi\sigma^*)/\tilde{X}$ pair, but qualitative. The multiple maxima in the rotational distributions depend on the bending quantum numbers of the underlying resonances $|S_2(\mathbf{v})\rangle$: The stronger the NH bending excitation of the state in the upper adiabatic cone S_2 , the more structured the rotational distribution.

Conclusions. Quantum mechanical Fano interference and Fano resonances are predicted in the $\pi\sigma^*$ photochemistry of pyrrole. Two interference scenarios are found. In the case of states ${}^1A_2(\pi\sigma^*)/\tilde{X}$, weakly coupled at the conical intersection, the interfering reaction pathways are diabatic; in the case of strongly coupled states ${}^1B_1(\pi\sigma^*)/\tilde{X}$, the interfering pathways are adiabatic. The photofragment distributions are affected by the interference in either case, but the second — adiabatic — mechanism is much more efficient in generating hot photofragments. The interferences are stable with respect to increasing number of vibrational degrees of freedom, reflecting the high degree of vibrational adiabaticity in the photodissociation of pyrrole.⁹ NH bond dissociation is a dominant non-radiative relaxation mechanism for many heteroaromatic molecules with pyrrolic chromophores, such as indoles or tryptophan. Moreover, the conical intersections with the ground electronic state \tilde{X} , driving the Fano interference, are known to be a common feature of the $\pi\sigma^*$ states repulsive along the X—H bonds of aromatic molecules with acidic groups (X=O or N). Numerous theoretical and experimental studies confirm this conclusion.^{7,10–13} We therefore expect the Fano interference mechanisms, described in this Communication, to be operative in the $\pi\sigma^*$ photochemistry of a broad class of model UV biochromophores.

References

- 1 A. Warshel, *Angew. Chem. Int. Ed.*, 2014, **53**, 10020.
- 2 K. Liu, *Adv. Chem. Phys.*, 2012, **149**, 1.
- 3 H. Guo, *Nat. Sci. Rev.*, 2015, **2**, 252.
- 4 S. Formosinho and L. G. Arnaut, *J. Photochem. Photobiol.*, 1993, **75**, 21.
- 5 A. L. Sobolewski, W. Domcke, C. Dedonder-Lardeux and C. Jouvet, *Phys. Chem. Chem. Phys.*, 2002, **4**, 1093.
- 6 A. Migani, L. Blancafort, M. A. Robb and A. D. DeBellis, *J. Am. Chem. Soc.*, 2008, **130**, 6932.
- 7 M. N. R. Ashfold, G. A. King, D. Murdock, M. G. D. Nix, T. A. Oliver and A. G. Sage, *Phys. Chem. Chem. Phys.*, 2010, **12**, 1218.
- 8 X. Liu, A. L. Sobolewski and W. Domcke, *J. Phys. Chem. A*, 2014, **118**, 7788.
- 9 M. N. R. Ashfold, B. Cronin, A. L. Devine, R. N. Dixon and M. G. D. Nix, *Science*, 2006, **312**, 1637.
- 10 G. M. Roberts and V. Stavros, *Chem. Sci.*, 2014, **5**, 1698.
- 11 X. Xu, J. Zheng, K. R. Tang and D. G. Truhlar, *J. Am. Chem. Soc.*, 2014, **136**, 16378.

- 12 B. Marchetti, T. N. V. Karsili, M. N. R. Ashfold and W. Domcke, *Phys. Chem. Chem. Phys.*, 2016, **18**, 20007.
- 13 C. Xie, J. Ma, X. Zhu, D. Yarkony, S. Xie and H. Guo, *J. Am. Chem. Soc.*, 2016, **138**, 7828.
- 14 P. G. Jambrina, D. Herraes-Aguilar, F. J. Aoiz, M. Sneha, J. Jankunas and R. N. Zare, *Nat. Chem.*, 2015, **7**, 661.
- 15 U. Fano, *Phys. Rev.*, 1961, **124**, 1866.
- 16 J. Jortner, *Pure Appl. Chem.*, 1970, **24**, 165.
- 17 A. E. Miroshnichenko, S. Flach and Y. S. Kivshar, *Rev. Mod. Phys.*, 2010, **82**, 2257.
- 18 M. S. Child and S. Chapman, *J. Phys. Chem.*, 1991, **95**, 578.
- 19 S. T. Cornett, H. R. Sadeghpour, H. R. and M. J. Cavagnero, *Phys. Rev. Lett.*, 1999, **82**, 2488.
- 20 B. Kim, K. Yoshihara and S. Lee, *Phys. Rev. Lett.*, 1994, **73**, 424.
- 21 A. Hishikawa, K. Ohde, R. Itakura, S. Liu, K. Yamanouchi and K. Yamashita, *J. Phys. Chem. A*, 1997, **101**, 694.
- 22 J. T. Brandon, S. A. Reid, D. C. Robie and H. Reisler, *J. Chem. Phys.*, 1992, **97**, 5246.
- 23 D.-S. Ahn, S.-Y. Kim, G.-I. Lim, S. Lee, Y. S. Choi and S. K. Kim, *Angew. Chem. Int. Ed.*, 2010, **49**, 1244.
- 24 G. Wu, S. P. Neville, O. Schalk, T. Sekikawa, M. N. R. Ashfold, G. A. Worth and A. Stolow, *J. Chem. Phys.*, 2015, **142**, 074302.
- 25 D. A. Blank, S. W. North and Y. T. Lee, *Chem. Phys.*, 1994, **187**, 35.
- 26 V. Vallet, Z. Lan, S. Mahapatra, A. L. Sobolewski and W. Domcke, *J. Chem. Phys.*, 2005, **123**, 144307.
- 27 H. C. Longuet-Higgins, U. Opik, L. H. M. Price and R. A. Sack, *Proc. R. Soc. A*, 1958, **244**, 1.
- 28 B. O. Roos, P.-Å. Malmqvist, V. Molina, L. Serrano-Andres and M. Merchán, *J. Chem. Phys.*, 2002, **116**, 7526.
- 29 A. B. Trofimov and J. Schirmer, *Chem. Phys.*, 1997, **214**, 153.
- 30 O. Christiansen, J. Gauss, J. F. Stanton and P. Jørgensen, *J. Chem. Phys.*, 1999, **111**, 525.
- 31 M. H. Palmer and P. J. Wilson, *Mol. Phys.*, 2003, **101**, 2391.
- 32 S. Faraji, M. Vazdar, V. S. Reddy, M. Eckert-Maksic, H. Lischka and H. Köppel, *J. Chem. Phys.*, 2011, **135**, 154310.
- 33 S. P. Neville and G. A. Worth, *J. Chem. Phys.*, 2014, **140**, 034317.
- 34 B. Cronin, M. G. D. Nix, R. H. Qadiri and M. N. R. Ashfold, *Phys. Chem. Chem. Phys.*, 2004, **6**, 5031.
- 35 G. M. Roberts, C. A. Williams, H. Yu, A. S. Chatterley, J. D. Young, S. Ullrich and V. G. Stavros, *Faraday Discuss.*, 2013, **163**, 95.
- 36 H. Köppel, Diabatic Representation: Methods for the Construction of Diabatic Electronic States. In *Conical Intersections*, W. Domcke., D. Yarkony, D. and H. Köppel, Eds., World Scientific, Singapore, 2004; p. 175.
- 37 'PolyWave' is a package of FORTRAN90 programs for iterative quantum mechanical calculations of bound/resonance states, photoabsorption/photoemission spectra, and photofragment distributions in molecules with up to six internal degrees of freedom and many coupled electronic states. It is available from S.Yu.G. upon request .
- 38 M. H. Beck, A. Jäckle, G. A. Worth, G. A. and H.-D. Meyer, *Phys. Rep.*, 2000, **324**, 1.
- 39 J. C. Slonczewski, *Phys. Rev. Lett.*, 1963, **131**, 1596.
- 40 S. Yu. Grebenshchikov, R. Schinke, Z.-W. Qu and H. Zhu, *J. Chem. Phys.*, 2006, **124**, 204313.
- 41 M. S. Child and M. Shapiro, *Mol. Phys.*, 1983, **48**, 111.
- 42 A. Garcia-Vela, R. B. Gerber, D. G. Imre and J. J. Valentini, *Phys. Rev. Lett.*, 1993, **71**, 931.

Supplementary information for:

Fano Resonances in the Photoinduced H-Atom Elimination Dynamics in $\pi\sigma^*$ States of Pyrrole

Sergy Yu. Grebenschchikov* and David Picconi

*Department of Chemistry, Technische Universität München,
Lichtenbergstr. 4, 85747 Garching, Germany*

I. AB INITIO MOLECULAR HAMILTONIAN

A. The form of the molecular Hamiltonian

(1) The molecular Hamiltonian,

$$\hat{H} = \begin{pmatrix} \hat{T} & 0 & 0 \\ 0 & \hat{T} & 0 \\ 0 & 0 & \hat{T} \end{pmatrix} + \begin{pmatrix} V^X & V^{XA_2} & V^{XB_1} \\ V^{XA_2} & V^{A_2} & V^{A_2B_1} \\ V^{XB_1} & V^{A_2B_1} & V^{B_1} \end{pmatrix}, \quad (1)$$

is set in the basis of three locally diabatic electronic states $\tilde{X}A_1$ (abbreviated as X or A_1), A_2 , and B_1 ; the state symmetry labels refer to C_{2v} geometries. Pyrrole is described using (a) three Jacobi coordinates $\mathbf{R} \equiv (R, \theta, \phi)$ of the dissociating H-atom relative to the center of mass of the pyrrolyl fragment (the so-called ‘disappearing modes’; see Fig. S1) and (b) 21 dimensionless normal modes \mathbf{Q} of pyrrolyl, calculated at the equilibrium geometry of the fragment (the so-called ‘non-disappearing modes’; examples of them are given in Fig. S2). The normal modes \mathbf{Q} are partitioned into four blocks according to the irreps Γ of the C_{2v} symmetry group, $\mathbf{Q} = \{\mathbf{Q}_{a1}, \mathbf{Q}_{a2}, \mathbf{Q}_{b1}, \mathbf{Q}_{b2}\}$.

(2) The kinetic energy operator in Eq. (1) is set in the body-fixed principal axis frame for the zero total angular momentum of pyrrole (atomic units are used hereafter):

$$\hat{T} = -\frac{1}{2\mu} \frac{\partial^2}{\partial R^2} - \frac{1}{2} \sum_{\Gamma=a_1, a_2, b_1, b_2} \sum_i^{\Gamma} \omega_{\Gamma}(i) \frac{\partial^2}{\partial Q_{\Gamma}(i)^2} + \frac{\mathbf{j}^2}{2\mu R^2} + \frac{1}{2} \left(\frac{j_x^2}{I_x} + \frac{j_y^2}{I_y} + \frac{j_z^2}{I_z} \right). \quad (2)$$

The first term is the kinetic energy of the relative motion of the H-atom and pyrrolyl; μ is the corresponding reduced mass. The second term refers to pyrrolyl vibrations; the

* Electronic mail: Sergy.Grebenschchikov@ch.tum.de

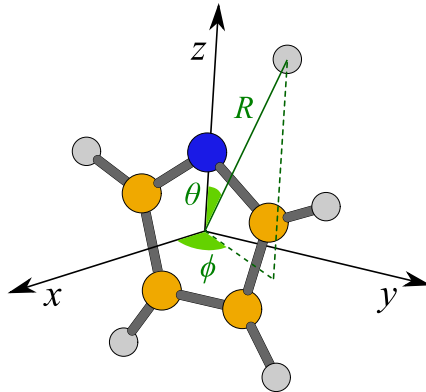
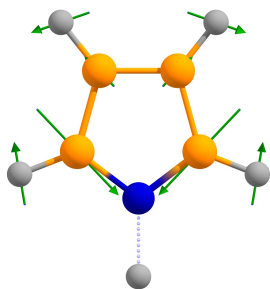
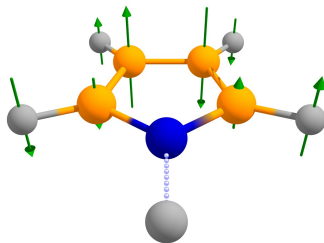


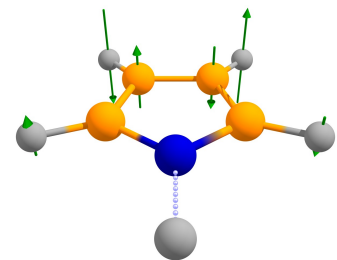
FIG. S1: Body-fixed pyrrolyl axes and Jacobi coordinates (R, θ, ϕ) for the detaching H atom in pyrrole (H - gray; C - orange; N - blue).



$Q_{a1}(5)$ ($\omega = 1558 \text{ cm}^{-1}$)



$Q_{a2}(1)$ ($\omega = 533 \text{ cm}^{-1}$)



$Q_{a2}(3)$ ($\omega = 932 \text{ cm}^{-1}$)

FIG. S2: Pyrrolyl normal modes used in the quantum mechanical calculations. The a_1 modes are the totally symmetric in-plane distortions. The out-of-plane a_2 modes are antisymmetric with respect to the reflection planes σ_v , σ'_v and symmetric with respect to rotations about the C_2 axis.

sum \sum_i^Γ runs over the vibrational modes i belonging to the irrep Γ . The last two terms describe the orbital motion of the H-atom and the rotational motion of the rigid pyrrolyl ring; $\mathbf{j} = (j_x, j_y, j_z)$ is the pyrrolyl angular momentum operator and the inertia constants I_x , I_y and I_z are evaluated at the fragment equilibrium geometry; the C_{2v} symmetric pyrrolyl ring lies in the yz -plane, with z being the C_2 axis (see Fig. S1).

(3) The elements of the diabatic potential energy matrix in Eq. (1) are constructed as sums of two groups of terms,

$$\mathbf{V}(\mathbf{R}, \mathbf{Q}) = \mathbf{V}_R(\mathbf{R}) + \mathbf{V}_Q(\mathbf{Q}|\mathbf{R}) \quad (3)$$

Functions $\mathbf{V}_R(\mathbf{R})$ of the three disappearing modes are constructed using spline interpolations of the ab initio points calculated on a dense coordinate grid (R, θ, ϕ) . Functions $\mathbf{V}_Q(\mathbf{Q}|\mathbf{R})$,

depending on the 21 non-disappearing modes \mathbf{Q} , are constructed in the spirit of the vibronic coupling model,¹ with pyrrolyl treated as a semirigid ring using quadratic Hamiltonians, and parameters depending on the interfragment distance R .

(4) The diagonal elements V^α have the form ($\alpha = X, A_2, B_1$):

$$V^\alpha(R, \theta, \phi, \mathbf{Q}) = V_R^\alpha(R, \theta, \phi) + \sum_i^{a_1} \kappa_i^\alpha(R) Q_{a_1}(i) + \frac{1}{2} \sum_\Gamma \sum_{i,j} \gamma_{\Gamma,ij}^\alpha(R) Q_\Gamma(i) Q_\Gamma(j). \quad (4)$$

where $\kappa_i^\alpha(R)$ are the R -dependent gradients (vanishing for all modes but a_1) and $\gamma_{ij}^\alpha(R)$ are the R -dependent normal mode Hessians matrices evaluated at $\mathbf{Q} = \mathbf{0}$; matrices γ^α are four-block diagonal: $\gamma^\alpha = \gamma_{a_1}^\alpha \oplus \gamma_{a_2}^\alpha \oplus \gamma_{b_1}^\alpha \oplus \gamma_{b_2}^\alpha$.

(5) The off-diagonal diabatic couplings $V^{\alpha\beta}$ are

$$V^{\alpha\beta}(R, \theta, \phi, \mathbf{Q}) = V_R^{\alpha\beta}(R, \theta, \phi) + \sum_i^{\Gamma_\alpha \times \Gamma_\beta} \lambda_i^{\alpha\beta}(R) Q_{\Gamma_\alpha \times \Gamma_\beta}(i). \quad (5)$$

The functions $V_R^{\alpha\beta}(R, \theta, \phi)$ are the coupling elements between the regularized quasi-diabatic states constructed on the ab initio coordinate grid as suggested by Köppel et al.² Although they do not have a simple analytical representation, they are forced to follow the lowest allowed orders in the symmetry-adapted spherical harmonics near conical intersections, namely $V_R^{A_1A_2} \sim \sin^2 \theta \sin(2\phi)$ and $V_R^{A_1B_1} \sim \sin \theta \cos \phi$. The \mathbf{Q} -dependent coupling terms for X/A_2 and X/B_1 are linear in the vibrational modes of a_2 and b_1 symmetry, respectively. The coupling matrix element $V^{A_2B_1}$ between the states A_2/B_1 is not included in the quantum mechanical calculations.

(6) The quasi-diabatic representation of the Hamiltonian of Eq. (1) is local, and a given off-diagonal matrix element is non-zero only in the vicinity of the respective conical intersection. For the second term in Eq. (5), this is achieved by using the following functional form for the coupling strength $\lambda_i^{\alpha\beta}$:

$$\lambda_i^{\alpha\beta}(R) = \lambda_{\text{CI},i}^{\alpha\beta} \exp \left(- \left| \frac{R - R_{\text{CI}}^{\alpha\beta}}{\Delta} \right|^n \right), \quad (6)$$

where $R_{\text{CI}}^{\alpha\beta}$ is the position of a conical intersection between $\alpha/\beta = X/A_2$ or X/B_1 . The parameters $\lambda_{\text{CI},i}^{\alpha\beta}$, Δ and n are tuned ‘by eye’ in order to obtain smooth diabatic Hessians for the coupled states. For the first term in Eq. (5), similar attenuation functions are applied to the (R, θ, ϕ) -dependent mixing angles of the regularized adiabatic-to-diabatic transformation.

B. Ab initio parameters of the molecular Hamiltonian

(1) The matrix elements of the molecular Hamiltonian are found from the electronic structure calculations performed along the minimum energy path (MEP) for the hydrogen detachment from the NH group. The MEP is evaluated on a grid in the Jacobi coordinate R in the lowest excited state ${}^1A_2(\pi\sigma^*)$. The grid consists of 37 points chosen between $R_{\min} = 3.5 a_0$ and $R_{\max} = 8.3 a_0$ (at short distances the spacing is $\sim 0.1 a_0$, in the asymptotic region it is $\sim 0.4 a_0$). The resulting energy profiles are shown in Fig. 1 of the main paper. Along MEP, the molecule is constrained to C_{2v} geometries (i.e., $\theta, \phi = 0$). Aug-cc-pVTZ (AVTZ) basis set of Dunning³ is used and further supplemented with the diffuse s and p functions added to the N and H atoms of the dissociating bond (one set of s and p functions for N and two sets for H). The exponents of these functions are derived in an even tempered manner from the most diffuse s and p functions of the AVTZ basis by dividing the exponents successively by a factor of 3.0.⁴ This extension is necessary to correctly describe the Rydberg character of the A_2 and B_1 states, and the resulting basis set is referred to as AVTZ+.

(2) Most calculations are performed at the CASPT2 level of theory. The reference wavefunctions are obtained from the state-averaged CASSCF calculations including the $1A_1$, $1A_2$ and $1B_1$ states. The active space (eight electrons in seven orbitals) comprises five π valence molecular orbitals, three of b_1 and two of a_2 symmetry, the $9a_1(\sigma)$ and the $10a_1(3s/\sigma^*)$ orbitals. Electronic structure calculations are performed using the highest possible symmetry. In particular, the a_1 , a_2 , b_1 and b_2 blocks of the Hessian matrices are calculated separately using C_{2v} , C_2 , C_s and C'_s symmetries, respectively. Coordinate dependent transition dipole moment (TDM) functions, necessary to properly describe the optical excitation of the $\pi\sigma^*$ states from the ground electronic state, are calculated at the CASSCF level.

(3) Table I summarizes the characteristic features of the three calculated electronic states of pyrrole. The ordering of the electronic states at the Franck-Condon point is correctly reproduced by the present CASPT2 calculations. Vertical excitation energies of the $\pi\sigma^*$ states are underestimated by 0.4 eV-0.6 eV compared to the CCSD and MRCI results; the agreement with the known experimental values is within similar bounds. The accuracy of the calculated dissociation thresholds is slightly better. Tables II and III provide further characterization of the molecular Hamiltonian and give the dimensionless coupling strength parameters $\kappa_c = \lambda/\omega$ for the coupling modes of a_2 and b_1 symmetries, respectively. The

TABLE I: Characteristic data of the ab initio potential energy surfaces of the three lowest electronic states of pyrrole: Vertical excitation energy T_v (in eV); band origin T_0 (in eV), which includes ZPEs of the ground and the excited electronic states; quantum mechanical thresholds D_0 for the electronic channels diabatically correlating with the calculated states (in eV). Available theoretical and experimental results are shown for comparison.

Diabatic state	T_v	T_0	T_0 (exp)	Dissociation channel	D_0^a	D_0 (exp.)
$\tilde{X}^1A_1(\pi\pi)$	0.0	0.0	0.0	H(1S)/pyrrolyl(1^2A_1)	5.09	—
	4.80 ^a	4.32	<4.88 ^d	H(1S)/pyrrolyl(1^2A_2)	3.40	4.07 ^d
$1^1A_2(\pi\sigma^*)$	5.17 ^b					
	5.59 ^c					
	5.45 ^a	5.30	5.86 ^e	H(1S)/pyrrolyl(1^2B_1)	3.96	4.62 – 4.67 ^f
$2^1B_1(\pi\sigma^*)$	5.88 ^b					
	5.84 ^c					

^aThis work; CASPT2.

^bRef. 5; CCSD.

^cRef. 6; MRCl.

^dRef. 7.

^eRef. 8.

^fDFT⁹ and MRCl¹⁰ methods estimate the difference in the threshold energies $D_0(1^2B_1) - D_0(1^2A_2)$ to be in the range of 0.55 eV—0.60 eV.

frequency ω is taken to be the pyrrolyl frequency at the respective intersection.

(4) The potential energies of the states \tilde{X} , A_2 , and B_1 as functions of the disappearing modes are found on a three-dimensional grid (R_i, θ_j, ϕ_k) , with the nodes R_i being grid points on the MEP; the CASPT2 method and the C_1 symmetry are used. The polar angles θ_j cover the range $[0^\circ, 90^\circ]$ with a step of 5° ; energies for $\theta > 90^\circ$ are extrapolated. The grid in the azimuthal angle ϕ ranges from 0° (H-atom in the σ'_v plane) to 90° (H-atom in the σ_v plane) with a step of 15° ; energies for larger ϕ are reconstructed using C_{2v} symmetry of the pyrrolyl ring. The quasi-diabatic representation near the X/B_1 conical intersection is constructed from the adiabatic energies using the regularized adiabatic-to-diabatic transformation (ADT) method of Köppel et al.² In the next step, all matrix elements set on the grid are interpolated with cubic splines. The angular modes do not couple the states X and A_2 at either $\phi = 0^\circ$

TABLE II: Vibrational frequencies $\omega(i)$ (in cm^{-1}), coupling strengths λ_i (in cm^{-1}), and the dimensionless coupling strength parameters $\kappa_c = \lambda_c/\omega_c$ for the vibrational modes of a_2 symmetry at the X/A_2 conical intersection.

Mode	λ_c	ω_c	κ_c
$Q_{a_2}(1)$	574.0	551.8	1.04
$Q_{a_2}(2)$	759.0	895.7	0.85
$Q_{a_2}(3)$	213.0	940.3	0.23

TABLE III: Vibrational frequencies $\omega(i)$ (in cm^{-1}), coupling strengths λ_i (in cm^{-1}), and the dimensionless coupling strength parameters $\kappa_c = \lambda_c/\omega_c$ for the vibrational modes of b_1 symmetry at the X/B_1 conical intersection. For the angle θ , λ_θ is evaluated as a gradient $\partial V/\partial(\sin \theta)$ at the intersection.

Mode	λ_c	ω_c	κ_c
θ	19751.00	854.00	23.12
$Q_{b_1}(1)$	1151.00	823.6	1.40
$Q_{b_1}(2)$	600.00	765.2	0.78
$Q_{b_1}(3)$	265.00	875.3	0.30

or 90° , and the small coupling matrix element $V^{XA_2}(R, \theta, \phi)$ is set as an analytic function $V^{XA_2}(R, \theta, \phi) = \lambda_{\text{ang}}^{XA_2}(R) \sin^2 \theta \sin(2\phi)$, with $\lambda_{\text{ang}}^{XA_2}(R) = c[1 - \text{atan}((R - R_0)/\Delta R)]$. The parameters in this function are chosen ‘by eye’ in order to give smooth diabatic curves for $\phi \neq 0^\circ, 90^\circ$.

(5) The parameters of the \mathbf{Q} -dependent part of the Hamiltonian are calculated as first and second derivatives with respect to deviations from the MEP. To this end, the dimensionless normal modes \mathbf{Q} are constructed using the Hessian matrix at the equilibrium pyrrolyl geometry via

$$Q_i = \sum_r \sqrt{\frac{\omega_i M_r}{\hbar}} U_{ir} X_r = \sum_r L_{ir} X_r, \quad i = 1, 21 \quad \text{and} \quad r = 1, 27 \quad (7)$$

where $\{X_r\}$ are the 27 Cartesian coordinates of all atoms; M_r is the mass of the atom associated with the coordinate X_r ; ω_i is the frequency of the normal mode Q_i ; $\{U_{ir}\}$ is the matrix of eigenvectors of the mass-weighted Cartesian Hessian, after the removal of the

rows corresponding to the global translations and rotations. Next, the Cartesian gradient and the Cartesian Hessian for the pyrrolyl ring are calculated along the MEP $\mathbf{Q} = \mathbf{Q}_{\min}(R)$ and transformed to the basis of the dimensionless normal modes giving the gradient vector $\mathbf{g}^\alpha(R)$ and the Hessian matrix $\gamma^\alpha(R)$. The gradient $\mathbf{g}^\alpha(R)$ vanishes only for the state A_2 ; for the states \tilde{X} and B_1 , it differs from zero. For these states, the gradient $\boldsymbol{\kappa}^\alpha(R)$ at $\mathbf{Q} = \mathbf{0}$ is reconstructed using the gradient $\mathbf{g}^\alpha(R)$ and the Hessian $\gamma^\alpha(R)$:

$$\boldsymbol{\kappa}^\alpha(R) = \mathbf{g}^\alpha(R) - \gamma^\alpha(R)\mathbf{Q}_{\min}(R) , \quad (8)$$

For some blocks of the adiabatic Hessian, a local quasi-diabatic representation is constructed: The Jacobi distance R is the tuning mode for the conical intersections \tilde{X}/A_2 and \tilde{X}/B_1 , and the blocks a_2 and b_1 diverge as R approaches an intersection. The diabatic matrix elements, smoothly depending on R , are found using a transformation akin to the ADT method of Köppel et al.². For example, for the \tilde{X}/A_2 pair, one finds

$$\begin{aligned} \gamma_{ij}^X(R)|_{\text{dia}} &= \tilde{\gamma}_{ij}^X(R)|_{\text{adia}} + 2 \frac{\lambda_i^{XA_2}(R)\lambda_j^{XA_2}(R)}{V_R^X(R, 0, 0) - V_R^{A_2}(R, 0, 0)} \\ \gamma_{ij}^{A_2}(R)|_{\text{dia}} &= \tilde{\gamma}_{ij}^{A_2}(R)|_{\text{adia}} - 2 \frac{\lambda_i^{XA_2}(R)\lambda_j^{XA_2}(R)}{V_R^X(R, 0, 0) - V_R^{A_2}(R, 0, 0)} , \quad \Gamma_i = \Gamma_j = a_2 . \end{aligned} \quad (9)$$

Similar equations hold for the \tilde{X}/B_1 pair of states. The local character of the diabatic functions is guaranteed via the R -dependence of the coupling coefficients λ_i defined in Eq. (6).

(6) The photodissociation dynamics in the $^1\pi\sigma^*$ states is sensitive to the coordinate dependence of the TDMs expressed as a Herzberg-Teller expansion,

$$\boldsymbol{\mu}(\mathbf{R}, \mathbf{Q}) \approx \boldsymbol{\mu}_R(\mathbf{R}) + \boldsymbol{\mu}_Q(\mathbf{Q}) , \quad (10)$$

in which only linear (and therefore additive) deviations from the Franck-Condon geometry are taken into account. The expansion coefficients are calculated at the CASSCF level of theory as numerical first derivatives of the TDMs with respect to nuclear displacements along the normal modes.

II. QUANTUM MECHANICAL CALCULATIONS

(1) The absorption spectra and the product state distributions, discussed in the main paper, are calculated using the Hamiltonian of Eq. (1) in which some coordinates are dynamically

TABLE IV: Summary of the calculations reported in the main paper.

	Included states	Included coordinates	T_v [eV]	Transition dipole moment
M1.	X and A_2	$(R, Q_{a_2}(3))$	3.96	$\mu = g_3 Q_{a_2}(3)$
M2.	X and A_2	$(R, \theta, \phi, Q_{a_1}(5), Q_{a_2}(1), Q_{a_2}(3))$	4.20	$\mu = g_1 Q_{a_2}(1) + g_3 Q_{a_2}(3)$
M3.	X and B_1	(R, θ)	5.69	$\mu = g_\theta \sin \theta$
M4.	X and B_1	(R, θ, ϕ)	5.69	$\mu = g_\theta \sin \theta \cos \phi$

active (i.e. ‘included’) while others are kept fixed to their asymptotic values (i.e. ‘excluded’). These coordinate choices are listed in Table IV. Note that the vertical excitation energies depend on the number of included a_1 modes; the corresponding values are shown in Table IV. The dynamics of the coupled pairs of states X/A_2 and X/B_1 are studied separately, as was previously done in Ref. 4.

(2) Most of the reported calculations of the absorption spectra, bound and resonance eigenstates, and the product state distributions are performed using the program package PolyWave.¹² The code is applicable to general complex symmetric molecular Hamiltonians \mathbf{H} represented as $N \times N$ matrices in the basis of N coupled diabatic electronic states. The time correlation functions, the energy dependent T -matrix elements, and the cross sections are calculated on equal footing using global in energy Chebyshev expansion of the propagator, thus allowing comparisons with both pump-probe and frequency resolved experiments. Filter diagonalization is performed in order to calculate the spectrum of metastable resonance states providing dynamical assignments of diffuse structures in the absorption spectra. The discrete variable representation (DVR) is used in the calculations. For the R coordinate, 100 potential optimized DVR points are used in the range $3.0 a_0 - 14.0 a_0$. For the angular coordinate θ , 100 Gauss-Legendre DVR points are used in the range $(0, \pi)$, and the coordinate ϕ is represented using 32 DVR points selected uniformly between 0 and 2π . The grids for the vibrational coordinates from the \mathbf{Q} -space consist of up to 32 potential optimized DVR points. The product state distributions are calculated using the method of Balint-Kurti et al.¹³

(3) The calculation M2 in Table IV is performed using the multi-configurational time-dependent Hartree method (MCTDH) as implemented in the Heidelberg MCTDH package.¹⁴ The primitive grid in R consists of 98 sine DVR grid points chosen between $3.3 a_0$ and

13.0 a_0 ; the (θ, ϕ) -dependent functions were represented using a two-dimensional Legendre DVR with $j_{\max} = 71$ and $m_{\max} = 21$; for the mode $Q_{a1}(5)$ 25 harmonic oscillator DVR grid points were used; for the modes $Q_{a2}(1)$ and $Q_{a2}(3)$ 17 harmonic oscillator DVR points were used. The MCTDH wave function is expressed in the multi-set form expressed using five (combined) modes $\{R, (\theta, \phi), Q_{a1}(5), Q_{a2}(1), Q_{a2}(3)\}$ with the scheme of $\{(18, 16), (24, 11), (14, 10), (7, 6), (7, 6)\}$ single-particle functions for each combined mode and each state. Final state populations were calculated using the flux analysis method, as implemented in the MCTDH code.¹⁵

(4) The vibrational distributions of pyrrolyl in the in-plane mode $Q_{a1}(5)$ and in the coupling mode $Q_{a2}(1)$ for the photon energy $E_{\text{ph}} = 3.86 \text{ eV}$, corresponding to a Fano resonance, are compared in Fig. S3(a) and (b) with the distributions emerging in a direct dissociation (isolated state 1A_2). The distributions in the direct process (orange sticks) mainly reflect the projection of the initial state $\mu|\tilde{X}(\mathbf{0})\rangle$ onto the vibrations of the free pyrrolyl. Both the in-plane mode $Q_{a1}(5)$ and the coupling mode $Q_{a2}(1)$ remain cold (only $v = 0, 1$ are populated). Near resonance, these distributions spread to higher vibrational quantum numbers (blue sticks). This additional vibrational excitation is due to the dark diabatic component $|\tilde{X}(\mathbf{v})\rangle$ amplified by the coordinate dependence of the vibronic coupling \hat{H}_{CI} . The vibronic coupling is weak, and the extra excitation due to $\hat{H}_{\text{CI}}|\tilde{X}(\mathbf{v})\rangle$ is limited to few quanta. Since the vibronic coupling is linear in the a_2 modes, the sequence of two diabatic transfers [Eqs. (2) and (3) of the main text] can induce an excitation by maximum two quanta in the coupling modes.

Note that the experimental detection of the interference structures in the photofragment distributions can be hindered by the small width of Fano resonances. For example, the photofragment kinetic energy measurements of Ashfold and co-workers,⁷ performed at fixed photolysis wavelengths, can easily miss narrow resonance states. In contrast, PHOFEX spectra of pyrrole, discussed in the main text, are well suited to resolve the interference effects emerging from the conical intersection.

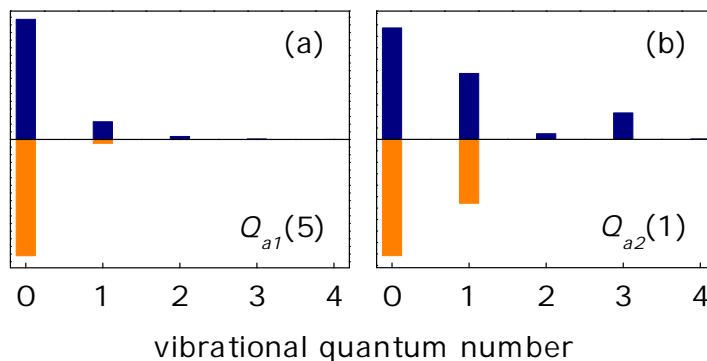


FIG. S3: (a) The vibrational distribution for the pyrrolyl mode $Q_{a1}(5)$ calculated for the excitation energy $E_{\text{ph}} = 3.86 \text{ eV}$, corresponding to a Fano resonance, as a blue stick. The distribution calculated at the same energy for the isolated state ${}^1A_2(\pi\sigma^*)$ is shown with orange color. (b) The same as in (a), but for the pyrrolyl mode $Q_{a2}(1)$.

-
- ¹ H. Köppel, L. S. Cederbaum, and W. Domcke, *Adv. Chem. Phys.* **57**, 59 (1984)
- ² H. Köppel, J. Gronki, and W. Domcke, *J. Chem. Phys.* **115**, 2377 (2001)
- ³ T. H. Dunning, *J. Chem. Phys.* **90**, 1007 (1989)
- ⁴ V. Vallet, Z. Lan, S. Mahapatra, A. L. Sobolewski and W. Domcke, *J. Chem. Phys.* **123**, 144307 (2005)
- ⁵ O. Christiansen, J. Gauss, J. F. Stanton, and P. Jorgensen, *J. Chem. Phys.* **111**, 525 (1999)
- ⁶ M. H. Palmer and P. J. Wilson, *Mol. Phys.* **101**, 2391 (2003)
- ⁷ B. Cronin, M. G. D. Nix, R. H. Qadiri and M. N. R. Ashfold, *PCCP* **6**, 5031 (2004)
- ⁸ M. H. Palmer, I. C. Walker and M. F. Guest, *Chem. Phys.* **238**, 179 (1998)
- ⁹ A. J. Gianola, T. Ichino, R. L. Hoenigman, S. Kato, V. M. Bierbaum and W. C. Lineberger, *J. Phys. Chem. A* **108**, 10326 (2004)
- ¹⁰ A. Motzke, Z. Lan, C. Woywod and W. Domcke, *Chem. Phys.* **329**, 50 (2006)
- ¹¹ W. H. Miller, N. C. Handy, and J. E. Adams, *J. Chem. Phys.* **72**, 99 (1979)
- ¹² ‘PolyWave’ is a package of FORTRAN90 programs for iterative quantum mechanical calculations of bound states, dissociative resonance states, photoabsorption or photoemission spectra, as well as product state distributions in molecules with up to six internal degrees of freedom and $N \leq 9$ coupled electronic states. The package is available from the author upon request.

- ¹³ G. G. Balint-Kurti, R. N. Dixon, and C. C. Marston, *J. Chem. Soc. Faraday Trans.* **86**, 1741 (1990)
- ¹⁴ G. A. Worth, M. H. Beck, A. Jäckle, and H.-D. Meyer. The MCTDH Package, version 8.4, see <http://mctdh.uni-hd.de>
- ¹⁵ A. Jäckle and H.-D. Meyer, *J. Chem. Phys.* **105**, 6778 (1996)